

Investigations of Detector Methods for Gamma-Ray Spectroscopy with PARIS



Oliver James Roberts
Doctor of Philosophy

University of York
Department of Physics

October 2010

Abstract

This thesis describes the theoretical and practical application of various detector methods intended for use in the construction of a new high efficient 8π calorimeter intended for γ -ray spectroscopy called PARIS (Photon Array for the studies of Radioactive and Ion Stable beams).

Simulations of various forms of the calorimeter, associated efficiencies, and fold distributions have been studied using GEANT4 and ROOT. It was found that the most cost efficient way to produce this detector array, was to adopt a cubic design that allows for multiple physics cases and synergies with already existing and proposed arrays, at the end of the SPIRAL2 beam line in GANIL, France.

An investigation of $\text{LaBr}_3(\text{Ce})$ and $\text{CsI}(\text{Na})$ scintillators was performed to determine the most efficient arrangement for PARIS. Various detector methods to increase the overall performance of PARIS were studied. This included the testing of a novel SiPM detector, and various phoswich configurations, to optimise the resolution and timing requirements specified by the collaboration. The tests include the general response, pile-up, particle discrimination, and beam test of these methods. These results are discussed thoroughly in the following chapters.

It is hoped that the conclusions of these results will help steer the decision of a final design before construction begins. Discussions on how this work can be furthered with newer technologies are given. Recommended future physics cases that can benefit greatly with the use of the PARIS array, have also been presented, and are already attracting attention within the nuclear physics community worldwide.

Contents

Abstract	ii
Acknowledgements	xiii
Declaration	xv
1 Introduction	1
1.1 PARIS	1
1.2 The SPIRAL2 Facility in GANIL	3
1.3 Overview of the Thesis	4
1.4 Introduction to Future Physics Cases for PARIS	5
1.4.1 Jacobi Shape Transition	6
1.4.2 Heavy Ion Radiative Capture	9
1.4.3 Ab Initio α -Clustering Study	11
1.4.4 Extensions to Hadron Physics	13
1.5 Other Physics Cases	17
2 Scintillator Detectors; Light Collection & Electronics	18
2.1 Introduction	18
2.2 Scintillation Crystals	18
2.2.1 Organic Detectors	19
2.2.2 Plastic Scintillators	22
2.2.3 Inorganic Crystals	22
2.3 Lanthanum Bromide Scintillators	23
2.3.1 Cerium Activator Impurity Concentrations	23
2.3.2 PMT Selection and Blue Sensitivity	24

2.4	CsI(Na), BaF ₂ and other scintillators for PARIS	25
2.5	Light Loss in Scintillators	27
2.6	Photomultiplier Tubes	29
2.6.1	Voltage Dividers	32
2.6.2	Pulse Shapes and Linearity	32
2.6.3	Noise	34
2.7	NIM Modules	35
2.7.1	Amplifiers	36
2.7.2	Other Important NIM Modules	37
2.7.2.1	Fan-In Fan-Out (FIFO)	37
2.7.2.2	Charge to Digital Modules	38
2.7.2.3	Coincidence Units	38
2.7.2.4	Discriminators	39
2.7.2.5	Time to Amplitude Converters (TAC)	39
2.7.2.6	Multi-Channel Analyser (MCA)	39
3	Simulations for PARIS	41
3.1	Simulation and Analysis Software for PARIS	41
3.1.1	GEANT4 Software	43
3.1.1.1	Events Generator and class	43
3.1.1.2	Geometry and detector representation	44
3.1.1.3	Tracking	44
3.1.1.4	Physics	45
3.1.2	ROOT and Radware software packages	47
3.1.2.1	ROOT	47
3.1.2.2	Radware	49
3.2	Constructing the PARIS Array	49
3.2.1	Segmentation	50
3.2.2	Effects of Doppler Broadening	51
3.2.3	Energy Resolution and Efficiency Graphs	53
3.2.4	Investigation of Various Geometries for PARIS	55
3.2.4.1	Absorption Efficiency of a Truncated Pyramid	55
3.2.4.2	Absorption Efficiencies of the Rectangular Design	57

3.2.4.3	Absorption Efficiencies of the Conical Design . . .	57
3.2.4.4	Energy Resolution of Various Geometries	59
3.2.5	Cubic Design	63
3.2.6	The "Prototype" and New PARIS Cubic Design	64
3.2.7	Analysis and Experimental Simulations	65
3.2.7.1	Simulated Work Involving a Collimated Source .	65
3.2.8	Other Parameters of the Array	71
3.2.8.1	The length of CsI	71
3.2.8.2	The Addition of Gaps	74
3.2.8.3	Variations of the Incident Angle of the Source . .	76
3.2.9	Total Energy Deposition on a Novel Highly Segmented Array	78
3.2.10	Larger Arrays and the 4π Calorimeter	80
3.2.11	The 4π Array and Comparative Studies with AGATA . . .	83
3.2.11.1	FastRad, GDML and "Shifted Cube" Designs . .	84
3.2.11.2	Comparative Simulations with AGATA	87
3.3	Simulation of a Physics Case	90
3.3.1	Motivation for the Reaction: $^{163}\text{Dy}(^3\text{He},^4\text{He})^{162}\text{Dy}$	94
4	LaBr₃(Ce) Scintillator and Phoswich Detector Testing	100
4.1	Energy Response and Self Activity of a 1.5" LaBr ₃ (Ce) detector .	100
4.1.1	Self Activity	100
4.1.2	Actinide Contamination	101
4.1.3	Energy Response of the LaBr ₃ (Ce) scintillator	103
4.2	Neutron Activation and Detector Response	105
4.2.1	Neutron Capture	105
4.2.2	Experimental set-up and First Results	106
4.3	(n, γ) Pulse Shape Discrimination	108
4.4	Introduction to the Phoswich Detector	111
4.4.1	Initial Testing and Signal Optimisation.	111
4.4.2	Energy Resolution and Position Sensitivity	113
4.5	Neutron Response in the Phoswich	117
4.5.1	Pulse Shape Discrimination	117
4.5.2	Neutron Activation	118

4.6	Timing	119
4.6.1	Introduction and Set-up	119
4.6.2	Timing Measurement Results and Analysis	120
4.6.3	Improvement on the Timing Measurements	123
4.7	Pile-Up	124
4.8	Pile-Up Measurement Results and Analysis	125
4.9	Summary of the Tests on the Phoswich and LaBr ₃ (Ce) Detectors	128
5	Development of Large Area Avalanche Photo-Diodes for Light Collection	131
5.1	Introduction to Silicon Detectors	131
5.1.1	Theory	131
5.1.1.1	Charge Carriers	132
5.1.2	Silicon Photomultipliers	133
5.1.2.1	Signal to Noise Ratios and Dark Current	134
5.2	Experiment Methods and Results	137
5.2.1	Pulser and Gamma-Ray Response	138
5.2.2	Temperature Response	139
5.2.2.1	Method and Resulting Outcomes	139
5.3	Response Testing of the Detector	143
5.4	The New SensL SiPM Detector Arrays	144
5.4.1	Timing Tests	147
5.4.2	Other Extensions	149
5.4.2.1	Position Sensitivity	149
5.4.2.2	Further Investigations with LYSO(Ce)	153
5.5	Future Experiments	157
6	High Energy Calibration Beam Tests	159
6.1	Introduction	159
6.2	²⁷ Al(p,γ) ²⁸ Si High Energy Beam Test	159
6.2.1	Resonant Capture Reactions	160
6.2.1.1	Target Thickness and Yield	161
6.2.2	Experimental Set-Up	163
6.2.3	Analysis and Results	164

7 Summary and Future Work	174
7.1 Summary	174
7.2 Future Work	179
Appendices	183
A Future Physics Cases	184
B Simulation Work	187
B.1 Using Add-back Techniques	187
B.2 Examples of other PARIS Designs	188
B.3 Additional AGATA Spectra	190
C Simulation of Physics Case	191
C.1 Photo-peak Efficiency Response of CACTUS	191
C.2 Additional Gates of the Simulated ^{162}Dy case	192
List of References	200

List of Figures

1.1	Various methods proposed for the calorimeter design.	2
1.2	SPIRAL 2 with the S ³	4
1.3	GDR line shapes for various deformations in ⁴⁶ Ti.	7
1.4	GDR strength functions for 3 different spins for ¹²⁰ Cd and ⁴⁶ Ti.	8
1.5	Projection of θ_π , with 4.4 MeV gamma ray.	16
2.1	Energy level diagram of an organic scintillator.	20
2.2	The band structure in inorganic scintillators	23
2.3	Variations in cerium concentrations	24
2.4	An example of a photomultiplier tube	31
2.5	The constructed voltage divider	31
3.1	An outline of the process behind the simulation work for PARIS	42
3.2	4x4 array of the simulated PARIS detector.	50
3.3	Segmentation of the two layers.	51
3.4	A simulated 662 keV photo-peak.	54
3.5	A GEANT4 image of the truncated pyramid design.	56
3.6	Absorption spectrum of the smaller truncated pyramid design.	56
3.7	A spectrum of a 1 MeV gamma (1”x1”x4” cubic segment).	58
3.8	Absorption efficiencies of γ rays (1”x1”x4” cubic segment).	58
3.9	A GEANT4 image of the conical design.	59
3.10	Comparison of a 1 MeV γ -ray for each 1”x1”x4” segment.	61
3.11	Comparison of a 15 MeV γ -ray for each 1”x1”x4” segment.	61
3.12	Comparison of a one MeV γ -ray for each 2”x2”x4” segment.	62
3.13	Comparison of a 15 MeV γ -ray for each 2”x2”x4” segment.	63

LIST OF FIGURES

3.14	Simulation of a 4x4 array	64
3.15	Simulation of a unique two-shelled array	65
3.16	3x3 LaBr ₃ absorption spectrum	67
3.17	3x3 CsI absorption spectrum	68
3.18	Energy deposition trend of the 3x3 LaBr ₃ array	68
3.19	Energy deposition trend of the 3x3 CsI array	69
3.20	The central detector (shaded) in a 3x3 detector array	70
3.21	The central detectors(shaded) in a 4x4 detector array	70
3.22	Energy vs. Absorp. eff. for LaBr ₃ in 3x3 array.	72
3.23	Energy vs. Absorp. eff. for LaBr ₃ in 4x4 array.	72
3.24	Energy vs. Absorp. eff. for CsI in 3x3 array.	73
3.25	Energy vs. Absorp. eff. for CsI in 4x4 array.	73
3.26	Comparison of energy deposition in both arrays.	74
3.27	Different gap sizes and inner absorption efficiency.	75
3.28	Different gap sizes and outer absorption efficiency.	76
3.29	Energy spectrum of a 800 keV γ -ray at various incident angles . .	77
3.30	Energy spectrum of a 15 MeV γ -ray at various incident angles . .	77
3.31	A 6x6 and 3x3 array of LaBr ₃ (Ce) and CsI crystals.	79
3.32	A 3x3 and 6x6 arrays of LaBr ₃ (Ce) and CsI crystals.	79
3.33	The total absorption efficiencies of each array size.	81
3.34	Energy deposition in a 6x6 array of 1"x1"x4" LaBr ₃ (Ce) crystals. .	81
3.35	Energy deposition in a 6x6 array of 1"x1"x4" LaBr ₃ (Ce) crystals. .	82
3.36	Energy resolution of a one MeV γ -ray for several array sizes. . . .	83
3.37	Energy resolution of a 15 MeV γ -ray for several array sizes. . . .	84
3.38	One of the CAD files used with the FastRad software.	85
3.39	The geometry after being exported from FastRad to GDML.	85
3.40	The shifted cube design without the beam-pipe.	86
3.41	The final array of 1" LaBr ₃ (Ce) segments.	87
3.42	Total absorption efficiency with the final design.	87
3.43	The AGATA array, with multi-colour cluster segments.	88
3.44	LaBr ₃ (Ce) AGATA array spectrum	89
3.45	Absorption efficiencies of LaBr ₃ (Ce) AGATA and cubic geometries. .	90
3.46	Absorption efficiencies of the cylinder detectors.	91

LIST OF FIGURES

3.47 Comparison of the CACTUS array at 1 MeV	93
3.48 Comparison of the CACTUS array at 5 MeV	93
3.49 Comparison of the CACTUS array at 12 MeV	94
3.50 ^4He - γ coincidence energy matrix	95
3.51 Simulated NaI(Tl) spectrum of ^{162}Dy with no gate applied.	96
3.52 Simulated LaBr ₃ (Ce) spectrum of ^{162}Dy with no gate applied.	97
3.53 NaI(Tl) spectrum gated on 2^+ to 4^+	97
3.54 LaBr ₃ spectrum gated on 2^+ to 4^+	98
3.55 NaI(Tl) spectrum gated on 8^+ to 10^+	98
3.56 LaBr ₃ spectrum gated on 8^+ to 10^+	99
4.1 The decay due to the contamination from ^{227}Ac	101
4.2 α -contamination present in the detector	102
4.3 α -scintillation properties when calibrated with γ rays	103
4.4 A ^{137}Cs spectrum with observed contamination from ^{138}La and ^{227}Ac	104
4.5 Results of the FWHM measurements	105
4.6 Calibrated activated spectrum of a 1.5" LaBr ₃ (Ce) detector.	107
4.7 The isotopes that undergo neutron activation.	108
4.8 (n, γ) pulse shape discrimination.	110
4.9 Source sensitivity of the detector.	114
4.10 Energy measurements with fitted parameter	115
4.11 Energy measurements with numerous sources at various angles.	116
4.12 Spectrum changes of a ^{152}Eu source due to varying angles.	117
4.13 Phoswich pulse shape discrimination over a 2 MeV range	118
4.14 Calibration spectra of the neutron activation in the phoswich.	119
4.15 Set-up for phoswich timing coincidence measurements.	120
4.16 Intrinsic timing resolution of the electronics.	122
4.17 Timing responses for both scintillators with 400 ns delay	122
4.18 Another ^{57}Co HV plateau measurement with LLD=150 mV.	127
4.19 ^{57}Co source as measured by the phoswich detector with a low bias.	128
4.20 ^{57}Co source as measured with a high LLD threshold.	129
5.1 The supply board provided by SensL	137
5.2 The detector mounted to the heat sink.	140

LIST OF FIGURES

5.3	The poor response with a ^{137}Cs source	141
5.4	The response of the SiPM with increasing temperature.	142
5.5	The circuit diagram of the preliminary detector board.	145
5.6	The final board developed for the SiPM array.	146
5.7	The 662 keV photo-peak in ^{137}Cs showing the SiPM response. . .	147
5.8	Timing resolution of the 1" x 1" x 6" CsI(Tl) and SiPM detector set-up.	149
5.9	Position sensitivity of the first array.	151
5.10	Position sensitivity of the second array.	152
5.11	Position sensitivity of the third array.	152
5.12	Position sensitivity of the fourth array.	153
5.13	The self-activity of LYSO	154
5.14	Calibration Tests with LYSO and SiPM.	155
5.15	The configuration of the switches on the board used with the SiPM.	156
5.16	The position sensitivity of the SiPM and board with LYSO(Ce). .	157
5.17	The position sensitivity of the SiPM and board with LYSO(Ce). .	157
6.1	An example of the phoswich channel electronics set-up.	163
6.2	PSA with the $\text{LaBr}_3(\text{Ce})/\text{NaI}(\text{Tl})$ phoswich.	165
6.3	Calibration of the $\text{LaBr}_3(\text{Ce})/\text{NaI}(\text{Tl})$ phoswich.	165
6.4	$\text{LaBr}_3(\text{Ce})$ linearity as a function of the gate.	167
6.5	PSD of the phoswich after analysis.	168
6.6	The populated levels with the large $\text{LaBr}_3(\text{Ce})$ scintillator.	169
6.7	The populated levels with the phoswich detector (PW1).	170
6.8	Linearity of the PW1 detector and $\text{LaBr}_3(\text{Ce})$ scintillator.	172
6.9	Decay schemes of the four populated resonances.	173
7.1	Timeline of the PARIS collaboration.	182
A.1	Numerous proposed physics cases intended for PARIS	185
A.2	Numerous proposed physics cases intended for PARIS	186
B.1	A CAD drawing of a proposed 4π set-up for PARIS.	188
B.2	One of the spherical designs for PARIS.	189
B.3	Absorption efficiency of the $\text{LaBr}_3(\text{Ce})$ AGATA array	190
B.4	Fold distributions of the $\text{LaBr}_3(\text{Ce})$ AGATA array	190

LIST OF FIGURES

C.1	Photo-peak efficiency for various E_γ	191
C.2	NaI(Tl)/LaBr ₃ ratio of photo-peak efficiency for E_γ	192
C.3	NaI(Tl) spectrum gated on $6^+ \rightarrow 4^+$	192
C.4	LaBr ₃ spectrum gated on $6^+ \rightarrow 4^+$	193
C.5	NaI(Tl) spectrum gated on $8^+ \rightarrow 6^+$	193
C.6	LaBr ₃ spectrum gated on $8^+ \rightarrow 6^+$	194

Acknowledgements

First and foremost, I would like to offer my thanks and gratitude to my supervisor, Dr. David Jenkins, who has supported me unconditionally throughout my thesis. I attribute my Ph.D. work to his constant encouragement and effort, which lead to the completion of a concise and fulfilled thesis.

In the close knit community of the Nuclear Physics Group at York, I have been aided for many years by the various areas of expertise of those around me. Of these people, I wish to single out Dr. Pankaj Joshi who helped in making sure my experiments in the lab worked the way they should. His support and advice were quickly sought, and always taken in the highest regard. Paul Davies, as well as having to bear the brunt of my frustrations towards C++ coding, has helped provide good arguments about Physics and life in general, both of which he would usually win. It would be lackadaisical of me not to mention the other people in the group that contributed in their own unique way to the seemingly endless tea breaks and larking around. To name them: Adam Tuff, Iain, Lianne, Carine, Ed, James (Seamus), Phil, Jamie, John, Christian, Tim, and Harith (Bob). Thank you all guys for contributing to the experience!

Beyond Physics (which sometimes can be quite hard to comprehend), Leon Loveridge and Rebecca Ronke always ensured I was alive, occasionally surprising me with gifts of the edible sort and hours of MarioKart. Thanks chaps!

I'd also like to take the time to thank my fiancée Clara, for always being there on those days where I could not bring myself to look at

my thesis. She always knew the right things to say and was very supportive.

The Department of Physics has provided the support and equipment I have needed to produce and complete my thesis and STFC has funded my studies. I would also like to thank the PARIS collaboration for their constructive, and supportive efforts when undertaking my research, especially Michal Ciemala, without whom I would have given up on Geant4 a long time ago.

Finally, I thank my parents and family in Liverpool for supporting me throughout all my studies at University.

Declaration

This thesis has been submitted for the degree of Doctor of Philosophy in accordance with the regulations of the University of York. The work contained herein has not been previously submitted for any other degree.

The simulation and experimental work outlined in this thesis was performed solely by the author under the supervision of Dr. D.G.Jenkins, with the guidance of the PARIS collaboration.

Signed

Oliver James Roberts

Chapter 1

Introduction

Nuclear Physics is the study of behaviour of atomic nuclei within matter, where γ -ray spectroscopy is employed to study and measure the radioactivity of nuclei. Unlike Geiger counters which only determine the count rate, γ -ray spectroscopy determines both the number of counts, and energy of γ rays emitted from radioactive nuclei. These measurements are usually acquired with, but not confined to, scintillation or semi-conductor detectors, with the analysis of the resulting signal done with modules. Maintaining a good signal is crucial in extracting the associated timing and energy information, where the analysis of the resulting spectrum allows for the study of the behaviour of many phenomena. However, as reactions and their mechanisms become increasingly complex, with statistics and cross-sections becoming lower, more sophisticated beam-lines and detector methods are needed to further research.

1.1 PARIS

The Photon Array for the studies with Radioactive Ion and Stable Beams, PARIS, is a newly formed collaboration, the aim of which is to design and build a high efficiency calorimeter for medium resolution spectroscopy and detection of γ -rays over a large range of energies. The project is to also provide an array to act as a energy-spin spectrometer for incident γ rays. The current design consists of two shells of crystals; a highly granular inner shell of $\text{LaBr}_3(\text{Ce})$, and an outer layer of crystals with a lower granularity, larger volume and higher stopping

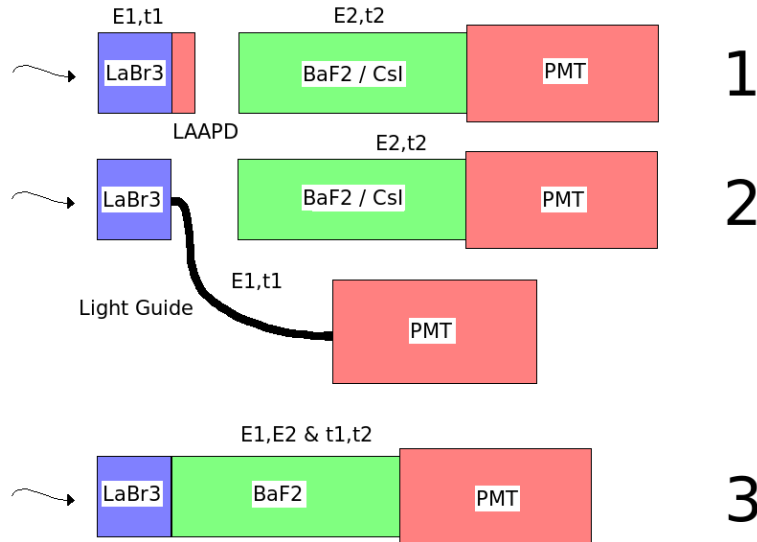


Figure 1.1: Various methods proposed for the calorimeter design[1].

power (e.g. CsI(Na)). This outer shell of inorganic alkali halide crystals will be used to measure high energy photons, and act as a Compton suppressor. Various methods to be used for the readout of the data are shown in figure 1.1, where the proposed arrangements include; Si-large area avalanche photo-diodes (LAAPDs), two different scintillators joined together in a phoswich set-up, or another configuration involving light-guides.

Given the outstanding energy and timing efficiencies of the calorimeter, the detector should cover as much of the 4π area as possible. Unlike the highly efficient 4π detector array AGATA (Advanced GAMMA Tracking Array), composed of germanium tracking detectors, PARIS will take on a square configuration, deviating from the geodesic form used in many detector set-ups. The reason for this is down to flexibility. In a configuration such as AGATA, it is mechanically unfeasible to build a flexible support structure that would allow for synergies with other arrays and different source distances. The incorporation of a modular array that can do both of these tasks would expand upon the number of applications and physics cases originally intended.

1.2 The SPIRAL2 Facility in GANIL

High intensity beams at the new SPIRAL2 facility in GANIL, will allow us to further expand our knowledge of the behaviour of the nucleus. The creation of compound nuclei under extreme conditions using the broad range of exotic beams available from SPIRAL2, will allow the study of reactions where high values of angular momentum induced by fusion reactions are expected, one of many examples of what SPIRAL2 can achieve. The study of various phenomena in nuclear physics at high values of temperature and rotation, will allow for reaction mechanisms to be studied in detail. Intense and stable beams produced by the LINAG, will investigate neutron rich nuclei close to the proton drip line by using transfer or deep-elastic scattering methods. However, studies far from the valley of stability will result in reactions where increasingly tiny cross-sections with large backgrounds produced by these beams, makes it harder to extract essential information. Successful acquisition of this data will lead to significant advancements in various fields where a next generation calorimeter needs to be constructed.

The proposed future experiments and physics cases put constraints on what is needed for PARIS. The energy resolution needs to be in the region of 3-5 % for γ -ray energies less than 10 MeV. At energies greater than 10 MeV, the use of $\text{LaBr}_3(\text{Ce})$ scintillators should provide superior resolution (1-2 %), rivalling energy resolutions in the same energy regions produced by semi-conductor detectors. Due to some of the proposed physics cases having low cross-sections and high background, a high efficiency must be maintained, with a resolution of 5 % expected for the sum energy. A high resolution γ -ray multiplicity filter of $\Delta M/M = 4[2]$ will also be implemented. To remove any unwanted background, having a time-of-flight resolution of the order of hundreds of picoseconds is essential, which is exactly within the capabilities of $\text{LaBr}_3(\text{Ce})$ detectors, able to achieve timing resolutions of the order of 260 ps[3].

One of the proposed beam-lines will feature a separator spectrometer called "S³" at the exit of the linear accelerator equipped with a rotating target, two-stage separator and mass spectrometer. The S³ device is designed for experiments which use very high intensity stable beams from SPIRAL2, where heavy ions from

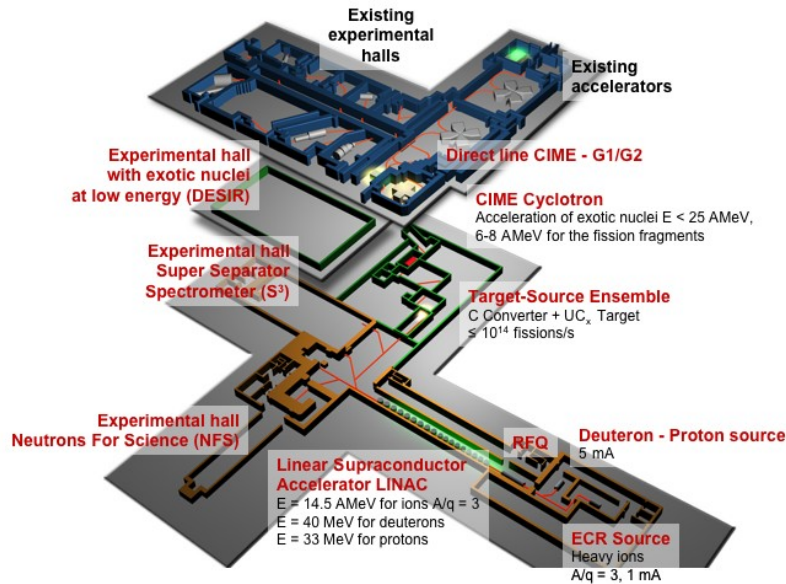


Figure 1.2: SPIRAL 2 with the S³[4].

helium to uranium will be used with intensities of $1\text{p}\mu\text{A}$ to 1p mA , allowing the study of a full range of physics cases. Along S³ are several areas where the set-up of various arrays for α , γ , and electron spectroscopy have been proposed. Of these projects, a proposed silicon array to study direct reactions called GASPARD (Gamma Spectroscopy PARTicle Detector) will be set-up on this beam-line alongside PARIS, where it is hoped a synergy between the two arrays can be used to increase the calorimeter efficiency for select physics cases.

1.3 Overview of the Thesis

The main aim of this project was to work along side the PARIS collaboration in their efforts to design, simulate and construct the next generation energy spectrometer for S³ on the SPIRAL2 beam-line. The motivation behind the need for an array is presented in chapter two, where a number of physics cases have been presented with a focus on how they can be improved with the use of the timing properties found in LaBr₃(Ce) scintillators. To exploit the outstanding properties of LaBr₃(Ce) scintillators within the calorimeter, various detection methods and testing under various circumstances were performed to further design plans for

1.4 Introduction to Future Physics Cases for PARIS

the calorimeter. The details of the initial simulation work on various geometries the calorimeter took initially in GEANT4, is presented in chapter four.

The final shape and detector set-up of the calorimeter is yet to be formally agreed on, and thus extensive work on the detector methods outlined in figure 1.1 were performed to further this decision prior to construction of a prototype array. This included a comparative study of the energy resolution and simulation work performed by myself and collaborators, examples of which are presented in chapter three. The phoswich arrangement was also tried and tested as a cost effective alternative to purchasing large $\text{LaBr}_3(\text{Ce})$ scintillators, with limited effect on the overall performance. Other important tests on the particle discrimination methods that would be employed were also investigated, as a large number of collaborators are interested in pursuing the calorimeter primarily for experiments involving giant dipole resonances (discussed in section 1.4.1). Therefore, it was important to test the neutron response of various scintillators. The results of the subsequent neutron activation after testing with a AmBe source and timing signatures of both the $\text{LaBr}_3(\text{Ce})$ and phoswich detectors is explained in chapter five. Following these tests done with the scintillators, the work was extended to SiPMs; a type of large area avalanche photo-diode detector, incorporating a power board that generates its own bias from a standard 5 V supply and photo-multiplier (PM) technology. A series of energy source and timing tests with these detectors was investigated. The results of these gamma source tests and other spectroscopic methods using these detectors are outlined in chapter six.

In the final chapter, the in-beam characteristics of the phoswich were studied to test the response of the scintillators with high energy γ -rays. There is little literature on how $\text{LaBr}_3(\text{Ce})$ scintillators perform during beam tests, and how linear their response is with increasing energy. A summary of the significant advances and results of each of these findings is presented in the final summary, with further direction this research can take also outlined.

1.4 Introduction to Future Physics Cases for PARIS

There are many flagship experiments for the PARIS calorimeter, the first of which is scheduled for next year (2011) using just the prototype. It is expected that in

2014-2015, the 2π or 1π calorimeter will be fully built and operational. Outlined are a few of the proposed experiments for the early stages of calorimeter development, where only a couple of segments, or a 1π distribution of detectors, are needed.

1.4.1 Jacobi Shape Transition

For nuclei with high angular momentum and spin, one observes a transition from an oblate ellipsoid to a hyper-deformed, extremely elongated prolate shape. These Jacobi ellipsoids are elongated and are slightly tri-axial. The transition to this Jacobi shape is signalled by a sudden drop in rotational frequency, at a critical angular momentum, at high spin. Any further increase in the angular momentum results in lower rotational frequencies until fission occurs, in much the same nature as a rapidly rotating liquid drop, and thus is a very good representation of the liquid drop model in nuclear physics. Following this collective model, the collective rotation of the nuclei gives us a signal when Jacobi shape transitions are occurring due to the energy of a γ ray in a transition band. This corresponds to a decrease in this energy for increasing angular momentum which results in a "giant back-bend" effect. This contributes to the giant dipole resonance (GDR) line-shape, a very sensitive signature of this event. The main experimental problems that occur when trying to observe Jacobi shapes is in preparing nuclei at angular momenta above the phase transition, and isolating the consequent gamma radiation from those corresponding states. In such experiments, the multiplicity and sum energy of the incident gammas, play a crucial role in extracting the GDR profile precisely. The introduction of new exotic stable beams in SPIRAL2 will help in meeting the conditions favourable for the fusion evaporation mechanism necessary to examine this phenomenon.

As of today, there is very strong evidence that Jacobi transitions occur in light and medium-mass nuclei[5]. However, due to the narrow range in excitation energy and angular momentum at lower mass ranges, and proximity to fission at higher mass, the study of this effect in nuclei is very difficult. In light of this, it is hoped that PARIS will be used to probe this phenomena in nuclear physics by studying Jacobi shape transitions in ^{44}Ti , proposed by Adam Maj et al. This is

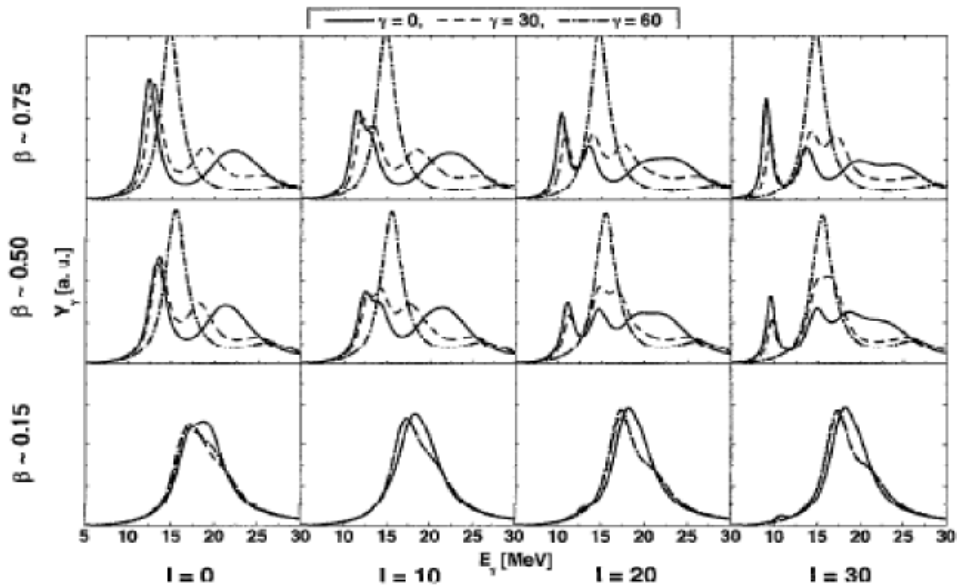


Figure 1.3: GDR line shapes for various deformations in ^{46}Ti [6].

to be done with the prototype configuration, with a 170 MeV ^{12}C beam upon a ^{32}S target, or a 450 MeV ^{32}S beam incident upon a ^{12}C target.

PARIS can improve on these measurements, using the properties of the $\text{LaBr}_3(\text{Ce})$ scintillators to extract the GDR profile neatly by determining the multiplicity and sum energy accurately, and thus deducing an entry point on a (E^*, L) GDR plot¹. The differential technique is particularly effective in determining shape phase space transitions. This method relies on neighbouring compound nuclei being produced by different reactions, which helps in extracting information of a defined region within the (E^*, L) plots[2]. Thus, the inner layer of $\text{LaBr}_3(\text{Ce})$ scintillators will be highly granular, and act as a multiplicity filter and sum-energy calorimeter, a mandatory requirement in order to optimise this technique. Due to the broad range of energies, measured over a wide range of temperatures, the extraction of the GDR width relies heavily on high resolution and superior efficiency as well as good time of flight (ToF) measurements.

However, neutrons are produced during the GDR process by photons, and

¹Excited energy at which the compound nucleus is populated plotted against angular momentum, L .

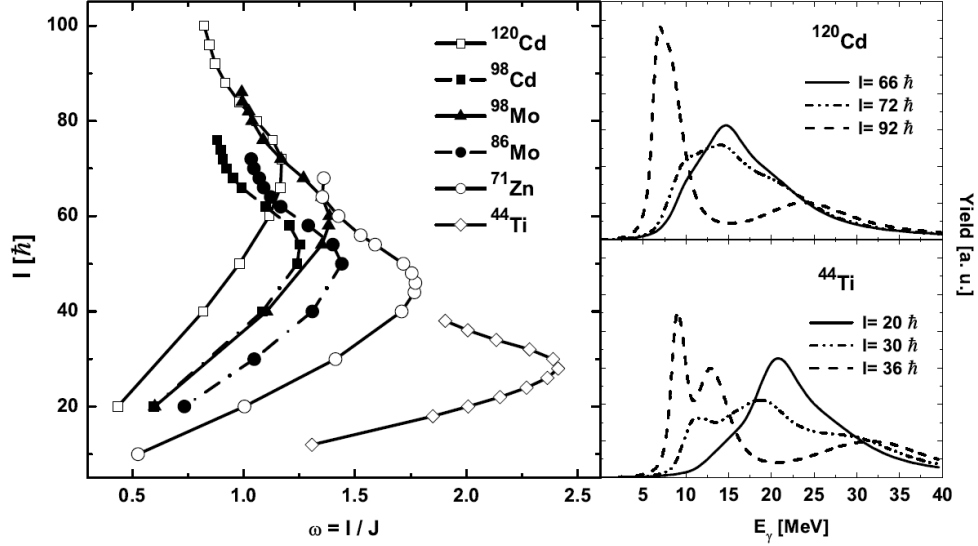


Figure 1.4: GDR strength functions for 3 different spins for ^{120}Cd and ^{46}Ti . [2]

have energies between 5 and 40 MeV. The yield of neutrons are proportional to the length of material traversed by these photons and the photo-neutron cross-section when produced with an electron beam. The yield of these neutrons are calculated by integrating over the photon energy spectra, differentials of the photon path lengths and the photo-neutron cross sections. Saturation is observed when the energies impinging on the target are greater than 50 MeV, or when the target thickness is roughly 10 radiation path lengths, in the case of a beam of electrons [7].

$$Y_{GDR} = \frac{6.023 \cdot 10^{-4} \rho f N_n}{A E_o} \int_{E_{th}}^{E_{max}} \sigma_{GDR}(k) \frac{dl}{dk} dk \quad (1.1)$$

Where the terms are explained in table 1.1

As in this case for neutrons generated from an electron beam, it can be assumed that neutrons will also present a problem to some degree when investigating the GDR reaction mechanism with other types of generated beams. Therefore, due to neutron activation within the phoswich and $\text{LaBr}_3(\text{Ce})$ detectors at thermal levels (chapter four), more work needs to be researched to see how much of an issue this will be when looking at this particular physics case. Some

1.4 Introduction to Future Physics Cases for PARIS

Solid Dimensions	Terms & Explanation	Units
Y_{GDR}	GDR neutron yield	neutron electron ⁻¹ MeV ⁻¹ ,
ρ	target density	g/cm ³
f	isotope fractional abundance	-
N_n	neutrons / photo-neutron reaction	-
A	atomic weight	g mol ⁻¹
E_o	electron energy	MeV
$\sigma_{GDR}(k)$	photo-neutron cross section	mb
dl/dk	differential photon track length	cm MeV ⁻¹
k	photon energy	MeV
E_{th}	threshold energy of the reaction	MeV
E_{max}	upper energy limit of the reaction ¹	MeV

Table 1.1: Explanation of the terms described in equation 1.1, with the terms also presented.

measurements of various neutron energies should be undertaken with a neutron gun to determine how much activation will take place, and whether other isotopes present in other components of the detector might contribute to what has already been seen.

It has been hypothesised that the synergy of several modular walls of the PARIS array consisting of these LaBr₃(Ce) scintillators and AGATA, along with an effective recoil separator or filter detector, will further research in this field. However, problems might occur due to neutron activation in the scintillators at high neutron energies due to large neutron capture cross-sections present in several isotopes of the proposed detector array. Consequently, more research needs to be done in this field before studies are performed in order to better understand the possible outcomes under experimental conditions.

1.4.2 Heavy Ion Radiative Capture

Excited states in ¹²C and ¹⁶O, for example, can not be accurately described by the shell model. An excited state of ¹²C was predicted by Fred Hoyle, and was essential in describing the nucleosynthesis of carbon in helium-burning red giant

1.4 Introduction to Future Physics Cases for PARIS

stars, where discrepancies in describing the abundances of heavy elements in the universe were finally resolved. The existence of this Hoyle state allows carbon to be produced via the triple- α process, where a resonance at 7.367 MeV, is observed due to $\alpha(\alpha,\gamma)^8\text{Be}$ reaction. Small variations in the potential created by nucleon-nucleon interactions has an effect on the triple- α process[8]. The combination of two α clusters to form ^8Be has a threshold of ~ 92 keV where additional capture via the $^8\text{Be}(\alpha,\gamma)^{12}\text{C}$ reaction allows population of a 0_2^+ state just above this threshold.

In the potential well of the nucleus, there exist quasi-bound states with a positive energy, where an incident projectile particle is trapped in one of these states and forms a compound nucleus. In this case, the two nuclei share their nucleons momentarily, raising the whole system to an excited level. This system of nuclei now have no "memory" of their previous configurations, and subsequently decays by emitting a γ ray, or undergoing fission, as in the case for large nuclei. This is essentially the basis for heavy ion radiative capture, where nuclei larger than $A = 4$ fuse together producing an excited system which subsequently decays by γ -ray emission. This experiment is hard to study due to the very small cross-sections of the particles, and deformed nuclei. A specific case of radiative capture that the PARIS collaboration are interested in, is the case of heavy ion radiative capture with $^{12}\text{C}(^{12}\text{C},\gamma)^{24}\text{Mg}$. This is a very rare and resonant exothermic reaction that occurs in stars, emitting a large amount of energy (13.93 MeV), and is described by:



It has been known for some time that several resonances occur in this reaction due to the molecular arrangement of the nucleons in the resulting fused nuclei, with a bandhead at ~ 10 MeV. Low-lying vibrational and rotational states exist for grossly deformed non-spherical nuclei, where intrinsic excitation is seen in the K-rotational band. The most common low-lying vibrational excitations in deformed nuclei are quadrupole vibrations which carry two units of angular

1.4 Introduction to Future Physics Cases for PARIS

momentum; $K = 0$, $K = 1$, where the latter is the most commonly found and are γ vibrations[9].

Previous work with DRAGON in TRIUMF, has allowed for the detection of low lying resonances at $E_{c.o.m} = 6, 6.8, 7.5$ and 8 MeV. This study resulted in the observation of a bandhead at 10 MeV for low energy states ($E_{c.o.m} = 6, 6.8$ MeV) which was not detected previously due to pile-up in the NaI(Tl) detectors. Peaks corresponding to transitions at 2754 keV ($4^+ \rightarrow 2^+$), 3866 keV ($3^+ \rightarrow 2^+$) and 4238 keV ($2^+ \rightarrow 0^+$) have also been observed.

The experiment was performed with the large Gammasphere detector array. Despite the high detector efficiency of the array, and high resolution of the germanium detectors, the original radiative capture reaction was unable to be reproduced effectively. The efficiency of detection above $8-9$ MeV was very poor, and resulted in very low statistics for energies higher than this region.

It is hoped that PARIS, and the use of $\text{LaBr}_3(\text{Ce})$ scintillators, would attempt to reproduce original radiative capture measurements and search for higher multiplicity pathways in highly excited states of ^{24}Mg . By exploiting the awesome timing properties of these scintillators, discrimination of the particles coming out the exit channel can be more easily identified. A high resolution crystal like $\text{LaBr}_3(\text{Ce})$ coupled to a recoil separator, will be able to identify individual states more clearly and possibly discover more about the reaction mechanism in the $9-12$ MeV region where there are a high density of states, which are hard to resolve with current set-ups. Large volumes of $\text{LaBr}_3(\text{Ce})$ that are exposed to such high energies, will allow high resolution spectra to be obtained with a greater amount of statistics and precision.

1.4.3 Ab Initio α -Clustering Study

The shell model has been very effective in defining how the atom is held together under the assumption that neutrons and protons form the foundations of the nucleus, where their potential is defined by their nucleon-nucleon reactions. Using this method a large number of ground and excited states, found at the decay thresholds in $N=Z$ nuclei (well established at $A < 30$), can be accurately

1.4 Introduction to Future Physics Cases for PARIS

described. In many instances, they are associated with chains of α particles forming elongated and exotic shapes, used to determine the properties of $4n$ nuclei. The nucleus of ${}^8\text{Be}$ is the simplest α cluster, with a ground state 92 keV above the α - α threshold; a narrow resonance. Associated with this ground state is a rotational band, where the 2^+ and 4^+ states are broad resonances, discovered during the analysis of elastic scattering data. These were assigned by the α -cluster model, which also predicts an enhanced E2 transition probability due to the deformed nature of the band, but has yet to be observed experimentally due to the minute γ -decay branching ratios of the states. The widths of the lowest energy levels are determined using the α channel, as other decay channels are not energetically possible. Using the α -cluster model and potential, the E2 widths of the first two excited states were calculated to be 8.3 meV and 0.46 eV (B(E2) values of ~ 75 W.u. and ~ 19 W.u.)[10]. Studies to observe the direct transition between the 4^+ and 2^+ states with the reaction ${}^4\text{He}(\alpha, \gamma){}^8\text{Be}$, predicted excitation energies of the resonances to be 2.8 and 10.7 MeV, with corresponding peak cross sections of 14 and 134 nb[10].

Previous measurements of the radiative branch of the 4^+ resonance was measured to be $\sim 10^{-7} \pm 30\%$, which ultimately failed to discriminate between the α -cluster model and ab initio calculations[11] due to systematic effects. An investigation into improving this error to within a uncertainty of 10% was investigated using a similar setup to the previous experiment, performed with four ${}^4\text{He}$ beams with energies between 19 and 29 MeV, incident upon a helium gas target at 600 torr. This was done by myself and colleagues at the Tata Institute of Fundamental Research (TIFR) in Mumbai, India. An array of 38 BGO detectors was positioned around the target chamber to detect the γ rays from the 2^+ resonance at 3.04 MeV due to radiative α capture. These α particles were detected in a $500\mu\text{m}$ annular double sided silicon strip detector (DSSiSD), with 32 rings in θ (16 in θ_{left} and 16 in θ_{right}) and 16 ϕ sectors placed in front of the beam at 0° . The events were triggered by using a triple coincidence of logic signals from both halves of the 32 rings in the DSSiSD detector and the BGO array. The energy and timing information from each of the silicon strips and BGO detectors was processed in a CAMAC data acquisition system, with the energy calibrations being performed by scattering α particles on mylar and carbon targets. The common

1.4 Introduction to Future Physics Cases for PARIS

start and stop signals of the six time-to-digital converters (TDCs) used, were the BGO and DSSiSD respectively. Three gates were applied to BGO detectors 1-16, 17-32 and 33-38 using a charge-to-digital converter (QDC), before they were fed into the TDC. Similarly for the stop channel, the DSSiSD detectors had 3 gates applied to 16 channels from both θ_L and θ_R and 16 channels from the ϕ sector by analog-to-digital converters (ADCs), before the TDCs. A heavymet shield was used around the $1\mu\text{g}/\text{cm}^2$ thick Kapton windows due to beam interactions with the polyionide window, creating a background due to the excitation of ^{12}C to 4.4 MeV.

This interesting physics case can certainly benefit with the addition of a $\text{LaBr}_3(\text{Ce})$ array. While the results from the experiment are only very preliminary, an immense improvement with an array of fast timing scintillators would result in much better coincident measurements. ToF measurements between the DSSiSDs and BGO detector used with the QDCs and TDCs in forming a start and stop system, can be significantly improved upon due to the superior timing properties of $\text{LaBr}_3(\text{Ce})$ (several ps) when compared to BGO¹. Improvement in this measurement would ultimately result in more precise cross section measurements due to better separation and identification of the regions of interest within this transition. Not only would there be a significant improvement in the timing measurements, but also in the sum-energy spectra, where the energy resolution efficiency of $\text{LaBr}_3(\text{Ce})$ is also very superior. The BGO arrays quote 7.9 %, 12.5 % and 11.5 % for the observed 4.4, 8 and 10 MeV gammas respectively[11]. Such an experiment would be easy to reproduce with a PARIS array as only a small number of detectors are required, where even a few would make a remarkable impact within this area of research.

1.4.4 Extensions to Hadron Physics

There also exists opportunities to extend these physics cases to hadron cases, where a new array of fast timing and high efficiency detectors has the potential to further research. One such case is photo-production by neutral pions incident

¹BGO (with a timing resolution of hundreds of nanoseconds), was used in coincidence with the DSSiSDs.

1.4 Introduction to Future Physics Cases for PARIS

on a ^{12}C target, exciting the ^{12}C to the well known 4.4 MeV level. This is of great interest in helping understand the dominance of Δ baryons. All Δ baryons decay via the strong force to a nucleon and pion, where the amplitudes of the charge states depend on the isospin coupling¹. Pions are the lightest mesons, and are used to explain the role of the strong force. π^0 s have spin zero and are a superposition of the π^+ and π^- mesons, which are both composed of $u\bar{d}$ and $\bar{u}d$ quarks respectively. The amplitude of the photo-production of π^0 (in this case), allows for a better understanding of the interaction mechanisms of the Δ resonance in the nuclear environment. The Dalitz decay of π^0 results in the emission of a pair of photons 98% of the time². This dominance of the Δ resonance helps in determining the probability of π^0 photo-production from both neutrons and protons. Measurement of this incoherent process to discrete nuclear states allows allocation of isospin and spin selection rules in aiding with the study of various components of the photo-production amplitude[12]. Although a relatively well studied production mechanism, little data exists on the population of discrete states in residual nuclei using the (γ, π^0) reaction due to poor resolution in previous detector systems.

Various targets were used in the neutral pion photo-production experiments in the experiment by Tarbet, carried out with the Crystal Ball detector and Glasgow photon tagger at the Mainz Microtron (MAMI). The Crystal Ball is a 672 element NaI(Tl) detector array with 94% of the 4π area covered, where an incident photon produces an electromagnetic shower that deposits 98% of its energy within 13 clusters[12], revealing an angular resolution of several degrees for incident photons. Several improvements to the detector array include a MWPC and PID detector, in order to acquire information regarding the impinging charged particles within the detector array. The photon beam was tagged, with a width of 2 MeV within a range of 120-819 MeV, incident upon a 1.5 cm ^{12}C target. Photons subsequently released during this reaction were detected by Crystal Ball in

¹ Δ baryons are a spin excitation of the nucleon doublet. While the nucleon will have two quark spins aligned and one opposite (only two possible flavours; uud, and udd, corresponding to isospin 1/2), Δ baryons have all three quark spins aligned. This allows for the isospin to extend to 3/2 resulting in four possible flavour states; uuu, uud, udd and ddd.

²The rest of the time π^0 decays to $e^+ + e^- + \gamma$

1.4 Introduction to Future Physics Cases for PARIS

coincidence with the charged particles impinging on the central PID and MWPC detectors, where the target position was determined by reconstructive vertex positioning from the MWPC to within an accuracy of 0.5 mm.

Neutral pions are identified in the Crystal Ball detector array from the 2γ decay. The energies of the photons from the Crystal Ball array were plotted against their π^0 polar angles, with the projection of the energy distributions for $\theta_\pi = 78 \pm 2^\circ$ presented in figure 1.5, where the background was due to isolated low-energy photons from the main π^0 decay, verified by additional GEANT3 simulations. Due to this background, two fits were added to the data, where the background was found to be exponential in nature. A substantial part of the strength of this Gaussian 4.4 MeV peak may arise from several transitions from high-lying states, where the strongest branching ratio to the 4.4 MeV state is 2.1% from the 15.2 MeV state; not a by-product of Δ excitation. In determining what states are involved in the final 4.4 MeV peak, the incoherent yield at some angle α had to be converted into a cross-section, using the efficiency of the Crystal Ball array in simultaneously detecting π^0 s and 4.4 MeV γ rays, utilising GEANT3. By deducing the angular distribution, the GEANT3 simulations showed a strong reliance on the $\sin^2(2\alpha)$ term in the results. Similar independent calculations also suggest that spin-dependent terms contribute significantly to the incoherent excitation strength of the 4.4 MeV peak. The result of the application of this novel decay photon method, is the derivation of incoherent cross sections, which are in agreement with a theoretical Δ -hole model calculations.

Optimal timing and energy resolution efficiencies need to be of a high calibre, in order to be successful in observing the photo-production of pions in ^{12}C . An array of $\text{LaBr}_3(\text{Ce})$ scintillators might thus be useful in furthering advances made in this field due to the superior energy resolution when large volumes are used to detect high energy γ -rays. Replacing the $\text{NaI}(\text{Tl})$ segments with $\text{LaBr}_3(\text{Ce})$ would remarkably improve the resolution of the 4.4 MeV level seen in ^{12}C to around $\sim 2\%$. Therefore, it would be a very interesting case to redo this experiment with such a set-up, not only to test the detector performance with these exotic particles, but to also acquire better results regarding this photo-production process. Tagging and coincident measurement methods incorporated in this study would also rely heavily upon the timing qualities of the scintillators used, where $\text{LaBr}_3(\text{Ce})$ would

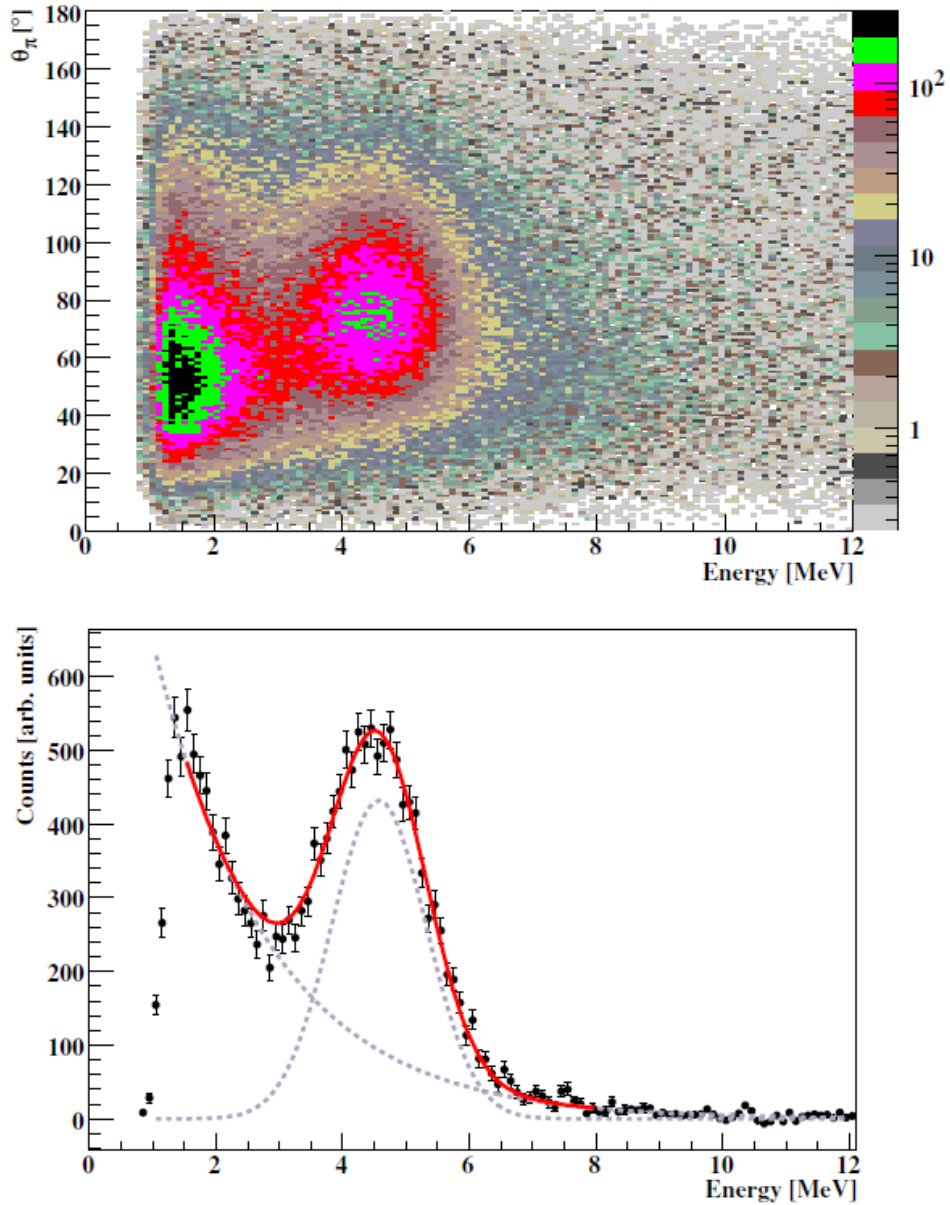


Figure 1.5: Projection of θ_π , with 4.4 MeV gamma ray from $^{12}C^*$ [12].

also help in accounting for the shape of the background, where the coincidence peak for π^0 - γ coincidences was ~ 30 ns wide, with 4% of the random events being attributed to the background. In general, the total systematic uncertainty in the cross sections was found to be of the order of ~ 10 %, with the majority of the uncertainty due to the inefficiencies of the detector calculations, a number that can be greatly improved with an array like PARIS.

1.5 Other Physics Cases

As we have seen, there are many cases where an array of $\text{LaBr}_3(\text{Ce})$ scintillators in an array such as PARIS, would greatly further many fields within nuclear physics. These areas all have different specifications and parameters to consider where the modular design of the PARIS would allow for greater flexibility at incorporating as many of the proposed cases as possible, a list of which is given in appendix A, figures A.1 and A.2.

There are many other physics cases, which can benefit from a $\text{LaBr}_3(\text{Ce})$ array, such as the Gammasphere set-up in Argonne. The set-up with Gammasphere and suppressor BGO crystals allows for high resolution and detector efficiencies, however the timing of this system has not been optimised. A synergy of HPGe detectors and $\text{LaBr}_3(\text{Ce})$ scintillators would improve ToF measurements substantially, allowing for better particle discrimination. The ToF between the charge plates located at the focal plane of the beam (FMA), and Gammasphere is one of three ToF set-ups, the others use the BGO scintillators and beam chopper. The result is a E-dE set-up where squaring the ToF and plotting it against energy gives the masses of the recoils and particles. The M/q separator would then aid in picking out the recoils, where an improved timing resolution (and thus ToF), would result in excellent separation.

Hopefully, during the construction of the prototype, and eventually, the entire calorimeter, advancements that have been hypothesised can be proved, and the fields mentioned within this chapter can undergo a renaissance of results that will advance our understanding of the nucleus and the many mechanisms associated with radiation and particle interaction.

Chapter 2

Scintillator Detectors; Light Collection & Electronics

2.1 Introduction

Scintillator detectors are widely used in nuclear and particle physics for particle and γ -ray detection, through the emission of light due to incident particles making contact with the detector. The emitted light is subsequently collected and amplified in a photomultiplier tube (PMT), where the scintillation is converted into electrical pulses. These pulses are later analysed, each holding important information regarding the interaction of the incident radiation within the scintillator. There exist various types of scintillator detector (organic, inorganic alkali halides, etc.), each having a different mechanism responsible for its output of light. This chapter will examine how these mechanisms work for each type of scintillator, and what this ultimately means when detecting radiation.

2.2 Scintillation Crystals

In general there are two main types of scintillator detector; organic scintillators and inorganic scintillators. However, the inorganic crystals were principally used, and thus will be examined in detail, briefly commenting on the other types of scintillators for completeness.

2.2.1 Organic Detectors

Organic scintillators are composed of hydrocarbon compounds, containing benzene structures. They are commonly found in both liquid or crystal form, with the former usually a combination of various organic scintillators in a solvent. The scintillation mechanism for this variety of detector is due to transitions made by free valence electrons in the molecule, thus making it strictly due to the chemical nature of the scintillator. De-localised electrons occupying the π -molecular orbitals in the material get excited in the ionisation interaction, resulting in excitation to electron and vibrational levels.

In the π -molecular orbital, there exists various singlet and triplet spin states, with the ground state of the system denoted by the S0, singlet state. Any levels above this state are an excited variation of both the singlet and triplet states, with the ground system of the triplet state being T0. At both the ground and excited levels of the single and triplet spin states exist a fine structure, with energy spacings of the order of a few keV, relating to the vibrational modes each molecule can possess.

The derivation of these different states is purely a quantum mechanical effect. Quantised angular momentum takes the form:

$$\|S\| = \sqrt{s(s+1)}\hbar \quad (2.1)$$

Where $\|S\|$ is the norm of the quantised spin vector, s is the spin quantum number associated with spin angular momentum and \hbar is the reduced Planck constant.

Given a direction, z , spin projection on this axis is given by:

$$s_z = m_s\hbar \quad (2.2)$$

Where m_s is the secondary quantum number that ranges from $-s$ to $+s$ in steps of one, which generates values of $2s+1$ as values for m_s [13].

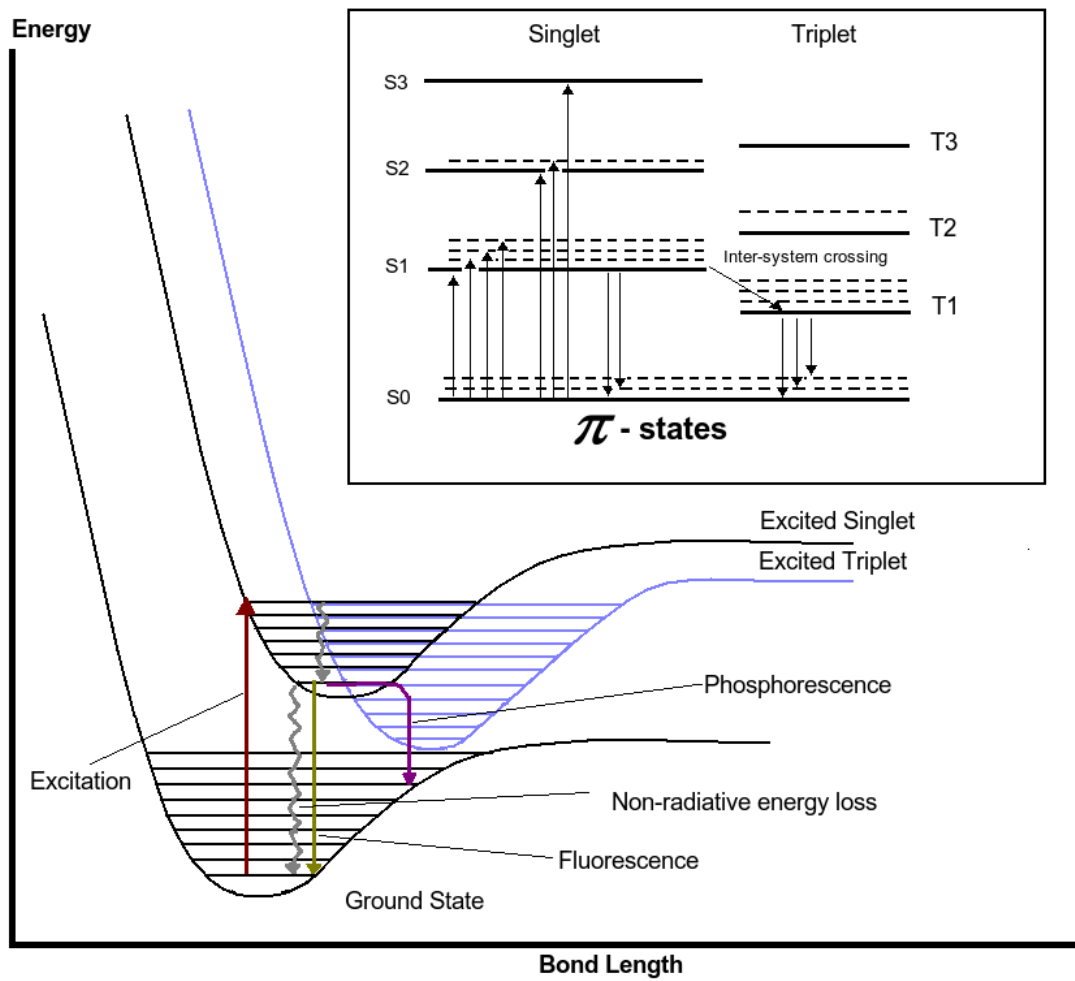


Figure 2.1: Energy level diagram of an organic scintillator.

2.2 Scintillation Crystals

Since both spin vectors S_1 and S_2 are quantised, for the electron, there exists only two directions along the z-component which results in a "spin-up" and "spin-down" term; $S = \pm \frac{\hbar}{2}$. If $S_1 = -S_2$ (ie. anti-parallel), then the total spin is $S_T = S_1 + S_2 = 0$, where the magnitude of the total spin is 0 and the quantum number, m_s , has to be zero. If S_1 and $S_2 \neq 0$, then the vector is also non-zero. The only non-zero value is \hbar in magnitude, which leaves; $m_s = -1, 0, +1$, which are triplet states. A single spin state with total spin of zero is known as a singlet state. The singlet state is anti-symmetric with respect to the exchange of the spin, and follows a two electron spin state:

$$\psi_s(S_1, S_2) = \frac{1}{\sqrt{2}}[\psi_{\uparrow}(S_1)\psi_{\downarrow}(S_2) - \psi_{\uparrow}(S_2)\psi_{\downarrow}(S_1)] \quad (2.3)$$

Similarly, a triplet state where $m_s = -1, 0, +1$, is described as:

$$\psi_{t,m=1} = \psi_{\uparrow}(S_1)\psi_{\uparrow}(S_2) \quad (2.4)$$

$$\psi_{t,m=0} = \frac{1}{\sqrt{2}}[\psi_{\uparrow}(S_1)\psi_{\downarrow}(S_2) + \psi_{\uparrow}(S_2)\psi_{\downarrow}(S_1)] \quad (2.5)$$

$$\psi_{t,m=-1} = \psi_{\downarrow}(S_1)\psi_{\downarrow}(S_2) \quad (2.6)$$

Singlet excitations decay within a few picoseconds without the emission of radiation, known as internal degradation. The intermediate state, S^* , undergoes a probable radiative decay to one of the vibrational states in S_0 , known as fluorescence, described by the prompt component figure 2.1. A similar internal degradation process is found in the triplet spin system, although without an intermediate step. Transitions from T_0 to S_0 are highly forbidden by multipole selection rules. It is more favourable for the T_0 state to interact with a molecule at the ground state and subsequently decay to the intermediate and ground states in the singlet spin state instead, producing phonon emission. This process is responsible for the delayed component in scintillator light. It is this molecular nature of the luminescence process in these organic scintillators that make them an attractable alternative to mainstream scintillators for particle identification.

2.2.2 Plastic Scintillators

Plastic scintillators are the most widely used of the organic scintillators due to their exceptional fast timing properties. Plastic scintillators, like organic liquids, are solutions of various organic scintillators in a solid plastic solvent. Extremely fast signals make plastic scintillators very attractive, as they possess exceptionally high light output, and a decay constant of the order of 2-3 ns. They can also be easily cut and machined into various shapes, therefore making them cost efficient as well.

2.2.3 Inorganic Crystals

Inorganic crystals, with high stopping powers and high light outputs, are the most popular scintillator to use in the field of particle and nuclear physics. Inorganic scintillators are principally alkali halide crystals that contain a small activator impurity. It is this impurity that plays a key role in one of the processes behind the scintillation mechanism.

As discussed previously, the scintillation mechanism in organic scintillators is due to the molecular constituents of the detector. However, in inorganic scintillators, the mechanism is due to the electron band structure in the crystals. When incident radiation interacts with the scintillator crystal, two processes can occur. The first is, ionisation within the crystal which occurs due to the excitation of an electron from the valence band to the conduction band, creating a free electron-hole pair. However, the second process involves the creation of an exciton; the excitation of an electron from the valence band to a exciton band just below the conduction band. The electron-hole pair remains de-localised, moving freely within the material. However, the presence of an activator or impurity acts as a generator of electron levels, occurring in the previously forbidden energy gap. This means that the impurity forms a trap by which any moving de-localised electron-hole exciton pair moving near the impurity can undergo ionisation with the corresponding atom. Free electrons will also fall into any holes left behind and make a transition from its excited state to the ground state, emitting radiation if allowed. Other more "exotic" processes, include scintillator afterglow and quenching. Afterglow arises due to the de-trapping and recombination of charge

carriers during long periods of excitation, which results in a delay of the scintillation light, due to an increase in the decay time of the electrons to the ground state. Quenching effects however, are due to the de-excitation processes in the scintillator mechanism, which results in no emission of radiation, and a reduced light output.

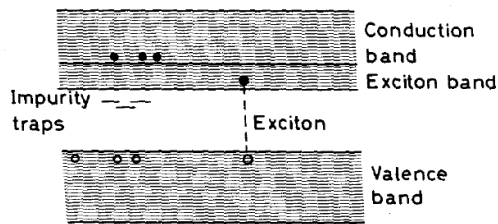


Fig. 7.7. Electronic band structure of inorganic crystals. Besides the formation of free electrons and holes, loosely coupled electron-hole pairs known as excitons are formed. Excitons can migrate through the crystal and be captured by impurity centers

Figure 2.2: The band structure in inorganic scintillators[14]

2.3 Lanthanum Bromide Scintillators

LaBr₃(Ce) is a relatively new inorganic scintillator that has been gaining popularity for use in γ -ray spectroscopy due to its excellent timing resolution (~ 200 ps depending on the size of the detector), energy resolution ($\sim 2.8\%$ at 662 keV for a 1" scintillator), high efficiency and light output (60,700 photons/MeV with a Ce³⁺ concentration of 0.2 %). The decay times are generally quick with the fast components having a value of between 15-23 ns depending on the Ce³⁺ concentration[15].

2.3.1 Cerium Activator Impurity Concentrations

The concentration of the cerium impurity in LaBr₃(Ce) will produce variations in which processes occur during the scintillation process. Due to the changes in the scintillation mechanisms, the information that can be obtained from the PMT afterwards will differ slightly.

The peak emission wavelength of LaBr₃(Ce) scintillators lie in the blue-UV part of the electromagnetic spectrum; $\lambda_{max} = 350$ nm (characteristic of Ce³⁺

2.3 Lanthanum Bromide Scintillators

TABLE I
SCINTILLATION PROPERTIES OF $\text{LaBr}_3:\text{Ce}$ WITH DIFFERENT Ce^{3+}
CONCENTRATIONS

Ce^{3+} Concentration (%)	Light Output (Photons/MeV)	Rise Time (ns)	Decay Times (ns)
0.2	60,700	3.5	23 ns (93.4%), 66 ns (6.6%)
0.5	60,000	3.4	26 ns (93%), 66 ns (7%)
1.3	47,000	2.9	16.5 ns (97%), 66 ns (3%)
5	55,300	0.7	15 ns (97%).

Figure 2.3: A table presenting variations in Cerium concentrations and subsequent effects[3].

luminescence), making them compatible with most alkali PMTs. However, the shortcoming of these detectors, is that they exhibit self-activity which can be seen as deceptive lines in experimental data. These spurious lines could limit the practicality of the detector and its uses, especially for low level counting applications in underground mines, for example.

2.3.2 PMT Selection and Blue Sensitivity

The choice of PMT is incredibly important in wanting to optimise the signal by adhering to the properties of the scintillator, and thus keeping as much of the original height and information from the luminescence as possible. In order to do this, the PMT has to be selected depending on what properties are needed in the experiment. For timing purposes, fast PMTs exist where the transit time jitter associated with the electrons travelling to the first dynode from the photo-cathode is important. Other equally important properties of these PMTs also include the number of photo-electrons released by the photo-cathode, and the resulting spread in the gain of the electron multiplier in the PMT. As the peak emission wavelengths between the scintillator and PMT needed to be well matched, the sensitivity to blue light plays a vital role. This is due to the fact that higher

2.4 CsI(Na), BaF₂ and other scintillators for PARIS

blue sensitive devices increase the number of photo-electrons and subsequently, the timing resolution of the set-up. Although the timing signal depends heavily on whether the anode signal is used and the way it is constructed, PMs with a blue sensitivity range of 13-15 $\mu\text{A}/1\text{mF}$ will give the best results when coupled to LaBr₃(Ce) scintillators, for example. In some PMTs a "parasitic" component is implemented to improve the rise time of the resulting anode pulse, by placing a screening grid inside the last dynode. This results in an improvement of charge collection due to a reduced ToF of the electrons between the last dynode and anode. A low time-of-flight between the last dynode and anode, and good charge collection at the anode is consequently observed. However, two components are observed in the resulting anode signal; the main component due to the collection of electrons from the last dynode, and another signal that is shifted relative to the main component. This "parasitic" component is induced due to electrons travelling towards the anode from the last dynodes, where the resulting charge from this shifted component triggers the fast discriminator, increasing the triggering point. This triggering point is much too high when compared to the main component, where the statistical properties of the scintillation detectors requires a low fraction of the anode pulse height, in order to achieve the best time resolution[16].

This is the technology used in XP20D0 PMTs developed by Photonic, and supplied to Saint Gobain for use with their BrillanCe 380 scintillators. FWHM timing values of ~ 90 ps and 200 ps for the 1332 and 511 keV γ -ray lines in ²²Na and ⁶⁰Co respectively, were observed. These results were obtained by using the 2026 variation of the XP20D0 PMT with a blue sensitivity of 14 $\mu\text{A}/1\text{mF}$ [16]. These values are comparable to several other PMTs developed by other companies, such as R5230 by Hamamatsu. The PMT used in the tests in York was a fast Hamamatsu R7057 model PMT with a blue sensitivity of 11 $\mu\text{A}/1\text{mF}$.

2.4 CsI(Na), BaF₂ and other scintillators for PARIS

Numerous proposals for the set-up of the outer array of crystals to be used in PARIS have been suggested, where long BaF₂, CsI(Na) or NaI(Tl) scintillators from existing arrays; such as Chateau de Cristal or HECTOR, remain the most favourable solutions. Each of these scintillators have different properties that

2.4 CsI(Na), BaF₂ and other scintillators for PARIS

make them compatible with the inner array of LaBr₃(Ce) scintillators in the calorimeter.

CsI(Na) is an inexpensive crystal which has a maximum emission of 420 nm, and is thus well matched to bialkali PMTs in terms of peak wavelength. It also possesses a high γ -ray stopping power due to its relatively high density (4.51g/cm³) and is a very rugged material. The material also possesses a relatively high light output of $\sim 41,000$ photons/MeV. However, it has a much poorer efficiency compared to LaBr₃(Ce) scintillators, with a FWHM of $\sim 6\%$ at 662 keV. It is also hygroscopic like LaBr₃(Ce) crystals, where exposure to air results in the degradation of its surface scintillation properties.

A possible way to improve the properties of these crystals further, is to introduce the presence of Br⁻ ions into the CsI(Na) crystal, as there is no dramatic drop in the light yield. These new CsI-CsBr(Na) crystals have a higher transparency in the Na activator emission region, as the Br⁻ impurity does not appear in the resulting spectra, thus the characteristics of the luminescence are identical to the standard CsI(Na)[17]. Long exposure of CsI(Na) crystals to moist air leads to a degradation in surface scintillation properties, especially the light yield. However, the CsI-CsBr(Na) crystals only show a reduction in the overall light yield of $\sim 10\%$, a dramatic improvement in the resistance against moist air when compared to the standard crystals. However, the resulting energy resolution is slightly worse at 6.4 - 6.7 % at 662 keV when compared to the standard CsI(Na) crystals; $\sim 6.2\%$. However, by using a digital high performance multi-channel analyzer (MCA), studies reveal an improvement of the energy resolution to $\sim 5.5\%$ FWHM at 662 keV[18].

Another scintillator used extensively during the research and development stages of these detectors, especially for applications involving the SensL Silicon-PM (SiPM) detectors, were CsI(Tl) crystals. A CsI crystal doped with thallium was used with the SensL detectors due to the match in emission wavelength ranges and sensitivity. The crystal was obtained from Hilger crystals, with a quoted decay time of 1 μ s and light output of 52,000 photons/MeV, it was found to be significantly brighter than what was found for the sodium doped variant of CsI. Its peak emission wavelength (λ_{max}), was found to be approximately 565 nm, making it an attractive and viable option to use with SiPMs. CsI is also rather

dense (4.51 g/cm^3), giving it a respectable stopping power needed for localising as much of the incident γ -ray energy as possible within the scintillator. The light emission between a face of this scintillator and glass is quoted as 22.9 % by the data sheet provided by Hilger crystals [19] and at 662 keV, was found to have an energy resolution of $\sim 6 \%$ [20].

The properties of a NaI(Tl) scintillator were also investigated as an alternative to CsI(Na) in the phoswich arrangement. NaI(Tl) scintillators are extensively used, with a high light output of 38,000 photon/MeV, and rapid decay time of 250 ns, it is a versatile material that can be created and shaped effortlessly. Although not as dense as other scintillators (3.63 g/cm^3), it produces a very high signal, where under optimum conditions 10^4 photo-electrons can be produced (second only to LaBr₃(Ce)[21]). The differences between the response of this scintillator and the CsI(Na) scintillator when used in the phoswich detector method, are discussed later in chapter four.

Barium Fluoride is a very common halide scintillator used in γ -ray spectroscopy due to its transparency and ability of being one of the fastest scintillators to detect γ rays and other high energy particles. It is a non-hygroscopic and dense (4.893 g/cm^3) material that provides a high amount of stopping power. However, BaF₂ has a refractive index of ~ 1.47 at peak emission, which is not as compatible with the refractive index of the acquired PMT glass. This becomes important when trying to optimise the efficiency of the light transported through the detector system, where BaF₂ has a poor light output (between 1,400 and 9,500 Photons/MeV with corresponding decay constants of 0.6 ns and 630 ns respectively), when compared to other scintillators. Despite having a fast and slow response, both of these components glow in the UV part of the spectrum with peak emissions of 220 nm or 310 nm respectively, making compatibility with PMTs increasingly difficult as alkali PMTs tend to peak at $\sim 400 \text{ nm}$.

2.5 Light Loss in Scintillators

The method and subsequent problems involved with coupling the PMT to a scintillator will now be examined, where the amount of light collected, and how

2.5 Light Loss in Scintillators

that light is transported through the detector system, dictates the overall detector efficiency.

Light loss from the scintillator and PMT is the main issue, where the light can escape by absorption through the scintillator material. However, this is only valid if the attenuation length is comparable to the total path length of the photons, as shown in equation 2.7. The size of the detector becomes crucial, as the intensity of light falls off exponentially by approximately e^{-1} . However, typical attenuation lengths are typically between 0.5 and 1 metre, and thus are only likely to be of real concern to large detectors.

$$L(x) = L_o \exp\left(\frac{-x}{l}\right) \quad (2.7)$$

Where l is the length of attenuation, x is the length of the path travelled by the light and L_o is the initial intensity of the light.

The biggest amount of light loss is due to light escaping through the boundaries of the scintillator, since only a fraction of light will come into contact with the PMT. However, depending on the incident angle of the incoming radiation that travels to the boundary regions, the light will either be reflected back into the crystal or partially reflected, depending on whether the incident angle is greater or less than the Brewster angle, Θ_B ¹. As a result, there should a medium surrounding the scintillator with a very small refraction index to minimise the Θ_B , which in the case of modern scintillators today is a layer of air in between the scintillator and reflective material.

Any loss of light within the scintillator will ultimately effect the energy resolution and efficiency of the detector, although due to different points of emission of electrons, the amount of light output reaching the photo-cathode will cause variations in pulse height. To limit the amount of light loss to the scintillator boundaries, it is common practise to wrap the scintillator in aluminium foil. Aluminium is a common reflective sheet that can be used to reflect the escaping light back into the PMT via numerous reflections, although not ideally used if there are a lot of reflections initially. The coupling of the scintillator and PMT is done

¹The Brewster angle is 42° for a refractive index; $n_{scint} \sim 1.5$

with an optical grease, so as to eliminate all air pockets. Air pockets that are still present, will trap light, resulting in inefficient light transmission and a poor output. The silicone grease must also have a refractive index similar to that of the scintillator and PM window. In inorganic scintillators, this becomes an issue as the refractive indices are not as well matched. The silicone grease BC630 from Saint Gobain, was used in coupling most of the scintillators in this thesis.

The last step is ensuring that the connections between the scintillator, PMT, and voltage divider are all light tight. This is done by wrapping black electrical tape around the detector system. Corners and bends in the detector geometry need to be addressed the most, as it is highly probable that light will leak from these areas. In the case of areas where there might be a high magnetic field due to close proximity of a beam-line, for example, a magnetic shield may also need to be applied.

Attention will now shift to how PMTs might perform when used with a scintillator under experimental conditions.

2.6 Photomultiplier Tubes

A photomultiplier tube or PMT, is an electron tube that converts scintillation pulses into electrical current. They are extremely sensitive to light, and are used mostly with scintillation crystals. The basic design consists of a photo-cathode made of sensitive material, followed by a number of dynodes to collect and amplify the initial electrical current. The dynode string or electron multiplier system results in an output at the anode where the entire signal can be read, although usually a signal can be taken at any point along the dynode string. These inner workings of a PMT are housed in an evacuated glass tube, making use in low pressure environments (i.e vacuum) unfavourable. Another drawback of using PMTs is that due to the way they work, the presence of a magnetic field will ultimately affect the performance of the detector. This is due to the transit of the electrons within the PMT being shifted as the number of photo-electrons that come into contact with the photo-cathode, and the subsequent number that are amplified within the dynode string is greatly varied and reduced, leading to the acquisition of spurious data.

2.6 Photomultiplier Tubes

During operation, a bias high voltage is applied at the cathode. When incident radiation strikes the photo-cathode after travelling through the scintillator crystal, an electron is emitted due to the photoelectric effect. This electron is then focused towards the first dynode by an electrode where it is accelerated to the first dynode in the electron multiplier chain, where contact with the dynode results in the secondary emission of electrons.

$$E = h \cdot \nu - \phi \quad (2.8)$$

These, secondary electrons are created and are similarly accelerated to the second dynode where this process repeats itself, resulting in a cascade of the initial electrons, plus additional secondary, tertiary electrons etc., from interactions with previous dynodes. After acceleration down the 8-12 dynode string, the resulting cascade is collected at the anode, where the resulting current can be amplified further and subsequently analysed.

Photomultipliers are considered to have an approximately linear output, where if the PMT is assumed to be linear, any number of photons corresponding to the interacting radiation, will be directly proportional to the amount of current generated in the anode. The addition of a scintillator when coupled to a PMT, provides the sum energy deposited, since scintillators produce photons in proportion to the amount of energy deposited by γ rays.

The photo-cathode converts the incident light to electrical current via the photoelectric effect (figure 2.4). The efficiency of converting the incident light to electrical current depends strongly on the wavelength and frequency of the incoming light, general structure of the scintillator, and the number of photo-electrons released divided by the number of incident photons on the cathode. The quantum efficiency can thus be derived by considering these parameters, where typical quantum efficiencies for PMTs range from 15 - 40 %, and peak in efficiency at ~ 400 nm.

To work effectively, PMTs need a voltage divider to run in conjunction with the main voltage supply.

2.6 Photomultiplier Tubes

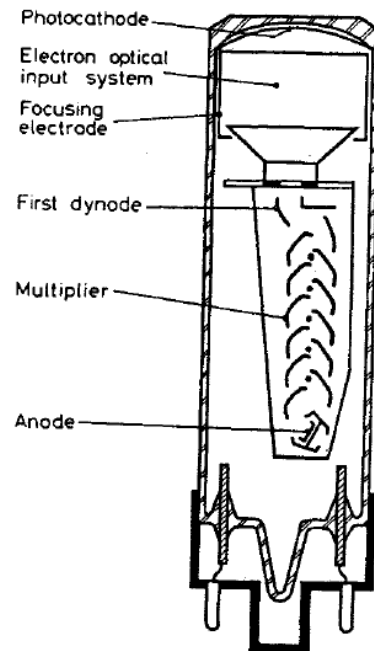


Figure 2.4: An example of a photomultiplier tube[14]



Figure 2.5: The constructed voltage divider

2.6.1 Voltage Dividers

Voltage dividers consist of a chain of resistances of varying strengths in a system designed to give a desired output voltage for each dynode in the string. Variable resistances can be added for fine adjustment, since large potential differences between each of the dynodes due to fluctuations in the current can arise, resulting in the degradation of both the linearity and overall gain. It is therefore essential to maintain the potentials by using a "bleeder" current in parallel with the resistance chain to discharge the energy in the capacitors. The presence of a bleeder guarantees a minimum load, which helps to regulate the voltage supply when the normal load is changing, and is commonly used with power supplies of vacuum tube amplifiers to avoid the occurrence of changes to the linearity and overall gain in the PMT[22]. The variation in the gain is shown in equation 2.9, where I_{an} is the anode current, I_{bl} is the bleeder current, n is the number of stages and δ is an emission factor.

$$\frac{\Delta G}{G} = \frac{I_{an}}{I_{bl}} \frac{n(1 - \delta) + 1}{(n + 1)(1 - \delta)}, \quad (2.9)$$

Shifts in the linearity and gain result in a surge of electrical current due to quick electron transit times through the PMT, known as peak currents. To maintain linearity through the dynode string, a bleeder current with several decoupling capacitors can be fitted so that potential drops in the anode current. This is due to a surge in the peak current in the final stages, which can now be avoided. These capacitors release the additional charge needed to overcome any peak increase, and are recharged during periods when the anode current is larger than the peak current rate. In some instances, Zener diodes are used instead to replace the resistors in the later stages of the dynode string[22].

2.6.2 Pulse Shapes and Linearity

The linearity of a PMT depends heavily on the type of dynode configuration used, and the current travelling through the tube. For a PMT to remain linear, the

total amount of current needs to be fully collected at each dynode in the string before moving onto the next dynode, so that the initial cathode current will be directly proportional to the current travelling through the PM. Incidentally, this current collection depends on the applied voltage and the differences between each stage, where at a given current, increases with applied voltage, until a threshold or saturation level is reached. At this point, it can be said that all the current has been collected, due to the space charge being swept away due to an increase in voltage around the emitting electrode.

The PMT can be regarded as a current generator due to producing a current at the anode where the total charge of the system is proportional to the initial number of electrons emitted from the photo-cathode. The circuit elements in the PM can be represented by the following equations, where the light from the scintillator can be described as an exponential decay[22].

$$I(t) = \frac{GNe}{\tau_s} \exp\left(-\frac{t}{\tau_s}\right) \quad (2.10)$$

Where G is the gain of the PMT, N is the number of photo-electrons emitted by the cathode, e is the electron charge, and τ_s is the decay time associated with the scintillator. With this information, the equation takes the form[22],

$$I(t) = \frac{V}{R} + C \frac{dV}{dt} \quad (2.11)$$

Where V is the signal height or voltage, R is the resistances and C is the capacitance in the set-up. The solutions from this result are expressed in terms of the signal height, V(t),

$$V(t) = \begin{cases} -\frac{GNeR}{\tau - \tau_s} \left[\exp\left(-\frac{t}{\tau_s}\right) - \exp\left(-\frac{t}{\tau}\right) \right] & \tau \neq \tau_s \\ \left(\frac{GNeR}{\tau_s^2} \right) \cdot t \cdot \exp\left(-\frac{t}{\tau_s}\right) & \tau = \tau_s \end{cases} \quad (2.12)$$

For instance when the output circuit time constant of the resulting pulse ($\tau=CR$), is much less than τ_s , the signal is small, and the pulse is not integrated (current mode of operation). However, the original decay time of the signal and quick rise time (which is dependent on τ), are maintained. When $\tau \gg \tau_s$, the signal is larger, the decay time is longer, and the pulse is integrated (voltage mode of operation). The rise time follows τ_s approximately, whereas the decay time now closely follows the output τ [22]. The signal output is observed to be much higher in the voltage mode of operation and thus makes it more favourable to use than the current mode. This mode is more prone to pile-up due to the longer decay time, and thus has a limited counting rate. Altering the resistance at the anode allows the desired pulse form and τ to be achieved. Utilising the current mode would allow for a higher count rate, but due to the significantly smaller amplitudes, would be prone to fluctuations generated from the photo-cathode. More information regarding pile-up and its subsequent effects on scintillator detectors will be discussed in chapter 4.7.

2.6.3 Noise

Noise is a familiar problem when trying to record and analyse pulse shapes using a PMT. To optimise the performance of both the detector and scintillator, and obtain excellent pulse shapes, the set-up needs to be properly grounded. Even when there is no bias voltage being applied to the PMT, a small current still exists. This dark current can have several sources due to leakage currents, radioactive contamination, damage, and light or ionisation phenomena within the detector set-up. However, it is most likely due to thermionic emission from the cathode and dynodes (Ohmic losses). The latter due to thermal emission can be described by the Richardson equation[14] where the exponential nature shows by lowering the temperature, noise is also reduced.

$$I = AT^2 \exp\left(\frac{-e\phi}{kT}\right), \quad (2.13)$$

Where; A is an arbitrary constant, ϕ is the work function, T is the temperature (K), and k is the Boltzmann constant. In general, dark currents in PMTs should be of the order of several nano-amperes, thus contributing a very small fraction of the overall effect from noise, compared with other detectors; such as semiconductors. Noise in the detector is principally due to the statistical nature of processes involved in photo-emission. Fluctuations in the anode signal due to the variation in the number of photo-electrons, and subsequent electrons emitted in the dynode string[14] contribute to around $\sim 10\%$ of the overall statistical noise. This is due not only to fluctuations in the number of secondary electrons emitted, but also due to transit times between each dynode. The statistical noise due to the nature of the photoelectric effect near the photo-cathode makes up the largest component of the amount of total noise in the PMT.

2.7 NIM Modules

Up until now, the set-up of a detector system has been discussed, and the scintillation processes involved in the luminescence procedure investigated. However, a lot more integration and shaping processes go on after the generation of photo-electrons in the the dynode string and their passing through the voltage divider. The electrical pulses have to be configured in a system that extracts and optimises the performance of these detector systems. This modular system established in particle and nuclear physics is the Nuclear Instrument Module (NIM) system, where basic electronic kit such as amplifiers, are constructed in versatile modules which are held in standardised bins. The modules are created according to mechanical and electronic specifications so that any NIM module can fit into any NIM bin. The power bins supply four standard DC voltages (-12 V, +12 V, -24 V and 24 V), to up to a maximum of 12 single-width modules. This NIM system is very flexible and all the necessary modules needed for any experiment can be set up in a bin and moved around. This cost efficient use of instrumentation is utilised in laboratories worldwide to ensure that experiments run efficiently and that the resulting signal characteristics are optimised.

2.7.1 Amplifiers

After the generation of a signal from the PMT, it is generally fed into an amplifier or pre-amplifier where the signal is shaped and amplified for further processing. Adjustable gains feature on most amplifiers that allow for pulse height information analysis, where the amplitudes of the signal need to be preserved. However, the most important use of amplifiers are their ability to shape pulses, where optimisation of signals at low counting levels (and high background rates), help in maintaining a good peak-to-background ratio. Aside from low counting rates, pulse shaping is also crucial in its ability to correct situations where several pulses are generated at a high count rate, which results in a phenomenon known as pile-up. Pulses from pre-amplifiers are generally exponential in nature and can have a tail as long as several hundred micro-seconds, where the amplitude of this pulse is proportional to energy. If a second signal arrives within a time; τ , of the initial pulse then the amplitudes of both pulses are superimposed, giving spurious information about the energy. To avoid this, the counting rate needs to be reduced to less than $1/\tau$, or the pulse tail needs to be shortened through pulse shaping using an amplifier. This is discussed in more detail in chapter four.

The most common technique for pulse shaping is sending the incident step-function signal through a CR (capacitor-resistor) filter at a low frequency, before passing it through a RC (resistor-capacitor) filter at a high frequency. This results in an improvement in the signal to noise, and provides the basis for CR-RC pulse shaping. Optimisation of the signal to noise is obtained by applying differentiation and integration time constants, the values of which depend heavily on the characteristics of the incoming pulse. Unfortunately, a side-effect of using this technique is the presence of an undershoot in the resulting shaped pulse, due to the application of an inappropriate differentiation constant to the exponential tail pulse. Theoretically, an infinitely long tail pulse will have no undershoot, however a cut-off point needs to be assigned for real pulses. It is the assignment of a cutoff point that causes these undershoots to occur, which can be rectified by using a pole-zero cancellation circuit, utilising a Laplacian transform on the circuit[23]. In some cases, pole-zero cancellation circuits don't eliminate this problem completely, due to DC coupled capacitors at the output of an amplifier

creating an instance where the undershoot reappears again, which may be due to subsequent residual differentiations. This is best avoided by using a large capacitance on an adjoining capacitor so that the time constant of the output capacitor is large in comparison to the signal, the differentiation effect is thus reduced along with the height of the undershoot.

If the duration between the pulses is shortened, and there is likely to be an overlap of pulses, the undershoot becomes more exaggerated resulting in a fluctuating baseline. Amplifiers with a baseline restorer setting are designed to combat this sort of problem by using circuits at the output stage to shorten the decay time of the undershoot, by shorting the capacitor to ground after receiving a pulse. An alternative solution to this problem, is to use a bipolar signal output as when the pulse passes through a coupling capacitor, it leaves no residual charge. This results in no baseline shifts, and at high count rates, becomes a better candidate for producing spectra with optimum resolution. Bipolar signals are also widely used in timing applications as the zero cross-over point provides a good place to trigger discriminators. However, at low count rates, the signal-to-noise generally favours unipolar pulses. In most of the cases, a undershoot was seen in the $\text{LaBr}_3(\text{Ce})$ pulses and several amplifiers were used to try and shape this bipolar pulse to the best of our ability despite using a unipolar setting. In the end, a short decay constant and low gain was applied using several amplifiers, the best of which was a spectroscopy amplifier developed by ORTEC.

2.7.2 Other Important NIM Modules

2.7.2.1 Fan-In Fan-Out (FIFO)

A Fan-in circuit accepts a number of inputs of an electronic logic gate and delivers an AND gated signal, in various polarities. A Fan-Out circuit allows one signal to be divided into several identical signals with the same characteristics over the entire electronic system. The FIFO module can be linear; accepting both analog and logic signals, or just manufactured for accepting logic signals only.

2.7.2.2 Charge to Digital Modules

A charge to digital module or QDC, is a relatively new module designed to gate and digitise pulses before sending them on to a CAMAC for processing. They work by measuring the integrated charge of the incoming signal, and applying a gate. The module purchased from CAEN has 16-32 channels, each of which have a negative input with 50Ω impedance. Each of the channels are converted to a voltage level by a QAC (Charge to Amplitude Conversion). Each QAC output is subsequently converted by two ADCs in parallel; one ADC incorporates an incoming gain of x1 gain, while the other incorporates a gain of x8. A dual input range is also featured, avoiding saturation, while increasing the resolution. The outputs of the QAC sections are also converted by two fast 12-bit ADCs, where techniques are employed to improve any differential non-linearity[24]. A QDC is needed for each detector in order to discriminate between the slow and fast components in the phoswich detector.

2.7.2.3 Coincidence Units

A coincidence occurs when two or more logic input signals occur within the same time interval set by a discriminator. As a result, a logic signal is subsequently generated, if otherwise, there is no signal. The method used in this thesis for coincidence measurements is using the sum of the incident signals to pass a threshold set by a discriminator by adjusting the timing so that both pulses occur within the same amount of time. This can be done using a Gate and Delay Generator (G&DG), which manipulates the signal width and time to what is desired without compromising the information. Thus, the resolving time of the coincidence between these two overlapping signals depends heavily on the adjusted width of the signals and the minimum timing requirements by the electronics to ensure the signals overlap. This logic gate module performs an "AND" operation on the acquired signals, whereas other logic gates can perform other operations such as "OR" and "NOT". Boolean laws and operations are only briefly mentioned here as the majority of the experiments were done using analog setups[23].

2.7.2.4 Discriminators

A discriminator is used to set a threshold on an input signal so that it can segregate pulse heights above a certain value. After this procedure, a logic signal is generated if the case is true, otherwise no response is issued. Pulses that are large enough to appear above this threshold are transformed into logic signals for further processing using other electronics. Discriminator modules are commonly used to eliminate background noise for timing resolution measurements, typically using the constant-fraction method or other methods of triggering. A common method of triggering is using the leading edge method; the moment a pulse crosses a set threshold level in time. However, due to the amount of walk seen in the output, this method of triggering was not used. Instead, the constant-fraction triggering technique, which requires a logic signal to be generated at a fraction of the peak height (typically 50 %), was used during the timing measurements. This was to ensure the timing results were as precise as possible, resulting in a cleaner TAC output.

2.7.2.5 Time to Amplitude Converters (TAC)

The duration between two incident logic pulses is converted (by a module called a Time-to-Amplitude Converter), into an output whose pulse height is proportional to the time between the two signals. Timing measurements by a TAC occur when a START pulse from an incoming signal releases a discharge from a capacitor which gets cutoff and subsequently discharges on arrival of a STOP signal. This is used in determining the timing resolution as a function of the interval between the two pulses, where the total charge collected is proportional to the time difference between the START and STOP signals. Gating on the coincidence and using a single channel analyser (SCA), will produce a cleaner TAC output. This will ultimately result in a smaller width of the outgoing timing pulse, and thus a very good timing resolution when analysed in an MCA.

2.7.2.6 Multi-Channel Analyser (MCA)

A Multi-Channel Analyser, or MCA, digitises the amplitude of an incoming pulse with an ADC. These pulses are sorted according to pulse height and number, by

incrementing the memory channel (which is proportional to the digitised value of the pulse). As a result, each pulse height corresponds to a memory location where the amplitude information is stored. The conversion gain dictates the resolution of the MCA, and involves the total number of channels used within an applied voltage range becoming digitised from 128 to $\sim 16\text{k}$ channels. The input signals have to meet the rise time and widths requirements to allow the ADC enough time to digitise the pulses, facilitated by external modules. In addition to this procedure and the memory allocation, other pieces of electronic circuitry are equipped on the MCA, such as discriminators and gates, which help in the collection of specific parts of data.

Having commented on the essential background and commented on various aspects of the experimental set-up, the research and development of the PARIS array can now commence. The next chapter will examine the theoretical aspects of developing the array using Monte Carlo and other simulation methods to develop and predict the response of a fully working calorimeter under different conditions.

Chapter 3

Simulations for PARIS

3.1 Simulation and Analysis Software for PARIS

The preliminary proposal made by the PARIS collaboration was to design a detector of a predominately cubic design, with two layers of scintillator crystals. It is envisaged that the inner diameter of this set-up can be changed to accommodate a larger or smaller array, as it is mechanically feasible to do so. These two layers would allow for synergies with other detector arrays such as AGATA and GASPARD. This makes the cubic geometry more attractive than the conventional 4π geodesic design. However, how does one construct and simulate such a novel concept? In answering this question, the basics behind the simulation and analysis packages needs to be understood where figure 3.1 shows the steps behind the simulation work. The basic foundation is presented where the addition of segmentation and various other parameters are discussed, and the results shown. The results from these preliminary simulations will lay the foundation for the development of more sophisticated designs, culminating in simulations of the full calorimeter proposed by the collaboration. Other fully tiled geometries were also explored and simulated to determine the improvements in efficiencies with a geodesic design. An example of this, was the simulation of a physics case with an existing 4π NaI(Tl) detector array at the University of Oslo called CACTUS, where a comparison was made when the detector material was substituted with LaBr₃(Ce).

3.1 Simulation and Analysis Software for PARIS

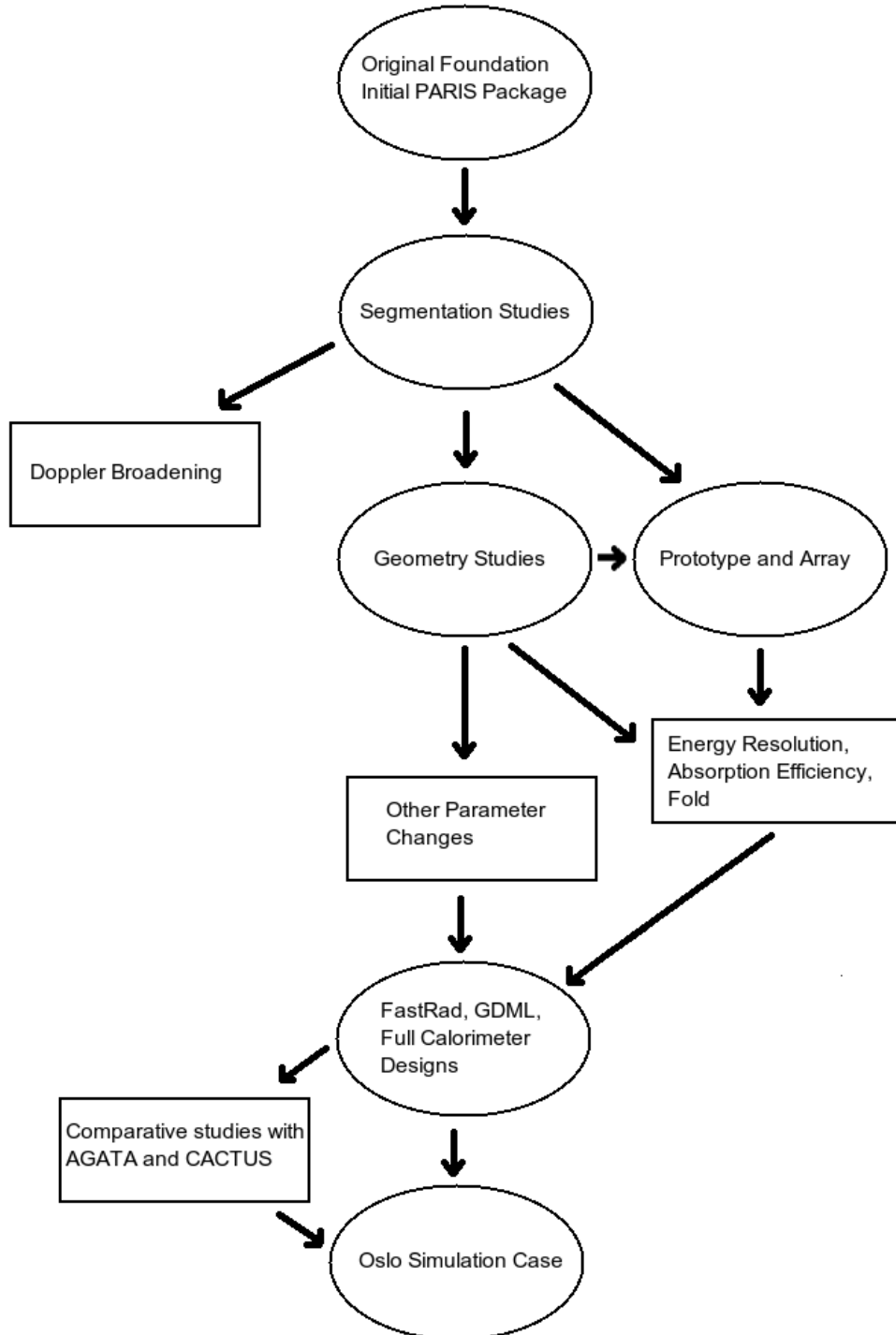


Figure 3.1: An outline of the process behind the simulation work for PARIS

3.1.1 GEANT4 Software

GEANT4 is a toolkit developed by engineers and scientists at CERN and other institutions worldwide, to simulate the passage of various types of particles and radiation through different mediums using software and object-orientation technology in C++, which has a huge energy range from the eV to TeV scale.

The toolkit has a hierarchical structure of domains that are linked together when the program is compiled with a GNU makefile. Several domains that are necessary to construct a physics case include the following:

- The geometry and material of the detector used.
- Particle interaction within the detector medium or other matter.
- Tracking of the particle. i.e how many steps to move the particle.
- The hit pattern, event and track management.
- Visualisation and user interface framework.

3.1.1.1 Events Generator and class

An interface to external physics event generators for the generation of the primary particles (which define the desired physics events), is performed in the events section, where particles are represented by independent special classes. These classes can be interfaced to link various separate classes together using codes that are linked to the physics generators. This segregated system allows a simulation program to be independent of various defined physics generators, and to be independent of the specific solution. Moreover, the decay chains of various particles can be imported from the physics generator.

The class G4Event represents an event; the main unit of simulation. After the simulation of the event, this class passes on the information needed for other classes down the chain of the program and disposes of less-meaningful information. It contains primary vertexes and particles before processing the event, where particle interactions, digitisation generated by the simulation and trajectories of

3.1 Simulation and Analysis Software for PARIS

the simulated particles, is found and stored. G4Event is never stored and a conversion code is needed to link the corresponding classes. The benefits of this independence for G4Event becomes apparent in situations where pile-up occurs, as digitisation can be postponed until two or more events are processed. This makes use of information about the timing, so that the detector signals can be generated as the consequence of overlapping signals.

3.1.1.2 Geometry and detector representation

The geometry category within the program, where refinements and advances from previous simulation packages have been made to cope with detector volumes of more exotic shapes and sizes. Noticeably, an interface for Computer Aided Design (CAD) is available allowing a broader range of compatible geometrical designs.

In GEANT4, there exists logical and physical volumes, where a logical volume represents a detector element that can hold other volumes inside it. One thus has access to information independent of its physical position in the detector. A physical volume is the spatial positioning of the logical volume with respect to an enclosing mother (logical) volume. This leads to the concept of a hierarchical structure of volumes, providing they do not overlap.

The logical volume can be defined as a solid of various shapes, such as rectangular boxes, trapezoids, spherical and cylindrical sections or shells. This becomes important later as each shape has a unique separate code for each of their properties, the concept of which is known as Constructive Solid Geometry (CSG). More complex solids can be created, defined by their bounding surfaces, and are categorised in a Boundary Representations (BREPs) sub-category[25].

3.1.1.3 Tracking

The transportation process moves the particles via an outlined process, for which the tracking does not depend on the particle type nor on the specific physics process. Each particle is moved step by step with a tolerance that preserves the necessary tracking precision without compromising the execution of the process. This optimises the processing power of the CPU as the performance of the simulation depends on the time spent moving particles by one step, the primary focus

3.1 Simulation and Analysis Software for PARIS

of the tracking category. However, for a particle at rest the maximum allowed step is minimised and the steps needed from all the related processes are also reduced.

A physics process possesses one or more characteristics depending on its nature represented by the actions in the tracking category:

- *at rest*, for particles at rest.
- *along step*, is responsible for energy loss or secondary particle production that happen continuously along a step, such as Cherenkov radiation.
- *post step*, occurs at the end of each step, such as secondary particle production by a decay or interaction.
- *Along step* actions occur cumulatively. For the above three actions, each physics process has a "GetPhysicalInteractionLength", which has a step defined, and a "DoIt" method that generates the action. Subsequently, the tracking eventually reviews all physics processes and actions for the given particle, and decides which one is utilised.

3.1.1.4 Physics

The types of action previously mentioned are defined in the base class; G4VProcess. All physics processes conform to this basic interface. However, different approaches for each of the sub-domains exist; for hadronic processes, an additional area has been prescribed due to the large number of complicated outcomes that could occur.

For particle decay, the step length is calculated from the lifetime of the particle. The generation of decay products requires information regarding branching ratios and other theoretical distributions for multi-body interaction and decays. Similarly to the particle decay action, there exists an electromagnetic physics action that manages the electromagnetic interactions of leptons, photons, hadrons and ions. The electromagnetic package is organised as a set of class categories:

- *Standard*: Handles the processes for electron, positron, photon and hadron interactions.

3.1 Simulation and Analysis Software for PARIS

- *Low Energy*: Extrapolates alternative models which covers an energy range lower than the standard category.
- *Muons*: Handles the interactions involving muons.
- *X-rays*: Specifically coded to deal with physics cases involving X-rays.
- *Optical*: Specifically coded to deal with physics cases involving optical photons.
- *Utils*: A collective class that is used by other categories.

In general there are seven main subcategories within the physics category; electromagnetic, hadron, transportation, decay, optical, photo-lepton/hadron, and parametrisation, with the electromagnetic and hadron subcategories subdivided. Each process is defined with a header and source file, which is abstract and common to all processes.

Various models are included for the decay and transitions of particles that need to be taken into consideration when assigning a step process, so that CPU optimisation is not compromised. There are also extensive databases of electromagnetic processes, such as Compton scattering, synchrotron radiation, etc., that need to have range cuts assigned. For electromagnetic physics it is important to have a range cut which is uniform across particles and materials in order to design a coherent set of processes. This also means that the interaction length also depends on the cut, where energy loss also needs to be addressed with regards to electrons, positrons and muons. This is done by generating a new class, for example; "G4VeEnergyLoss", which finds the continuous energy loss of electrons and positrons, as well as constructs a range and energy loss table for various materials, more information of which can be found on the GEANT4 website ¹.

The low energy package includes the photo-electric effect, Compton scattering, Rayleigh scattering, bremsstrahlung and ionisation. A low energy process is also available to handle the ionisation by hadrons and ions. In the high energy (>2 MeV) domain; the Bethe-Bloch formula, and for low energies; (<1 keV for

¹<http://geant4.cern.ch/>

3.1 Simulation and Analysis Software for PARIS

protons) the free electron gas model, are applied respectively. In the intermediate energy range parametrised models based on experimental data are used[25].

GEANT4 also has an ideal framework for modelling the optics of scintillation and Cherenkov detectors and their associated light guides. This is due to its unique capacity of commencing the simulation with the propagation of a number of incident charged particles and completing it with the detection of optical photons on photo-sensitive areas. The catalogue of processes at optical wavelengths includes refraction and reflection at medium boundaries, bulk absorption and Rayleigh scattering.

Scintillation materials that have been doped with an impurity have a characteristic light yield and intrinsic resolution which broadens the statistical distribution. The average yield can have a non-linear dependence on the local energy deposition. Scintillating materials also have emission time spectra with one or more exponential decay time constants, with each decay component having its intrinsic photon emission spectrum. These empirical parameters are particular to each material and must be supplied by the user. A Poisson distributed number of photons is generated according to the energy lost during the step, where the photons originate evenly along the track segment and are emitted isotropically with a random linear polarisation.

Models used for cross-sections and nuclear reactions (which become important when considering a simulated beam test with PARIS, or when investigating subsequent activation with neutron sources), are not summarised here but can be found in detail on the GEANT4 website along with many other parameters.

3.1.2 ROOT and Radware software packages

Several other types of software were used to explore and test the aims set out by the PARIS collaboration to aide with investigations into the structure of the proposed calorimeter.

3.1.2.1 ROOT

The ROOT system is a set of frameworks, used to handle and analyse large amounts of data. The data is defined as a set of objects, with specialised storage

3.1 Simulation and Analysis Software for PARIS

methods that allow manipulation of separate parts of various objects independently of the rest of the data. This includes methods for histograms, curve fitting, graphics and other methods such as the inclusion of visualisation classes that processes the data in either batch mode or separately. The command language is in C++ due to the inclusion of a CINT C++ interpreter, which allows for macros to be utilised quickly as the compile/link steps are not necessary.

The system has been designed in such a way that it can call on databases (in parallel) within clusters of workstations or many-core machines. ROOT is an open system, that can be dynamically extended by linking external libraries, making it a premier platform on which to build data acquisition, simulation and data analysis systems.

The backbone of ROOT is the layered class hierarchical system which consists of ~ 1200 classes grouped in about 60 libraries divided into 19 main categories. Most of the classes originate from a common base class; "TObject", as it enables the implementation of some essential infrastructure inherited by all descendants of this class.

The classes in the ROOT base category provide the most low-level building blocks of ROOT. These classes include; TClass, TStorage, TFile, and TSystem. These classes provide general purpose data structures like; arrays, lists, trees, and maps, for example. The histogram category provides classes for advanced statistical data analysis, like multi-dimensional histograms using short, long, float or double values, with fixed or variable bin sizes.

The documentation classes allow the creation of C++ header and source files, inheritance trees, class indices, macro's and session transcripts. Most ROOT classes are derived from the TObject class, which defines various methods for comparing objects, for graphics hit detection, for example.

The ROOT object I/O facility supports the streaming of data structures from the memory to a buffer. This buffer can than be to stored in a ROOT binary machine-independent file, an XML file, or over a network. The C++ run-time system gives no access to type and structure information, and so the ROOT system uses CINT, which parses¹ the class header files and generates a dictionary (in the form of a C++ function).

¹Checks the syntax and builds the data structure to the design specified in the code.

3.1.2.2 Radware

Radware is a software package developed at Oak Ridge National Laboratory, and incorporates a graphical interface for analysing gamma-ray coincidence data, as well as displaying spectra. Several programs are incorporated in the Radware package, namely; `gf3`, `escl8r`, `levit8r` and `4dg8r`. Of these programs, the `gf3` program was used frequently in fitting, analysing and manipulating spectra and reproducing the data in a 1-D histogram. The other programs involve coincidence matrices (`escl8r`) and four dimensional versions of gamma coincident matrices (`levit8r` and `4dg8r`)[26].

The `gf3` program involves generating a `.spe` file from an ascii text output file from a multi-channel analyser (MCA). Once the spectrum has been made, the user has the power to manipulate the data, where several spectra can be overlaid and represented differently by changing the scale on the axes. The data can also be calibrated, and peaks fitted with various methods that give the user a broad and flexible range of choices when studying their data, more information on which can be found on the software website¹.

3.2 Constructing the PARIS Array

The proposal made by the PARIS collaboration; to design a detector array of a cubic design, is much more flexible than the other proposed designs due to the two modular layers of scintillators featured in the calorimeter (see figure 3.2). The inner layer of scintillators can be changed to accommodate another array, making the cubic array an attractive and versatile design.

¹<http://radware.phy.ornl.gov/gf3/gf3.html>

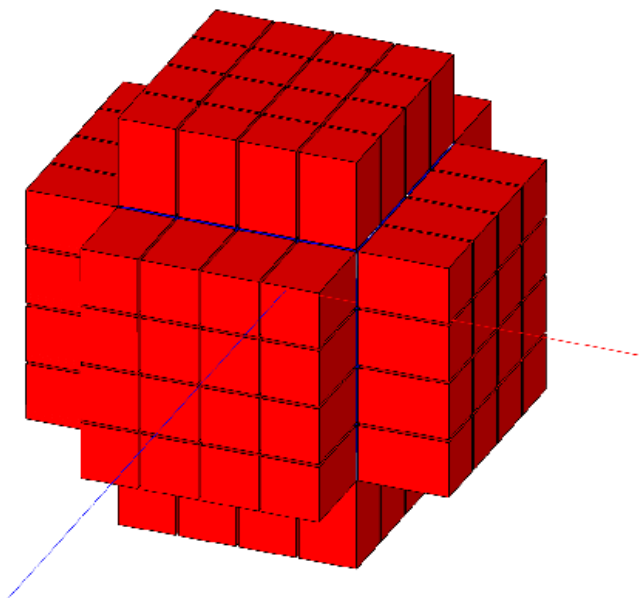


Figure 3.2: 4x4 array of the simulated PARIS detector using 2"x2"x2" LaBr_3 (not shown) and 2"x2"x6" CsI crystals (Red).

3.2.1 Segmentation

The cube first needs to be segmented into a shape that would be most suitable for γ -ray spectroscopy. The idea is to create six modular detector walls, where each wall will be composed of an array of scintillators, 2"-4" in length (although in-depth analysis later reveals the optimal size). To segment geometries in GEANT4, one has to create a set-up file, with relevant codes in the include and source files. Once these have been made, the resulting segment or module, can then be tiled into an array.

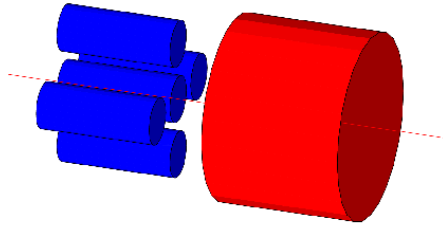


Figure 3.3: Segmentation of the two layers.

Originally simulations were computed with the design shown in figure 3.3, later replacing the the tubes with cubes. This type of geometry becomes important when the Doppler effect is applied, as it is crucial to know where to place the segmented volumes to exploit Doppler beaming.

3.2.2 Effects of Doppler Broadening

When a γ -ray is emitted by a moving source along a horizontal trajectory it displays a Doppler shift, where it is detected at an angle θ , with a different energy to its initial energy, E_0 . The equation for non-relativistic Doppler shift follows the form:

$$E = E_0(1 + \beta \cos(\theta)) \quad (3.1)$$

Where β is the recoil velocity in units corresponding to the speed of light. In the case of non-relativistic motion, β will have to have an upper limit defined. For PARIS, the maximum recoil velocity needed to achieve the desired detector performance will be in the region of $\beta_{max} = 0.1$, where one observes a 10 % Doppler shift between 0° and 180° . Therefore, a 5 MeV γ -ray will be detected with a shift in its initial energy of 500 keV.

As we know, an incident γ -ray is detected as a function of angle ranging from 0° to 180° . However, at high values of β where the velocity of the recoil is starting

3.2 Constructing the PARIS Array

to approach speeds close to the speed of light c , there is a breaking of symmetry due to the Lorentz boost as $\theta \rightarrow \theta + 90^\circ$, and thus get a discrepancy between the classical Doppler formula and the relativistic equation:

$$E_d = \frac{E_0}{\gamma} \frac{1}{1 - \beta \cos(\theta)}, \quad \gamma = \frac{1}{\sqrt{1 - \beta^2}} \quad (3.2)$$

Therefore, for PARIS physics cases where recoil velocities are 10 % of the speed of light or lower, the classical formula for Doppler shift can be used. For values nearing the speed of light, the relativistic formula above should be used. Looking further into this phenomena, one needs to explain the effect Doppler broadening has as well, as it can have implications on the design and granularity of the calorimeter.

Doppler broadening is an observed spread of measured energy in a stationary detector caused by γ rays being emitted from a moving nuclei. When the velocity is increased for the nucleus, the opening angle the nucleus sees is increased as well. As a result the uncertainties comes from the resolution of the detector and from Doppler correction of the form:

$$\Delta E_{Total} = \sqrt{(\Delta E_{Res})^2 + (\Delta E_{Dopp})^2} \quad (3.3)$$

In general, Doppler broadening can be broken up into three major terms; the opening angle ($\Delta\theta$), the uncertainty in the direction of the source ($\Delta\theta_r$), and the absolute value of the recoil velocity ($\Delta\beta$)[27]. The effect this has on the opening angle of the detector is determined by deducing the best opening angle for each segmented detector.

Recent simulations have shown that a realistic number of detectors can be used to cover a large amount of solid angle at the desired granularity, allowing for a number of reactions up to $\beta = 20\%$ with 1" crystals placed 20 cm from the source. Doppler broadening simulations also show that a 2" detector at a distance of 15 cm gives $\Delta\theta = 9.61^\circ$, and 2" detectors placed roughly half a metre from a source results in a lower opening angle of $\Delta\theta = 3^\circ$ [27]. The total broadening for

the LaBr₃ system was found to be 3.16 keV and 4.24 keV for doppler broadening of 1 % and 3 % respectively[27], in the case of a well known recoil. In cases where there are uncertainties with the recoil, one needs to place an error on the velocity, $\theta\beta$. This was estimated earlier for $\beta_{max} = 0.1$ (with values of $\Delta\theta_r = 5^\circ$ and 10°), to be ~ 0.01 .

3.2.3 Energy Resolution and Efficiency Graphs

In γ -ray spectroscopy, a key component in investigating what happens to the target and projectile is by observing the resulting energy spectra. In the next set of simulations, an energy resolution was defined by introducing new variables into an expression that uses σ to define the FWHM, similar to the expression:

$$\sigma = \frac{FWHM}{2.35}. \quad (3.4)$$

An approximation for how the energy resolution varies with increasing energy was derived from simulations, and found to be roughly $FWHM/E = 77.1 \pm 1.2 \cdot E^{-1/2}$, in good agreement with experimental results¹.

The simulated energy resolution was calculated by obtaining a fit, where an equation added to the file that generates the spectra assumes a FWHM of 3% at 662 keV. Consequently, a FWHM of ~ 21 keV and σ of ~ 9 keV were recorded. Similarly, one finds the energy resolution of CsI to be $\sim 6.4\%$ at 662 keV, corresponding to a FWHM and σ of 41.2 keV and 17.5 keV respectively. However, similar calculations had to be done for the spread in the incident beam energy, where at 10 MeV one assumes it will have 1 % resolution, corresponding to a σ of ~ 42.6 . This method was later replaced by; $FWHM/E = 77.1 \cdot 1/\sqrt{(E)}$ in %, where σ is calculated to be:

$$\sigma = \frac{0.771}{2\sqrt{(2\ln 2)} \cdot \sqrt{(E)}} = 0.327\sqrt{(E)}. \quad (3.5)$$

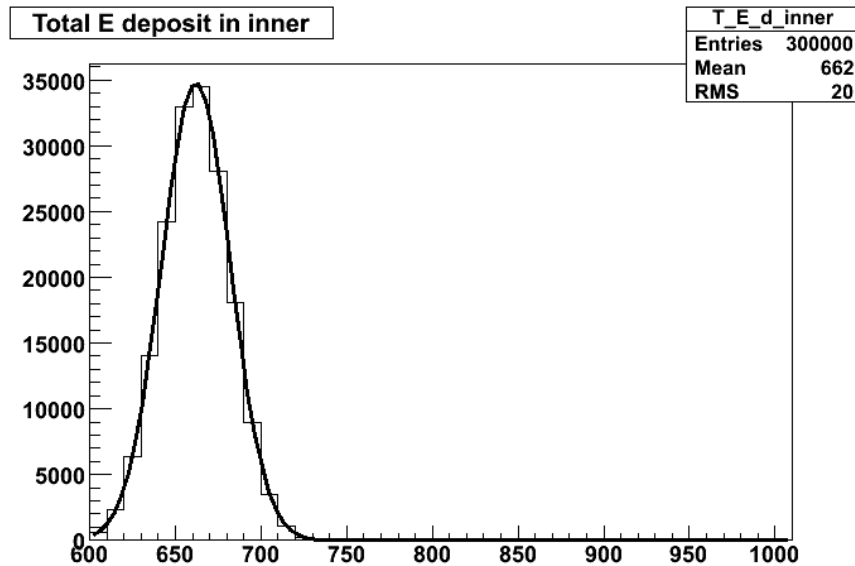


Figure 3.4: A Gaussian fit to the simulated 662 keV photo-peak with $\sim 3\%$ resolution.

After defining the energy resolutions, a noticeable difference between both the CsI and LaBr₃ crystals was observed, where the resolution of a LaBr₃ detector at 662 keV can be seen in figure 3.4. These simulations neglected the doping concentrations of both the LaBr₃ and CsI crystals, where the timing properties of both crystals rely heavily on their respective doping impurities and their concentrations. In the case of the LaBr₃ scintillators, any improvement in the energy resolution due to the cerium dopant was very slight. The improvement was in the amount of scintillation produced, and its effect on the out-going signal which was not simulated in detail. The main purpose of the CsI(Na) scintillators was to act as an absorber of high energy γ -rays, where the timing is irrelevant. Thus the doping concentrations and simulations involving the outer CsI segments were also not deemed necessary.

¹Although a more complete fit takes the form: $\text{FWHM}/E = (A \cdot E^{-1} + B)^{1/2}$, where $A = 5034.9 \pm 62.8$ and $B = 0.165 \pm 0.015$ [28]

3.2.4 Investigation of Various Geometries for PARIS

Up until now, only the absorption efficiencies¹ and response due to detector fold in cubic arrays have been investigated. However, different geometries that are potentially available for use in the PARIS calorimeter were also studied. The first set of simulations studied the relative absorption efficiencies and discrepancies in energy resolution for various sized crystals, the parameters of which were fixed. Thus, their volumes would depend greatly upon the geometry used. Later, the same volumes were used for all of the tested geometries, where the outcomes of the energy resolutions based on these results are presented.

3.2.4.1 Absorption Efficiency of a Truncated Pyramid

Typically in high efficiency calorimeters and arrays, detectors are arranged into a geodesic, 4π distribution, resulting in higher amounts of absorption and less dead space. As this is the case, simulations were conducted with two shapes; a conical shape of a thickness from its frustum to its base, and a truncated pyramid. The shapes were originally tested as individual segments and later compared to the rectangular shape, proposed for the cubic configuration of the PARIS calorimeter. The source distance between the detector faces was kept the same at 15 cm, so that the isotropic projection of γ -ray radiation² for all the presented cases were roughly equal.

As more detectors are positioned isotropically in a radial distribution around the target area, an increase in the optimisation of the angular coverage and efficiency is observed. In reality, the LaBr_3 scintillators are too expensive to manufacture into this pyramidal shape. However, simulations were performed with a pyramid measuring an inch across the incident face, with a length of four inches.

At one MeV, $\sim 6.5\%$ of the incident γ -ray energies are deposited, which tails off rapidly at higher energies. The angular coverage and slopes of the truncated

¹Absorption efficiency in this chapter refers to the full-energy peak efficiency for either a single segment, or for the whole array. The latter is calculated by summing energy deposits for each crystal and comparing it to the emitted energy.

²The incident γ -rays were of various energies with a multiplicity of one.

3.2 Constructing the PARIS Array

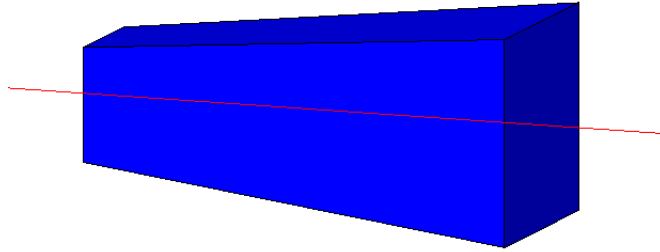


Figure 3.5: A GEANT4 image of the truncated pyramid design.

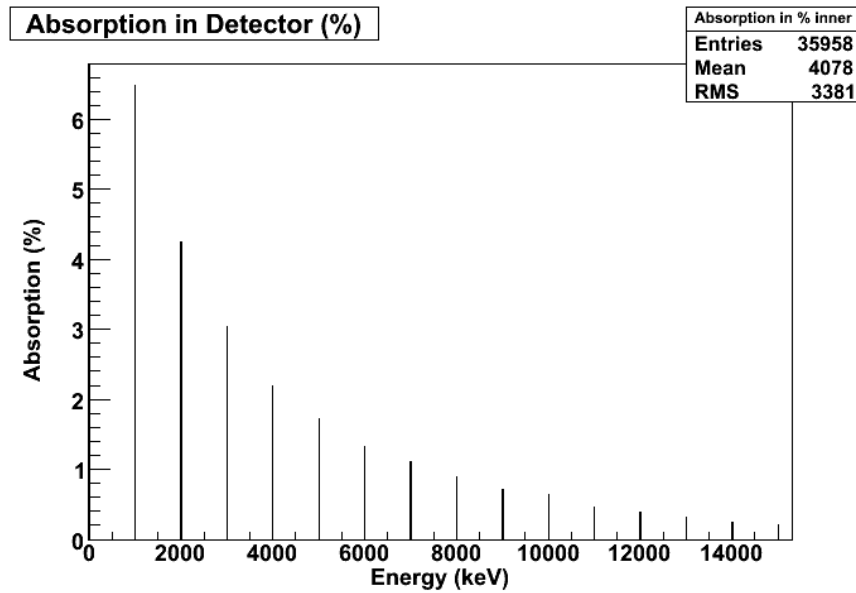


Figure 3.6: Absorption spectrum of the smaller truncated pyramid design.

3.2 Constructing the PARIS Array

pyramid should result in a greater amount of absorption, where the deposition of energy that interacts and scatters inside the detector is contained within a larger volume than the rectangular style. As this geometry covers a larger solid angle in the calorimeter, a greater amount of γ -ray energies are expected to become deposited in the crystal. However, simulations seem to indicate that this is not strictly the case, and a lower absorption efficiency is observed. The source was calibrated so that all the γ rays were projected onto the front face, 15 cm from the source at an angle similar to that of the solid angle coverage of the detector. Doubling the dimensions results in a higher amount of absorption ($\sim 19\%$ absorption for one MeV γ -rays and 3% of 15 MeV γ -rays). The absorption efficiency was poor, despite absorbing higher energy γ -rays effectively. However, incorporating these segments into a geodesic array will eliminate dead space and possibly increase the overall detector efficiency.

3.2.4.2 Absorption Efficiencies of the Rectangular Design

It was proposed that a 1" x 1" x 4" crystal would be more suitably sized in terms of absorption efficiency and cost, where later simulations explored the efficiency of one segment, later increasing this to 2" x 2" x 4". It was found that for the smaller segments, 11% of one MeV γ -rays deposited their energy in the crystal, which decreases to $\sim 1\%$ at 15 MeV. Similar simulations involving various γ -ray energies projected at a source distance of 15 cm upon the entire face of the crystal were also investigated¹, where the larger 2" x 2" x 4" scintillator registered $\sim 25\%$ and $\sim 6-7\%$ of one and 15 MeV γ -rays becoming totally deposited in the detector respectively. An energy spectrum is shown in figure 3.7 for the case of a one MeV γ -ray incident on a 1" x 1" x 4" detector, with the trends for energy deposition within that volume at various energies shown in figure 3.8.

3.2.4.3 Absorption Efficiencies of the Conical Design

The design of this detector was a conical pyramid, with the top removed to reveal a frustum that was assigned a diameter of 2.54 cm (1") for the plane incident

¹Simulations investigating the passage of γ -rays travelling through the material by placing the source in the centre of the crystal volume were also tested.

3.2 Constructing the PARIS Array

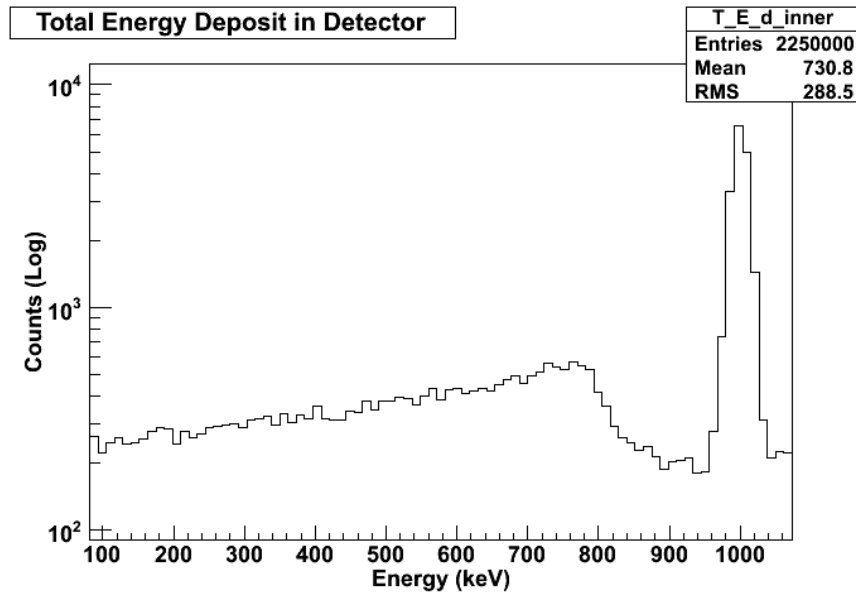


Figure 3.7: A spectrum of a 1 MeV gamma ($1'' \times 1'' \times 4''$ cubic segment).

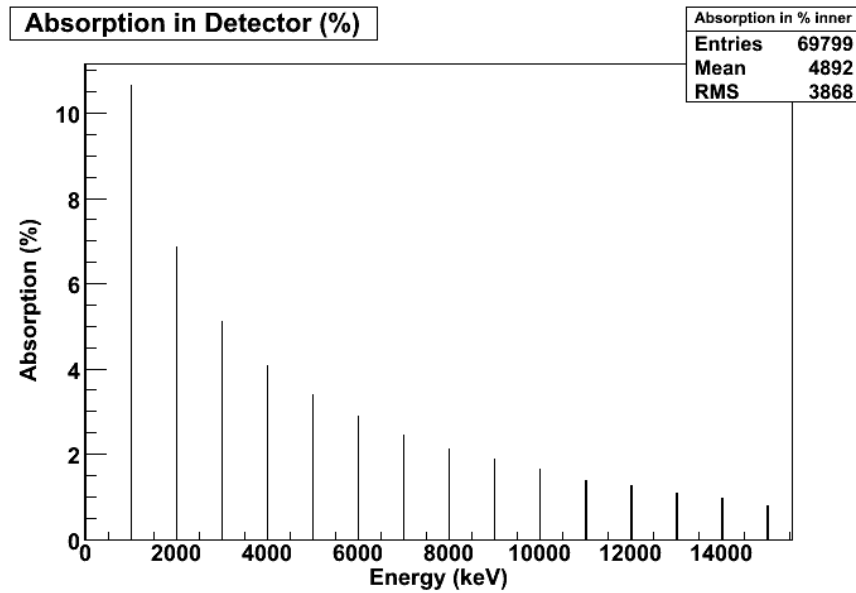


Figure 3.8: Absorption efficiencies of γ rays ($1'' \times 1'' \times 4''$ cubic segment).

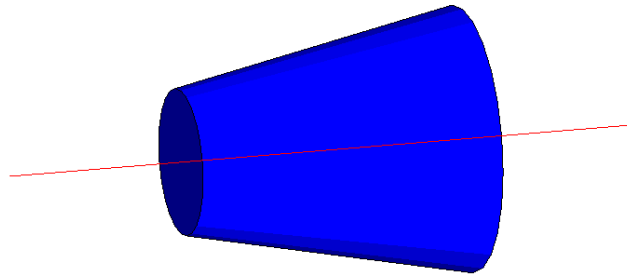


Figure 3.9: A GEANT4 image of the conical design.

to the source. The bottom of the cone had a diameter of roughly two inches; calculated so that the projection of the incident γ rays followed the geometry of the cone, as was done previously with the truncated pyramid design using similar values. The length was kept at four inches to remain consistent with the previous data sets, with the absorption efficiencies calculated by altering the dimensions of the front face between one and two inches. For the smaller cone geometry, 13 % of one MeV γ -rays and 2% of 15 MeV gammas were found to become absorbed within the detector. For the larger cone geometry; 29-30 % of one MeV γ -rays were found to deposit their energy, with 7-14 % becoming absorbed at higher energies ($<10\text{MeV}$).

Table 3.1 shows the results of these simulations, where the cone is observed to be better than the rectangular design for various sizes. However, it is hard to manufacture, so the cost-efficient solution would be to remain with the cubic geometry. The trapezoidal solid yields a poor amount of absorption, despite limiting the dead space by tiling it in a geodesic set-up.

3.2.4.4 Energy Resolution of Various Geometries

After investigating the trends in the amount of energy deposition over a large range of energies for various geometries, the effects of the energy resolution due to these geometries were studied. The approximations were initially derived from

3.2 Constructing the PARIS Array

Dimensions	Absorption in % (1 MeV)	Absorption in % (15 MeV)
1" x 1" x 4" Cube	11	1
2" x 2" x 4" Cube	25	6-7
1" x 1" x 4" Trap.	6.5	0.2
2" x 2" x 4" Trap.	19	3
1" x 1" x 4" Cone	13	2
2" x 2" x 4" Cone	29-30	7-14

Table 3.1: A comparison of the energy deposition trends for different geometries and sizes in the case of one and 15 MeV γ -rays.

fits for high energy γ -rays above \sim one MeV, used to generate the resolution graphs, the details of which were discussed in detail (section 3.2.3).

The FWHM fits generated by ROOT give an energy resolution of 2.8 - 3 % at 662 keV for LaBr₃, which is within an error of 0.15 %, and very close to experimental values. The parameter σ and its associated error were calculated by fitting a Gaussian curve in ROOT to the photo-peak of one of the energies. A preliminary estimate for 15 MeV γ -rays also revealed a resolution of around 0.69 ± 0.02 %, which seems to deviate from experimental findings as this sort of resolution is expected for energies between 17 and 18 MeV [28]. Overall, the fit gives results similar to experimental findings for energies less than 15 MeV within error. However after this, the relationship deteriorates and the values become less consistent with experimental results.

The spectra of each geometry with the 1" x 1" x 4" configuration was investigated in ROOT for one MeV γ -rays, where the comparisons between each geometry at one and 15 MeV are given in figures 3.10 and 3.11 respectively.

Of all the simulated cases, the truncated pyramidal design appeared to give the worst photo-peak resolution, while the cone had the best; where the clarity of the Compton edge reflects in the differences between the resolutions. In some cases, it is generally found that a greater volume will cause an increase in efficiency, due to less scattering. The amount of counts is poorer for the 15 MeV spectra as the histogram binning remained the same to be consistent with other simulations. The differences in the resolution of the escape peak from pair production are

3.2 Constructing the PARIS Array

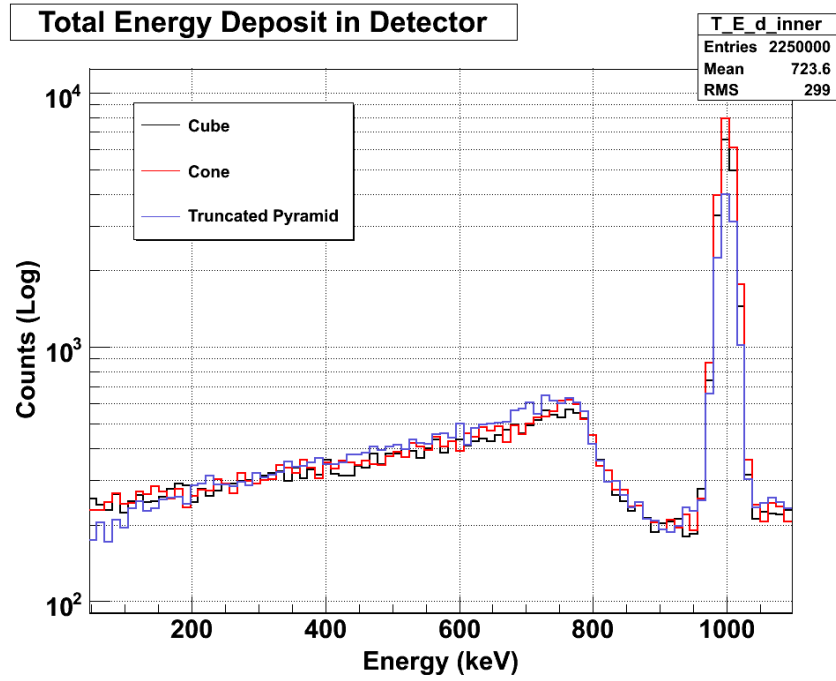


Figure 3.10: Comparison of a 1 MeV γ -ray for each 1" x 1" x 4" segment.

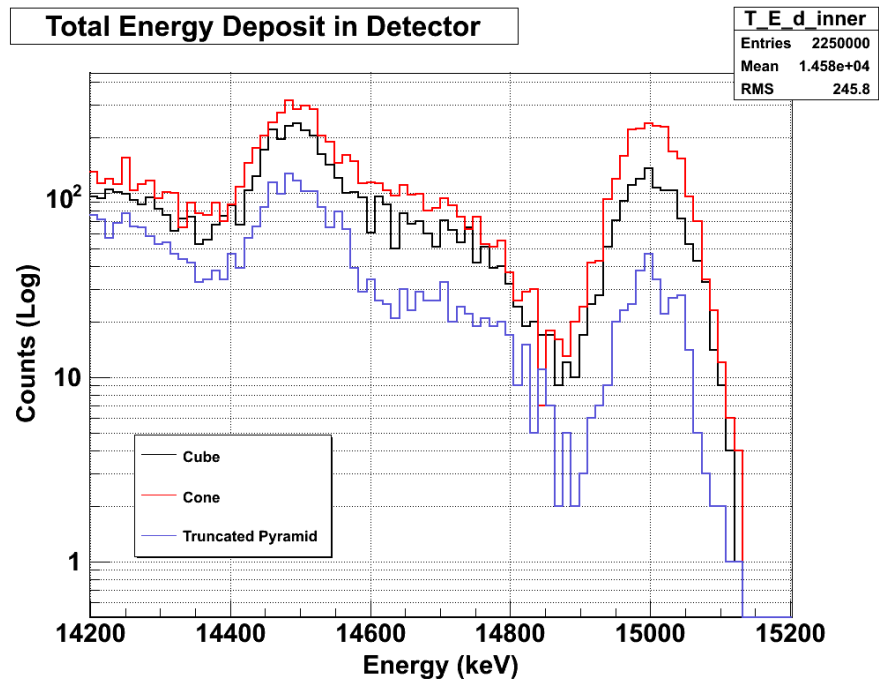


Figure 3.11: Comparison of a 15 MeV γ -ray for each 1" x 1" x 4" segment.

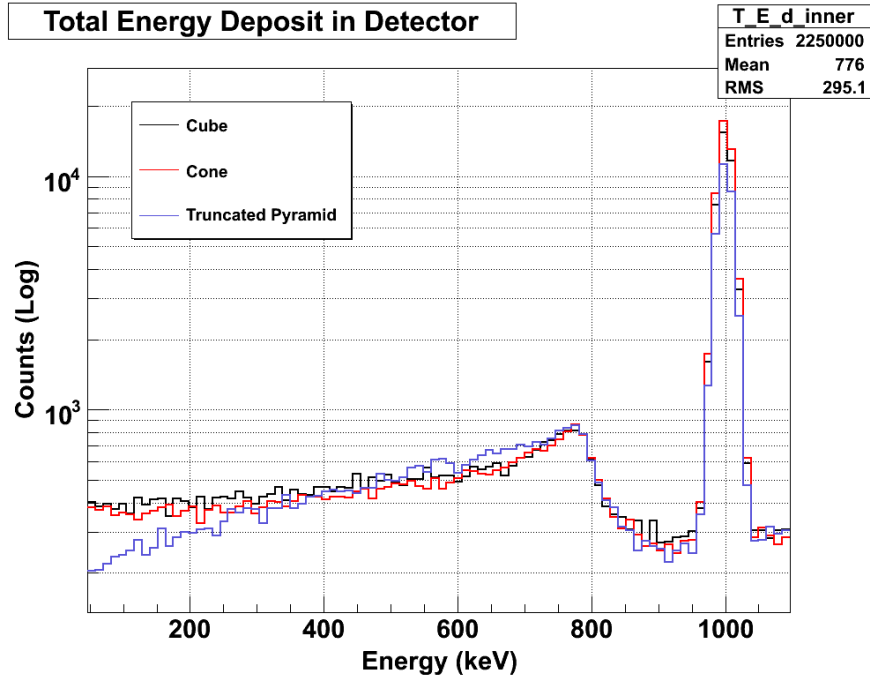


Figure 3.12: Comparison of a one MeV γ -ray for each 2" x 2" x 4" segment.

clearly seen in figure 3.11.

Similar results for the 2" x 2" x 4" segments for each geometry was also investigated, where the resolution of the Compton edge was observed to increase significantly due to an increase in Compton Scattering. The corresponding resolution graphs for an incident one MeV gamma are superimposed, to help determine which geometry gives the clearest energy resolution, and are presented in figures 3.12 and 3.13. The trapezoidal pyramid was still observed to have the poorest resolution, where in the case of higher energy spectra the differences in the simulated resolutions is apparent. The 1st escape and 2nd peaks are poorly represented compared to the photo-peak due to a higher amount total energy deposition.

From this study, one can conclude that the cone appears to have much more Compton scattering than the larger trapezoidal volume. An increase of energy deposition in the case of the truncated pyramid, results in a higher photo-peak efficiency and less scattering. However, it is extremely difficult to manufacture a scintillator of this design, which might not even be possible due to the chemical

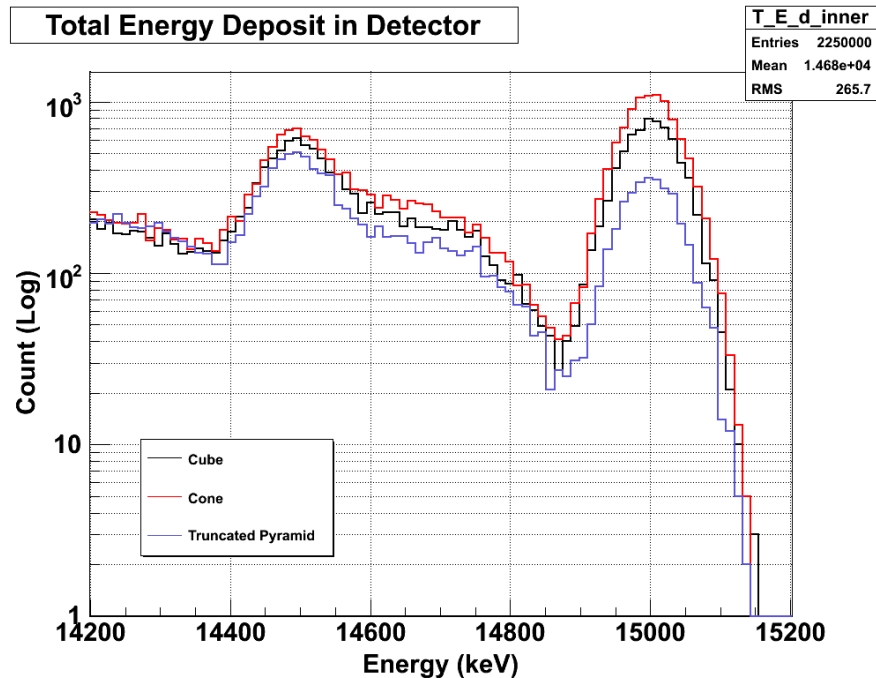


Figure 3.13: Comparison of a 15 MeV γ -ray for each 2" x 2" x 4" segment.

composition and cleaving planes the LaBr_3 scintillator naturally takes. Despite this, the trapezoidal solid unexpectedly exhibited a poor amount of absorption when compared to the other geometries, where the cubic design was seen to be the most beneficial geometry to use for the PARIS calorimeter. These results can be extended to analyse more realistic situations with the geometries tested, and investigate the effects segmentation plays for the overall calorimeter.

3.2.5 Cubic Design

As previously mentioned, this design is a working idea that differs from the standard geometrical arrangement of detectors, where the typical geodesic distribution fixes the diameter of the system, and allows for only a limited range of experiments. The introduced cubic design however, theoretically changes the diameter of the system of detectors, as the walls can be moved to a desired radius, replacing/subtracting additional modules as may be deemed necessary. The cubic configuration has segmented inner and outer shells, which were involved in several

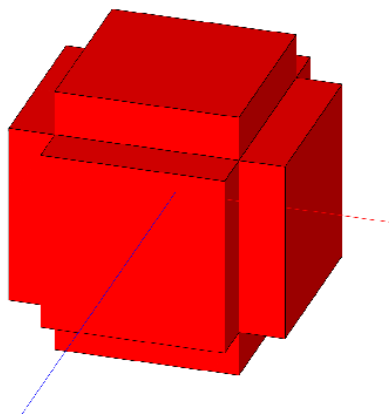


Figure 3.14: 4x4 array of the detector using 2"x2"x2" LaBr_3 and 2"x2"x6" CsI crystals (Red).

simulations, where comparative studies of the energy spectra and absorption of the crystals were investigated. In some cases, the scintillators in the inner shells were more segmented than the outer ones, and the two shells were independent of each other as can be seen in figures 3.14 and 3.15 .

3.2.6 The "Prototype" and New PARIS Cubic Design

Building on the results from the previous section, the focus now moves to generating a segmented calorimeter that would be more practical by arranging the segmented modules into an array. This "Prototype" would eventually be involved in the latest simulations of PARIS. A lot of questions arise as to which array of crystals would be better, and in turn, what size of crystals should be used to optimise the results. These questions will be answered by running several simulations with different parameters to determine which configuration would be best suited for experiments involving the use of γ rays.

Once the prototype has been tested using a collimated source incident along the X-axis (red), one can tile the best arrangement into the complete calorimeter. To do this, a new source file had to be created by integrating the code used for the prototype faces, and earlier models of PARIS. Aluminium will then be introduced between the gaps of the segmented detectors for add-back purposes,

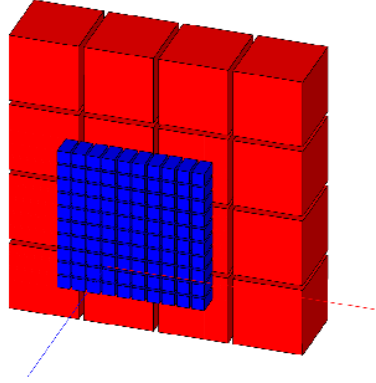


Figure 3.15: 10x10 array of LaBr_3 crystals and 4x4 array of CsI in the inner and outer shells.

as well as to observe what effect this will have on scattering. Other parameters, such as the length of CsI used in the second layer of the calorimeter will also be studied. Subsequent simulations will aid in deciding the best arrangement of the array, where different configurations of the PARIS array will be tested by simulating multiple scenarios with both an isotropic and collimated source of various multiplicities and incident energies. In achieving this with various arrangements of crystals, the simulations will help determine the optimum configuration PARIS will take.

3.2.7 Analysis and Experimental Simulations

3.2.7.1 Simulated Work Involving a Collimated Source

Several simulations and methods were tested that will aid in verifying which configuration is most beneficial under experimental conditions involving a collimated source projected on one of the walls of the calorimeter. The source was generated by manipulating the file in the set-up directory, responsible for the distribution of γ rays. These are projected onto the face of an array wall from a source distance, by changing the θ and ϕ , allowing all the incident radiation to deposit their respective energies within the array wall. The effects of these results will be used

3.2 Constructing the PARIS Array

when trying to construct a realistic representation of the detector array, which is investigated and introduced in this section.

In GEANT4, several analysis files were written to investigate the distribution of the incident radiation over the entire prototype wall, with respect to the central detector. In the case of 3x3 segmentation of the prototype wall, the central detector is the 5th crystal, where the adjacent detectors will give a good representation of the energy deposition trends relative to this detector. However, further segmentation changes the position of this central detector, and thus in a 4x4 array, there are four potential candidates¹.

As the dimensions of the crystal and array sizes change, the source must be attenuated to maintain the complete projection of the generated γ -rays onto the front face of the detectors. These changes are done within the sub-directory of the main program, where the dimensions of the collimated source are given in spherical coordinates. The γ -rays from the source are projected onto the prototype in the positive X-direction, with a set multiplicity upon various sized crystals. These crystals were arranged in either a 3x3 or 4x4 segmented array 15 cm from the source, and kept the same in all the simulated cases. The source distance for the 3x3 segmented arrays of 2" LaBr₃ crystals was set at 15 cm, and 20 cm for the outer CsI scintillators. For the case of 3" crystals in a 3x3 array, the source distance to the front of the LaBr₃ crystals was 22.5 cm, and 30 cm for the outer CsI crystals. Similarly for a 3x3 array of 4" crystals, the source distance to the front of the scintillators was increased to 30 cm and 40 cm for the LaBr₃ and CsI crystals respectively. The next sections will attempt to verify which configuration is the best option from these tests, where only the dimensions of the array and crystal sizes were changed. The deposition trends for energies between one and 30 MeV were observed, where if a reaction in more than one segment occurred (two-fold), then an algorithm can be written to add-back and reconstruct the initial γ -ray profile.

Initially, seven different γ -ray energies were projected onto a 3x3 segmented array of detectors 15 cm from the source, where the gaps between the crystals

¹The absorption efficiencies calculated from the energy deposition patterns, were measured with regards to the entire wall

3.2 Constructing the PARIS Array

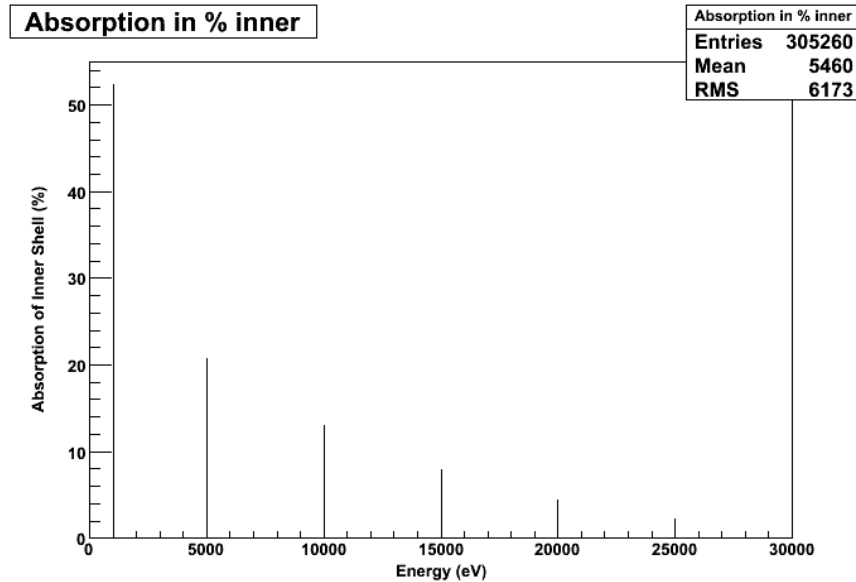


Figure 3.16: The absorption of 1-30 MeV gammas in a 3x3 array of 2”x2”x2” LaBr₃ crystals.

were neglected (i.e. set to zero)¹. The amount of energy deposition in more than one-fold within the array over a range of energies from one to 30 MeV, in 5 MeV increments, was observed. The absorption efficiency of the array wall as a result of the known total energy deposition patterns, was deduced by observing the number of counts absorbed with varying incoming energy. This was found to be $\sim 52\%$ for one MeV γ -rays in the LaBr₃ layer, where the total absorption was found to decrease with increasing energy. Similarly, only $\sim 17\%$ of incident γ -rays were found to deposit their total energy within the outer shell of CsI crystals. However this trend is different, as a peak in the amount of absorption occurs at $\sim 21\%$ for 5 MeV γ -rays. This is expected to be due to the high energy γ -rays escaping the small volume of material where not all of the energy is deposited.

The trends for the amount of total energy deposition within the array wall are shown in figures 3.18 and 3.19. The number of detector segments registering total energy deposition within the inner and outer layers of crystals reveal that only the central detector is really affected at low energies. The behaviour of how

¹The consequent discrepancies associated with this will be discussed later.

3.2 Constructing the PARIS Array

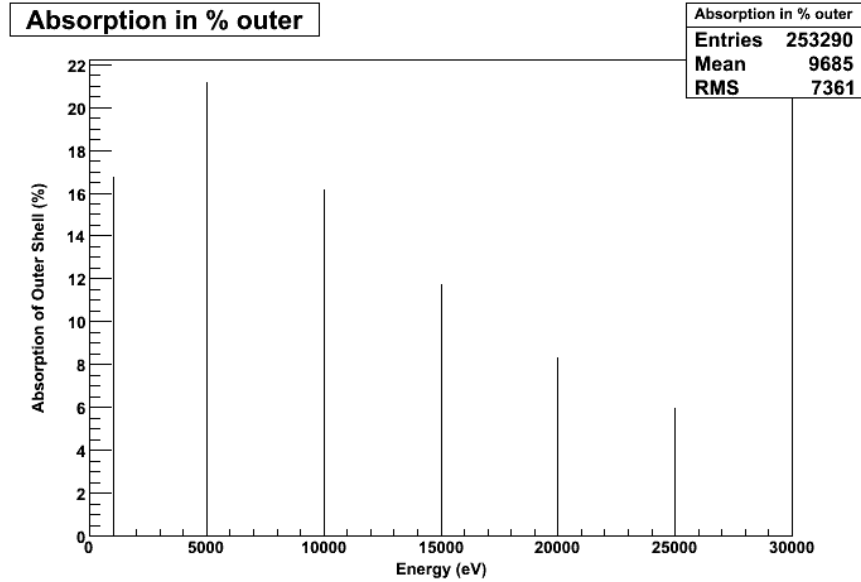


Figure 3.17: The absorption of 1-30 MeV gammas in a 3x3 array of 2" x2" x6" CsI crystals.

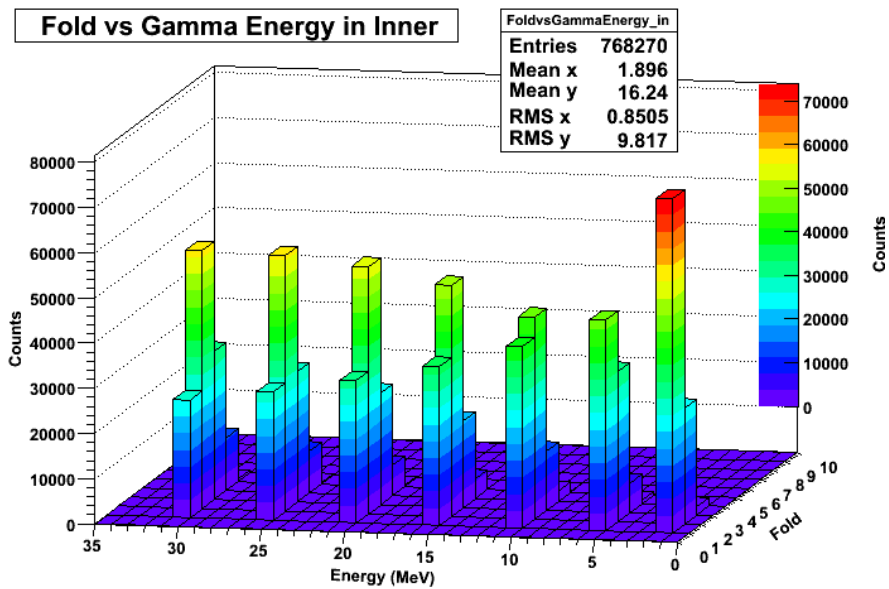


Figure 3.18: The energy deposition trend with respect to the middle detector in the 3x3 array of 2" x2" x2" LaBr₃ crystals

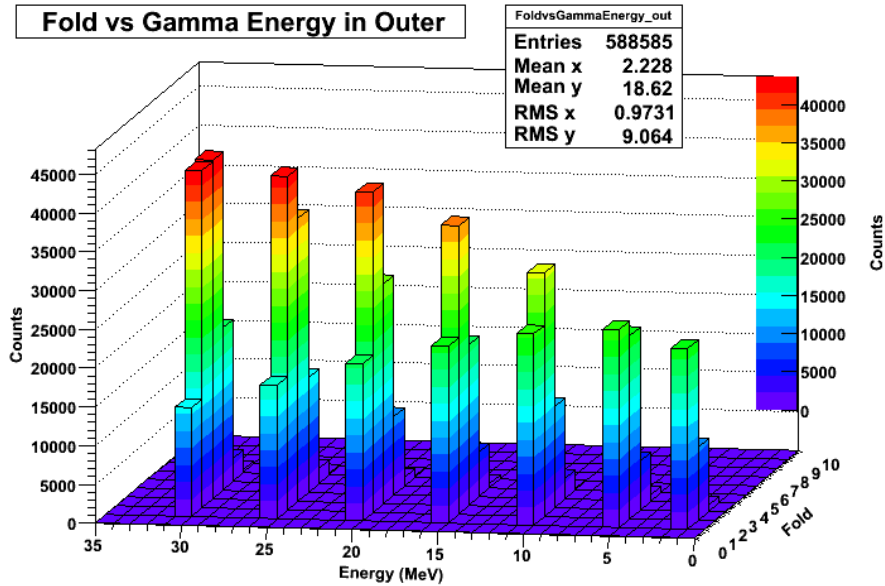


Figure 3.19: The energy deposition trend with respect to the middle detector in a 3x3 array of 2" x 2" x 6" CsI crystals

the energy is deposited reveals a majority of two-fold readings after ~ 10 MeV, peaking at 30 MeV. The trends regarding the total amount of energy deposited in the outer layer of CsI crystals reveals a similar trend, where an increase in energy is proportional to the number of detections in the wall. At low energies, most of the interactions are one-fold. However, this switches over to a two-fold majority at around 5-10 MeV.

Overall, an increase in the energy of the incident γ -rays result in an increase in energy deposition in more than one detector, as one expects. Increasing the size of the crystal allows for more energy deposition within a single segment, resulting in an increased amount of absorption. Simulations with larger 3" crystals in a 3x3 arrangement confirm this increase in the absorption efficiency ($\sim 70\%$ for one MeV gammas), where more interactions are observed to be allocated to these crystals. The outer shell of CsI scintillators reveal a poorer efficiency than the case involving 2" crystals due to an increase in the source distance¹, with $\sim 14\%$ of 5 MeV γ -rays depositing their total energy. The stopping power of the inner LaBr₃

¹The source distances to the front of the simulated arrays are set so that in the case when they are tiled to form the complete geometry, no overlapping elements of each wall exist.

3.2 Constructing the PARIS Array

1	2	3
4	5	6
7	8	9

1	2	3	4
5	6	7	8
9	10	11	12
13	14	15	16

Figure 3.20: The central detector (shaded) in a 3x3 detector array

Figure 3.21: The central detectors (shaded) in a 4x4 detector array

layer also results in a dramatic increase in the amount of total energy deposition above one MeV with respect to the central detector in this outer layer. These distributions are similar to the previous results shown in figures 3.18 and 3.19, with the dominance of one-fold interactions changing at around 10-15 MeV due to increased energy deposition in adjacent crystals. Similarly, increasing the size of the crystals to 4" gives an absorption efficiency of 80% for one MeV γ -rays in the inner layer, and a peak absorption efficiency of $\sim 9\%$ for 5 MeV γ -rays in the outer layer.

Enlargement of the array was also investigated to determine whether increasing the array size would be beneficial given the increasing scale and distances between each of the incident planes of the array and the source. The previous measurements were with respect to the central detector, in a 4x4 arrangement the "central" position had to be determined by changing the analyse file to accommodate the new geometry, where the "central" 6th, 7th, 10th and 11th crystals were arranged as in figure 3.21.

In the case of the 4x4 array where there are four potential candidates to measure the energy deposition trends in adjacent detectors around the centre of the array, only statistical variations between all 4 detectors was observed. Consequently, all simulations measuring the amount of detector fold when studying the energy deposition was performed with respect to the 6th detector in this large array.

3.2 Constructing the PARIS Array

Simulations using 2", 3" and 4" crystals were performed with seven different energies, incident on a 4x4 array of phoswich detectors in the prototype arrangement. The absorption efficiency of the inner layer of scintillators (which were 3" thick) was found to peak at 70% for one MeV γ -rays, which is fractionally larger than what was observed for 4" crystals. The outer layer saw a total energy deposition for both the 3x3 and 4x4 arrays, to be around 15-20% for 5 MeV γ -rays.

The number of counts for the larger crystals and arrays were observed to be significantly lower than the 2" crystals in a 3x3 array. This was due to an increased source distance, which ultimately plays a crucial role in the efficiency. However, the trends in the total amount of energy deposited at higher energies was found to be large, due to the increased volume size. The amount of total energy deposition in the outer layer of the array was observed to depend critically on the crystal size of the inner shell, where smaller crystals show that the majority of the deposition are two or three-fold. However, for larger 4" crystals, the amount of energy deposited fully in the array was found to be either one or two-fold. The overall trends for the absorption efficiencies for these cases can be found in figures 3.22 to 3.26.

3.2.8 Other Parameters of the Array

3.2.8.1 The length of CsI

Until now, the length of the outer shell of CsI crystals, has stayed fixed at 6". However, a short study was conducted to investigate whether an increase in this length would yield a higher count rate. The length of the CsI crystals was extended to 8", and simulated with γ rays of various energies.

The 4x4 inner layer of LaBr₃ crystals was placed 20 cm from the source. This is to ensure that when this wall and the other five are tiled to form the complete geometry, there are no overlapping volumes. The outer CsI crystals are placed 25 cm from the source, implying a size of 2"x2"x2" for the LaBr₃ crystals and 2"x2"x8" for the CsI crystals. The array was tested with similar incident energies to previous simulations of 1, 5, 10, 15, 20, 25 and 30 MeV. However, despite

3.2 Constructing the PARIS Array

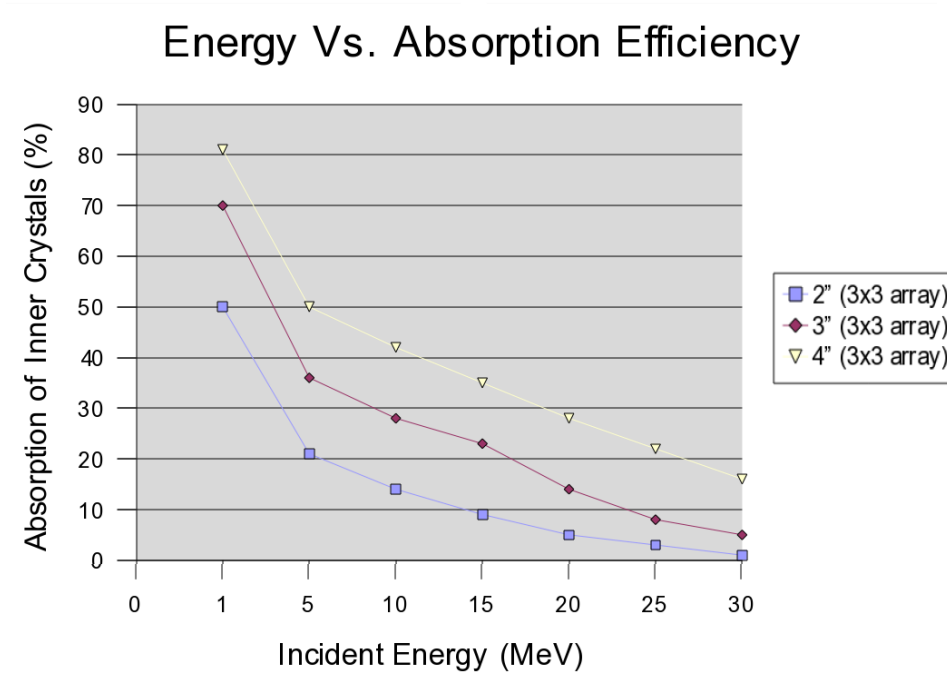


Figure 3.22: Incident energy plotted against absorption efficiency for LaBr_3 crystals in a 3x3 array.

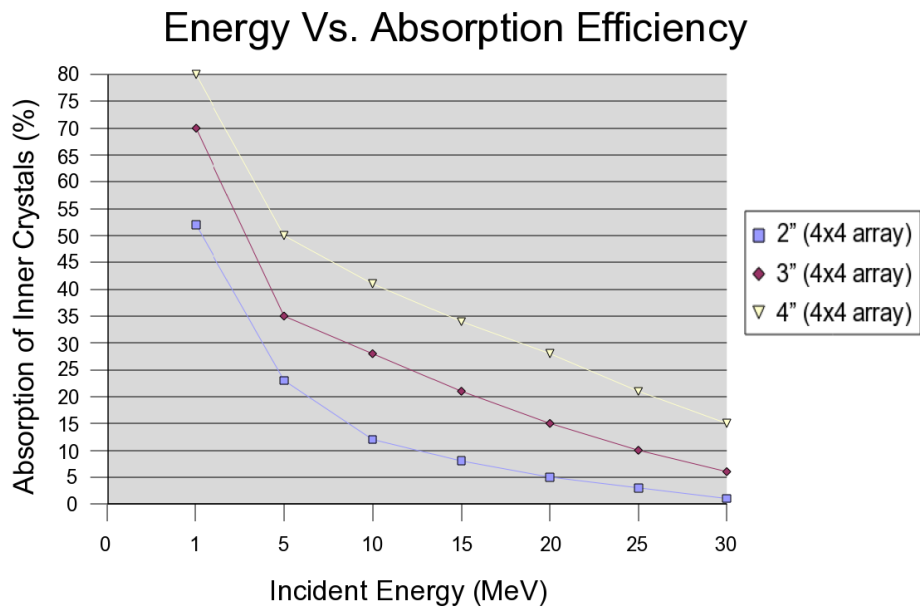


Figure 3.23: Incident energy plotted against absorption efficiency for LaBr_3 crystals in a 4x4 array.

3.2 Constructing the PARIS Array

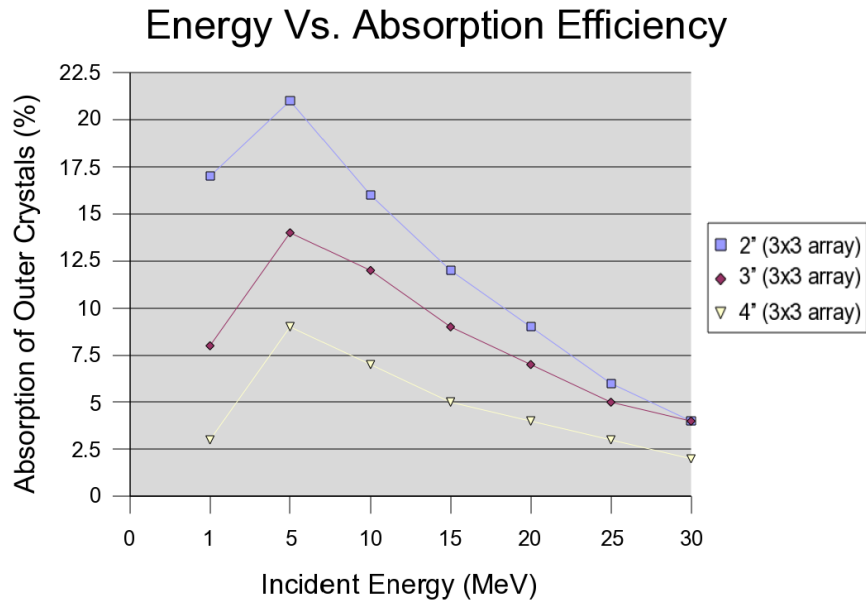


Figure 3.24: Incident energy plotted against absorption efficiency for CsI crystals in a 3x3 array.

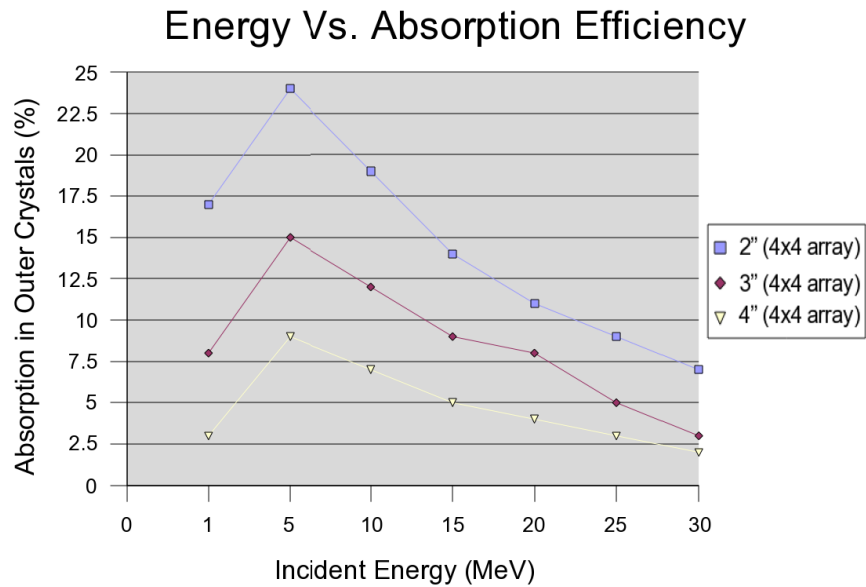


Figure 3.25: Incident energy plotted against absorption efficiency for CsI crystals in a 4x4 array.

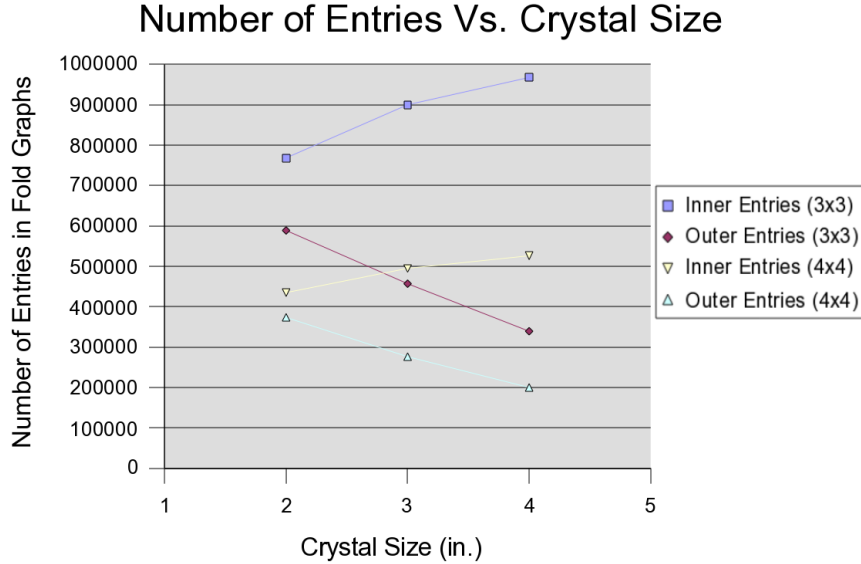


Figure 3.26: Number of entries plotted against the increasing crystal size for both 3x3 and 4x4 arrays.

expectations of a substantial increase, a rise of only $\sim 2.2\%$ in the absorption efficiency was observed. Similarly for larger crystals in a 4x4 array, an increase of around 2.3% was observed. Any increase in the efficiency for this configuration is not very substantial, and thus no simulations were conducted with larger CsI crystals. This was due to the expectation that an increase in the amount of absorption, number of counts, and absorption efficiencies would be negligible for most of the energy range studied. Despite the small increase of absorption due to this increase, the length of CsI will remain at 8" for the duration of the work presented in this chapter.

3.2.8.2 The Addition of Gaps

Due to wiring and cooling appliances that need to be fitted within the calorimeter, it is unrealistic to leave an absence of room between each detector segment. Consequently, gap sizes of 5 mm and 10 mm were initially added within a 4x4 array of 2" LaBr₃ crystals. The addition of these gaps were found to cause a reduction in the amount of total absorption by $\sim 18.6\%$ for the inner crystals,

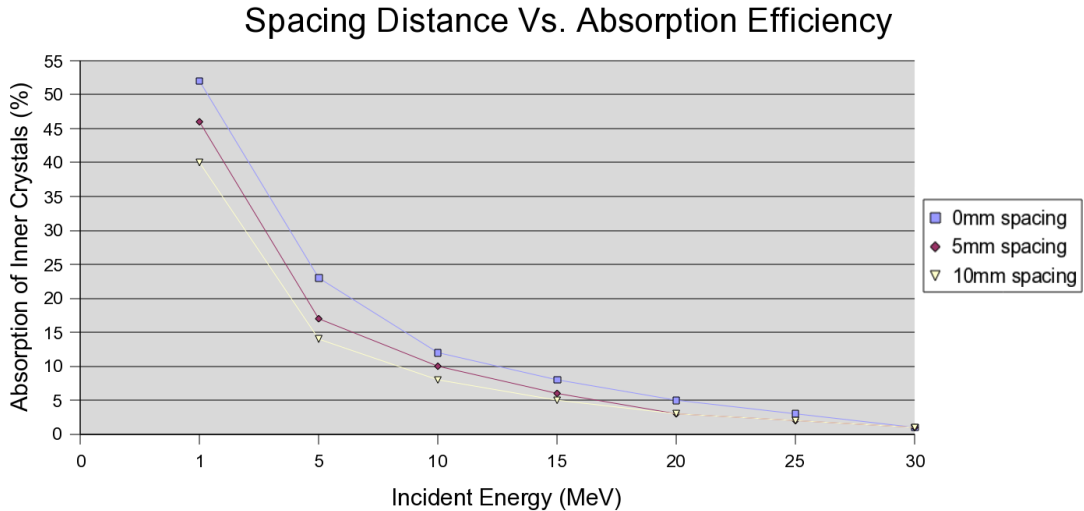


Figure 3.27: Different gap sizes and inner absorption efficiency.

and a reduction of $\sim 1.2\%$ for the outer shell, almost making the extension of the CsI crystal obsolete. Unlike the case of a 3×3 array of $2'' \times 2'' \times 2''$ LaBr₃(Ce), where 52% of incident one MeV γ -rays were absorbed (fig. 3.16), only 46% of one MeV gammas now seem to deposit their total energy within the array. All other incident energies experience a reduction in absorption efficiency of $\sim 2\text{-}3\%$. For the outer layer, the amount of absorption decreased by around 5.5%, with most of the loss in efficiency attributed to the incident 10 MeV γ -ray. All other energies seem to show a rise in absorption efficiency, especially low energy γ -rays; with an observed 3% increase for one MeV γ -rays.

Additional spacing between the inner and outer layers of the array wall results in a dramatic increase in scattering, where 10 mm spacing around the crystals results in energy deposition in as many as eight detectors. The absorption efficiency is also observed to be poorer, with a further reduction in efficiency of $\sim 33.8\%$ (compared to $\sim 52.4\%$ with no gaps) for the inner shell of crystals and $\sim 12.4\%$ (compared to $\sim 18.8\%$ with no gaps) in the outer shell. Due to the decrease in the efficiency with increased spacing between the crystals, simulations will maintain a limit of 5 mm.

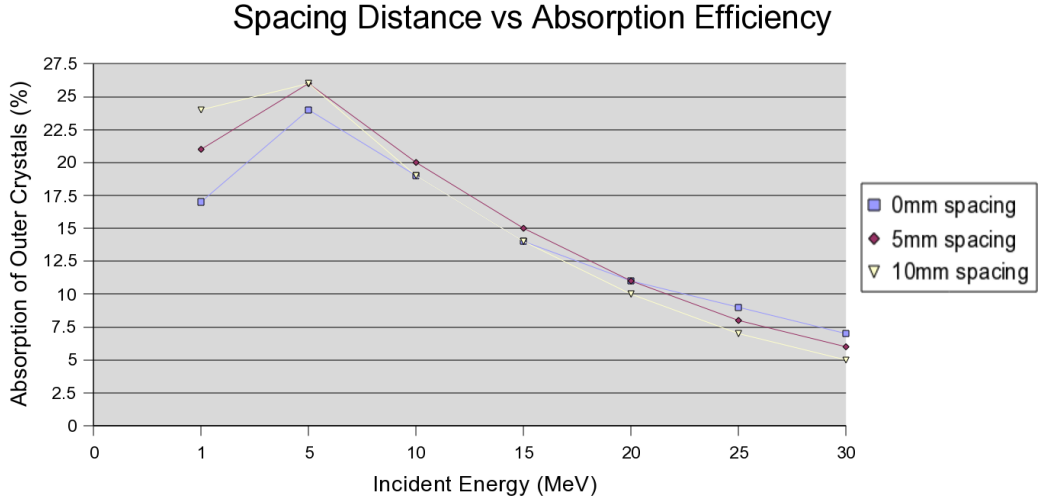


Figure 3.28: Different gap sizes and outer absorption efficiency.

3.2.8.3 Variations of the Incident Angle of the Source

Two configurations of the basic generator have so far been measured, where the effect of an isotropic source projected onto 6 walls of the PARIS calorimeter has been investigated, by studying the corresponding absorption and energy deposition patterns. A collimated source has also been projected onto a single wall of the calorimeter, and similarly measured. Realistically however, γ rays won't interact with the detectors head on all the time, and will be incident at various angles. This will undoubtedly have a profound effect on the efficiency of the crystals, as one γ ray will be absorbed by more neighbouring cells, resulting in a higher amount of energy deposition in adjacent segments.

A lot of parameters; absorption, efficiency, Doppler correction, add-back, etc., depend heavily on interactions within the geometry, where there is a strong dependence on the angle of the incident γ -ray. For instance, a γ ray travelling at $\theta = 0^\circ$ interacts with 2" of LaBr_3 and 6" of CsI. However, for a γ ray interacting with the detector wall at around $\theta = 45^\circ$ (the "maximum thickness"), the γ ray interacts with more matter since $2" \cdot \sqrt{2} = \sim 2.828"$, for the LaBr_3 segment alone.

This effect is seen in figures 3.29 and 3.30, where changing the incident angle of the beam in the generator file results in changes in the energy spectrum. The

3.2 Constructing the PARIS Array

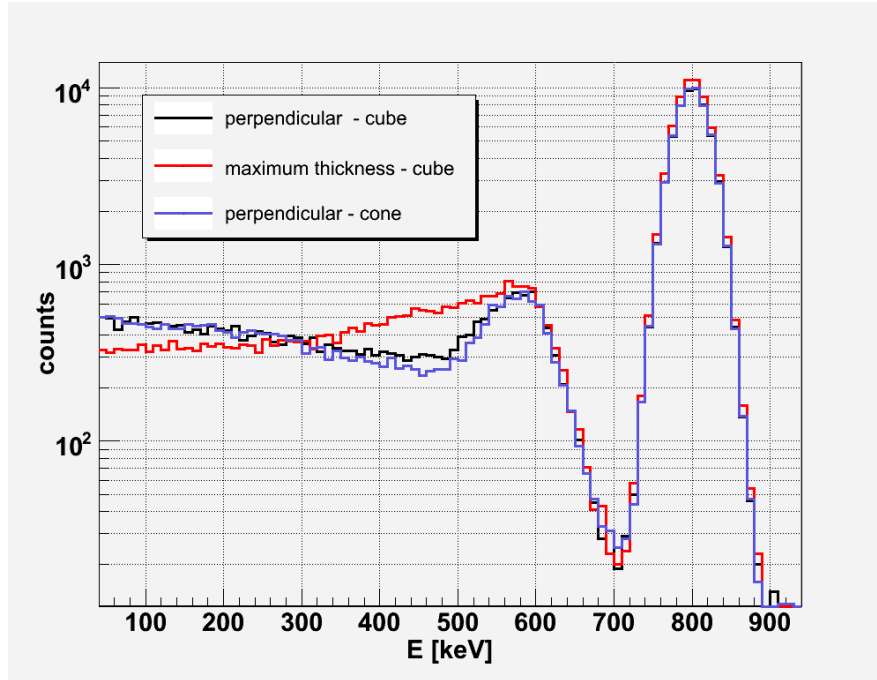


Figure 3.29: Energy spectrum of a 800 keV γ -ray at various incident angles[29].

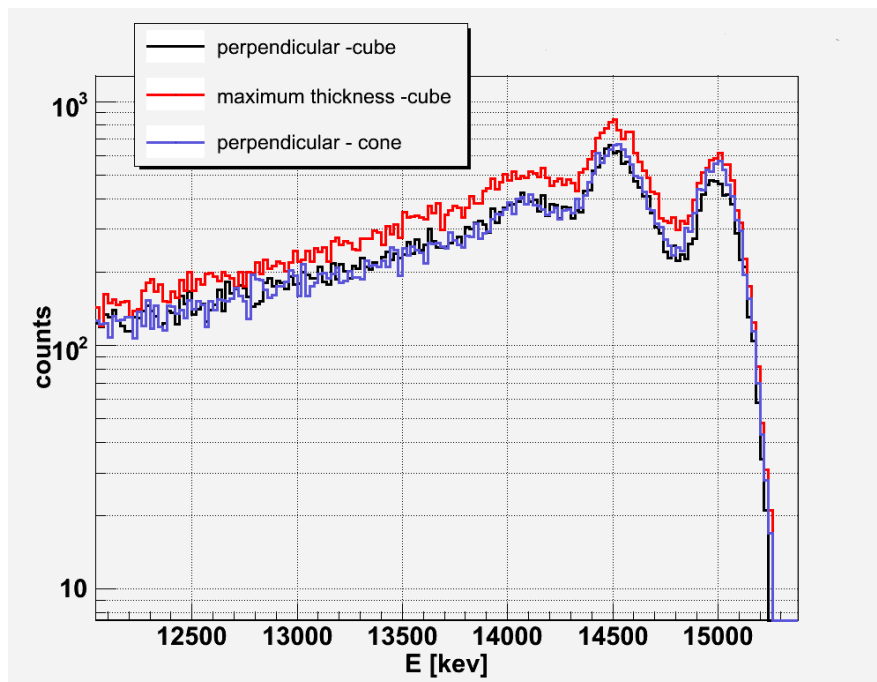


Figure 3.30: Energy spectrum of a 15 MeV γ -ray at various incident angles[29].

resolution of both an 0.8 and 15 MeV γ -ray is observed to be worse for large incident angles, or cases where there is likely to be the most interaction with the scintillator. This results from an increased probability of scattering as more of the scintillator medium is traversed, and generally leads to a higher number of fold interactions in adjacent detectors where optimisation of efficiency using add-back processes becomes increasingly difficult (see appendix B.1).

3.2.9 Total Energy Deposition on a Novel Highly Segmented Array

In addition to the simulations performed so far for the tiled prototype case, further segmentation of both CsI and LaBr₃ crystals were also tested by manipulating the already existing prototype file.

An array wall 6" in height and width was only used for these simulations, due to larger array sizes exhibiting a greater inefficiency. This is due to numerous volumes in each of the array walls overlapping with one another when the source distance is left unchanged, and the array size is simultaneously increased. Consequently, the array walls were tiled into the cubic configuration, where gaps of 5 mm between the segments were maintained in all the simulated cases. The source is projected isotropically from the centre of the calorimeter, with an assortment of energies between one and 30 MeV in 5 MeV increments.

Further segmentation of the inner layer of LaBr₃ crystals are shown in figure 3.31, where the dimensions of the segments are 1"x1"x1", and the outer layer of CsI crystals are each 2"x2"x6" in size. A very poor absorption efficiency due to a low number of events depositing their energy fully within the array, is observed. The number of n-fold interactions is much greater, with a peak in one-fold energy deposition for one MeV γ -rays. At higher energies of around 30 MeV, energy deposition is observed in an average of 3 detectors. A drop in the amount of energy deposition to two detectors or less occurs at energies less than ~ 20 MeV. In this scenario, it becomes apparent that measurements below 20 MeV are likely to be better due to this decrease in the amount of detector fold, which subsequently results in an easier reconstruction of the incident γ -rays.

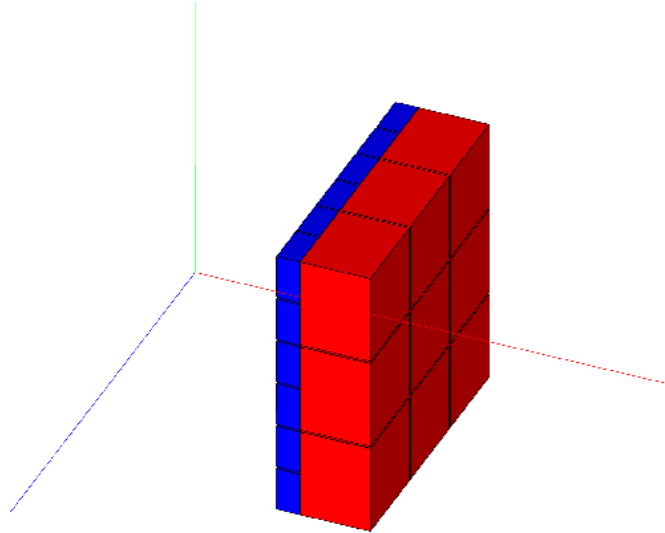


Figure 3.31: A 6x6 and 3x3 array of $\text{LaBr}_3(\text{Ce})$ and CsI crystals.

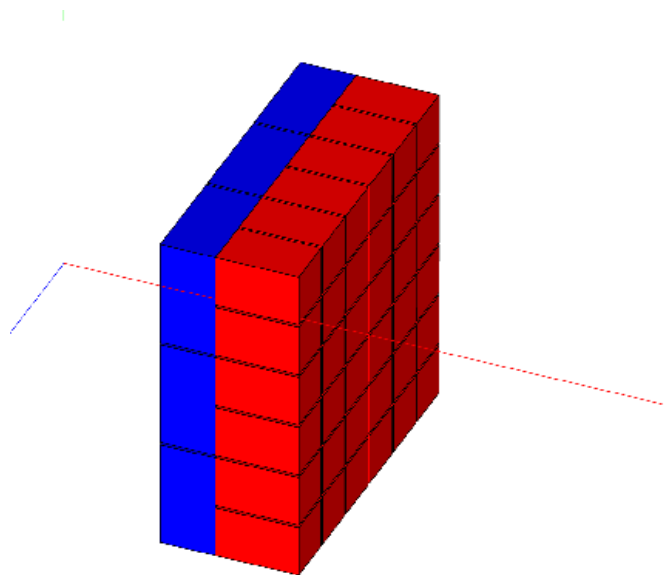


Figure 3.32: A 3x3 and 6x6 arrays of $\text{LaBr}_3(\text{Ce})$ and CsI crystals.

3.2 Constructing the PARIS Array

Reversing this case so that the the outer shell of CsI crystals are now thinly segmented (figure 3.32), results in the crystals exhibiting a low number of interactions and poor count rate. A majority of the total energy deposition above 15 MeV within the detector segments was observed to be three-fold in nature, with an increasing amount of energy being deposited in at least four, or even five detectors for energies around 30 MeV. Larger volumes of LaBr₃ segments also play a crucial role, as very little activity in the outer layer occurs due to a lot of absorption of incident low energy γ -rays (below 5 MeV).

Further segmentation seems to indicate that lowering both the sizes of the array and crystal increases the number of scattering events, and sacrifices a better detector fold distribution of the energy deposited. Consequently, it becomes apparent that the best arrangement to use would be a 4x4 array of 2" crystals. If the number of statistics was prioritised for the LaBr₃ layer only, where little add-back reconstruction is desired, then a larger volume of crystals within this shell would improve the results for this layer. However, if one was concerned with both the efficiency of the inner and outer shells of detectors, the arrangement of 2" crystals in a 4x4 array was found to be the optimal configuration to use.

Having come to a conclusion on the best set-up for the PARIS calorimeter, it is time to focus on the general response a set-up would have under experimental conditions, culminating in a theoretical simulation of a real physics case in nuclear structure.

3.2.10 Larger Arrays and the 4π Calorimeter

The detector array was subjected to incident radiation, and was simulated in various sizes before being tiled to complete the full calorimeter. The source distances were set to 6", 8", and 10" for the 6x6, 8x8, and 10x10 arrays respectively, where the crystal size was kept at 1"x1"x4". The absorption efficiency spectrum for each of the arrays tested are shown in figure 3.33, where the 10x10 array has the largest absorption efficiency.

After analysis of the absorption for each array, one can now focus on how the distribution of the energy deposition changes with varying array sizes. The source was projected onto the wall of the 6x6 array first, where the results were

3.2 Constructing the PARIS Array

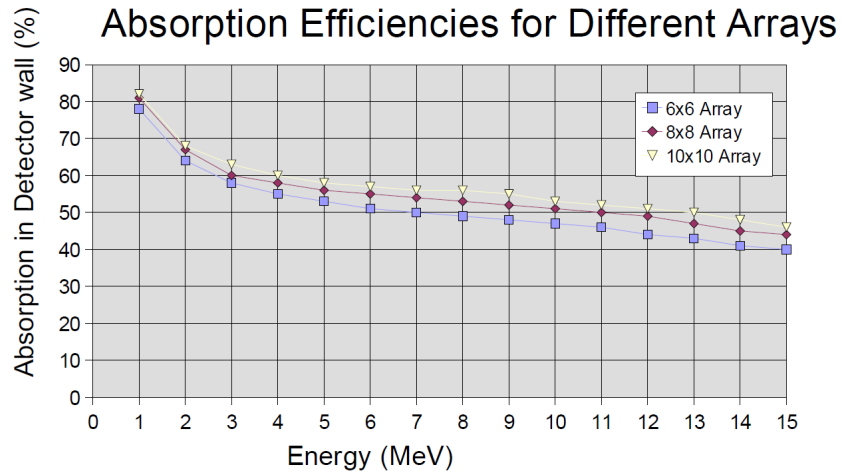


Figure 3.33: The total absorption efficiencies of each array size.

analysed with respect to one of the four central detectors. The results of the energy deposition in the smaller 6x6 array is shown in figures 3.34 and 3.35, where these histograms were produced showing the same distribution but from different angles.

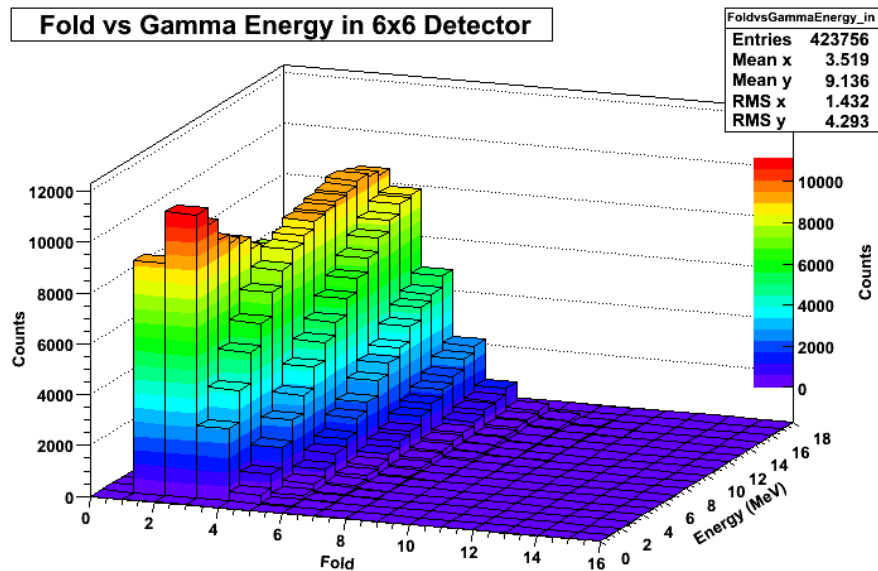


Figure 3.34: Energy deposition in a 6x6 array of 1"x1"x4" LaBr₃(Ce) crystals.

3.2 Constructing the PARIS Array

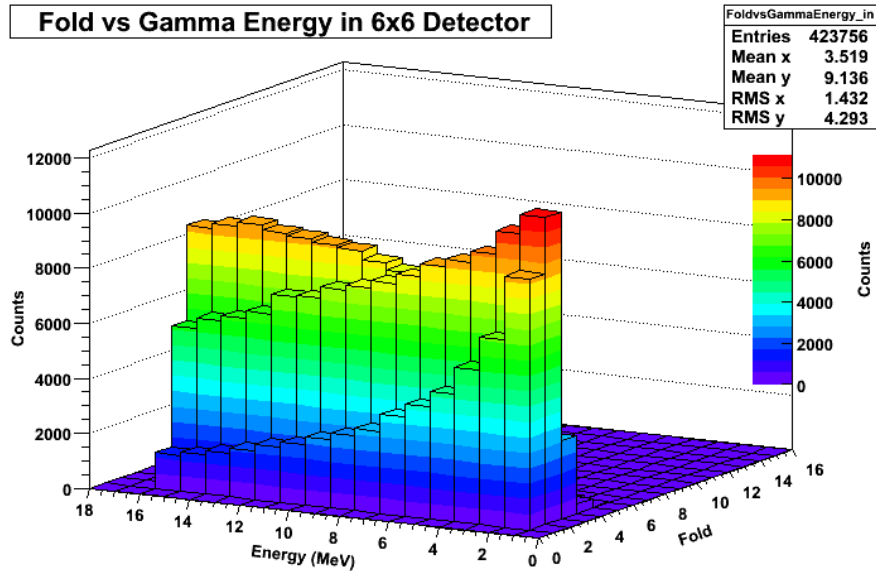


Figure 3.35: Energy deposition in a 6x6 array of 1”x1”x4” LaBr₃(Ce) crystals.

For a 6x6 array, a large amount of energy deposition within numerous segments was observed. A peak in the amount of total energy deposition within the array, occurs in at least two adjacent segments respective to the central detector, at energies up to ~ 7 MeV. After this, the majority of the deposition is held in at least three detectors, making add-back and reconstruction of the γ -ray profiles significantly harder. This trend continues to even higher energies, where the number of detectors registering deposited energy is six-fold. At incident energies of 15 MeV or greater, energy deposition is recorded in almost every segment of the array, where reconstruction of any γ -ray profile would involve a sophisticated algorithm. This is expected at higher and higher energies as the stopping power of the scintillators in the array become unable to contain the entire γ -ray track.

This simulation was also reproduced in the cases of larger 8x8 and 10x10 arrays, which contained 64 and 100 detectors on each wall respectively, and found to have similar results to the 6x6 case.

Applying the parameters for calculating the energy spectra previously described in section 3.2.3, values for the energy resolution were generated with respect to the entire wall of the calorimeter. Statistical discrepancies are only expected between the three different types of arrays, where only two energies and

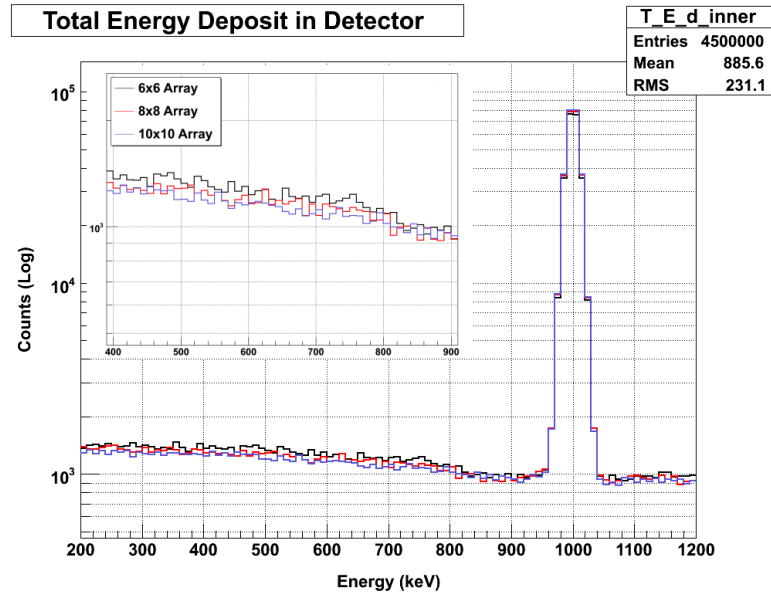


Figure 3.36: Energy resolution of a one MeV γ -ray for several array sizes.

their subsequent resolutions were studied. Examples of these for one and 15 MeV γ -rays, are shown in figures 3.36 and 3.37.

The photo-peaks for the one and 15 MeV γ -rays incident to the detector are observed to be very well defined, with a large number of counts. The difference between the arrays for the 15 MeV γ -rays are very small, although one can see a slight improvement in the resolution of the escape peak for the 6x6 array. In light of these findings, the next logical step would be to look at the overall calorimeter response, and to compare the absorption efficiencies one might observe with that of the Advanced GAMMA Tracking Array (AGATA), or another detector system. After these comparisons have been made, investigations into the energy resolution of various geometries can be studied.

3.2.11 The 4π Array and Comparative Studies with AGATA

More realistic and practical adaptations of the initial calorimeter design were introduced, as proposals for a more practical design were presented. However, before this can fully investigated, a more thorough understanding of just how efficient the cubic design is when compared to a conventional geodesic structure needs

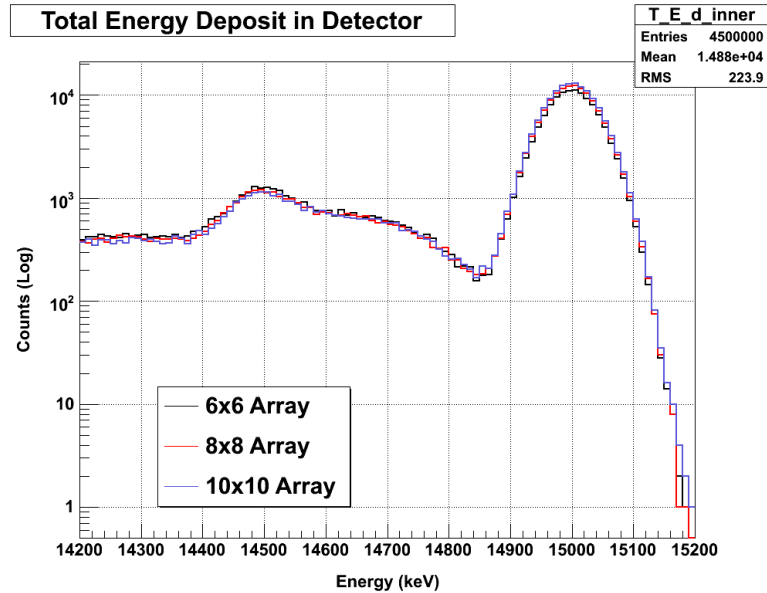


Figure 3.37: Energy resolution of a 15 MeV γ -ray for several array sizes.

to be studied. In order to make this comparison, a more developed, elaborate and practical cubic geometry needs to be constructed. As a result of this, several CAD drawings of different geometrical configurations within the PARIS calorimeter were drawn, that would later be incorporated into GEANT4 for testing. This was performed by using FastRad to convert the file into a GDML (Geometry Description Markup Language) format, which is compatible with GEANT4.

3.2.11.1 FastRad, GDML and "Shifted Cube" Designs

FastRad is an interface software for converting a CAD model with STEP (international standard for product data exchange) formatting, to another output file, for example; GDML. However, exporting the FastRad files over to GDML could only be done a segment at a time, where a larger number of segments for 1π or 4π distributions, could not be exported. This is due to a bug in the version of the software used at the time, and could only be solved by manually manipulating the file into GEANT4, using vector positioning of individual crystals to map the entire calorimeter.

Due to the difficulties with exporting the file into GDML, which was found

3.2 Constructing the PARIS Array

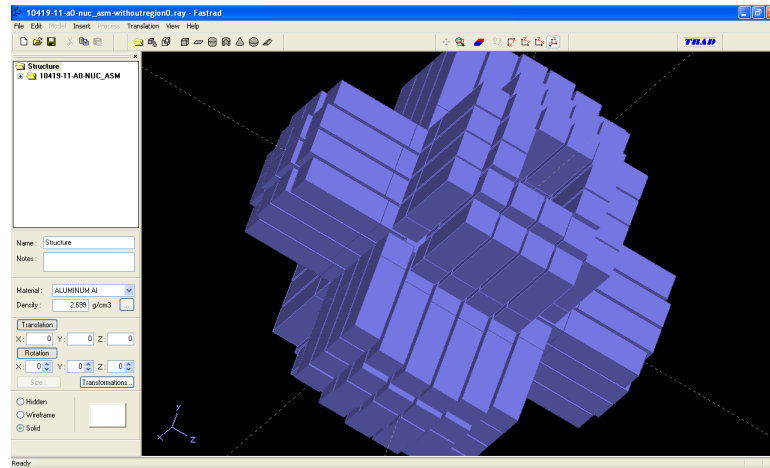


Figure 3.38: One of the CAD files used with the FastRad software.

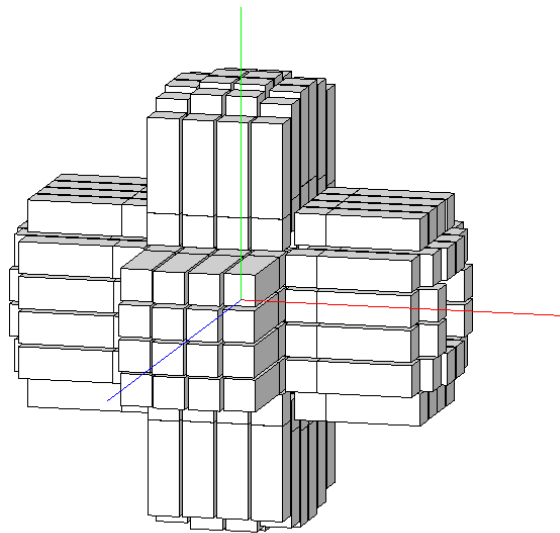


Figure 3.39: The geometry in figure 3.38, after being exported from FastRad to GDML.

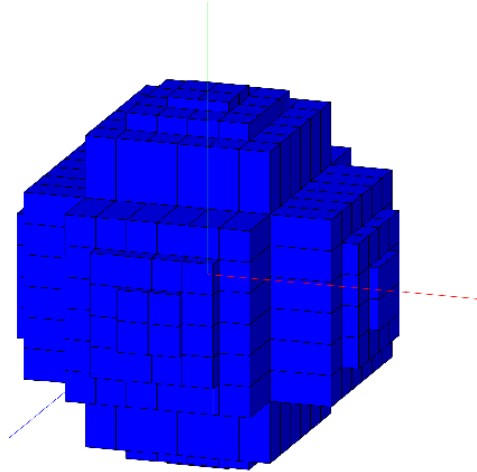


Figure 3.40: The shifted cube design without the beam-pipe.

to be a lengthy and time consuming process, a similar and simpler design was constructed in GEANT4. Some of these designs included a beam-pipe feature, and were modelled on earlier designs of the detector from previous simulations by other members of the collaboration¹. Shifts in the positioning of the segments, which are $1/5$ cm at the most, allow the cubic geometry to take on a more spherical shape where the source distances between the centre and the front face of any detector segment are calculated so that they are all the same. Simulations with this novel design of the cubic array involving shifts in the positioning of the crystal to increase the solid angle coverage, have shown that the absorption of energy within the segments (deposition of the incoming energy), was less than previously seen with the former designs.

Comparisons with the cubic designs until now, were investigated simultaneously with several spherical designs by other collaborators, where examples of these geometries can be found in appendix B.2, figures B.1-2. However, the most interesting comparison was to simulate the AGATA array after replacing its Germanium detectors with LaBr_3 , the subject of the next section.

¹Personal examples of similar designs have already been presented extensively in this chapter.

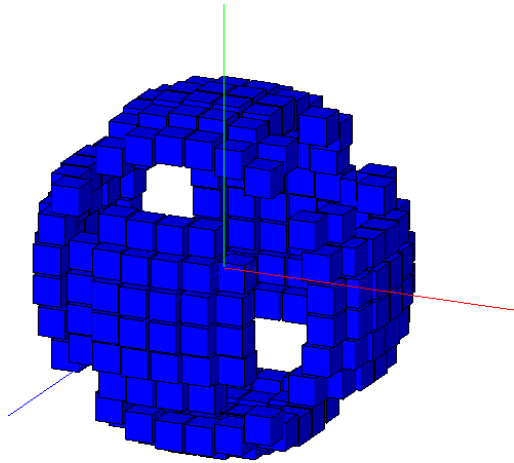


Figure 3.41: The final array of 1" LaBr₃(Ce) segments.

3.2.11.2 Comparative Simulations with AGATA

Numerous simulations were carried out to simulate the response of 1-40 MeV γ -rays in the AGATA geometry, in order to better understand the trends in the deposition of energy. The results of these simulations are presented within this section.

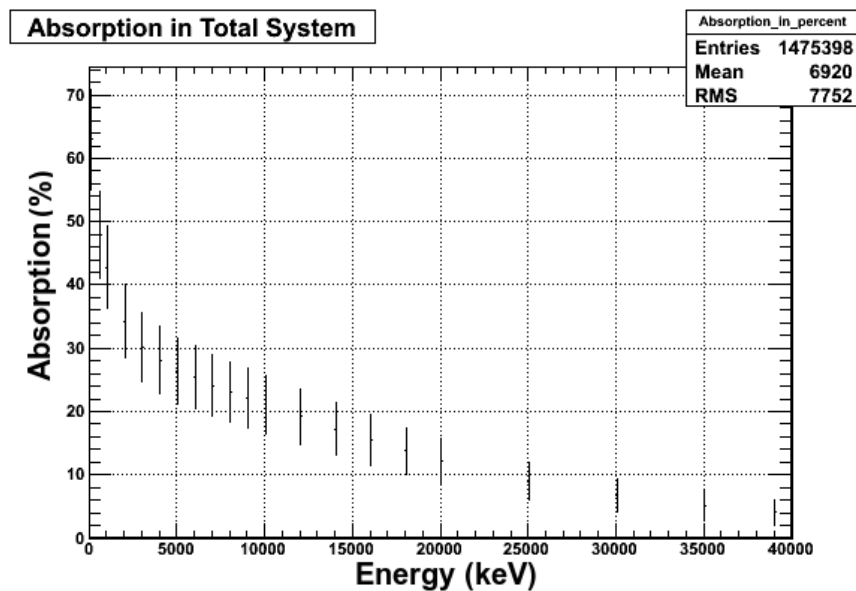


Figure 3.42: Total absorption efficiency with the final design.

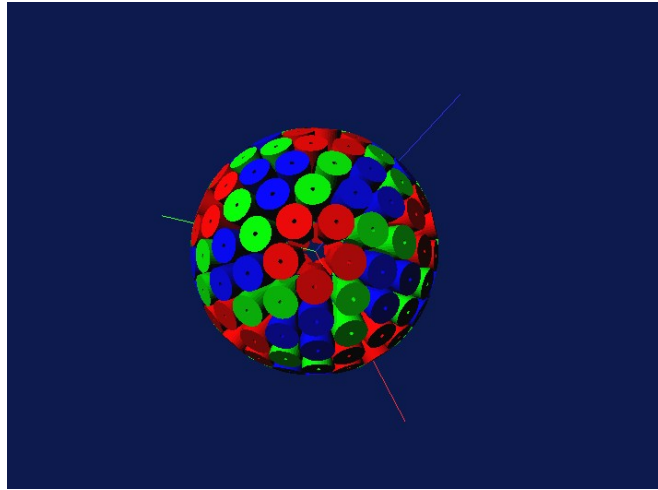


Figure 3.43: The AGATA array, with multi-colour cluster segments.

Initially, 200 2" x 2" x 2" detectors of LaBr_3 were tiled into the calorimeter array, with gaps left in the corners for the addition of a beam pipe. The design is shown in figure 3.41, where simulations with the inner layer of 2" x 2" x 4" LaBr_3 scintillators and outer shell of CsI segments, gave a full representation of the total absorption efficiency for the entire calorimeter. The total energy deposition of one MeV γ -rays, was found to be $\sim 44\% - 48\%$ for the LaBr_3 layer (figure 3.42). At higher energies (15 MeV), inner and total absorption efficiencies of $\sim 14\% - \sim 17\%$ were measured respectively.

Similar results were obtained with the AGATA geometry, substituting the germanium detectors with $\text{LaBr}_3(\text{Ce})$ scintillators. In this brief study, a comparison between these geometries would ultimately lead to a better understanding of the overall detector efficiency.

In the AGATA code, the generation of γ rays can be done by using a file outlining the rotational distribution of gammas, which includes various parameters that dictate how these gammas become incident on all the detectors. However, it was easier to write a separate file with the list of γ rays and tailor it accordingly, so that it could be read in, similar to how the γ rays are generated in the PARIS package. Numerous γ rays were generated between one and 20 MeV, presented in figure 3.44. The absorption efficiency of the total energy deposition of 20 to 40 MeV γ rays and one to 15 MeV gammas are presented in figures B.3-4 in

3.2 Constructing the PARIS Array

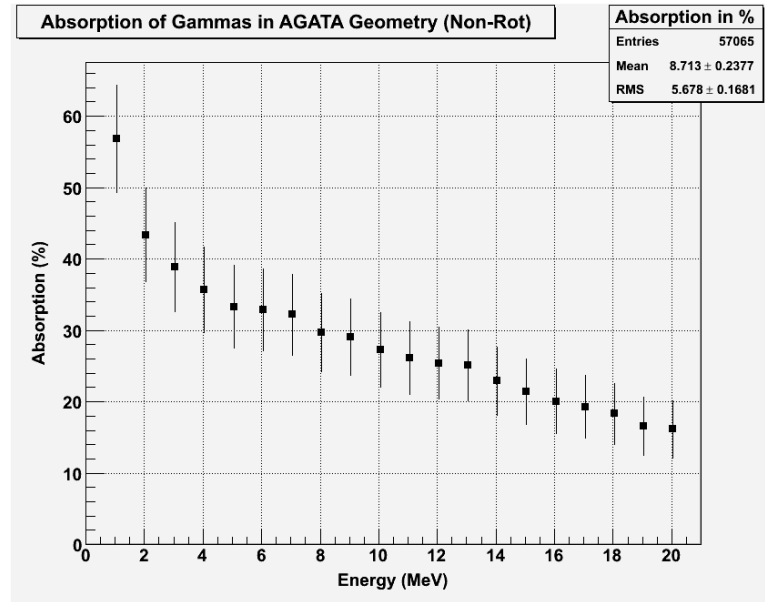


Figure 3.44: Absorption efficiency of the $\text{LaBr}_3(\text{Ce})$ AGATA array between 1 and 20 MeV

appendix B.

The amount of absorption efficiency is seen to be much larger for the AGATA array, even in comparison with the total absorption of the larger 2" x 2" x 4" and 2" x 2" x 6" scintillators used in the PARIS calorimeter. This is particularly discernible in figure 3.45, where for the intermediate values of energy (5-15 MeV, for example), the efficiency of the AGATA array is 5-10% better than the cubic configuration. This result can be expected due to the volume segments within AGATA being much larger, and also having better coverage over the 4π area.

A large number of simulations investigating a lot of potential scenarios and cases for geometries of various sizes, have given us a larger understanding of how the overall detector response changes with the alteration of several parameters. However, these assumptions are based on monochromatic source, with γ -rays projected towards a part of the detector, and are thus rather unrealistic. The next question one needs to address is; how a $\text{LaBr}_3(\text{Ce})$ array will perform for a given physics case.

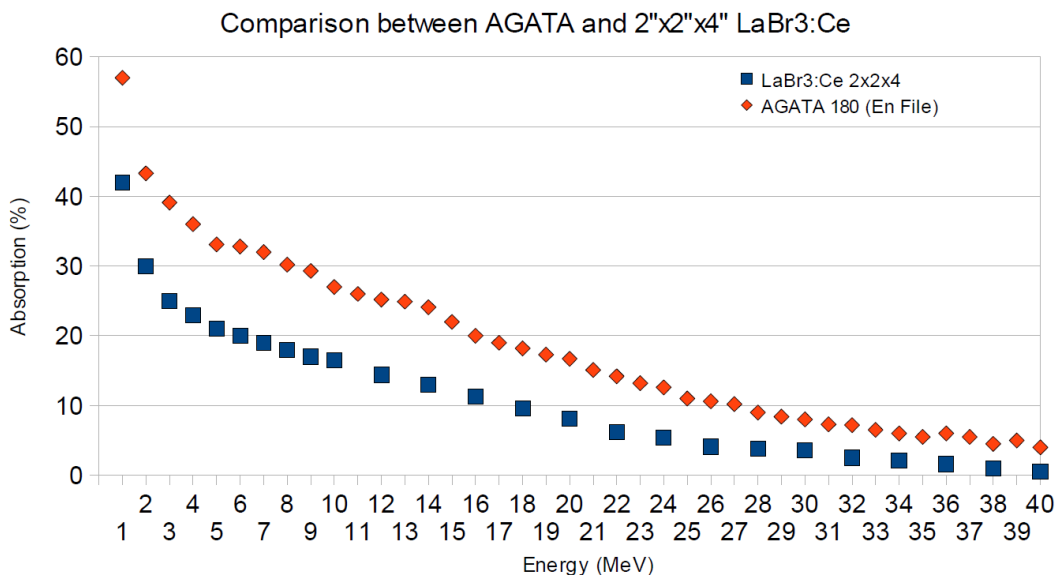


Figure 3.45: Absorption efficiencies of $\text{LaBr}_3(\text{Ce})$ AGATA and cubic geometries.

3.3 Simulation of a Physics Case

This section focuses on an array called CACTUS (which has a similar 4π geometry to AGATA), that was used to simulate a physics case at the university of Oslo. This geodesic array of 28 5" x 5" cylindrical $\text{NaI}(\text{Tl})$ scintillators has been the subject of a recent proposal to upgrade the existing array with similar sized $\text{LaBr}_3(\text{Ce})$ scintillators.

First, a series of simulations were performed to study the comparison in absorption efficiency of two individual volumes; 3.5" x 3.5" x 6" and 4" x 4" x 6" of $\text{LaBr}_3(\text{Ce})$ scintillators. The motivation was to observe if there was any justification for purchasing larger scintillators if the overall performance was not compromised. These segments were individually tested by projecting the source onto front face of the crystal at a similar distance to the fully tiled case. After these tests were concluded, the full CACTUS array was simulated with $\text{LaBr}_3(5\%:\text{Ce})$ scintillators over a broad range of γ -rays, ranging from 0.5-20 MeV, in 500 keV intervals. In the case of the full array, the isotropic distribution of these γ -rays was from a point source, 15 cm from the inner faces of the detectors.

Comparison of 3.5" and 4" diameter Lanthanum Halide Scintillators

Length extends to 6" with source distance of 15 cm

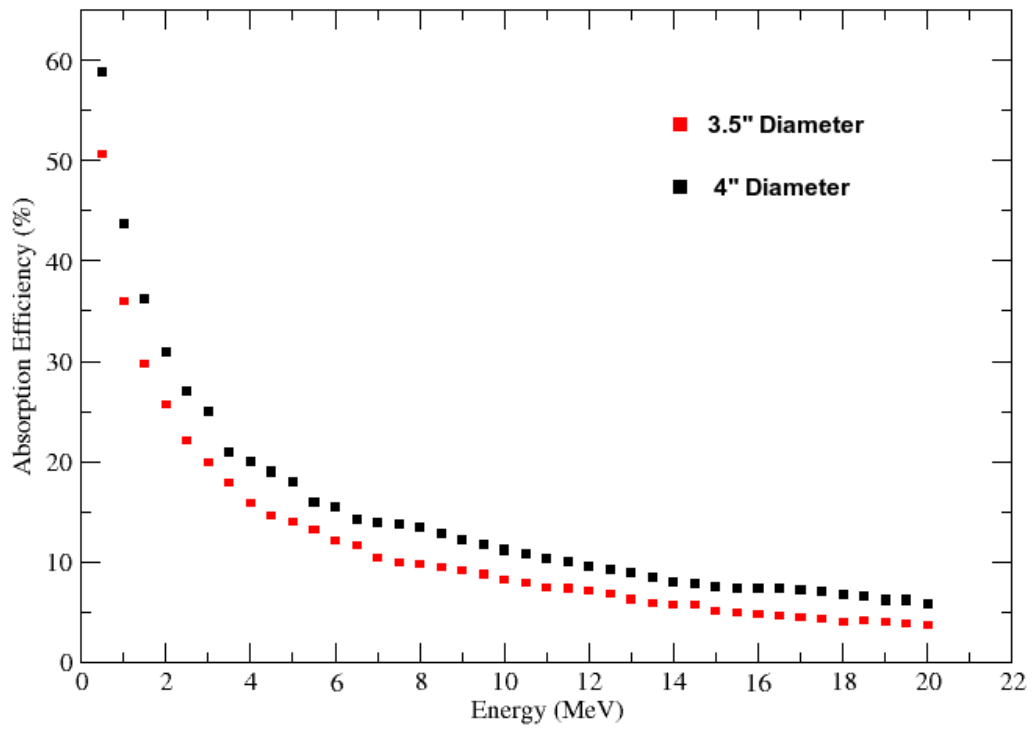


Figure 3.46: Absorption efficiencies of the cylinder detectors.

3.3 Simulation of a Physics Case

However, the CACTUS set-up in the simulation package also involved the inclusion of several collimators. The dimensions of each of these collimators are 1.7 cm thick, with an outer diameter of 7.3 cm at the front and 12.7 cm at the end, 10 cm in length. The lateral shielding consists of a 3 mm Pb layer wrapped around each detector. There is also 1.5 mm of Cu shielding in front of the collimators, where the source material is a 500 μm Co foil. While the simulations include shielding and collimators as well as the array, the PMT or electronics were not included. The spectra were analysed by counting both the total number of simulated γ -rays generated by the point source, and the number of those which are registered in the photo-peak¹. These figures regarding the results of these simulations are presented in appendix C, figures C.1-2.

At high energies, a smaller number of counts are observed in the photo-peak than in the 1st escape peak, likely to indicate that these γ -rays pass or scatter through the detectors and deposit their energy outside the material. The photo-peak efficiency for the 4" x 6" LaBr₃(Ce) crystals is also observed to be worse than the 5" x 5" NaI(Tl) segments in cases where $E_\gamma \geq 6$ MeV, as shown in figure C.1 in appendix C.

This likely to be due to the energy smearing incorporated in the simulations, which result in an increased number of counts in $E_\gamma \pm 2\sigma$. In the case of the simulations with NaI(Tl), a lot of the recorded γ -rays might come from the 1st escape peak because of the low resolution. This problem can easily be addressed in the future by adding shielding around the full array instead of between the detectors, allowing for the additional add-back of the escaped counts back into the full-energy peak.

A comparison of the energy resolutions between the NaI(Tl) and LaBr₃(Ce) arrays are shown in figures 3.47, 3.48 and 3.49, where a comparison of the measured photo-peaks at 1, 5, and 12 MeV are seen to be clearly resolved in the case of an array of LaBr₃(Ce) array, than with the NaI(Tl) array.

The positron-electron annihilation peak at 511 keV is clearly seen in all the spectra, but is considerably more resolved with the LaBr₃(Ce) array. The LaBr₃(Ce) array produces a σ at 1, 5, and 12 MeV of 10.4, 23.2, and 35.9 keV

¹Defined as the $\pm 2\sigma$ region around the energy of the emitted γ -ray, where σ is $1.52\sqrt{E}$ for NaI(Tl) and $0.328\sqrt{E}$ for LaBr₃(Ce).

3.3 Simulation of a Physics Case

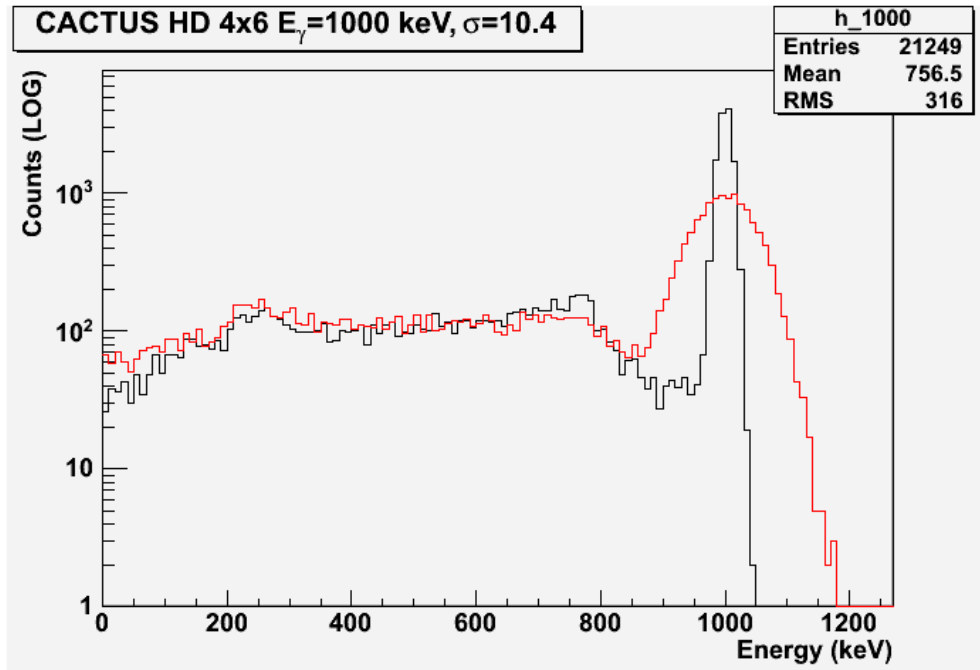


Figure 3.47: NaI(Tl) (red) and LaBr₃(Ce) (black) arrays for a one MeV γ -ray[30]

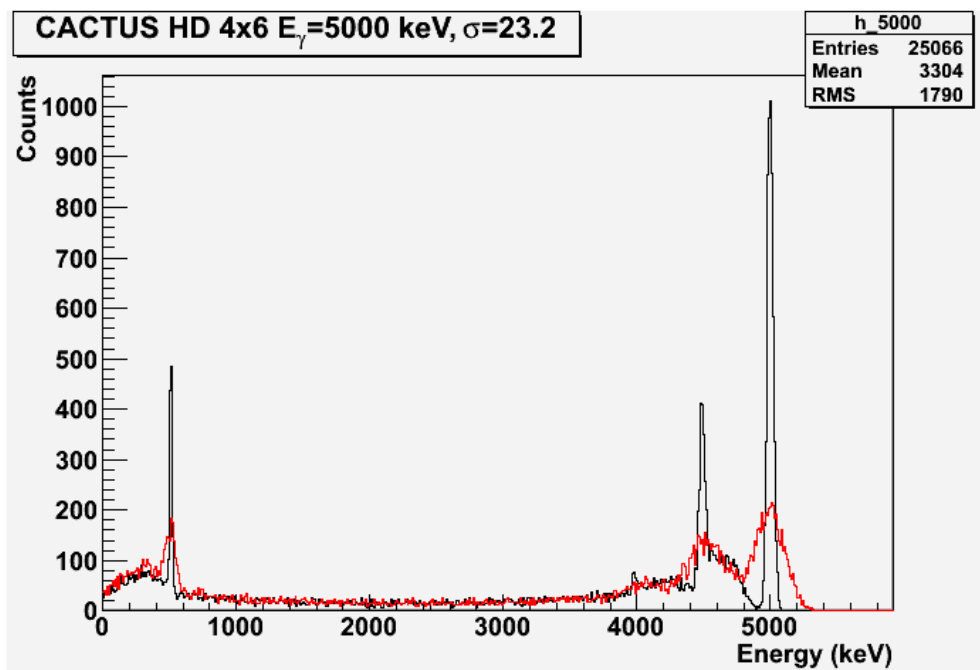


Figure 3.48: NaI(Tl) (red) and LaBr₃(Ce) (black) arrays for a 5 MeV γ -ray[30]

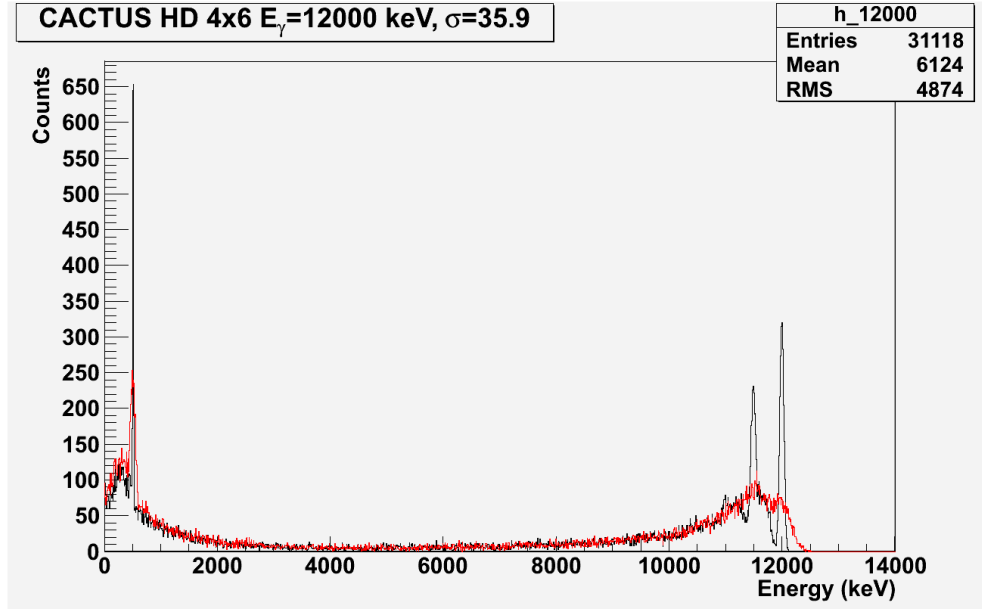


Figure 3.49: NaI(Tl) (red) and LaBr₃(Ce) (black) arrays for a 12 MeV γ -ray[30]

respectively. In the case of the NaI(Tl) crystals, σ values of 48.1, 107.5, and 166.5 keV were obtained for 1, 5, and 12 MeV γ -rays respectively.

3.3.1 Motivation for the Reaction: $^{163}\text{Dy}(^3\text{He}, ^4\text{He})^{162}\text{Dy}$

Recent experimental investigations contradict the once perceived notion that heavy nuclei behave "statistically" a few MeV above the yrast line, where even at an excitation energy of 8 MeV, there is little information to suggest the nucleonic motion becomes chaotic. This observation is supported by partial conservation of the K-quantum number[31] and preferred non-statistical γ -ray decays [32].

The nuclear level density is an essential parameter needed to determine the thermodynamic properties of nuclei, from which entropy, temperature and heat capacity can all be extracted, and subsequently used to describe the behaviour of a many-particle system. However, these values are difficult to obtain, and thus only the lowest excitation region; below 2 - 3 MeV, has been investigated.

The data is obtained through the reaction channel; (^3He , ^4He) or through the inelastic scattering reaction; (^3He , ^3He). In previous studies, the beam of ^3He ions had an energy of 45 MeV, delivered by the cyclotron at the Oslo National

3.3 Simulation of a Physics Case

Laboratory, where the beam time was 2 - 3 weeks. The γ -ray decay was measured in coincidence with the ejectile within a time window of 15 ns, using two Ge and 28 NaI(Tl) detectors, with a total efficiency of 15 % over a 4π solid angle.

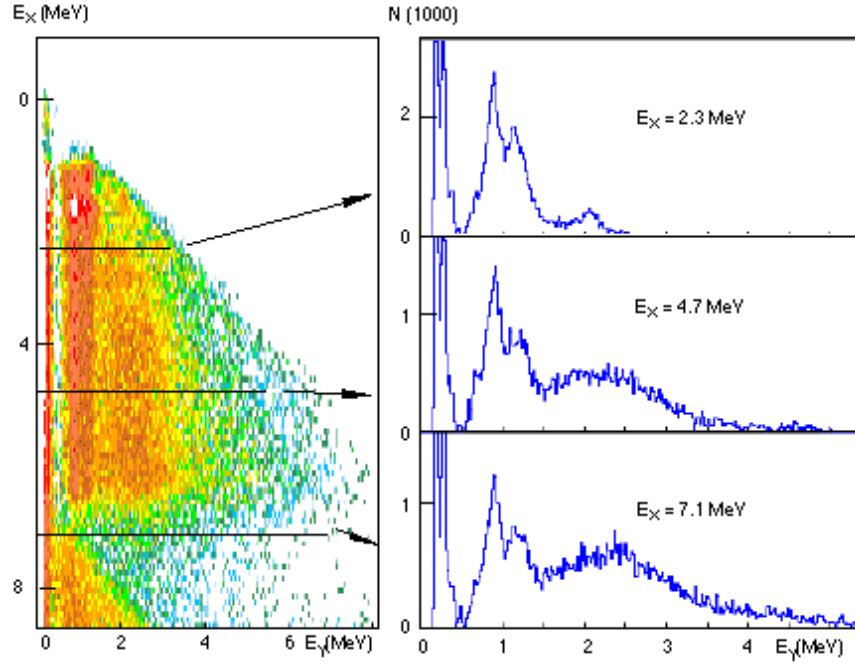


Figure 3.50: The ${}^4\text{He}$ - γ coincidence energy matrix for ${}^{162}\text{Dy}$, with γ -spectra from three initial excitation energies.[33]

In figure 3.50, the energy matrix of ${}^4\text{He}$ -particles and γ -rays in the ${}^{163}\text{Dy}({}^3\text{He}, {}^4\text{He}){}^{162}\text{Dy}$ reaction is displayed. In this matrix the ${}^4\text{He}$ particle energy has been transformed to the excitation energy in ${}^{162}\text{Dy}$, where the excitation energy is determined from the Q-value of the reaction and the kinematic energy associated with the outgoing charged ejectile.

The (E_γ, E_x) matrix in figure 3.50 reveals four components[33]:

- yrast transitions with $E_\gamma \sim 0.3$ MeV
- decay from vibration and two quasi-particle states with $E_\gamma \sim 1$ MeV
- decay in the continuum with $E_\gamma \sim 2$ -3 MeV

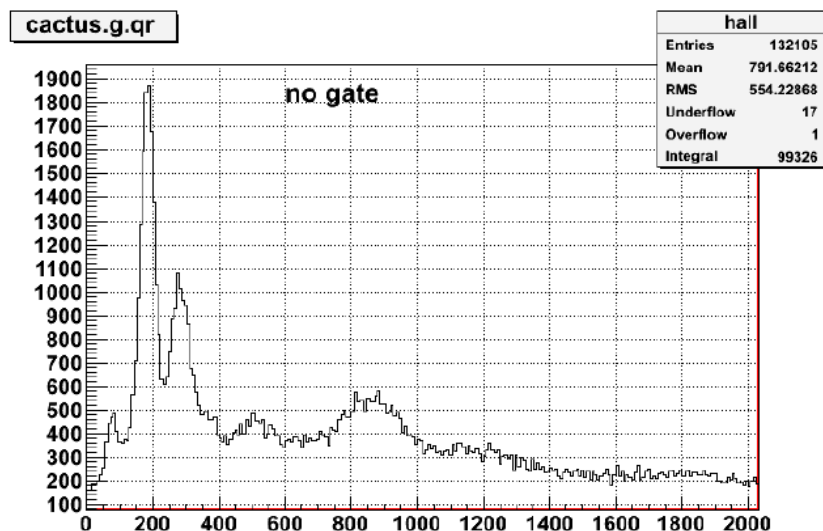


Figure 3.51: Simulated NaI(Tl) spectrum of ^{162}Dy with no gate applied.[30]

- direct decay to the ground band with $E_\gamma \sim E_x$.

Preliminary simulations of the CACTUS array with $\text{LaBr}_3(\text{Ce})$ are shown from figure 3.51 to 3.56. Where in these figures, several gates are applied for various transitions in ^{162}Dy . Looking at these spectra, it is clear that the resolution of the $\text{LaBr}_3(\text{Ce})$ array is far more superior to that of the NaI(Tl) array¹. Although not measured, significantly faster timing measurements can also be expected. Previously applied timing windows of ~ 15 ns can be greatly improved upon due to the quick rise and decay times of $\text{LaBr}_3(\text{Ce})$, leading to improvements in energy matrices such as those seen in figure 3.50.

An upgrade of the CACTUS array with $\text{LaBr}_3(\text{Ce})$ will enhance, and significantly optimise measurements for the $^{163}\text{Dy}(^3\text{He}, ^4\text{He})^{162}\text{Dy}$ reaction mentioned briefly in this chapter. This will likely further existing work on energy level density measurements, leading to more precise identification of already existing states, and possibly, unobserved ones. Of course, this is just one example of many

¹Other examples of the $6^+ \rightarrow 4^+$ and $8^+ \rightarrow 6^+$ transitions can be found in appendix C, figures C.3-6.

3.3 Simulation of a Physics Case

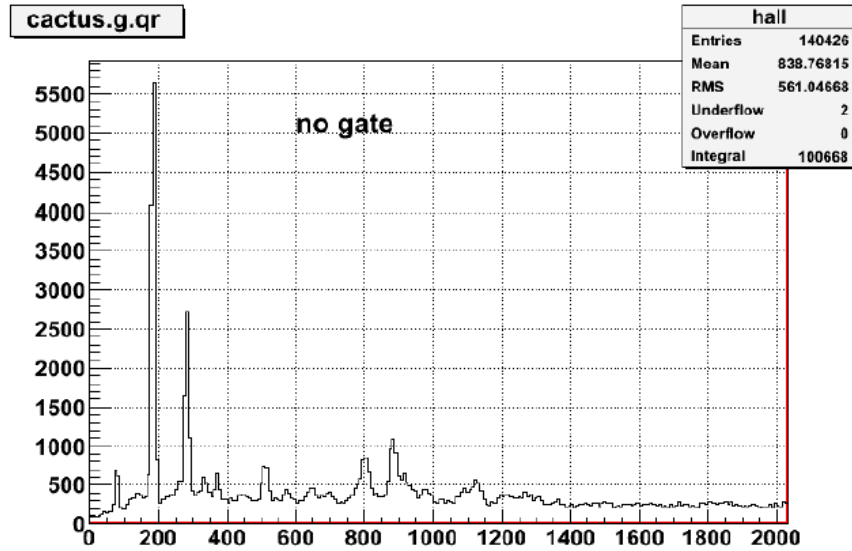


Figure 3.52: Simulated LaBr₃(Ce) spectrum of ¹⁶²Dy with no gate applied.[30]

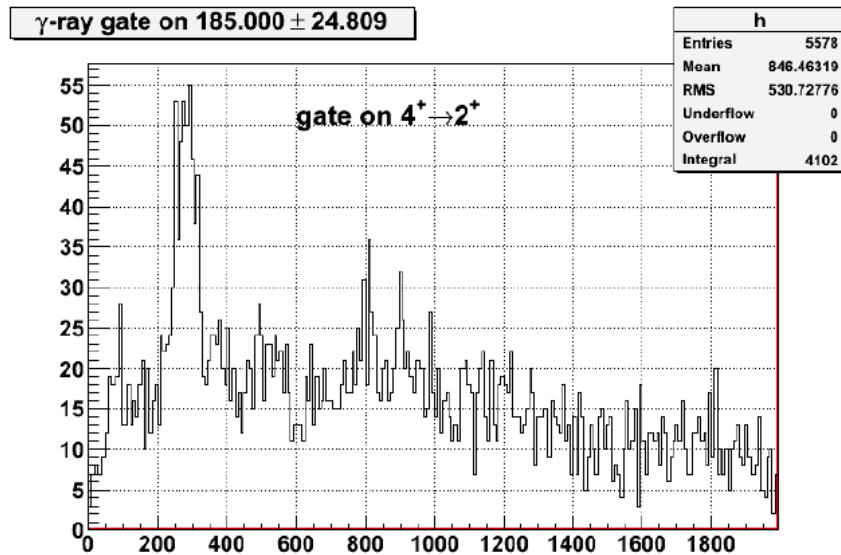


Figure 3.53: Simulated NaI(Tl) spectrum of ¹⁶²Dy, gated on the 4⁺ → 2⁺. [30]

3.3 Simulation of a Physics Case

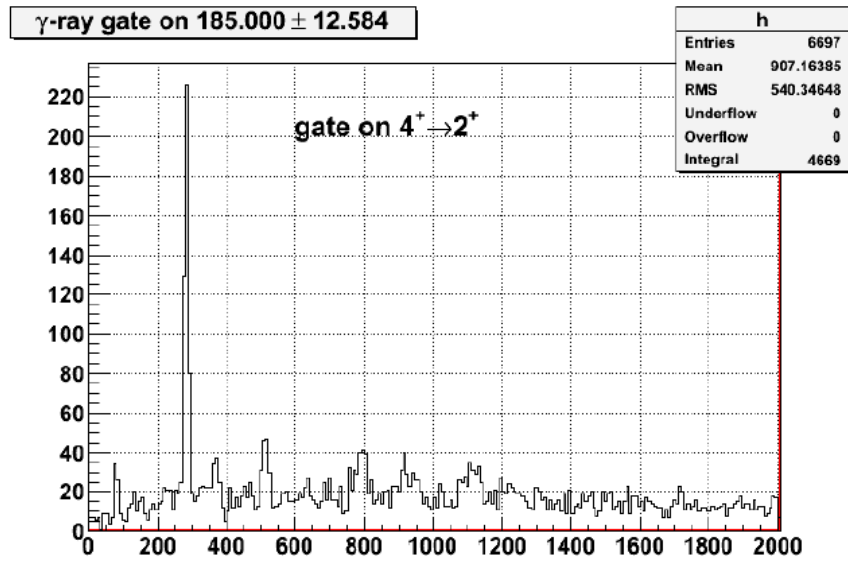


Figure 3.54: Simulated LaBr₃(Ce) spectrum of ¹⁶²Dy, gated on the $4^+ \rightarrow 2^+$. [30]

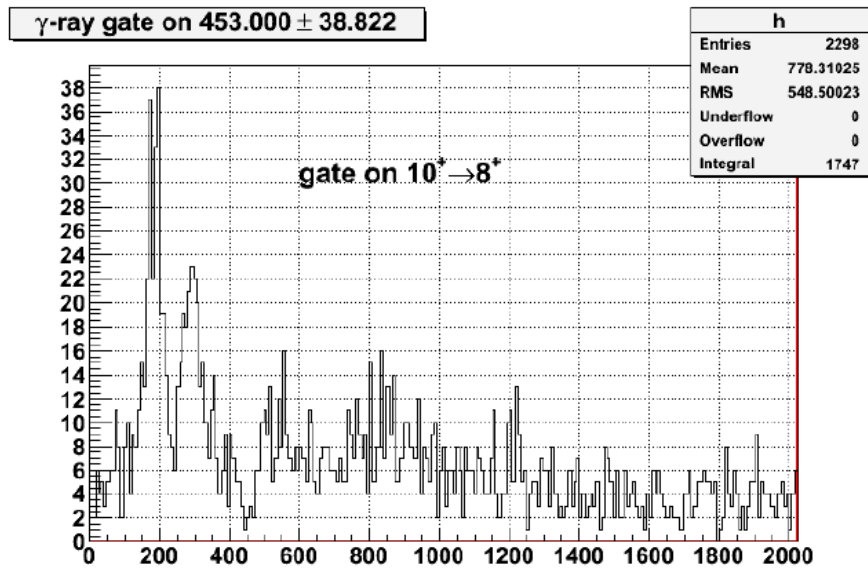


Figure 3.55: Simulated NaI(Tl) spectrum of ¹⁶²Dy, gated on the $10^+ \rightarrow 8^+$. [30]

3.3 Simulation of a Physics Case

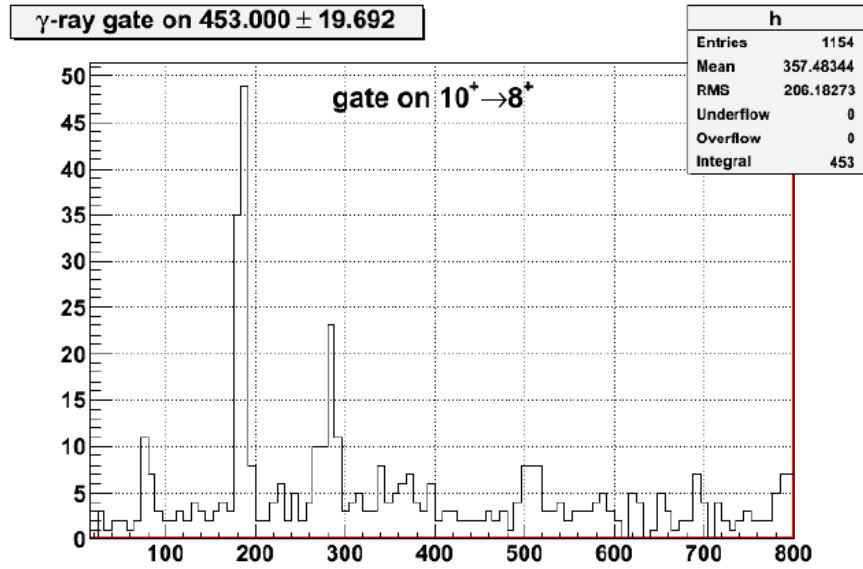


Figure 3.56: Simulated $\text{LaBr}_3(\text{Ce})$ spectrum of ^{162}Dy , gated on the $10^+ \rightarrow 8^+$. [30]

other areas of interest that have been simulated within the PARIS collaboration, where a comparison of the theoretical and experimental values will allow for a furthering of understanding within these areas.

Chapter 4

LaBr₃(Ce) Scintillator and Phoswich Detector Testing

4.1 Energy Response and Self Activity of a 1.5” LaBr₃(Ce) detector

Prior to testing with the neutron source, the natural radioactivity and initial energy response with laboratory γ -ray sources, was studied. The naturally occurring contamination spectrum due to the radioisotope ^{138}La and ^{227}Ac decay is also outlined, with studies on this self activity presented along with the response of the detector, when exposed to conventional sources such as ^{60}Co , ^{137}Cs , ^{152}Eu and ^{241}Am , used to test the linearity and energy response at less than 2 MeV. Pulse shapes were acquired, and adjustments were made to the signal prior to taking measurements to ensure the corresponding energy resolutions were optimised.

4.1.1 Self Activity

The self-activity within LaBr₃(Ce) scintillators is due to the presence of the radioisotope ^{138}La , a naturally occurring isotope with an abundance of 0.09 % and a large half life of 1.05×10^{11} years. In 66.4 % of its decays, ^{138}La undergoes electron capture to an excited state of ^{138}Ba via photon emission of a 1436 keV γ -ray. However, X-rays at 32 and 5 keV occur due to the reoccupation of the K and

4.1 Energy Response and Self Activity of a 1.5” LaBr₃(Ce) detector

L electron shell orbitals in barium, and displace the 1436 keV line due to their coincident nature[34]. The remainder of ¹³⁸La decays 33.6% of the time via beta emission to ¹³⁸Ce, emitting a 789 keV γ -ray from the 2⁺ state.

4.1.2 Actinide Contamination

The presence of naturally occurring α -contamination can be measured, as ²²⁷Ac is in the same periodic group (group IIIB) as Lanthanum, which results in four broad peaks in the background spectra. Of these decays, long lived ²²⁷Ac is the contributing element ($\tau_{1/2} = 21.2$ years), which β -decays to ²²⁷Th, and subsequently α -decays to ²⁰⁷Tl, as shown in figure 4.1. A spectrum with 4096 channels is enlarged to show both ²²⁷Ac contamination and the 4.44 MeV γ -ray with escape peaks in figure 4.2.

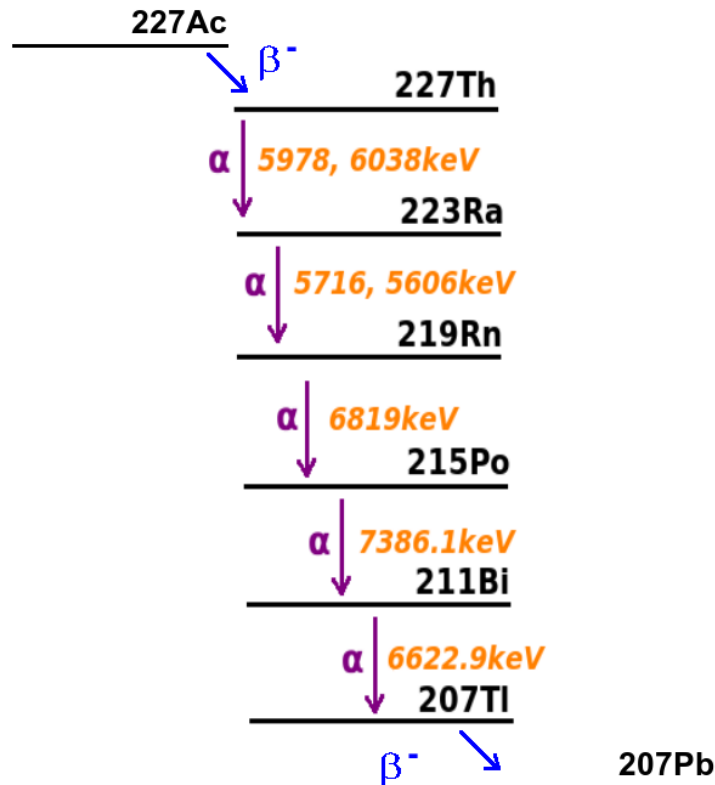


Figure 4.1: The decay due to the contamination from ²²⁷Ac.

4.1 Energy Response and Self Activity of a 1.5” LaBr₃(Ce) detector

By comparing the true values of these α energies and their measured energies, extraction of the properties of α -scintillation in the detector can be achieved. When calibrated with γ rays, α -particles were found to produce 65 % less light ($\frac{\alpha}{\gamma} = 0.35$), which is in agreement with a similar finding for LaCl₃(Ce) scintillators by Hartwell and Gehrke[35]. This quenching for α -particles is possibly due to the sensitivity of the scintillation mechanism for various particles[35].

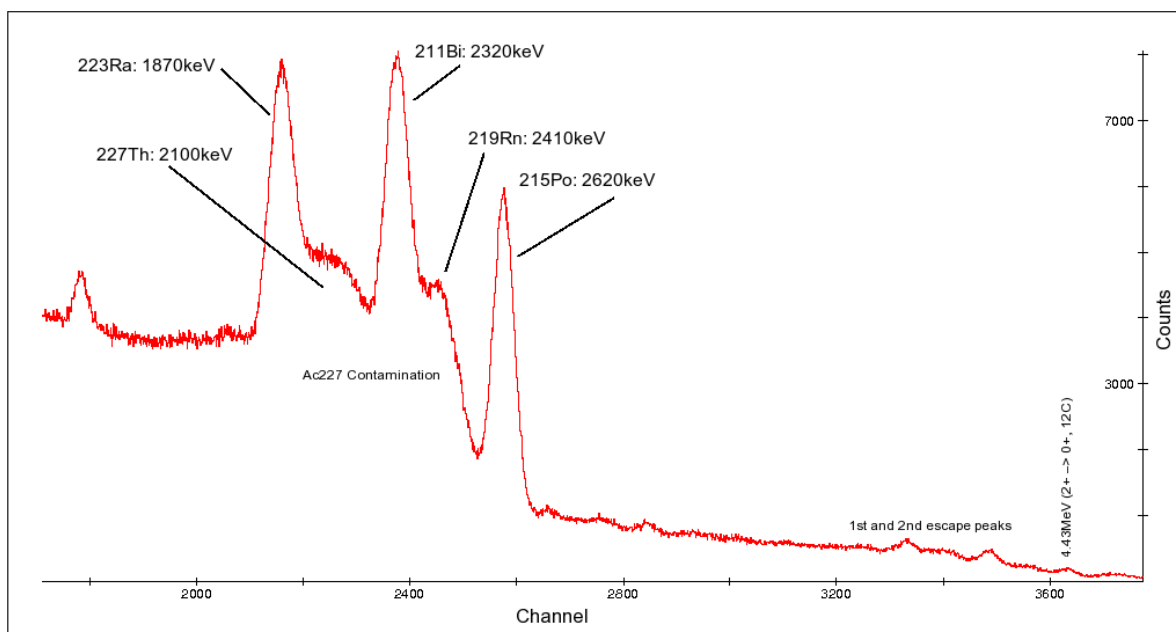


Figure 4.2: α -contamination present in the detector

Self counting measurements were made to estimate the background contamination rate within the scintillator. It was found that the highest counting rates were due to self activity from ^{138}La , where the substantial 32 keV X-ray photo-peak, had a counting rate of 0.3362 cps/cc. The 1473 and 789 keV photo-peaks due to the decays to ^{138}Ba and ^{138}Ce from ^{138}La , had lower count rates of 0.0386 and 0.0130 cps/cc respectively. The counts from the α -contamination were substantially lower at ~ 0.0063 cps/cc. This rough estimation of the counting rates seem to deviate from what is quoted by Saint-Gobain[34]. For the region between 0 and 255 keV, a counting rate of 0.226 cps/cc was observed for a similar sized

4.1 Energy Response and Self Activity of a 1.5” LaBr₃(Ce) detector

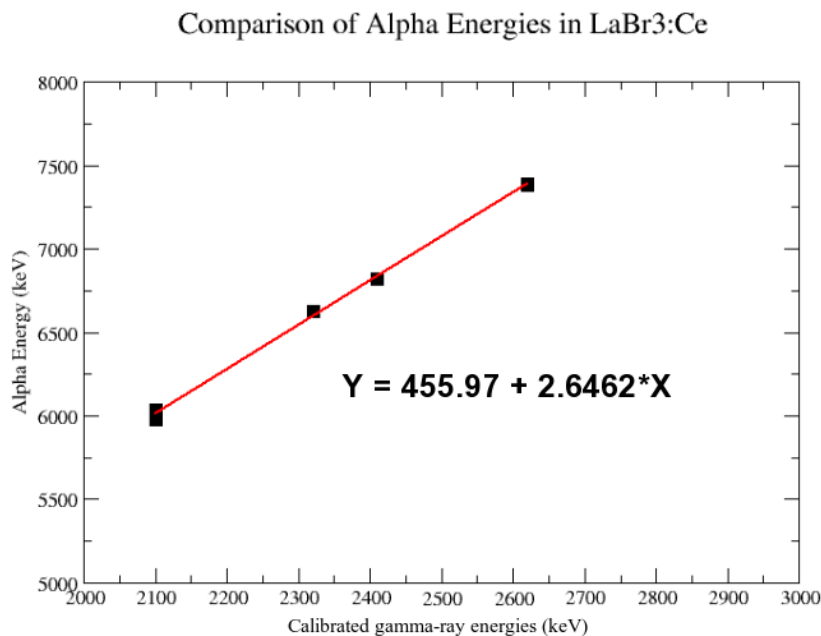


Figure 4.3: α -scintillation properties when calibrated with γ rays

1.5”x 1.5” scintillator. For the 790-1000 and 1473 keV photo-peak regions, counting rates of 0.065 and 0.068 cps/cc were observed, almost twice as much as what was recorded in the initial tests. The contamination from the α -decay was also found to be lower by an order of magnitude, where Saint-Gobain quote a counting rate of 0.034 cps/cc for any energies above 1.6 MeV. It becomes apparent in these results that the 45 minute spectrum yielded substantially lower count rates for a wide range of energies in comparison to the three day spectrum acquired by Saint-Gobain. This might be due to miscalculations in the rough estimation made with the data that was acquired in the lab. Another possibility lies in the fact that 45 minutes might not be enough time to acquire enough statistics to determine with accuracy, the photo-peak regions, due to the low counting rate.

4.1.3 Energy Response of the LaBr₃(Ce) scintillator

Initial measurements using several standard sources were used to test the threshold for saturation levels in the PMT. The pulses were analysed, and the energy

4.1 Energy Response and Self Activity of a 1.5" LaBr₃(Ce) detector

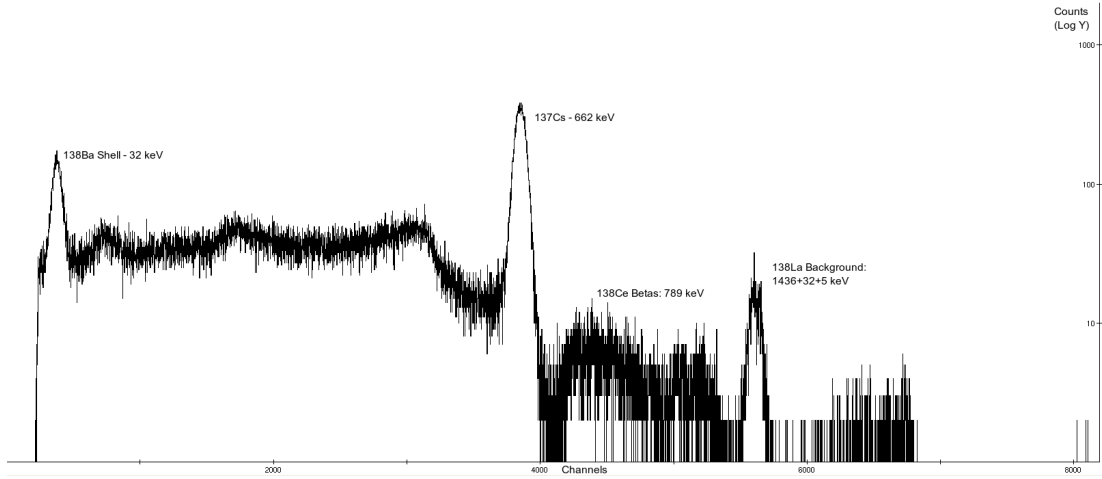


Figure 4.4: A ^{137}Cs spectrum with observed contamination from ^{138}La and ^{227}Ac .

Element	γ ray (keV)	FWHM (keV)	$E_{Res}(\%)$
^{241}Am	59.54	9.23	15.50
^{137}Cs	661.73	16.89	2.55
^{60}Co	1173.21	22.18	1.96
^{60}Co	1332.54	24.14	1.81

Table 4.1: Energy resolutions from LaBr₃(Ce) spectra

resolutions and subsequent FWHM efficiencies were examined. The energy resolutions were calculated for the ^{137}Cs , ^{241}Am and ^{60}Co sources. An example of the response of the 1.5" x 1.5" x 1.5" LaBr₃(Ce) when exposed briefly to a ^{137}Cs source, is presented in figure 4.4. This spectrum shows the FWHM of the 662 keV γ -ray peak to be 16.33 ± 1.15 keV, corresponding to a energy resolution of 2.6 ± 0.2 %. Many of the features of the spectrum from the radioisotope ^{138}La are also present in the spectrum.

Similarly, energy resolutions for other sources were obtained, with values of $\sim 2.0 \pm 0.1\%$ for 1173 keV and $\sim 1.8 \pm 0.1\%$ for 1332 keV in ^{60}Co . The values of other sources are shown in table 4.1, and were used to produce a rough calibration of the response in energy for this scintillator. The FWHM measurements were calculated using Radware, and have an error of ± 1.15 keV. These values of resolution were then taken and plotted against energy as shown in figure 4.5.

4.2 Neutron Activation and Detector Response

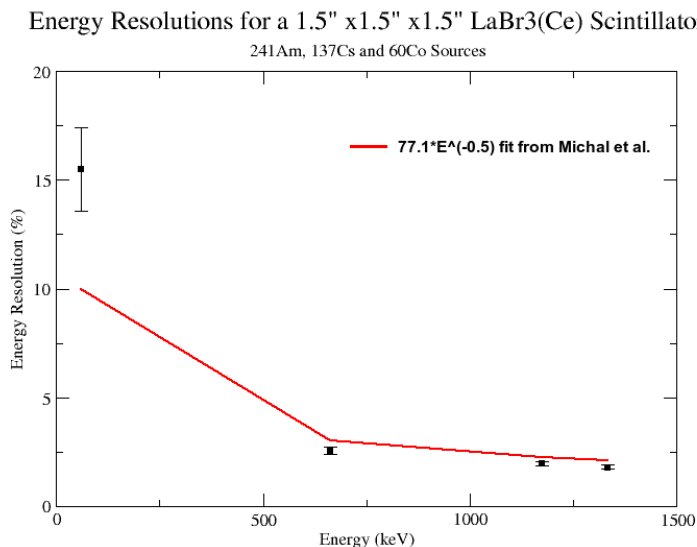


Figure 4.5: Results of the FWHM measurements made, with energy resolution plotted against increasing energy

The energy resolution of the LaBr₃(Ce) becomes worse at lower energies, which is expected for scintillators. The fit in red is based on high energy measurements made by a member of the PARIS collaboration, and whose results are published[28]. Although the resolutions are poor at lower energies, they are still better than standard NaI(Tl) detectors (7.0% at 662)[34]. Now that the resolution of the crystal has been thoroughly analysed, the pulse shapes of the crystal when subjected to a 10.5 GBq AmBe neutron source were studied.

4.2 Neutron Activation and Detector Response

4.2.1 Neutron Capture

The neutron response of these detectors was tested with the neutron source ²⁴¹Am/⁹Be, where a study of how neutron activation affected the scintillator was investigated. In the neutron source, α -particles emitted by ²⁴¹Am impinge on ⁹Be, creating an excited state of ¹²C in the following reaction:

4.2 Neutron Activation and Detector Response



The excited state, ${}^{12}\text{C}^*$, is short lived, and emits a 4.44 MeV γ -ray as it de-excites to the ground state via inelastic scattering¹. In order for this process to occur, the incident neutron energy needs to be high enough to excite the nucleus, as elastic scattering becomes increasingly likely at lower thermal energies.

Radiative neutron capture ie., $n + (Z,A) \rightarrow \gamma + (Z, A+1)$, has a cross-section related to approximately $1/v$, where v is the velocity of the neutron. Depending on the element, there might also be resonance peaks superimposed on the $1/v$ dependence, where at high energies, the probability of neutron capture is greatly enhanced. In this experiment, the majority of neutrons have a few hundred keV in energy on average, although one can expect a few fast neutrons, with energies greater than one MeV. Fast neutrons are likely to scatter inside the material unless they pass through some sort of moderation. During this scattering process, which can be either inelastic or elastic (depending on the energy), the fast neutrons will keep losing energy until thermal equilibrium is reached, where it is finally captured by the nucleus.

4.2.2 Experimental set-up and First Results

A 1.5" x 1.5" LaBr₃(Ce) scintillation detector coupled with a Photonis 2" XP20D0 PMT was obtained from Saint-Gobain Crystals. The operational voltage recommended by Saint Gobain was -1200V, however this resulted in a highly non-linear spectrum as the photon yield produced by the crystal is extremely high. Therefore, the working voltage was reduced to a rather low -900V, so that the detector was properly gain matched. The dynamic range was rather inconsistent and is possibly due to saturation phenomena inside the PMT, thus effecting the overall response in energy. An amplifier with a shaping time of 500 ns and low coarse gain was used to shape the anode signal. It was considered that the signal could have been read off one of the dynodes instead of the anode. However, reading

¹An example of which is defined as $A(n,n')A^*$.

4.2 Neutron Activation and Detector Response

off one of the dynodes would result in a degradation of the signal and thus the resulting energy resolution.

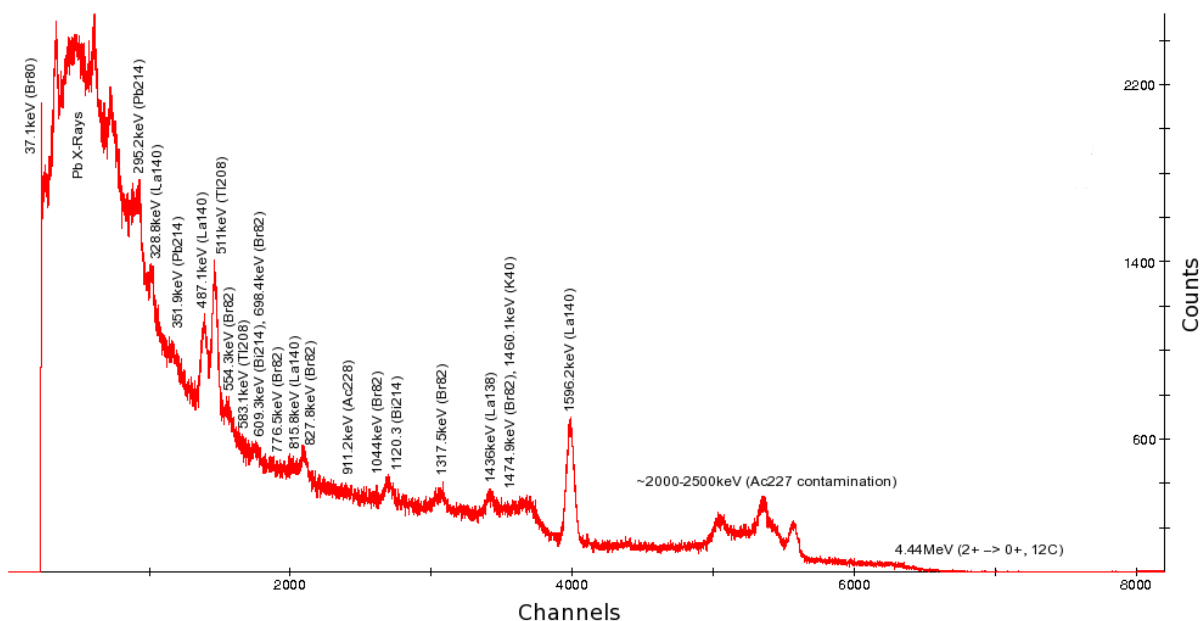


Figure 4.6: Calibrated activated spectrum of a 1.5'' LaBr₃(Ce) detector.

After the set-up was finalised, several calibration and background spectra of the LaBr₃(Ce) detector were obtained before being placed roughly 20 cm from the neutron source ²⁴¹Am/⁹Be. Due to the 4.44 MeV being one of many γ -rays present in this reaction, it was anticipated that these γ -ray transitions will be present in the final spectrum, along with the de-excitation of neutron activated isotopes within the detector medium. However, due to the small volume of the crystal being unable to contain the full energy deposition, the resulting 4.44 MeV γ -ray was hard to locate. Consequently, the FWHM of the photo-peak was found to be poor, where a fit in ROOT gave a resolution of $\sim 1.4\%$, with an error of that order of magnitude. However, the location of the transition of this γ ray allowed for the identification of excited states from both Lanthanum (¹⁴⁰La) and Bromine (⁸⁰Br, ⁸²Br). This is due to the large thermal neutron cross-sections of the two stable states in naturally occurring Bromine that contribute significantly to the activated spectrum of LaBr₃(Ce); ⁷⁹Br and ⁸¹Br, with abundances of 50.69 and

4.3 (n,γ) Pulse Shape Discrimination

49.31% respectively. The (n,γ) cross-sections for the formation of metastable ^{79}Br and ^{81}Br states are 2.5 and 2.4 b respectively (where $1\text{b} = 10^{-28}\text{m}^2$). However, for the formation of both ^{79}Br and ^{81}Br ground-states, the (n,γ) cross-sections are 8.3 and 0.24 b respectively[36]. The calibrated spectrum after activation is shown in figure 4.6. The calibrations were performed with various sources confined within a lead castle, where time lapse spectra were obtained offline to identify the excited states.

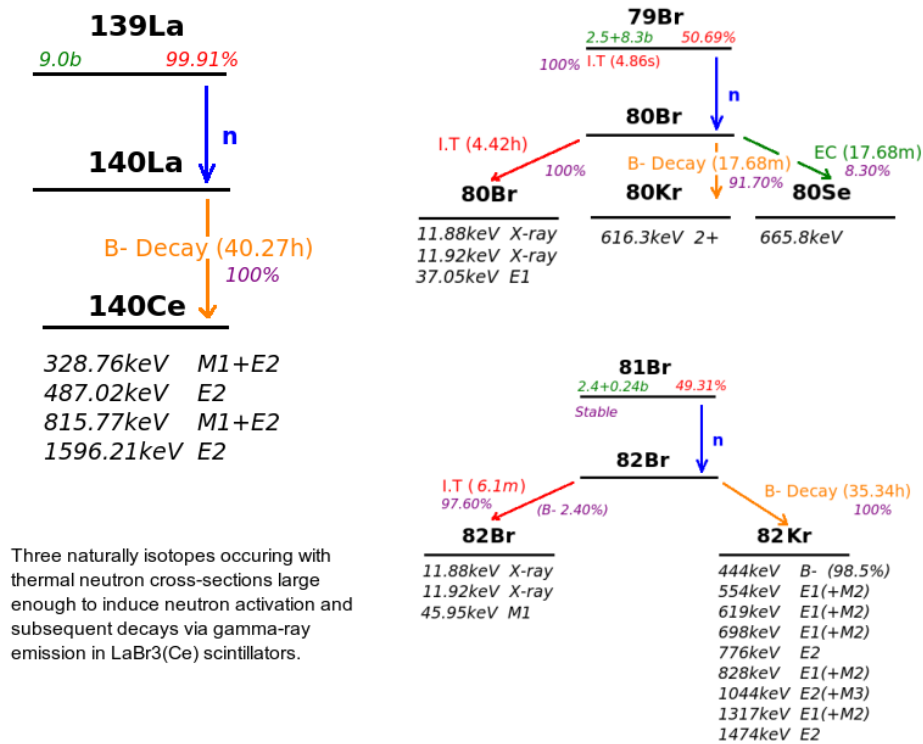


Figure 4.7: The isotopes that undergo neutron activation.

4.3 (n,γ) Pulse Shape Discrimination

Scintillator material exhibits a phenomena known as luminescence. If re-emission of this energy is immediately after the absorption (within 10^{-8}s) then this process is known as fluorescence. However, if the re-emission is delayed due to an excited

4.3 (n, γ) Pulse Shape Discrimination

state being metastable at the atomic level, another process known as phosphorescence occurs. The time evolution of this re-emission process can be accurately modelled on the equation[14]:

$$N = A \cdot e^{\frac{-t}{\tau_f}} + B \cdot e^{\frac{-t}{\tau_s}} \quad (4.2)$$

Where the magnitudes of the exponential decays; A and B , are different for each material and described by the fast and slow decay constants; τ_f and τ_s . These two components of the scintillation process N (total number of emitted photons), helps to describe the nature of the pulses timing. The finite rise time from zero to the maximum amplitude is usually shorter than the decay time for most scintillators, as one component of the decay constant is much quicker than the other. This results in a fast and slow component for each pulse, which forms the basis for the pulse shape discrimination technique.

Pulse shape analysis was carried out to see if one could discriminate between gamma and neutron pulse shapes. Generally, organic scintillators provide such discrimination due to delayed re-emission of energy. Several batches were recorded using two well known γ -ray emitters; ^{137}Cs (662 keV) and ^{60}Co (1173 & 1332 keV). Each data file was compiled into a single ascii file, where stringent gates were applied to the data from a written code that defined the slow and fast regions of each pulse, and extracted its information. This process is known as "software CFD", as the methods by which the fast and slow components are measured, are based on similar techniques used in NIM discriminator modules; by integrating the signal of each pulse, and evaluating the values for the fast and slow components via the zero cross-over (ZCO) method. At first the discrimination was fairly scattered, however dividing the slow component by the sum of both components improves the fit substantially, an example of which is shown in figure 4.8.

4.3 (n, γ) Pulse Shape Discrimination

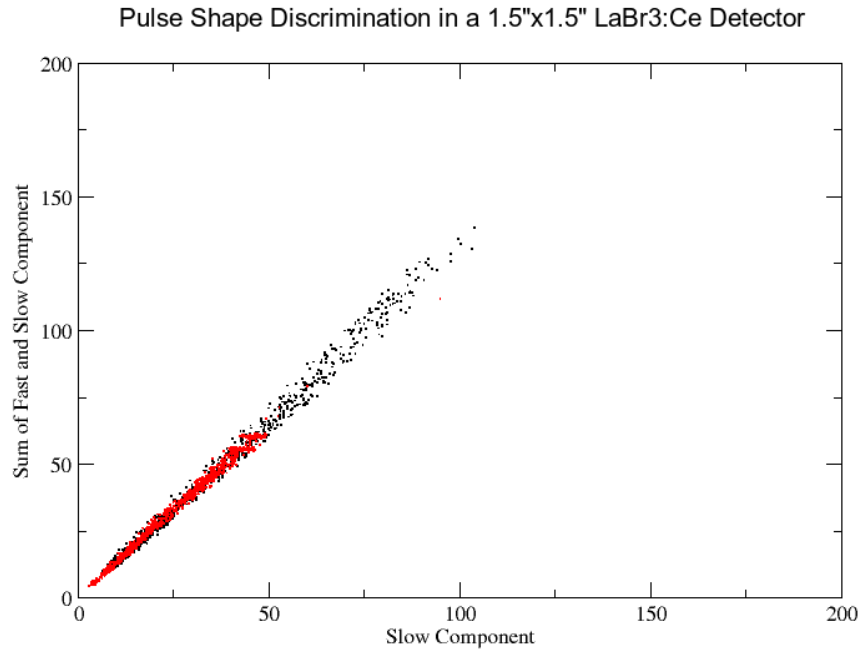


Figure 4.8: Fast and slow components from gamma and neutron anode pulse shapes to try to observe any discrimination.

In figure 4.8, the points in red were acquired with a ^{60}Co source, where the two thresholds correspond to the γ -ray photo-peaks at 1132 and 1332 keV. The points in black are a combination of fast and thermal neutrons, and coincident γ -rays from the source. The spectrum shows essentially no discrimination between both sets of data, unlike what one would expect for organic liquid scintillators, which have a delayed scintillation mechanism. The magnitude of the slow component is small, and the discrimination, if any, too small to be useful in experimental conditions. More coincidence measurements with a beam-line would help verify these results. It should be noted that no discrimination is possible by this proof of principle, which is expected in inorganic halide scintillators. However, one expects ToF measurements to be better at discriminating the response of the signal when subject to neutrons and gammas. It should be noted that separate studies done in this area with neutrons and charged particles in $\text{LaCl}_3(\text{Ce})$ reveal

modest discrimination [37].

4.4 Introduction to the Phoswich Detector

A Phosphor Sandwich or "Phoswich" Detector is a very efficient detector method, consisting of two dissimilar scintillators optically coupled to a single PMT or APD. The scintillators have two different timing signals, which allow the resulting pulse height in the output of the detector, to vary on the contribution of light from each scintillator. Discrimination of the two decay times and pulse shapes allow one to distinguish events that may have occurred in one scintillator, and not the other, or both. Phoswich detectors using these pulse shape discrimination techniques are also useful in reducing the background, allowing for the detection of events such as X-rays and beta particles[38]. As is the case with PARIS, a fast scintillator in front of a slower scintillator allows for dE/dx and energy deposition measurements within the smaller, faster detector. Particle discrimination techniques can then be performed in order to get good separation between different types of heavy charged particles using various methods, some of which are outlined in this section.

4.4.1 Initial Testing and Signal Optimisation.

A 1"x1"x2" LaBr₃(Ce) crystal was coupled to a 1"x1"x6" CsI(Na) scintillator with an epoxy resin and canned to form the detector, which was acquired from Saint-Gobain crystals. The difference in the decay times of both signals (roughly 20 ns and 600 ns for LaBr₃(Ce) and CsI(Na) respectively¹) allows both signals to be discriminated and read off one PMT, resulting in high detector efficiency due to a reduction in dead space. CsI(Na) typically has a resolution that is of the order of 8-10 % at 662 keV (for the crystal sizes used), compared to ~ 3 % found in the LaBr₃(Ce) crystal. No matter where a source is placed in proximity to the detector, it is thought that scattering will occur in both scintillators which will

¹These values for decay times are dependent on the quantity of dopant present in the scintillator. Typically for LaBr₃(Ce), a decay time of 23 ns is seen with a Ce³⁺ concentration of 0.2 %[3].

4.4 Introduction to the Phoswich Detector

Method	$E_{Res}(\%)$
TFA	4.36
QVC	5.19
ORTEC 572	5.50

Table 4.2: Energy resolutions at 662keV for scintillation in the front of the phoswich.

result in one signal with a combination of properties from both scintillators. As a result, one expects a degradation in energy and timing measurements (this is discussed later in more detail).

Due to the high light output of the $\text{LaBr}_3(\text{Ce})$ and $\text{CsI}(\text{Na})$ scintillators (roughly 63,000 and 41,000 Ph/MeV respectively), the working voltage was reduced from the advised -1500 V to -1200 V. The light was collected in a Hamamatsu R7057 PMT fitted with a voltage divider constructed at the University of York. The voltage divider was tailored to a model that is sold with the Hamamatsu R7057 PMT, however alterations to the resistances could be performed if necessary should the resulting gain be highly non-linear. Several amplifiers were used due to a bipolar signal output when using the unipolar outlet on various amplifier modules. This is possibly due to saturation effects, or impedance mismatching which could be improved with the use of a Charge-Digital Converter (QDC). As none were available, a comparative study of ORTEC 472A, 572 modules, TFA, and Charge-Voltage Converter (QVC) was done to try and optimise the signal. The best results were obtained with a TFA (ORTEC 474) which gave a resolution of $\sim 4.4\%$ at 662 keV. However, a roughly unipolar signal was observed along with very poor linearity, which ruled this out as a practical solution.

A specially designed NDE Bartek 202 Module intended for EUROBALL was used, utilising the (QVC) output. The output changes the signal by amplifying it slightly, with no shaping. A ^{137}Cs source was used in addition to a ^{22}Na source for a full energy calibration, at various bias voltages ranging from -1200 V to -1500 V. It was found that with a working HV of -1200 V, a resolution of $5.2 \pm 0.8\%$ was attainable for the 662 keV photo-peak from a ^{137}Cs source.

4.4 Introduction to the Phoswich Detector

The QVC was seen to be rather linear, despite a reduction in resolution compared to the TFA. Therefore, the QVC was used with the ORTEC 472A amplifier to see if this could improve the resolution while maintaining the linearity. Due to the square signal structure in the QVC, the amplifier integrates the flat peak, resulting in a bipolar distribution with an extended middle section between both the peak and trough. All information held in the signal for this region is consequently lost in the integration process, thus ruling out this method.

The ORTEC modules were specifically designed for use with Germanium detectors and consequently, the shaping times are too long to integrate the $\text{LaBr}_3(\text{Ce})$ signal properly (decay shaping constants are 500 ns and 250 ns for ORTEC modules 572 and 472A respectively). Placing the source at the front of the detector gives a resolution of 5.5 % at 662 keV with the 472A module, and a similar resolution with the 572.

However, issues with using these modules include the differing values of input impedance. It was found that $Z_{in} = 500\Omega$ for the 572 amplifier, and as a result, the module was modifying the input pulse fall time substantially, thus contributing to the signal degradation output. A variable resistor (13Ω to $10\text{k}\Omega$) was added in parallel to counteract this problem (shunt termination). A similar situation arose with the 472A ORTEC amplifier, $Z_{in} = 1\text{k}\Omega$. The result of the energy resolution measurements with these modules are shown in table 4.2.

4.4.2 Energy Resolution and Position Sensitivity

A ^{137}Cs source was placed at the front end of the detector, resulting in an energy resolution due to interactions predominantly in the $\text{LaBr}_3(\text{Ce})$ crystal. By optimising the shaping time for each scintillator ($0.5\ \mu\text{s}$ and $6\ \mu\text{s}$ for $\text{LaBr}_3(\text{Ce})$ and $\text{CsI}(\text{Na})$), the resolution was found to be 5.5 % and 8.6 % respectively. Similarly, by placing the source near the back of the detector, more scattering occurs in the $\text{CsI}(\text{Na})$, and energy resolutions of 13.09 % and 11.69 % were obtained, as shown in figure 4.9.

4.4 Introduction to the Phoswich Detector

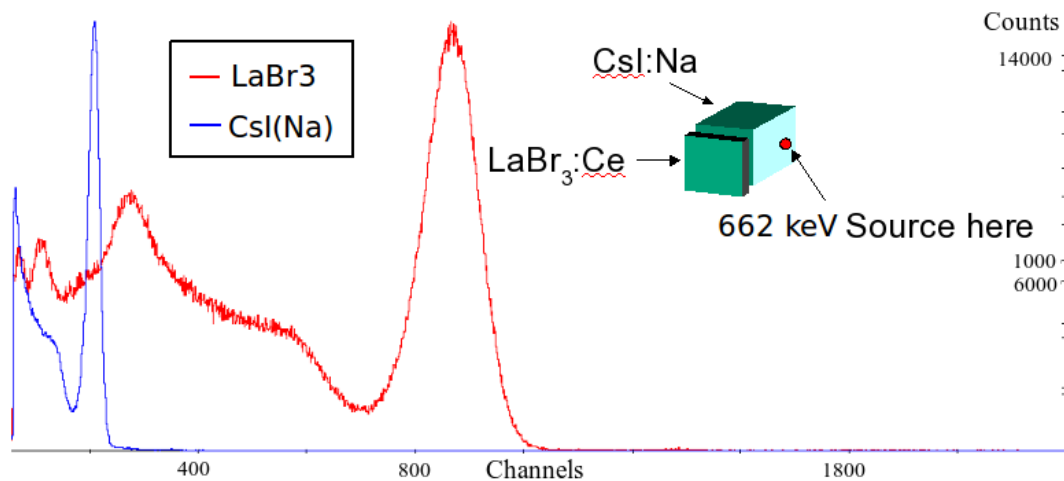


Figure 4.9: Position sensitivity of the detector when the source is placed at the back.

A problem may be encountered if a γ ray interacts with the middle of the detector close to where the crystals are joined, causing scintillation in both. This is still a problem that is being addressed via add-back algorithms. In cluster detectors, with a high number of detector segments (increased granularity), the add-back will strongly depend on the type of encapsulation offered by Saint-Gobain, and shielding of each detector. Shielding around the detectors will ensure that a large fraction of the γ -ray profile is kept in one detector. However, at higher energies this becomes harder to maintain, and thus add-back reconstruction will have to be used to stop any decrease in the detection efficiency.

Energy measurements were performed using the ORTEC 472A spectroscopy amplifier to determine resolution in the ~ 0.1 -2 MeV range. Since it was found that the TFA had previously been seen to give optimal energy resolution (4.2), it was compared with the ORTEC 472A amplifier, with the results presented in figure 4.10. Multiple sources were used for the calibration in order to find the nature of how the energy resolution changed with increasing energy. Sources such as ^{152}Eu , ^{137}Cs , ^{60}Co and ^{22}Na were used, along with activated peaks in $^{80,82}\text{Br}$ as calibration points.

The results were compared to similar studies at higher energies with 2" x 2" LaBr₃(Ce) scintillators [28], where a fit of $77.10(1.20)E^{-0.5}$ was obtained for en-

4.4 Introduction to the Phoswich Detector

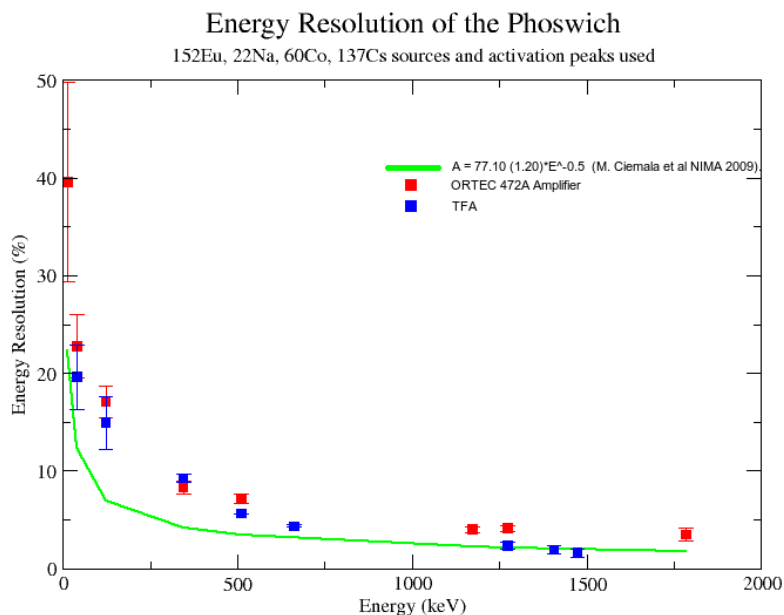


Figure 4.10: Energy measurements with fitted parameter from Ciemala et al[28].

ergies between 2-20 MeV. However, this fit does not give a good representation of the phoswich data due to signal degradation, principally from the CsI(Na) crystal. Since the resolution is typically higher for this scintillator, the combined signal is worse overall. Large errors were found when calibrating energies less than 100 keV, due to large amounts of background noise. The best results are given by a logarithmic fit, especially at lower energies. However, with a larger detector, a better fit could be achieved.

In addition to this, the position of the source was found to change the energy resolution as well, due to different angles of incidence resulting in scattering and scintillation in both the LaBr₃(Ce) and CsI(Na) crystals. A simple test of moving several sources to different angles and distances was conducted to review this effect. ¹⁵²Eu, ¹³⁷Cs and ²²Na sources were placed at distances of 0, 5, and 10 cm from the detector, at angles ranging from 0° to 135°. Several spectra were then taken to assess where likely points of scattering occurred and what effects this had on the resulting energy resolution, the results of which are presented in

figure 4.11.

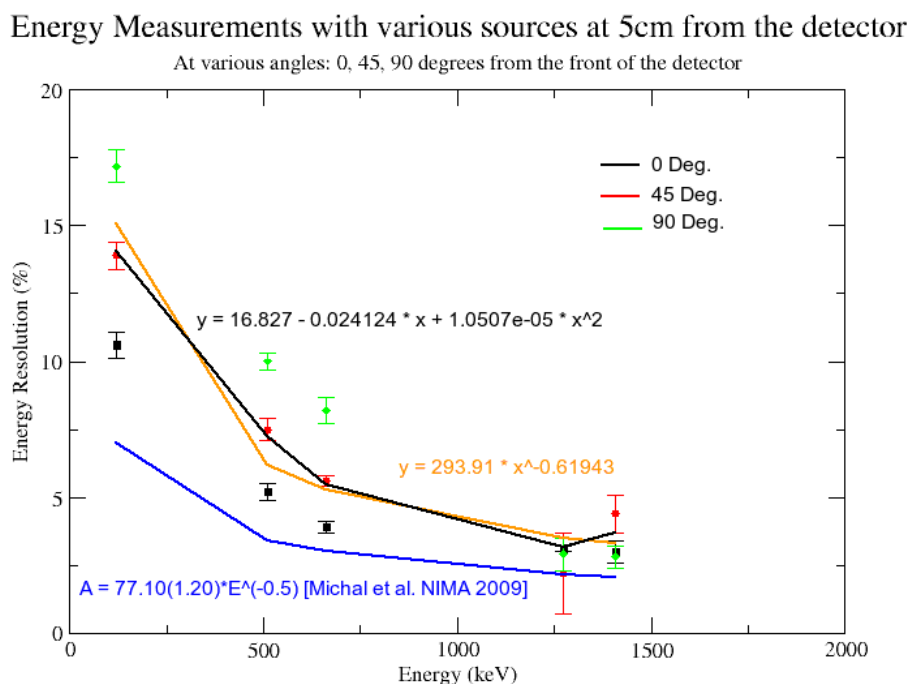


Figure 4.11: Energy measurements with numerous sources at 5 cm at various angles.

These energy measurements were performed with the phoswich detector operating at -1200V, with its signal amplified in a standard ORTEC 572 amplifier. A low gain, and a shaping time of 500 ns were used in all the measurements. The results presented in figure 4.11 show that at angles from 0° to 90° , good resolutions with standard calibration sources were recorded with this set-up. However at larger angles, scintillation occurs predominately within the CsI(Na) segment of the detector, resulting in very poor energy resolutions. In instances such as these, the shaping time will have to be changed in order to salvage any information. At angles of 135° or greater, the resolution is so poor that no decent results were recorded. Scattering at large angles such as these also results in deposition of energy in both scintillators, increasing the risk of observing double peaks.

4.5 Neutron Response in the Phoswich

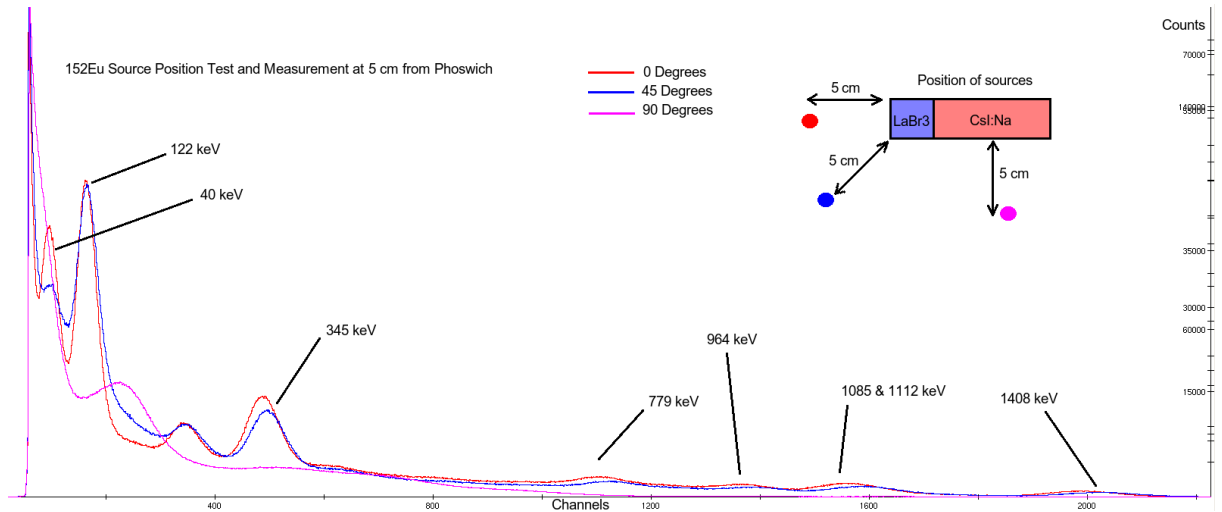


Figure 4.12: Spectrum showing changes in a ^{152}Eu source at 5 cm due to varying angles.

4.5 Neutron Response in the Phoswich

4.5.1 Pulse Shape Discrimination

Pulse shape analysis was carried out to see if n- γ discrimination was possible. Generally, organic scintillators provide such discrimination due to delayed re-emission of energy; however inorganic alkali halide crystals, such as $\text{LaBr}_3(\text{Ce})$ and $\text{CsI}(\text{Na})$ do not. Previous experiments performed with a 1.5" x 1.5" $\text{LaBr}_3(\text{Ce})$ detector show that the discrimination, was too small to be useful in experimental conditions.

In the phoswich detector, a similar result is observed. It was possible to extract information from the fast and slow components of the pulse by gating on 3 parts of the pulse, in a similar manner to the method described in section 4.3. The first gate in this discrimination methods is placed over the rise time of the pulse, from 50% of the pulse height to a point just before the minimum. The minimum itself, the 2nd gate, is excluded. The final gate is responsible for extracting information on the slower component of the pulse, and is set from 50% of the decay time until the end of the pulse. These sets of data were then acquired and fitted twice, each showing slight differences due to discrepancies in

4.5 Neutron Response in the Phoswich

the definition of the regions used in the gating process. The results of these gates are presented in figure 4.13, where "in-beam neutron data" represents recorded thermal and fast neutrons in coincidence with γ -ray transitions from ^{12}C and activated states within the scintillator. The anomaly in the top-right hand part of the spectrum is due to gain issues, resulting in saturation effects.

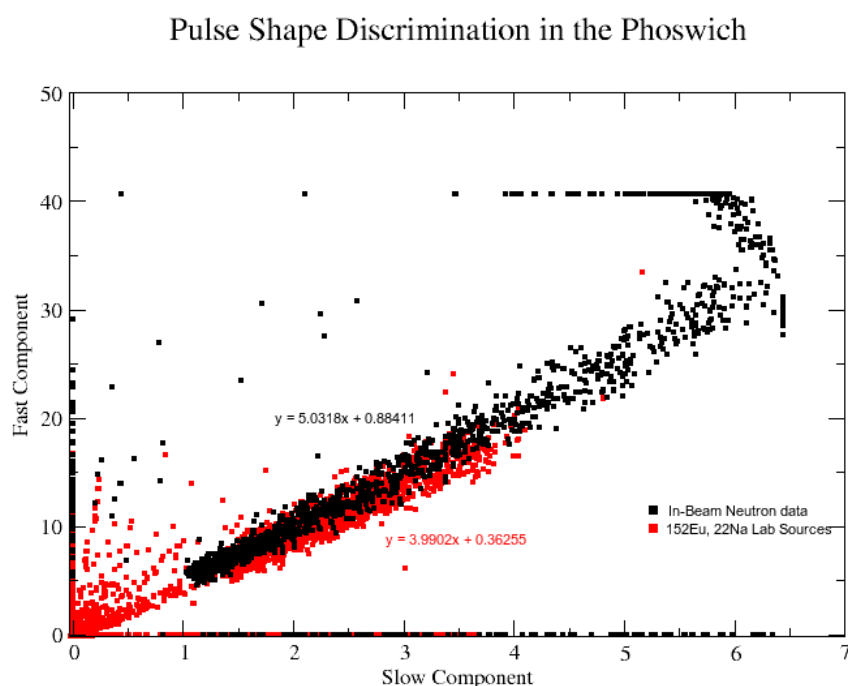


Figure 4.13: Phoswich pulse shape discrimination over a 2 MeV range

4.5.2 Neutron Activation

It is assumed that there is little n - γ discrimination, if any. However, when exposed to a neutron flux, most scintillators will respond at some level. Fast neutrons can be present which will produce prompt signals due to inelastic scattering within the scintillator.

The phoswich was placed 20 cm from the closed 10.5 GBq $^{241}\text{Am}/^9\text{Be}$ source, having found pile-up a persistent problem at shorter distances. A bias of -1200 V was used to power the detector, where the amplification was performed with an

ORTEC 472A shaping amplifier. The neutron response of the detector was then investigated, where activation of the detector material was observed, when placed in a lead castle. This activation is seen from the activated isotopes present in $\text{LaBr}_3(\text{Ce})$, where multiple 30 minute spectra were recorded over an 80 hour period in a shielded environment, revealing neutron activation. A few were selected at low energies and overlaid in figure 4.14.

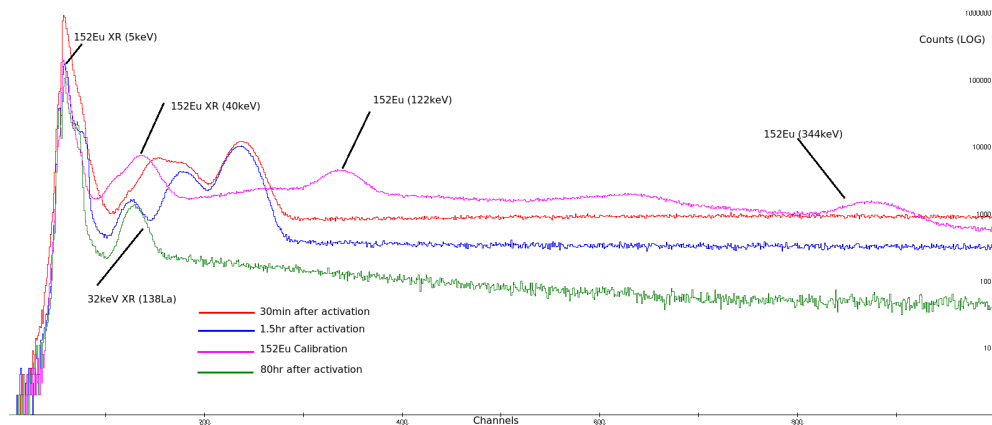


Figure 4.14: Calibration spectra of the neutron activation in the phoswich.

4.6 Timing

4.6.1 Introduction and Set-up

Coincidence timing tests of the phoswich detector were investigated by irradiating a 1" Bicron BaF_2 detector and both scintillators in the phoswich detector separately (1"x1"x2" $\text{LaBr}_3(\text{Ce})$ and 1"x1"x6" $\text{CsI}(\text{Na})$). BaF_2 has two components, a fast component with a decay time of approximately 600 ps and a slow component of 630 ns[38]. All the timing measurements will be with respect to the fast component of the BaF_2 detector. The phoswich detector was coupled to a fast Hamamatsu R7057 PMT, operated at -1200 V with 511 keV positron annihilation γ -ray pairs emitted from the ^{22}Na source. The BaF_2 detector formed the "start" channel in this timing circuit, while the phoswich detector formed the "stop" channel. The signals from both detectors were processed by an ORTEC-934 Quad Constant Fraction Discriminator (CFD). The signals were then delayed

in a ORTEC-416A Gate and Delay Generator, via a LeCroy-428F Fan in/out. These signals then proceeded into a ORTEC-467 Time to Pulse Height Converter (TAC). Data Acquisition (DAQ) was performed with an ORTEC Multi-Channel Analyser (MCA) unit, with pulses saved on a fast 500 MHz LeCroy Waveform oscilloscope at a sampling rate of 5 GS/s for rise time analysis. Data was accumulated using a LeCroy coincidence timing unit and ORTEC-996 Time Counter. Both channels were triggered by the coincidence unit externally to allow for better statistics.

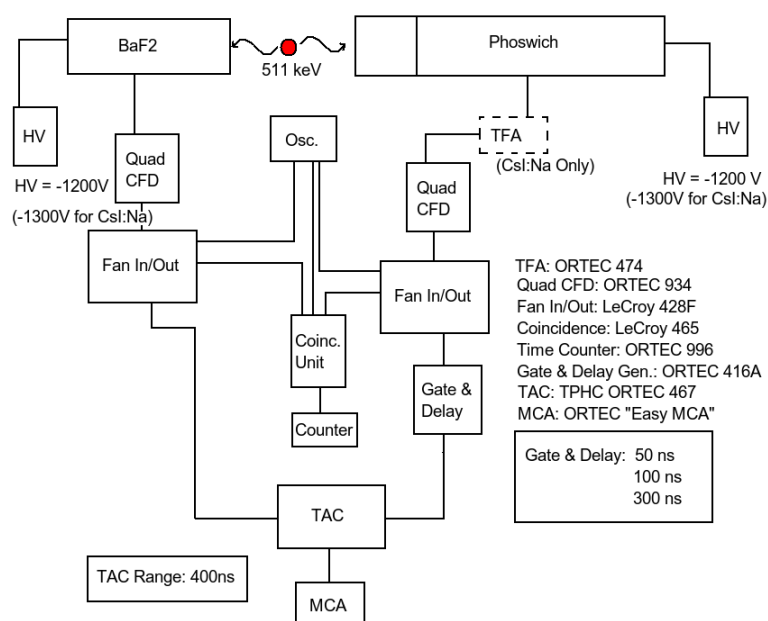


Figure 4.15: Set-up for phoswich timing coincidence measurements.

4.6.2 Timing Measurement Results and Analysis

A series of delays were used between the final BaF₂ and LaBr₃(Ce) signals, ranging from 50 to 500 ns. Two sets of data were collected; one set determining the timing information from the front end of the detector, and another set from the side of the detector, where scintillation is primarily within the CsI(Na) crystal. It was seen that the count rate of coincidences decreases substantially as the BaF₂ detector is moved along the side of the phoswich detector due to the bias voltage

being too low to record CsI(Na) pulses. Using delays of 100 and 300 ns within a TAC range of 400 ns, it was found that $45.0 \pm .01$ ps/ch was possible with the front end of the detector, and 167 ± 4 ps/ch was attainable when scintillation occurs primarily in the back of the detector. A timing resolution for the front end of the detector of 696 ± 13 ps was recorded for a delay of 100 ns¹. Similarly, a timing resolution of 24 ± 1 ns was obtained for the CsI(Na) scintillator in the phoswich detector, by placing the BaF₂ detector near the back of the detector with a TAC range of 2 ns (figure 4.17).

Timing resolutions of the electronics used with both detectors, were also obtained with a pulser. Delays of 50 and 100 ns were used to determine the calibration and resulting resolution, shown in figure 4.16. By keeping the experimental set-up for both cases where the ²²Na source is placed in close proximity to the front and back segments of the detector, resolutions of 125 ± 1 ps and 1.4 ± 0.1 ns were recorded for the front and back respectively. Subtracting these results from the actual measurements, was performed to achieve intrinsic timing resolutions for both scintillators. These results are displayed in table 4.3, noting that the initial and intrinsic resolution for the electronics are the same.

The initial and intrinsic timing resolutions for the case where gammas predominately deposit their energy in the LaBr₃(Ce) scintillator, was observed to be good. Although these resolutions are not as good as previous findings (~ 260 ps[3] for a 1"x1"x1" LaBr₃(5%:Ce) scintillator), the recently recorded values from this study are still fast enough to be used effectively in γ -ray spectroscopy. One should also not that different concentrations of the cerium dopant has important repercussions on the timing, where a FWHM timing resolution of 450 ns can be achieved with LaBr₃(0.2%:Ce) and 320 ps with LaBr₃(1.3%:Ce)[3].

Optimisation of this result is possible by using digitised electronics and hardware with a VME interface, similar to those found in a study by S.Brambilla et al.[39]. The signal from the CsI(Na) segment of the detector appears to contribute significantly to the timing response, with an intrinsic timing resolution of 24 ± 1 ns.

¹Strictly speaking, this is the self-timing of the BaF₂ scintillator, as the LaBr₃(Ce) decay component is faster than 600 ps.

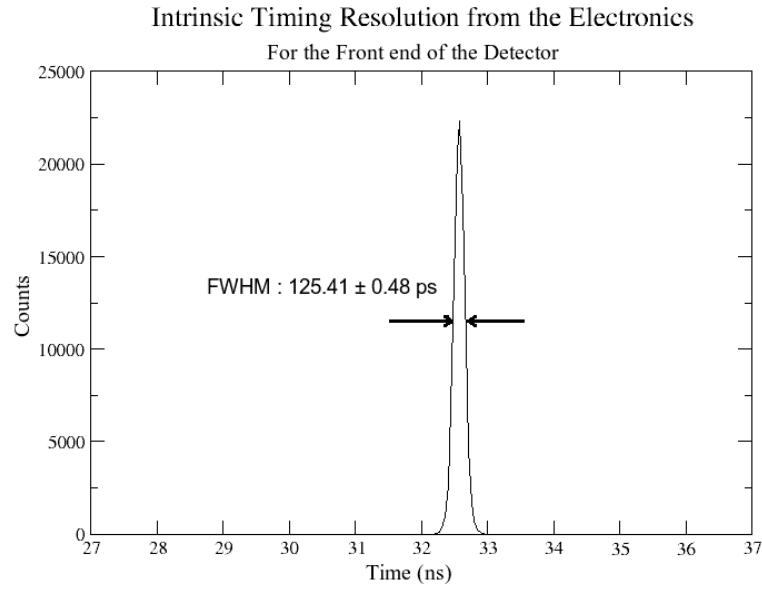


Figure 4.16: Intrinsic timing resolution of the electronics.

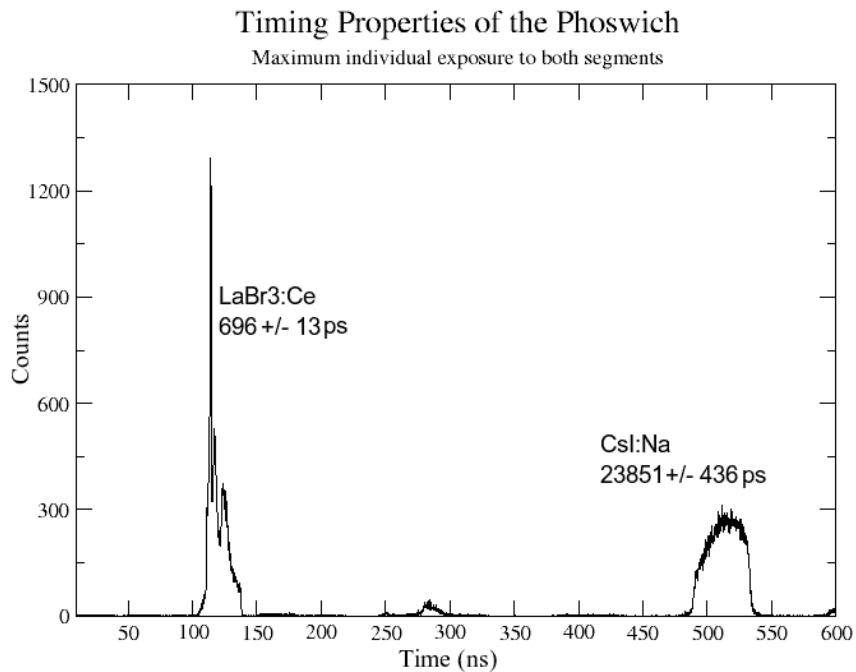


Figure 4.17: Timing responses for both scintillators with 400 ns delay (approx. 200ns internal)

Segment	Initial Res.	Timing(ps)/ch	Intrinsic Res.	Delay(ns)
LaBr ₃ (Ce)	696 ± 13	45.0 ± 0.1	685 ± 13	100
Front Elec.	125 ± 1	45.0 ± 0.1	125 ± 1	100
CsI(Na)	23851 ± 434	167 ± 4	23810 ± 426	400
Back Elec.	1436 ± 110	167 ± 4	1436 ± 110	400

Table 4.3: The initial and intrinsic timing resolutions of the scintillators and electronics. All measurements in ps unless otherwise stated.

4.6.3 Improvement on the Timing Measurements

An attempt to improve the previous set-up was investigated by adding a delay line amplifier (ORTEC 427A) and Timing SCA in each channel of the timing loop, the details of which can be found in a paper by T. J. Paulus[40]. By strobing the fast coincidence between the two outputs of these channels, a cleaner TAC output can be achieved. However, only a marginal improvement of around 40 ps, with an initial resolution of 665 ± 2 ps, was recorded. This small improvement is likely due to the fast component of the BaF₂ detector being only 600 ps. This can be improved by using a detector with comparable timing, another smaller LaBr₃(Ce), for example.

The electronics of the BaF₂ detector were also investigated to see if the amount of jitter and amplitude walk can be reduced. The BaF₂ signal was fed through a TFA, CFD, FIFO and Gate and Delay Generator circuit into the TAC with a range of 50 ns. The bias voltage was reduced to around $-1250V \pm 20$ V, and the source placed roughly an inch from the detector to reduce pile-up. Once this optimum set-up was achieved, initial measurements triggering on just the BaF₂ signal were performed. This resulted in a timing resolution of 89 ± 3 ps, with 6.4 ± 0.3 ps/ch. However, this excellent timing resolution could not be replicated with the phoswich detector due to a poor signal, where despite trying different values of bias and gain, the shaping with NIM electronics was still found to be extremely difficult. A considerable amount of walk also made setting the thresholds difficult, and thus constrained the timing resolution to ~ 660 ps.

4.7 Pile-Up

The principal purpose of investigating pile-up within the detector, was to increase our understanding of how the count rate of the phoswich detector varied at different biases. In doing this, a threshold for the counting rate at high γ -ray fluxes could thus be determined. The counting rate is seen to increase with the number of γ rays. This trend continues until a threshold is reached where the counting rate suddenly drops, resulting in increasing dead time, due to a phenomenon called "pile-up".

Pile-up, or more specifically, pulse pile-up, happens when pulses arrive into the detector at shorter time intervals relative to one another, than the pulse resolution time of the system. When a pulse occurs within the same time as another, their respective amplitudes can not be discriminated clearly, superimposing both pulse heights together. This is known as first-order or peak pile up, where recorded events are twice the expected energy of the incoming γ -ray energies. High order pile-ups can also be produced at 3 or 4 times the expected incident energy. If the two pulses occur with a larger difference in time, the MCA can analyse both pulses, but may record the amplitudes incorrectly. This is known as tail pile-up, where resulting counts are distributed in the wrong energy channels, resulting in a pile-up spectrum. Most spectrometers have a built in pile-up rejector that minimises these effects by altering the pulse resolution time, where below a minimum resolution time, τ_{min} , pulse pile-up can not be avoided. However, pulses that arrive one after another between a minimum time τ_{min} and time τ can be detected and subsequently rejected. This minimum resolution time for pulse pile-up depends heavily on front-end electronics, the type of scintillator or detector, and how the pulse pile-up rejector is implemented.

In counting applications, a procedure for finding the optimum working voltage is to make a "plateau" measurement. A plateau measurement is the measured count rate as a function of the applied bias voltage. Starting at a low voltage, just above the threshold for the PM (this depends on the manufacturer), only a minute number of counts are observed. As the HV supply is gradually increased, the number of counts rises sharply until it starts to flatten out at certain voltages. Above this plateau region, the number of counts increases sharply with an increase

4.8 Pile-Up Measurement Results and Analysis

in bias where the onset of after-pulses and discharges occurs within the PMT. The result is a plateau region where the count rate is least sensitive to the applied voltage. Applying the voltage in a fixed position within the centre of this plateau regions ensures that effects from variations in the gain due to drifts within the PM are kept to an absolute minimum. The plateau curve can be derived from the integration of the counting curve.

$$I(p_0) = \int_{p_0} Sp(x) dx \quad (4.3)$$

Where p_0 is the threshold or set lower limit, and $Sp(x)$ is the standard pulse height spectrum[41].

The HV plateau is sensitive to many parameters that can vary depending on what material, geometry, and PMT are used. Varying the threshold of the discriminator (CFD for example) will shift the curve, and thus these levels must be kept the same. The relationship between the gain and voltage can also change the appearance of the plateau curve when different PMT models are used, and thus care must be taken in selecting the PMTs. The response of the incident radiation on the detector/counter (dependent on the type of experiment), affects the performance of the HV curve as different sources and types of radiation can result in one counter having various plateaux. For these tests, β sources were consistently used throughout the experiment.

4.8 Pile-Up Measurement Results and Analysis

The performance of the phoswich detector was tested. CsI(Na) scintillators typically have a decay time of roughly 630 ns, whereas approximately 15 ns is a typical decay time for LaBr₃(5%:Ce) scintillators. The difference between these two decay times plays a crucial role at high γ -ray fluxes, where the count rate of gamma photons is inversely related to the characteristic time of a scintillation pulse. As a result, LaBr₃(Ce) scintillators are far more likely to be successfully used at high energy gamma fluxes.

4.8 Pile-Up Measurement Results and Analysis

CFD Setting	TFA Settings			PMT Setting
LLD, mV	T_{int}	T_{diff}	Gain	Plateau HV, V
50	OUT	OUT	x1	-1730
50	20	OUT	x4	-1700
50	20	OUT	x10	-1550
150	20	OUT	x10	-1750
150	20	OUT	x20	-1700

Table 4.4: Parameters used in the experimental set-ups.

The experimental set-up uses the phoswich detector coupled to a Hamamatsu R7057 PMT with coupling grease. The PMT pulse is altered in an ORTECTM Time Filtering Amplifier (TFA 474). A ORTECTM 473A CFD was used to eliminate low-level PMT noise. Counting of the pulses was performed on an ORTEC 996 CCNIM Timer and Counter. The Detector was irradiated with two ⁵⁷Co sources.

Several measurements were performed to determine the HV plateau curves, which involved testing various set-up methods and distances. The Lower Level Discriminator (LLD) levels of the CFD and TFA integration, and differentiation constants used in the experiment are shown in table 4.4 ¹. The integration and differentiation times are with respect to interaction with the front face of the detector. As a result, a low constant was chosen as it is anticipated that most of the scintillation will occur only in the LaBr₃(Ce) crystal, due to the low energy of the source. It is also widely expected that due to the saturation seen with LaBr₃(Ce) for this PMT, lower voltages were used resulting in a lower likelihood of witnessing CsI(Na) pulses.

Two ⁵⁷Co sources were used; a hot 4.2 mCi source, and a weaker 3.9 μ Ci source. The intensity of the incident gamma radiation onto the detector was controlled by changing the distance from the source position to the crystals.

Plateau curves are shown in figure 4.18 for the weak ⁵⁷Co source. The high voltages previously mentioned, were selected at the corresponding mid-points on

¹The -1550 Plateau HV is low due to the increased distance from the source and low gain compared to the other measurements.

4.8 Pile-Up Measurement Results and Analysis

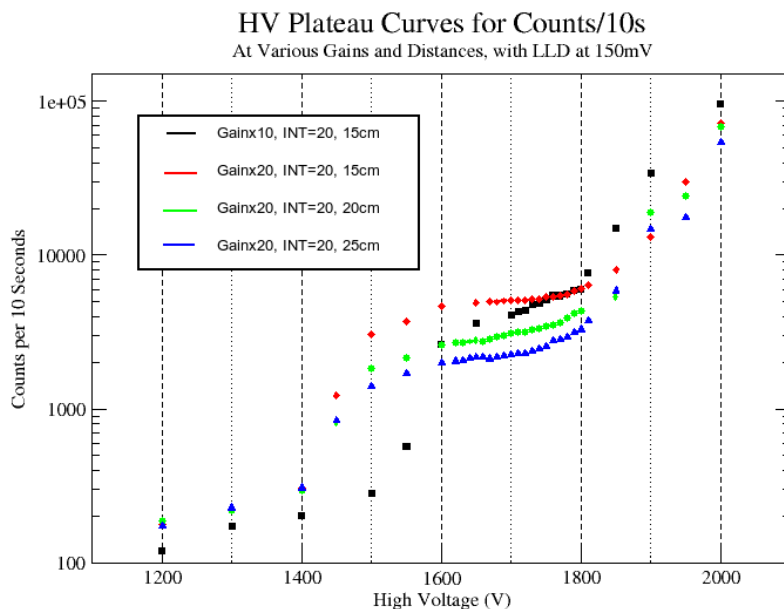


Figure 4.18: Another ^{57}Co HV plateau measurement with LLD=150 mV.

the plateaus. These were chosen as the operating voltages for the count rate experiments, to be consistent with the sampling region above the LLD threshold.

Results were generated based on ratios between "Measured" and "True" counts. Count rates from the weaker $3.9 \mu\text{Ci}$ ^{57}Co source were measured with the source at the same distances as in the measured count rate test with the hotter source. The counting rate with this weak source was far below the saturation threshold for the detector, given the superior timing properties of the $\text{LaBr}_3(\text{Ce})$ scintillator, and were taken to be the "true" count rate. As the positioning of the weak and hot sources were the same, the count rate should only change by a constant factor for each position. This experimental procedure is similar to that described in a technical study by Saint-Gobain [42]. In that study, the constant factor by which the "true" count rates differed when the hot and weak sources were placed at various positions, was obtained by moving the hotter source at positions further away from the detector, so that these "measured" count rates were essentially the same as "true" count rates. For this experiment, this was

4.9 Summary of the Tests on the Phoswich and LaBr₃(Ce) Detectors

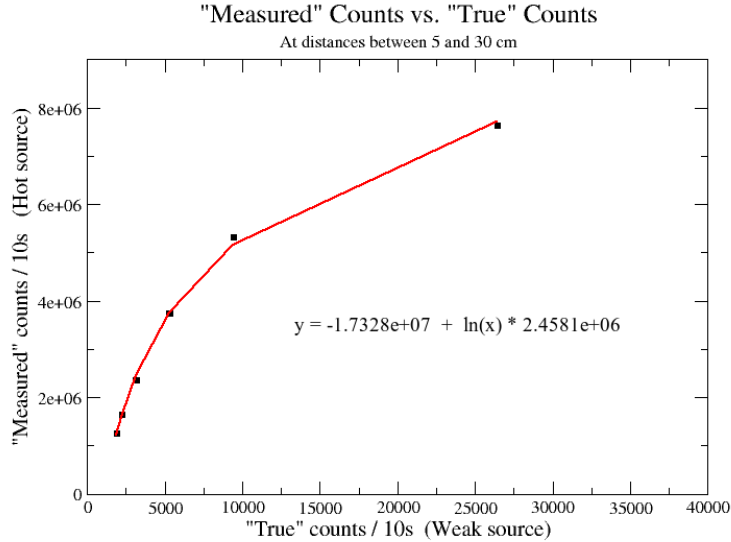


Figure 4.19: ⁵⁷Co source as measured by the phoswich detector with a low bias.

hard to replicate due to a difference in 3 orders of magnitude between both ⁵⁷Co sources. Unfortunately, there was no source that had an intensity between the two. The relationship between the measured and true counts of the ⁵⁷Co sources as measured by the phoswich detector, is shown in figures 4.19 and 4.20. A low gain and low bias setting (-1550 V) were used in figure 4.19, where the relationship with increasing gain, achieved by setting the LLD threshold to 150 mV, is shown in figure 4.20¹.

4.9 Summary of the Tests on the Phoswich and LaBr₃(Ce) Detectors

A series of tests were conducted to determine the response of several parameters of both a 1.5" cylindrical LaBr₃(Ce) scintillator and a phoswich detector. The performance of the 1.5" LaBr₃(Ce) scintillator was very good, despite problems initially with saturation due to the high photon yield, and subsequent poor gain

¹The fit for this instance is represented by a 4th order polynomial.

4.9 Summary of the Tests on the Phoswich and LaBr₃(Ce) Detectors

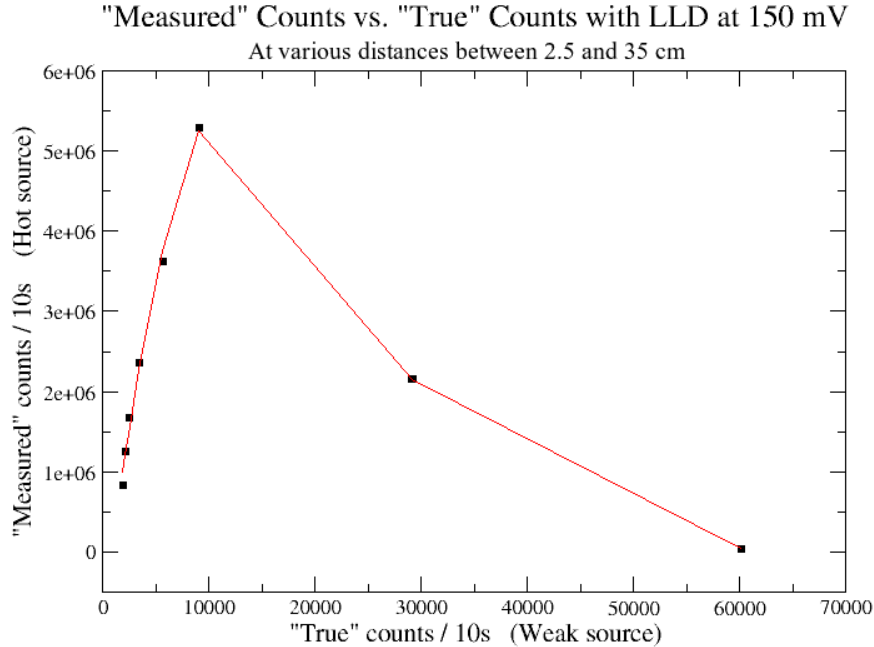


Figure 4.20: ⁵⁷Co source as measured with a high LLD threshold.

matching which resulted in non-linear spectra. However, once this was corrected, an energy resolution of $\sim 2.6 \pm 0.2$ % was observed as the value for the FWHM of the 662 keV γ -ray from ¹³⁷Cs. Subsequent exposure to the AmBe neutron source showed excitation of numerous isotopes due to large thermal neutron cross-sections in both Lanthanum and Bromine. This was identified and presented, with (n, γ) discrimination not being possible using PSA methods.

Similar results were found for the phoswich detector, although a degradation of the signal was seen and found to contribute to worse-than-expected timing and energy resolutions. A FWHM of ~ 4 % was recorded when the phoswich was placed near a ¹³⁷Cs source. The position of the sources was also investigated as different energies corresponded to scintillation in not one component of the detector, but in both. This meant the response of the LaBr₃(Ce) and CsI(Na) were superimposed in one spectrum. These findings were commented upon, noting that it was very important to take care when applying the bias and gain for the LaBr₃(Ce) as an optimised set-up for this scintillator might result in too little gain in the CsI(Na) component, resulting in a very low count rate from the

4.9 Summary of the Tests on the Phoswich and LaBr₃(Ce) Detectors

part of the detector. The timing resolution for the phoswich was found to be in the region of 600 ps when used in a start-stop set-up with a BaF₂ detector. Improvement of this value was limited by the fast timing component of the BaF₂ scintillator, and the set-up was poorly time matched. Pile-up measurements with the phoswich gave a rough estimate of the threshold at which the rate of counts become saturated and pile-up becomes a significant problem, found to be in the region of ~ 780 kHz.

It appeared at first glance that the phoswich method was not as great as had been expected. As this method was only one of several proposed by the collaboration, alternative tests using silicon large area avalanche photo-diodes were also investigated.

Chapter 5

Development of Large Area Avalanche Photo-Diodes for Light Collection

5.1 Introduction to Silicon Detectors

5.1.1 Theory

Semiconductor detectors are crystalline materials that have an energy band structure due to the arrangement of the outer shells of its atoms. In this band structure are three main regions; a conduction band which contains free electrons, a valence band which contain "holes", and an energy band gap between these two regions of ~ 1 eV. However, amongst these energy bands exist many discrete closely spaced levels, with levels being forbidden in the energy gap region. The existence of this region, lies in the overlapping nature of electron wave-functions due to the occupation of electrons within the lattice. The Pauli exclusion principle forbids more than one electron in the same state. Consequently, there are discrete minutely spaced levels due to degeneracy, in the outer shell of the atom. As the electron can carry two values of spin, there are potentially as many levels in a crystal lattice as there are electrons in the same state.

The highest energy band is the conduction band, where the electrons are disassociated from their atoms, free to move through the region, and entire crystal.

5.1 Introduction to Silicon Detectors

The electrons in the valence band are more tightly bound to one another, and remain with their parent atoms in the lattice structure.

In conductors (ie. metal), the energy gap between the valence and conduction bands is very small. However, in insulators the gap is large (~ 6 eV), where a high temperature is needed to excite the electrons from the valence band to the conduction band. A current will not be generated in an insulator as there is no movement of the electrons in the crystal due to the application of an external electric field. In conductors, there is an absence of this gap, and thus only a very minimal amount of thermal energy is needed to excite electrons up to the conduction band where they are free to move around the crystal. A current is generated with the application of an electric field. In the case of a semiconductor, the size of the energy gap lies between the two previous cases, where only a few electrons are excited across the gap into the conduction band by thermal energy, resulting in a small current when an electric field is applied. However, if the semiconductor is cooled, a decrease in the conductivity will arise as large number of electrons will fall into the valence band.

5.1.1.1 Charge Carriers

At $t > 0$ K, thermal energy is shared by the electrons in the crystal. A valence electron can cross the energy band gap to the conduction band if it has a sufficient amount of thermal energy to do so, by disassociating itself from its original covalent bond and drift through the material. This excitation process not only creates a free electron in the conduction band, but leaves a "hole" in the valence band, creating an electron-hole pair. When an electric field is applied to the material. The positively charged hole will move in the opposite direction to that of the negatively charged electron in the conduction band. The motion of these two opposing charges through the medium contributes to the conductivity of the crystal. The probability of thermal excitation of an electron across the band gap is dependent on the band gap energy, and temperature of the system.

After the formation of an electron-hole pair, both will randomly move through the medium due to the thermal energy that leads to diffusion away from the point of where they were created. This leads to a broadening distribution of the charges

as a function of time. A Gaussian function approximates the cross-section of this distribution as:

$$\sigma = \sqrt{2Dt} \tag{5.1}$$

where in Leo[43], the parameter D is defined as the diffusion coefficient over a time, t . This diffusion coefficient can be written as:

$$D = \mu \frac{kT}{e} \tag{5.2}$$

where μ is the mobility charge carrier, k is the Boltzmann constant, T is the absolute temperature (K) and e is the charge[44].

5.1.2 Silicon Photomultipliers

Silicon Photomultipliers (SiPMs) are devices sensitive to single photon interactions, where each microcell on the detector consists of avalanche photo diodes (APD) on a silicon substrate¹. This device allows the detection of single photon events (single photon counting applications), where the resulting signal is sequentially connected to silicon APDs. A dynamic range of signals can be generated due to the microcells coupled in parallel; from a single photon to several thousand at any given time. Every microcell contains a pn diode with a specifically designed avalanche region, which generates for low noise applications of single photo-electrons, a signal of $\sim 10^6$ electrons. The diode is biased above the breakdown voltage V_{Br} , where no current flows until a photon initiates an avalanche. Coincidentally, one of the outstanding features of the SiPM is the ability to measure a well resolved photo-electron spectrum, which is generally unachievable with a conventional PMT, due to the variability in the gain and excess noise. In general, the dynamic range is limited by the number of microcells, where each microcell can detect a single photon with a dead time of ~ 100 ns.

¹A quenching resistor (series resistor) is used to quench the avalanche.

5.1 Introduction to Silicon Detectors

Due to the discharge and recovery that occurs within this 100 ns interval, each microcell is limited to a counting rate of ~ 10 MHz[45].

Another outstanding feature of SiPMs is the linear relationship between the gain and applied bias voltage:

$$Gain = \frac{C(V_o - V_{Br})}{q} \quad (5.3)$$

Where q is the charge of the electron, C is the capacitance of the cell, and V_{Br} and V_o are the breakdown and bias voltages respectively. The photon detection efficiency or PDE, also increases with "over" bias voltage.

The output increases with over bias for two reasons:

- Increased gain leads to a larger amount of charge amplification
- PDE means that the number of photons detected increases as;

$$PDE = \eta \cdot \varepsilon \cdot F \quad (5.4)$$

where η is the quantum efficiency, ε is the probability of initiating an avalanche, and F is the "fill factor"¹.

5.1.2.1 Signal to Noise Ratios and Dark Current

Signal-to-noise is a measure used to quantify how much a signal has been corrupted by noise, where a ratio of higher than 1:1 indicates more signal than noise. Any undesired fluctuation is likely to compromise on the efficiency of the detector system, especially when establishing thresholds for analysis with NIM equipment.

¹The fill factor can be likened to the geometric efficiency, and is defined as the ratio of the sensitive to total area of a pixel.

5.1 Introduction to Silicon Detectors

Sources of noise near the beginning of the signal chain, undergo the same amount of amplification as the signal itself, unlike any noise afterwards, which is substantially lower. Noise for silicon PIN diodes, and PMTs generally follow the form[45]:

$$\frac{S}{N} = \frac{I_S}{\sqrt{2qFBG[I_S + (2I_D + I_B)]}} \quad (5.5)$$

for the S/N for a PMT, and;

$$\frac{S}{N} = \frac{I_S}{\sqrt{2qB[I_S + (2I_D + I_B)]}} \quad (5.6)$$

for the S/N of a PIN diode. Where I_S is defined as:

$$I_S = \frac{P \cdot PDE \cdot G \cdot q}{h\nu} \quad (5.7)$$

I_S , I_D and I_B are defined as the anode signal, dark, and background currents respectively, q is the electric charge, B is the bandwidth, F is the excess noise factor, G is the gain and P is the incident optical power.

At low signal levels the S/N ratio is dominated by noise generated by the dark current, and sets a limit for the sensitivity of the device. Dark current occurs when dark counts (due to thermally generated electrons in the active region), cause Geiger avalanches¹, the primary source of noise in SiPM detectors. This increases proportionally to the applied bias, where a trade-off between the bias voltage and amount of dark current results in an optimum bias point. A PDE at 2 V above the breakdown voltage was observed to be $\sim 9.5\%$, or ~ 460 nm.

¹Generated at a bias above the breakdown voltage in "Geiger mode", the avalanche is triggered by either a single photon or thermally generated carrier, that can only be quenched by reducing the bias to below the breakdown threshold.

5.1 Introduction to Silicon Detectors

Similarly, a PDE of $\sim 20\%$ can be obtained 4 V above the breakdown voltage of ~ 28 V, corresponding to a peak wavelength of ~ 470 nm. Therefore, one can assume that the SPM response is proportional to the number of microcells undergoing the breakdown in Geiger mode. Saturation occurs when 1000 photons are incident on the SiPM array over the microcell dead time (100 ns), or when the number of photons detected becomes comparable to the total number of microcells, giving a linear range of $\sim 10^2 - 10^3$. The theoretical single photon response (SPR) from the SiPM microcells is approximated by the function:

$$SPR = \frac{t^2 e^{-t/\tau}}{2\tau^2(3)} \quad (5.8)$$

where τ is the constant that effects the rise, recovery, and dead times of the outgoing pulse. The function is derived from simulations and does not account for Poisson statistics that occur experimentally, and therefore assumes a PDE of 100%.

The optimum bias voltage can be found by measuring the S/N ratio as a function of the bias voltage. At -20°C , the optimum bias voltage was found to be ~ 29.25 V, with an over bias of ~ 2.5 V. This corresponds to a S/N ratio of $\sim 85-90$ at the peak emission wavelength of the detector; 520 nm[45]. There are very small variances in the breakdown voltage with temperature, which can be neglected and treated as linear, and follows the relationship[45]:

$$V_{Br} = 0.023T + 27.2 \quad (5.9)$$

The bias voltage (~ 30 V) needed to run the device is considerably lower than standard PM's, making this detector system an attractive alternative. The small versatile size of this detector allows for excellent efficiency in γ -ray calorimeters, where these detectors also exhibit an independence to magnetic fields up to ~ 2 T. They also are seen to have a very stable and linear gain dependence with the bias (unlike conventional PMT's which exhibit a power law dependence).

5.2 Experiment Methods and Results

The solid state 4x4 array of 3.2 mm x 3.2 mm pixels, were operated at a low bias voltage of 30 V. As the pixel spacing is 200 μm , with 100 μm dead space over the outside of the array, the SiPM becomes an attractive alternative to PMT's.

SensL offers a pre-amplifier board built on the back of the main mother board that has a single SMA connector and provides a direct pre-amplified output. The amplifier is connected to the SMA output via a 50 Ω line matching resistor. The gain of the impedance amplifier is quoted as being $G = 470\text{V/A}$ [45]. A readout board supplies the power, which can be acquired from a wall mounted socket or power unit. Power can also be provided via several outlets on the board by separate +5 V, -5 V, and ~ 28 V (bias supply) DC power supplies. The power board generates all needed bias' from a single +5 V input. The power module distributes the power from a plug at the bottom of the multi-channel board, which is used to read out the signals. The bias voltage can also be reset by tweaking the potentiometer found on the board.

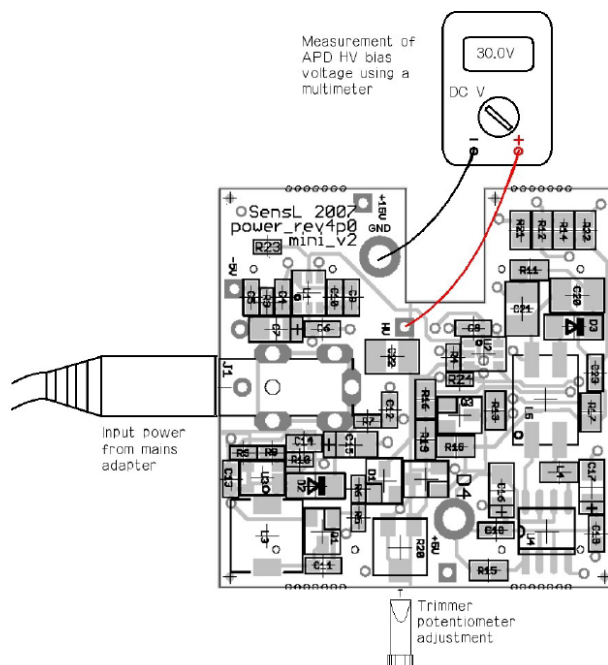


Figure 5.1: The supply board provided by SensL[45].

5.2.1 Pulser and Gamma-Ray Response

One of the preliminary tests performed with the SiPM, involved shining several LEDs into the detector, each having peak emission wavelengths in different regions of the electromagnetic spectrum. These were used with a pulse generator to test the response SiPM array in a light tight box, where it was expected that the green LED should generate the largest signal. However, there was a large amount of noise (~ 100 mV) associated with this LED due to the match in the peak wavelength emission of the LED and peak sensitivity in the wavelength of the detector.

Rise Time (ns)	Total Signal Time (ns)	Wavelength (nm)	Colour
90	300	635	High Red
40	290	600	Red
45	210	585	Yellow
60	220	565	Green
150	320	470	Blue

Table 5.1: Table showing the integrated response of the SiPM with various LEDs

A 50Ω resistor was used to try and reduce the noise, with the set-up placed in a sealed box in an attempt to achieve light-tight conditions. The repetition time on the pulser was kept at $10 \mu\text{s}$, with pulses having a duration of ~ 100 ns each. Appropriate BNC cable lengths were used to create a 30-40 ns delay between the start of the pulser and detector signal.

The rise time and total signal time of the LEDs, recorded using the total integrated signal of all 16 pixels, is shown in table 5.1. In general, the rise time was found to be approximately 40 ns for the green/yellow LEDs and considerably longer at redder and bluer ends of the spectrum. The total signal times fluctuated between 200 and 350 ns depending on what LEDs were used.

After individually testing the total response of all the pixels, the response of a single pixel was tested. This was done by masking the detector, leaving one pixel situated near the centre. A collimator was created in the card to direct most of the incident photons from the LEDs onto the pixel. Using this method, the dark

current \gg signal. However, due to the high gain of the individual microcells, the sensitivity that can be achieved is still better overall than conventional PIN diodes. The bias voltage was increased to within the breakdown voltage, where the gain and signal height increased along with the dark current. The voltage was reduced substantially to try and reduce the effects of this increase in dark current. Unfortunately, ~ 50 mV of noise, and a signal of ~ 80 mV was recorded.

5.2.2 Temperature Response

A group at the Institut Pluridisciplinaire Hubert Curien (IPHC) in Strasbourg had been working on similar tests with LAAPDs from Hamamatsu, which have a peak wavelength sensitivity in the blue part of the spectrum. At this institute, a container that can be cooled to low temperatures was used to test the response of the SensL detector with LEDs and various γ -ray sources.

5.2.2.1 Method and Resulting Outcomes

A copper plate with a network of pipes drilled beneath the surface to allow the flow of alcohol to cool the detector was used, where a hole in the centre allowed for the placement of the detector array to be stuck to the surface with thermal paste. The output for the integrated signal was allowed to travel out the back of the plate, through an additional hole drilled into the heat sink. The 7 cm^2 plate, with a thickness of ~ 2 cm, also had several holes bored into its surface to allow for the coupling of thermo-resistors to register changes in temperature.

The copper plate was then placed into a light tight cooling chamber, where the detector was optically bound to a CsI(Na) scintillator crystal.

CsI(Tl) and CsI(Na) scintillators were used. Both types of CsI scintillators are not as dense as LaBr₃(Ce) at $4.51\text{ g}\cdot\text{cm}^{-3}$, and not as bright at 41,000 ph/MeV and 52,000 ph/MeV[19][46] for CsI(Na) and CsI(Tl) respectively. CsI(Na) is well matched to bialkali PMTs, but not the SiPM, with a $\lambda_{max} = 420$ nm and decay time of 630 ns (discussed in the previous chapter). However, CsI(Tl) crystals are much better matched to the SiPM, with a $\lambda_{max} = 565$ nm and decay time of 1 μs .

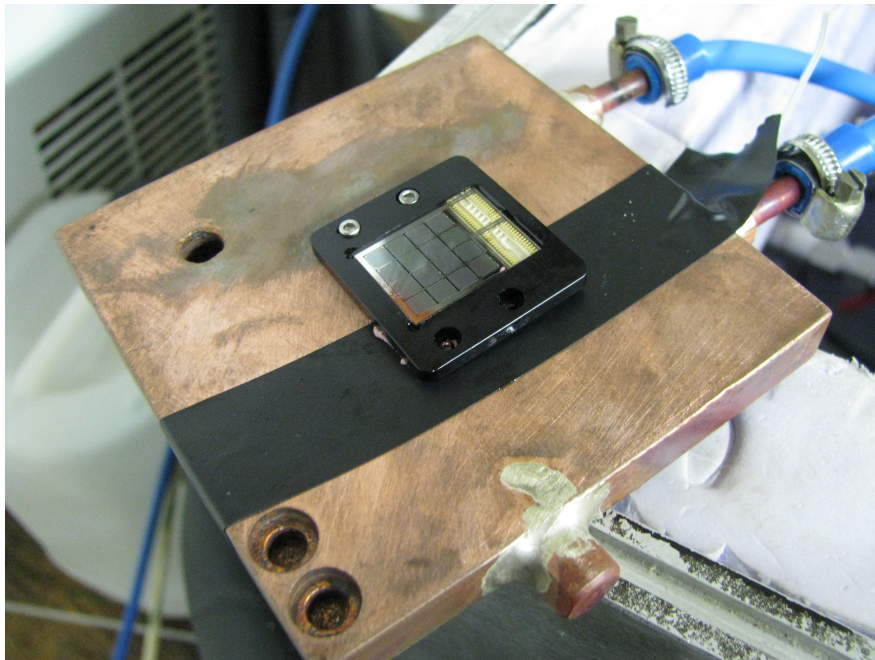


Figure 5.2: The detector mounted to the heat sink.

The SiPM detector was coupled to a CsI(Na) scintillator and placed in the container, where it was subsequently cooled. The detector was found to trigger on noise, due to the peak emission wavelength of the CsI(Na) being wrongly matched to the sensitivity of the detector. As a result of the poor S/N, no data was collected. The CsI(Na) was subsequently replaced with a 1 cm diameter CsI(Tl) scintillator, which was better matched to the detector. However, a respectable spectrum still could not be produced. The crystals were tested with the Hamamatsu APD and found to be working. The detector was also tested with a green LED to test the response, and was found to be working very well.

Tests were performed with ^{137}Cs and ^{60}Co calibration sources at room temperature after the SiPM had been optically bound to a CsI(Na) scintillator, and then a CsI(Tl) scintillator. However, both signals from each source were very weak and buried beneath noise. The signal from the amplifier was substantially improved, however the signal itself, had a lot of noise associated with it. This was not only due to grounding issues with the oscilloscope, but the fact the detector was operating 1-2 V above the breakdown voltage. It was subsequently turned

5.2 Experiment Methods and Results

down to around 27 V, where the dark rate was still overwhelming, which is shown in figure 5.3. Since the detector triggered on noise when coupled to the CsI(Tl) scintillator, the temperature tests were done with a green LED.

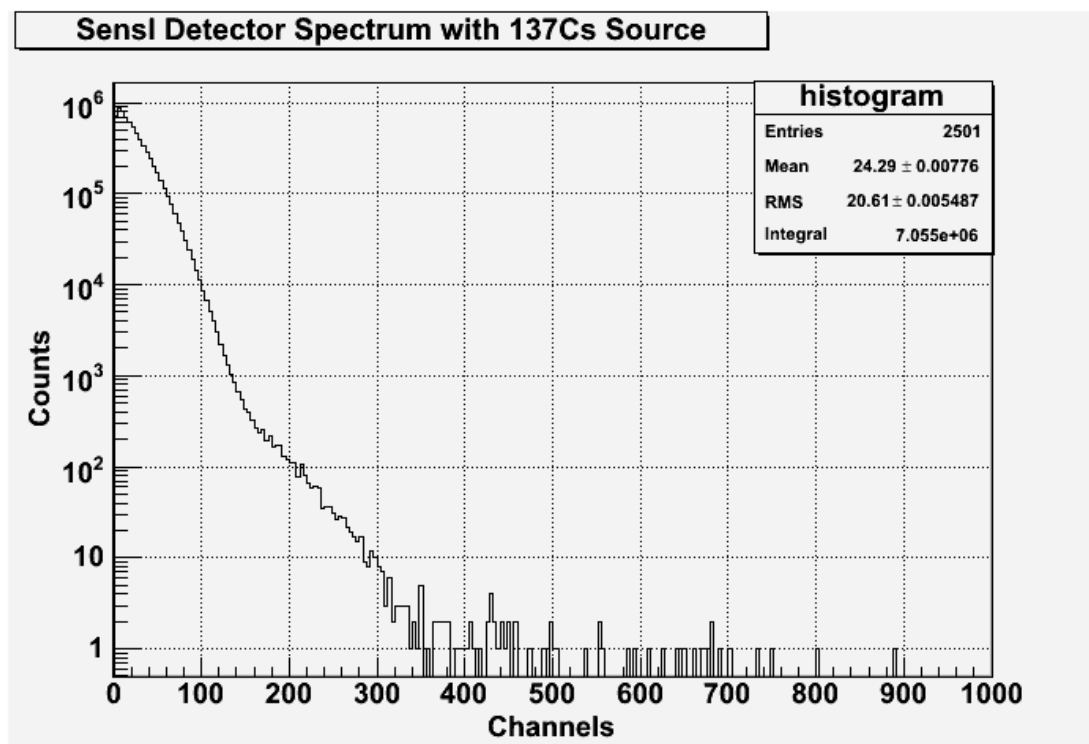


Figure 5.3: The poor response with a ^{137}Cs source

Several temperature readings were taken at 4°C intervals, between 30°C and 2°C over several hours, shown in table 5.2. A period of 1-2 hours were left between each reading to make sure the temperature inside the box had stabilised. Additional time was also allocated to ensure the temperature of the heat sink also stabilised, which was measured by a thermometer attached to the plate (PT 100 thermocouples were not used in this experiment). The result was a linear relationship between the FWHM resolution and the temperature shown in figure 5.4. Generally, most APDs exhibit an exponential relationship between these two parameters.

5.2 Experiment Methods and Results

Temperature ($^{\circ}\text{C}$)	Centroid	FWHM	Resolution (%)
30	6341.86	593.90	9.36
26	6861.49	616.94	8.99
22	7402.14	614.72	8.33
18	7866.96	647.80	8.23
14	8523.94	687.18	8.06
10	9018.91	713.29	7.91
6	9626.04	730.34	7.59
2	10180.74	754.53	7.41

Table 5.2: The integrated response of the SiPM with a green LED at various temperatures.

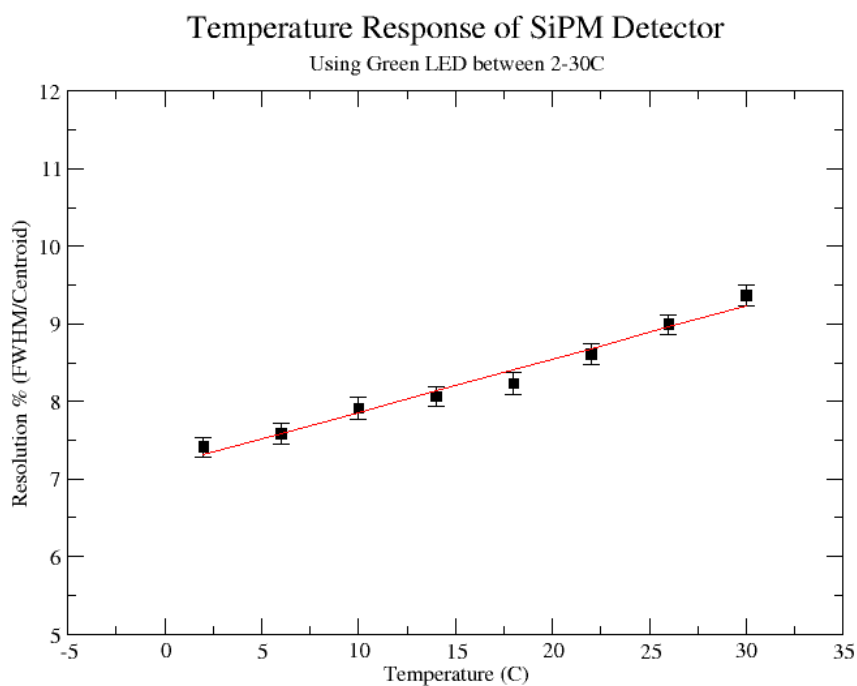


Figure 5.4: The response of the SiPM with increasing temperature.

5.3 Response Testing of the Detector

A comprehensive study of the breakdown voltage was performed, by adjusting the potentiometer to various biases to determine if the power supply was still consistent, and that little fluctuations and ripples were not occurring. However, peak drifts and discrepancies in the applied voltage were discovered, resulting in gain fluctuations and inaccurate FWHM measurements with increasing bias. A substantial amount of noise was also recorded when the detector was placed near any calibration sources.

Unlike conventional PMTs, at low signals the S/N is dominated by the amount of dark current from the detector. However at 500 nm, the S/N of the pixels on the SiPM detector is better or roughly equal to the PMT, as the efficiency for the SiPM detector becomes better than the PMT. The dark current of a SiPM pixel is ~ 100 nA, which becomes an excess noise factor at low signal levels. To make sure the signal integrity is not compromised, the incoming bias supply of ± 5 V must have a ripple and noise, of less than ~ 50 mV. By keeping this small unwanted periodic variation in the output of a DC power supply (ripple) to a minimum, the noise can be largely reduced. The crosstalk of adjacent pixels might also be contributing to the noise if they are also fired, which increases the gain at high electronic thresholds. Fluctuations from increasing the gain, in addition to ripple effects, will also produce excess noise. The motherboard and preamp PCB was consequently removed to reduce the amount of noise and improve the S/N, by using another pre-amp board, where the signals from the detector went straight to the pre-amp, which had an applied bias of 5 V. The SiPM electronics were tested with a pulser and green LED, along with various auxiliary capacitors and resistors, which continued to give good results. However any energy spectra associated with the coupling of the detector array to scintillators, were still inundated with noise.

Overall, tests with the SensL SiPM array were unsuccessful. However, four new detectors were acquired soon after these results, and subjected to similar tests to compare their response.

5.4 The New SensL SiPM Detector Arrays

Despite some positive outcomes for the previous tests with the SiPM detector, the energy resolution was found to be extremely poor and consequently, there were limitations to what could be achieved. A new variation of the original detector was bought to test the resolve of the detector to see if the results previously discussed, were due to noise being generated off the pre-amp board at the back of the detector.

The new SiPM array is based on a similar design to the previous detector, incorporating tiled pixels using flip-chip technology. The detector is sensitive to position and visible light within the 400-850 nm range. It has zero dead space on three sides, with pixel-to-pixel spacing of the order of 200 μm within the 4x4 array. Only 100 μm of dead space remains around the outside of the array, meaning that the space between two adjacent arrays, when tiled together, can be as low as 200 μm .

Four new detectors were bought with attached flexible printed circuit (FPC) cables (1-39 connections), that allowed for the detector to be attached to four separate mother boards. The connections allow for the output of each single pixel within the tiled array to be separately addressed. The shielded FPC cable connects to a pre-amplifier board, power supply and control electronics, where the shielded cables allow for protection from interference that can be caused by magnetic fields or radio frequency (RF) signals. The gain on each microcell (3640 microcells per pixel) is a large 10^6 , which allows for optimised performance at a low bias of ~ 30 V, 2 V above the breakdown voltage. The PDE is 10-20 % at $\lambda_{max} = 520$ nm, with a dark rate to be 8 MHz per pixel[45].

5.4 The New SensL SiPM Detector Arrays

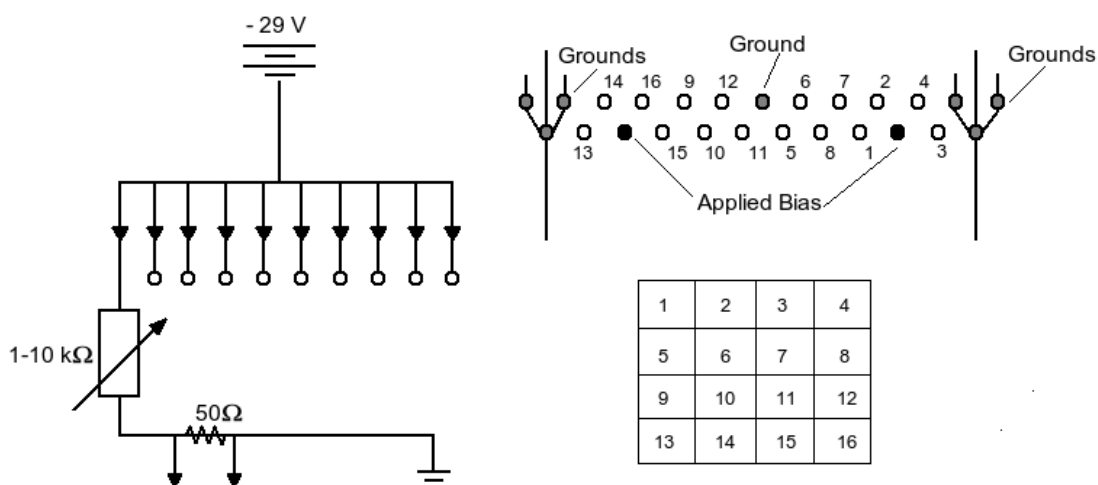


Figure 5.5: The circuit diagram of the preliminary detector board.

A board was created so that each individual pixel can be read separately, and also have the possibility of all 16 outputs from each pixel integrated together to give a larger signal. The electronics of the original board is shown in figure 5.5. Each outlet was soldered to a 3.9 k Ω resistor before being connected with a crocodile clip with other outputs. These were read and analysed by either an amplifier, TFA, or oscilloscope, where some of the outlets were for grounding and the applied bias. The bias is fed into 2 channels, where each one powers 8 of the 16 pixels (upper and lower halves). After testing the board and finding 15 of the 16 channels functioned well (pixel 13 was broken), 15 channel spectra were acquired to observe the energy resolution of a standard ^{137}Cs Source. Electrical tape was wrapped around a portion of the wire in proximity to the resistor in each channel, so that contact between each output along this wire did not make contact before travelling through the resistor. This would ultimately give mixed signals or a degradation in the outputs, resulting in spurious findings.

The smaller 1"x1"x1" CsI(Tl) was used before testing was performed with the larger 1"x1"x6" scintillator. A spectrum of the response with a ^{137}Cs source shows, that the FWHM of the 662 keV photo-peak was found to be 19.23 % when used with an amplifier at the recommended voltage of 30 V. Several other sources were used, including ^{152}Eu and ^{207}Bi . However, the resolution was too poor to observe any photo-peaks from the ^{152}Eu source, where the 344 keV line had the

5.4 The New SensL SiPM Detector Arrays

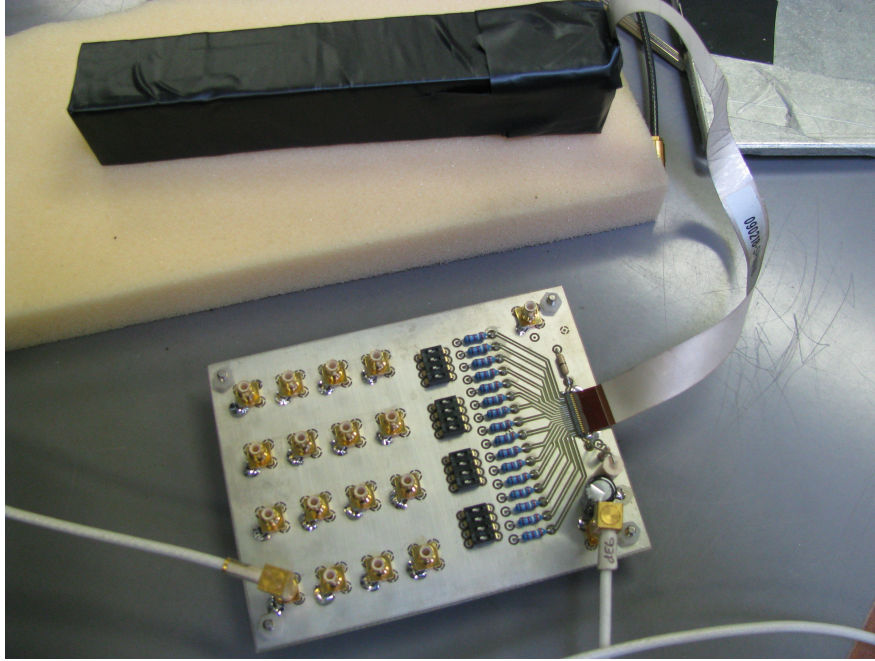


Figure 5.6: The final board developed for the SiPM array.

best signal-to-noise. The ^{207}Bi source was used to check the response of betas, where a little window was created in front of the scintillators for this purpose. However, none were detected. This is possibly due to the noise being rather high at low energies.

The smaller CsI(Tl) crystal was replaced with a longer 1"x1"x6" CsI(Tl) scintillator. Due to the increase in depth/length, there should be a reduction in the amount of noise, which will hopefully result in better spectra. However, during the wrapping and mounting process, the ends of the crystal were found to be poorly polished compared with the rest of the crystal possibly due to the cutting process and structure of the crystal, where the crystal might not cleave well in this direction.

Initially, the source was taped to the end of the scintillator, which should have given an accurate representation of the scintillator response in CsI(Tl). However, due to the length of the detector, and the low energy of the ^{137}Cs source, the majority of the energy deposition and scintillation happened about 4-5" from the detector, meaning a lower number of photo-electrons were recorded by the

5.4 The New SensL SiPM Detector Arrays

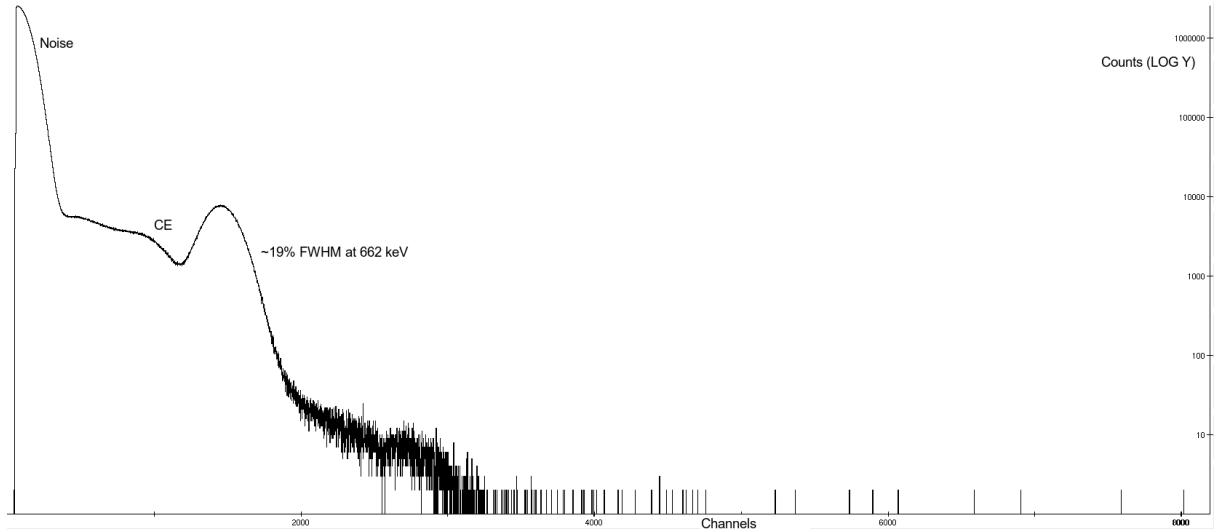


Figure 5.7: The 662 keV photo-peak in ^{137}Cs showing the SiPM response.

detector. To compensate for this, a similar measurement was made with the source placed on top of the scintillator, in proximity to the detector. The 100 mV signal was shaped with a standard ORTEC amplifier (model 572), and a FWHM of $\sim 35\%$ was observed for the ^{137}Cs source. The length of the the 1"x1"x6" crystal, and the long decay ($1\ \mu\text{s}$) of the scintillator might be contributors to this result. Consequently, the timing measurement results were also found to be poor in comparison with other scintillators. Factors that could possibly contribute to this result may rest with the board; poor contacts with the soldering on the board, and the bunched outputs within the crocodile clip. A higher energy source was tested to see if it was an issue with the photons not reaching the detector. Using a ^{152}Eu source, the resulting spectrum was also found to have very poor resolution. Consequently, it was decided that the energy resolution measurements could not be improved upon, and investigations into the timing properties begun.

5.4.1 Timing Tests

The timing resolution was then measured with this detector set-up by making a coincident measurement between two channels with a ^{22}Na source. There were major variations in the resolution due to the applied bias in the SiPM system, and

5.4 The New SensL SiPM Detector Arrays

also due to a considerable amount of walk from the discriminator. This caused variations in the rise time and amplitude of the signals. In light of this, the bias supply was reduced to within the limits of the detector, where the triggering was done by allowing the incoming logic signals to be generated at a constant fraction of the pulse height, independent of the amplitude. The incoming pulse is split in this process where one is delayed, and the other is inverted and attenuated. The two split pulses are then summed again to produce a bipolar signal with some zero cross over point (ZCO)¹. Therefore, this technique relies on an incoming unipolar signal with a consistent rise time.

A start-stop timing measurement was subsequently performed with a 1" BaF₂ detector (in the start channel), and 1"x1"x6" CsI(Tl) scintillator coupled to a SiPM. A newly developed board was used to replace the original existing board in the previous investigations. The new board (pictured in figure 5.6), is based on the original board set-up, where ~ 4 k Ω resistors are assigned to each channel/pixel. Switches were also added to the new board so that various configurations of tested pixels in the array could be utilised.

Before timing measurements were acquired, the CFD thresholds and TFA settings had to be adjusted so that the timing measurements would be optimised. A similar timing set-up was used to those done with the phoswich detector in the previous chapter. One of the issues encountered during the experiment was the amount of walk seen from the SensL detector (100 ns), which hindered the accurate placement of a threshold with the CFD for signals from the array. The applied bias voltage was lowered to around 5-10 V, just above the operation threshold, as the gain seen before was possibly too high, despite lowering gain settings on the TFA.

Before the actual start-stop measurement, a calibration test was performed by replacing the stop and start channels with a pulser. Several delays were chosen between 50 and 700 ns, within a 1 μ s scale on the TAC to help determine the centroids, which were plotted in XMGRACE. The slope was fitted to the data and used to calibrate the actual start and stop measurements with the BaF₂ and SiPM detectors, shown in figure 5.8. A FWHM timing resolution of ~ 90 -

¹This method was used instead of the leading-edge (LE) triggering due to its increased precision.

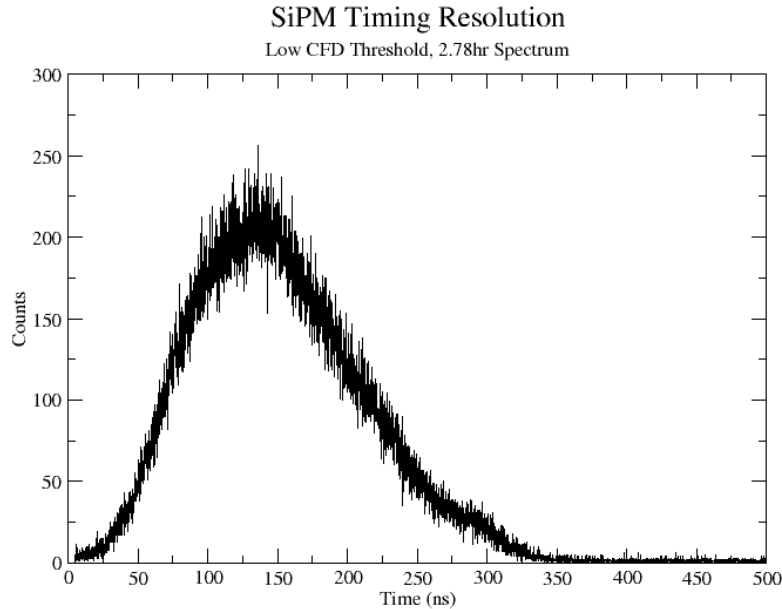


Figure 5.8: Timing resolution of the 1" x 1" x 6" CsI(Tl) and SiPM detector set-up.

100 ns was observed as a result, the best achievable resolution with this set-up. The FWHM timing resolution is expected to be slightly lower for the 1" CsI(Tl) scintillator. However in both instances, the resolutions were still found to be poorer than what was observed for the phoswich.

5.4.2 Other Extensions

5.4.2.1 Position Sensitivity

Another possibility that was briefly researched, was the investigation of the position sensitivity of all 16 SensL detectors by tiling the four arrays together. The SensL detector arrays were tiled along the side of the long 6" CsI(Tl) scintillator, mounted with optical grease (similar to BC630), and wrapped to ensure the system would be light tight. A standard calibration source was used to measure the integrated pixel response. When the appropriate switches are applied, all four array signals are integrated, in effect boosting the signal, and thus increasing the

5.4 The New SensL SiPM Detector Arrays

efficiency (limited amount of dead space when adjacent to one another). As the position of the source is moved along the edge of the scintillator, each of the four SiPM detectors should respond by exhibiting a decrease or increase in the pulse height of the integrated signal, depending on its proximity to the source.

As the four arrays were mounted to the CsI(Tl) scintillator, care had to be taken to ensure the set-up was light tight, and that no aluminium foil was in contact with the electronics on the detector board¹. Prior to the acquisition of each of the integrated array signals, the detectors needed to be gain matched with respect to one another. This was done by placing each of the detector arrays within a light tight box, that were subjected to light from a green LED, powered by a pulser. The pulses generated had duration and repetition times of 10 μ s and an amplitude of 11 V. The result of the gain matching, performed by tweaking the amplifier settings, are shown in table 5.3. As a result of this gain matching, all detectors should effectively have similar pulse heights when subjected to the same radiation, allowing for better sensitivity, making it easier to deduce whether any position sensitivity was possible.

Array Number	Amplifer Gain	Amplifier Coarse Gain	Shaping Time
Array 1	x2.1	x50	500 ns
Array 2	x0.1	x500	" "
Array 3	x8.1	x20	" "
Array 4	x8.1	x20	" "

Table 5.3: Various amplifier gains applied during the gain matching calibrations.

The measurements were very difficult due to \sim 50-75 mV of noise, and some slight walking effects seen from one of the arrays. There was also significant fluctuation in the current from both bias supplies due to one of the high voltage supplies performing poorly, or foil interfering with several signal outputs. A low energy source would have been ideal to use, however the length of the lead collimator (2") constrained the energy used. To ensure that a substantial number of gammas would deposit their energy in the scintillator, a ^{137}Cs source was used

¹Any foil touching the electrical contacts on the plastic detector board would short the circuit.

5.4 The New SensL SiPM Detector Arrays



Figure 5.9: Gain-matching process, with radiation incident primarily on the first array/channel.

with the lead collimator, and was placed alongside the scintillator, roughly opposite each array. The results are shown from figures 5.9 to 5.12, where examples of the detector response are shown to correspond well to the positioning of the source.

There is certainly a sensitivity of the detector response due to the positioning of the source, where channels 1-4 correspond to the arrays of the same allocation. The acquisition method is only preliminary, where improvements on these measurements and further analysis of the pulses can be performed. However, due to constraints on time, this was only briefly covered. In many instances, it would seem that the detectors surrounding the array that was subjected to the incident radiation, also registered a considerable number of counts. This was due to Compton scattering, and deposition of energy after the transportation of scintillation through the crystal. As a result, a mono-energetic source with a lower energy could be used with larger gaps between the detector arrays to optimise these results.

This is only one deviation of the research performed for PARIS. Several other areas of study can be furthered, such as producing a map of the approximate

5.4 The New SensL SiPM Detector Arrays



Figure 5.10: Gain-matching process, with radiation incident primarily on the second array/channel.



Figure 5.11: Gain-matching process, with radiation incident primarily on the third array/channel.

5.4 The New SensL SiPM Detector Arrays



Figure 5.12: Gain-matching process, with radiation incident primarily on the fourth array/channel.

location of the source, derived from coding, which would have many practical applications within nuclear physics and industry. The application of a magnetic field would also be interesting to study, a realistic consideration when using arrays in facilities with beams.

5.4.2.2 Further Investigations with LYSO(Ce)

Another brief extension of the work conducted with the new SensL SiPM arrays investigated the energy response of a small piece of cerium-doped Lutetium Yttrium Orthosilicate (LYSO(Ce)), tested with numerous γ -ray sources. The 1x1x30 mm crystal was small enough to fit across one of the row of detectors in the 4x4 array supplied by SensL. The switches on the newly developed boards were used to study the position sensitivity of the detector array by adding the signal from each pixel depending on the configuration of switches selected. The cumulative signal can then be read off for each row of pixels, or all 16, depending how the scintillator was orientated, and which pixels are selected. The result, is the observation of position sensitivity of the array.

The LYSO(Ce) scintillator was acquired from Saint Gobain, called PreLude420.

5.4 The New SensL SiPM Detector Arrays

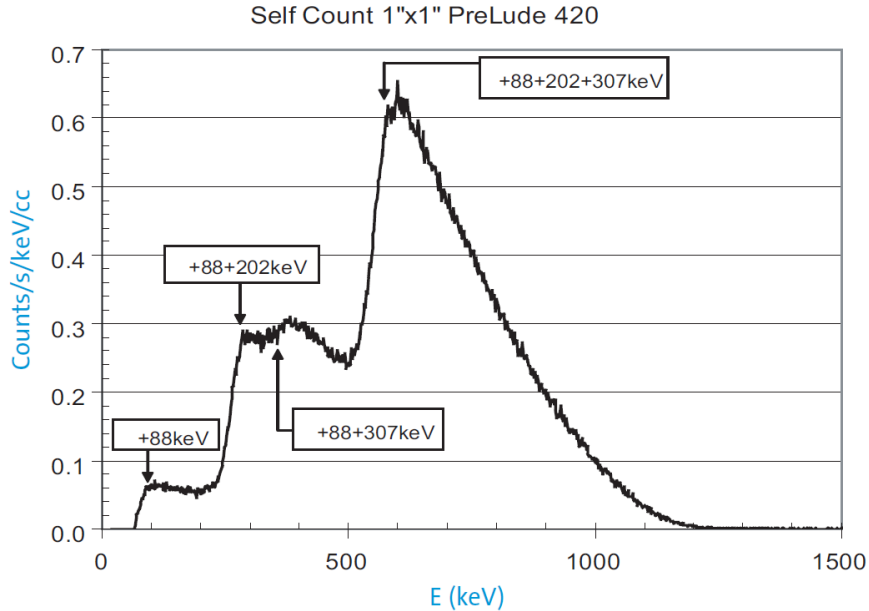


Figure 5.13: The self-activity of LYSO [47]

According to the data sheet available with this series, the light output is quoted to be $\sim 32,000$ ph/MeV, with a peak emission wavelength at 420 nm. It has an energy resolution of 7-8 % FWHM for the 662 keV photo-peak in ^{137}Cs , with a decay time of around 41 ns.

The small 1x1x30 mm scintillator was placed over four detectors on the 4x4 SensL array, optically bound using grease with similar characteristics to the widely used BC630 variety offered by Saint Gobain. Due to the 100 nm difference in the peak sensitivities of both the scintillator and the detector array, it is anticipated that the quantum efficiency of the scintillator (QE) will decrease from 25 % to 10 %, a 60 % decrease in efficiency. Therefore, it can be assumed that a substantial amount of the signal height will be lost due to this discrepancy. Care had to be taken with selecting appropriate calibration sources as despite the density of LYSO(Ce) being large ($7.1 \text{ g}\cdot\text{cm}^{-3}$), the stopping power is not significant enough for the detection of γ rays at around 500 keV or higher. Consequently, both ^{241}Am and ^{133}Ba sources were used in the low energy calibration, with the resulting spectra shown in figure 5.14.

LYSO(Ce) also has self-activity due to ^{176}Lu , a ground and isomeric state

5.4 The New SensL SiPM Detector Arrays

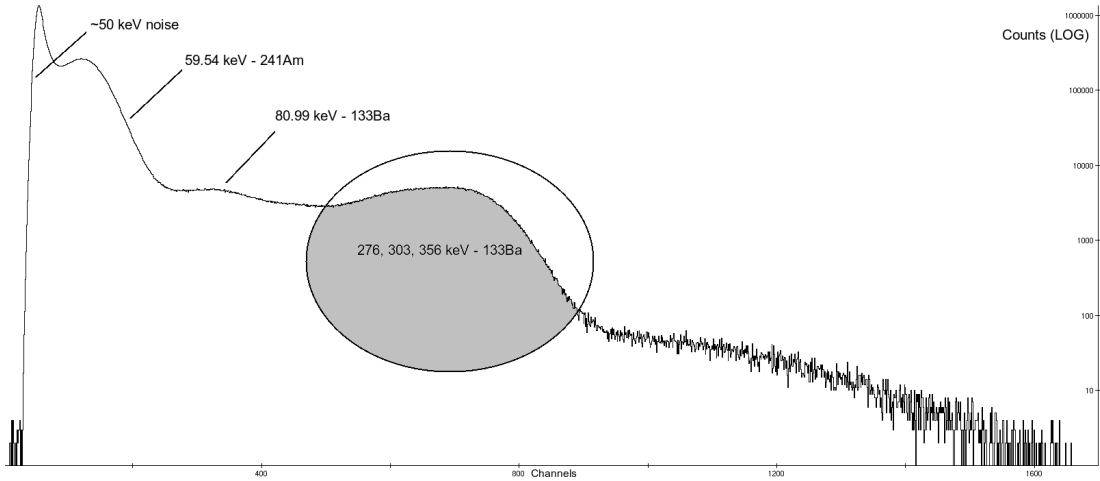


Figure 5.14: Calibration tests with ^{241}Am and ^{133}Ba sources on a 1x1x30 mm LYSO(Ce) scintillator coupled to four pixels on one SiPM array.

with transitions that undergo β^- decay nearly 100% of the time. This low rate (39 cps/g) of self-activity is shown in figure 5.13. The structure of this spectrum is attributed to some of the photons escaping and results in four sets of β - γ distributions in coincidence with one another.

The detector set-up only involved the amplification and gain adjustments of the signal with either a standard ORTEC amplifier or TFA. To avoid saturation of the signal due to the high light output, the fine and coarse gain settings on both the TFA and amplifier modules were kept low (x25-55). The shaping times were also kept very short, with a 500 ns shaping time constant applied from the amplifier, and the "OUT" settings as the integration and differentiation constants from the TFA. However, no considerable difference in signal optimisation was witnessed, with no module preferred over the other. An applied voltage near the breakdown (~ 29 V) was used, resulting in the acquisition of poor resolutions, with a noise level of approximately 50 keV. This made the analysis of the 60 keV peak from ^{241}Am , along with other gammas from the ^{133}Ba calibration source, very difficult due to poor energy resolutions, as seen in figure 5.14. These measurements were made by using readouts from four of the 16 pixels of one SiPM array, with the appropriate switches set so that the resulting signal is a culmination of the individual response of each pixel (figure 5.15).

5.4 The New SensL SiPM Detector Arrays

Many explanations can be used to describe the poor resolution, one of which could be that the reduction in signal height becomes a very substantial problem at lower energies due to the small size of the crystal, resulting in a poor S/N ratio. As the crystal is effectively only 1 mm thick over each detector in the array, the volume is simply too small to do any γ -ray spectroscopy for energies larger than ~ 400 -500 keV.

The position sensitivity of the SensL detector was also briefly tested where the LYSO(Ce) scintillator over one row of detectors was rotated 90° , so it was now covering four detectors in a column, rather than a row, as shown in figures 5.16 and 5.17. In the first instance, only a signal from the row of detectors in contact with the LYSO(Ce) had an output, any other output would have resulted in no signal. However, when the scintillator is rotated 90° so that one detector in each row is in contact with the scintillator, a cumulative signal is seen for each row. One output contains all the signal for the row, and the other outputs in that row contain no signal due to that additive nature of the circuit board. Therefore, position sensitivity is possible with this set-up, as the positioning of the LYSO(Ce) across the detector arrays result in different signal responses.

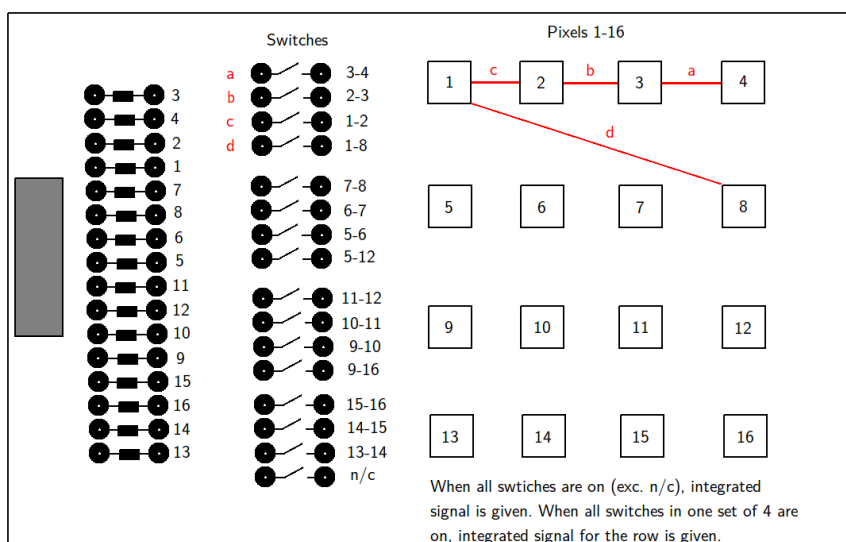


Figure 5.15: The configuration of the switches on the board used with the SiPM.

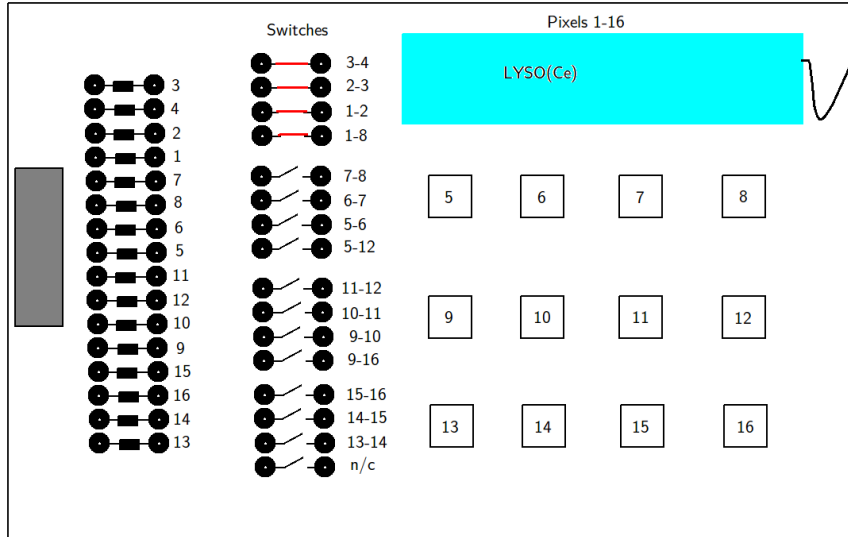


Figure 5.16: The position sensitivity of the SiPM and board with LYSO(Ce).

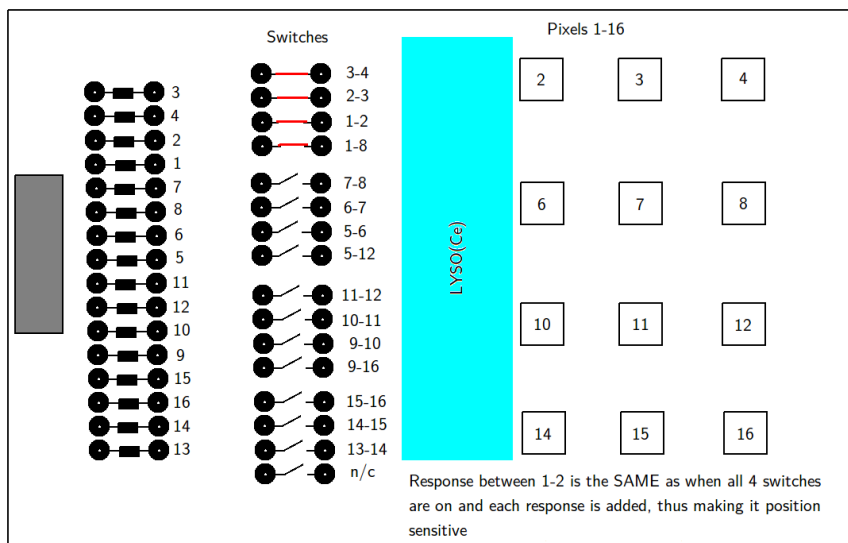


Figure 5.17: The position sensitivity of the SiPM and board with LYSO(Ce).

5.5 Future Experiments

There is a lot of interest in trying to develop SiPMs that are sensitive to the blue end of the electromagnetic spectrum, the area where the maximum light emission

5.5 Future Experiments

from $\text{LaBr}_3(\text{Ce})$ occurs ($\lambda_{max} = 380 \text{ nm}$). As of recently, only small pixels have been developed within this wavelength range, with current large APDs (such as the ones discussed in this chapter from SensL), having maximum light collection in the green part of the EM spectrum at $\sim 520 \text{ nm}$. The use of these detectors in unison with the two layers of scintillators proposed for PARIS, would further the reduction in dead space and increase the overall efficiency of the calorimeter.

Chapter 6

High Energy Calibration Beam Tests

6.1 Introduction

Until now, both the phoswich and LaBr₃(Ce) scintillation detectors have been subjected to tests at relatively low energies. A better understanding of the performance of these detectors under high energy experimental conditions, needs to be investigated. In this chapter, the results of a beam test in Strasbourg will be presented and their implications discussed.

6.2 $^{27}\text{Al}(p,\gamma)^{28}\text{Si}$ High Energy Beam Test

The experiment studied the resonant reaction $^{27}\text{Al}(p,\gamma)^{28}\text{Si}$, an important astrophysical reaction found in the r-p process that has numerous states up to 12 MeV. The aim was to populate a resonance in ^{28}Si with a beam energy of 767 keV, in order to study the response of the phoswich detector. Understanding the linearity of the detector, and how it would respond to high energy γ -rays, was paramount to any other subsequent measurements made. This needs to be known before any prototypes can be constructed.

6.2.1 Resonant Capture Reactions

A geometrical definition needs to be defined in order to know the probability of whether or not the desired nuclear reaction has taken place. The cross-section referring to the geometrical area of the projectile and target, is given by the expression; $\sigma = \pi(R_p + R_t)^2$, where R_p and R_t refer to the radii of both the projectile and target respectively. This classical relationship can be expanded upon, by incorporating quantum mechanics in the derivation of an energy-dependent expression; $\sigma = \pi\lambda^2$, where λ is the De Broglie wavelength.

Near the resonant beam energies (E_R), the cross-section is very high and thus, so is the reaction probability. These can be represented in terms of partial widths; one partial width to describe the formation of the compound (Γ_a), the other to describe the decay (Γ_b). The latter can also refer to the emission of γ -rays as well as describe the resulting particle, and can be written as:

$$\sigma_\gamma \propto \Gamma_a \Gamma_b, \quad (6.1)$$

A resonance is defined as "narrow" if the total partial width Γ^1 , is smaller than the resonance energy E_R .

The Breit-Wigner formula for a single resonance can be derived, where the total width is dependent on energy and only valid if the energy level separation is larger than the corresponding widths, (isolated resonances)[48].

$$\sigma(E) = \pi\lambda^2 \frac{2J + 1}{(2J_1 + 1)(2J_2 + 1)} (1 + \delta_{1,2}) \frac{\Gamma_a \Gamma_b}{(E - E_R)^2 + (\Gamma/2)^2} \quad (6.2)$$

Where,

$$\lambda = \frac{m_p + m_t}{m_t} \frac{\hbar}{(2m_p E_l)^{1/2}} \quad (6.3)$$

¹Where $\Gamma = \Gamma_a + \Gamma_b + \Gamma_x \dots$

Integrating the Breit-Wigner cross-section, $\sigma(E)$ allows us to probe the properties of the resonance, the area under the curve, and thus determine its strength[48]. A maximum resonance cross-section σ_R can be found since $E = E_R$, and is the area under a resonance curve equal to the product of $\frac{\pi}{2}\Gamma \cdot \sigma_R$.

$$\int_0^\infty \sigma(E)dE = \pi\lambda_R^2\omega\Gamma_a\Gamma_b \int_0^\infty \frac{1}{(E - E_R)^2 + (\Gamma/2)^2} \quad (6.4)$$

The expression $\frac{\Gamma_a\Gamma_b}{\Gamma}$ is an important parameter known as the width ratio (γ), and appears in the term $\omega\gamma$, which is used to define the resonance strength. This resonance strength $\omega\gamma$ depends heavily on the coulomb barrier of the reaction channel.

If the reaction channel $A(a,b)B$ occurs with the cross-section; $\sigma_r \propto \Gamma_a\Gamma_b$, then the elastic scattering channel ($A(a,a)A$) occurs, when $\sigma_e \propto \Gamma_a\Gamma_a$, and the total scattering cross-section, σ is equal to $\sigma_e + \sigma_r$. Once this width has been deduced, an appropriate target thickness needs to be selected so that the desirable resonance is populated.

6.2.1.1 Target Thickness and Yield

It is also imperative to know the target thickness, as the thickness will influence the the energy loss through the target, and the separation between the levels. These effects are clearly seen in the data presented later in this section, where the following theory behind the yield and target thickness will aid the reader in his or her understanding of the data.

If the target thickness Δx contains a given number of nuclei (n_o) within an area F , then the total area of the target under active study is $F_{act} = n_o\sigma$ given the target thickness is small enough to avoid overlapping of individual areas. Dividing F_{act} by the area F results in the derivation of the reaction yield per incident particle[48], Y :

$$Y = \frac{F_{act}}{F} = \frac{n_o\sigma}{F} \quad (6.5)$$

6.2 $^{27}\text{Al}(\text{p},\gamma)^{28}\text{Si}$ High Energy Beam Test

The target thickness should also be chosen to be smaller than the energy separation of the resonant states, ie. $\Delta E \gg \Gamma$. Thus the energy loss through the target, or dE/dx , needs to be calculated through a medium d [48] when the initial beam energy (E_o), is known.

$$d = \int_{E_o - \Delta E}^{E_o} \frac{dE}{dE/dx} \quad (6.6)$$

If the energy loss is greater than the resonance width, ie. more straggling in the target medium, then other resonance states may become populated around the resonance of interest resulting in a spread. This can be confirmed by studying the yield curves and list of other resonant states near the reaction channel region. If the energy loss is less than the resonance $\Delta \ll \Gamma$, then the yield Y , follows the resonance profile. However, if $\Delta \gg \Gamma$, and the energy dependence of variables such as λ^2 , Γ_a , Γ_b , Δ are negligible over the resonance region[48]. For a thick target, a maximum yield can be reached via the integration of the Breit Wigner function that results in a smoothed step function reaching $Y_{max}(\infty)$ for the reaction $E_o = E_R$, defined as[48];

$$Y_{max}(\infty) = \frac{\lambda^2}{2} \omega \gamma \frac{M + m}{M} \frac{1}{\epsilon}. \quad (6.7)$$

Where the inclusion of a mass ratio helps to describe a variable associated with the stopping cross-section (ϵ), typically given in the lab frame.

The region either side of this point is the resonance width, Γ , neglecting the beam straggling and subsequent spread in the target, which can have implications on the resulting reaction yield. For a finite target thickness, a ratio can be derived since equation 6.7 has a maximum at $E_o = E_R + \Delta/2$.

$$\frac{Y_{max}(\Delta)}{Y_{max}(\infty)} = \frac{2}{\pi} \arctan \frac{\Delta}{\Gamma}. \quad (6.8)$$

These are the basics needed to understand the processes behind this important nuclear astrophysics reaction. This background will help in determining what might be detected by the detectors given the different underlying considerations regarding target thickness, resonance widths, and strengths. With this knowledge, one can now begin to analyse the data, and begin to understand the subsequent results of the reaction.

6.2.2 Experimental Set-Up

Two phoswich detectors were used; the detector tested at York (1" x 1" x 2" $\text{LaBr}_3(\text{Ce})$ and 1" x 1" x 6" $\text{CsI}(\text{Na})$ scintillators), labelled "PW1", and a similar sized phoswich detector from Orsay where the larger segmented crystal was composed of $\text{NaI}(\text{Tl})$, labelled "PW2". A small 1" x 1" x 2" $\text{LaBr}_3(\text{Ce})$ scintillator and 2" x 2" x 4" $\text{LaBr}_3(\text{Ce})$ scintillator were used in addition to the phoswich detectors for comparative studies.

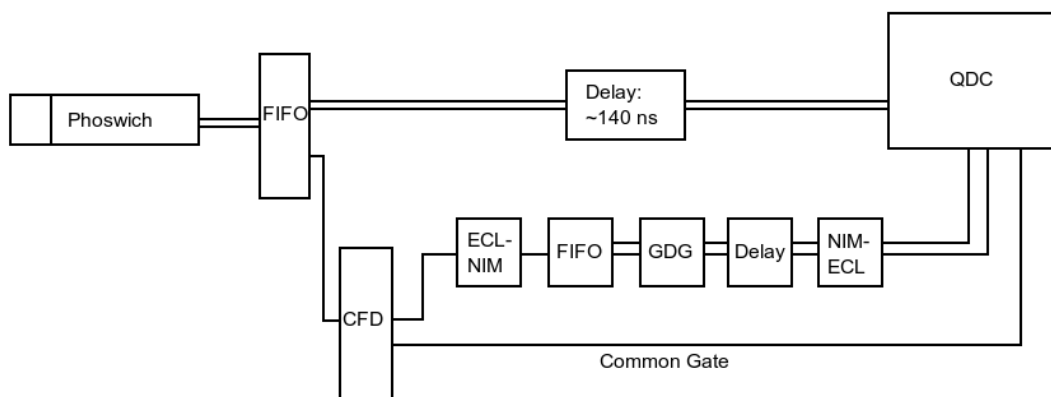


Figure 6.1: An example of the phoswich channel electronics set-up.

The 767 keV proton beam was delivered by a 4 MeV Van Der Graff generator at the IPHC in Strasbourg. A diagram of part of the electronics set-up for one of the phoswiches is shown in figure 6.1. Several CAEN charge-to-digital converter modules (QDCs) were used with the phoswich to resolve the different signals from both scintillators. Since each QDC has an individual common gate, two were used for each phoswich detector to discriminate each pulse. It is thought that the

longer pulses expected from the CsI(Na) and NaI(Tl) pulses (decay times of 630 and 250 ns respectively[42]), will appear as a distribution of points near the axis of the QDC with the longer gate. A 4/8 channel, 10 bit digitiser with a sampling rate of 1-2Gs/s was used to acquire the signals on the DAQ. The thresholds for the CFDs, ADCs, TDCs and QDCs were changed on a DAQ system.

6.2.3 Analysis and Results

The analysis was done predominately in ROOT, by reading the data with a buffer file. The data was acquired with a digitised set-up, where the buffer file reads each 32 bit sample, extracting 10 bits (only 10 bits were written to the file during the acquisition) from the first 2 bytes of the total 4 byte sample¹, with the rest discarded. At 1 ns/sample, a total of 3584 trace lengths were recorded on the oscilloscope with 3.5 μs time setting, with more acquired with another time setting of 7 μs . These traces of the signal acquired on the oscilloscope were also digitised, and helped contribute to figures 6.2,6.3,6.4. From this information, a code to analyse the pulses separately, incorporating several offline techniques based on methods used in CFD and other discriminator modules, can be used. However, calibrations were first performed with the buffer file, which allowed for both off-line and on-line analysis during the experiment, where initial testing with the QDCs for each phoswich was performed before the beam was introduced.

The fast pulses from LaBr₃(Ce), and slower pulses from the CsI(Na) scintillator are generally seen as one combined signal produced by the phoswich detector when scintillation occurs in both crystals. To resolve these fast and slow pulses of the phoswich detector individually, two QDCs was used to apply short and long gates to discriminate between the LaBr₃(Ce) and CsI(Na) signals respectively, with an individual "common" gate (a comparative channel), to check the electronics. These results are shown in figures 6.2 and 6.3, and are later verified by analysing pulse samples acquired on-line from the oscilloscope and digitised set-up.

¹8 bits to 1 byte

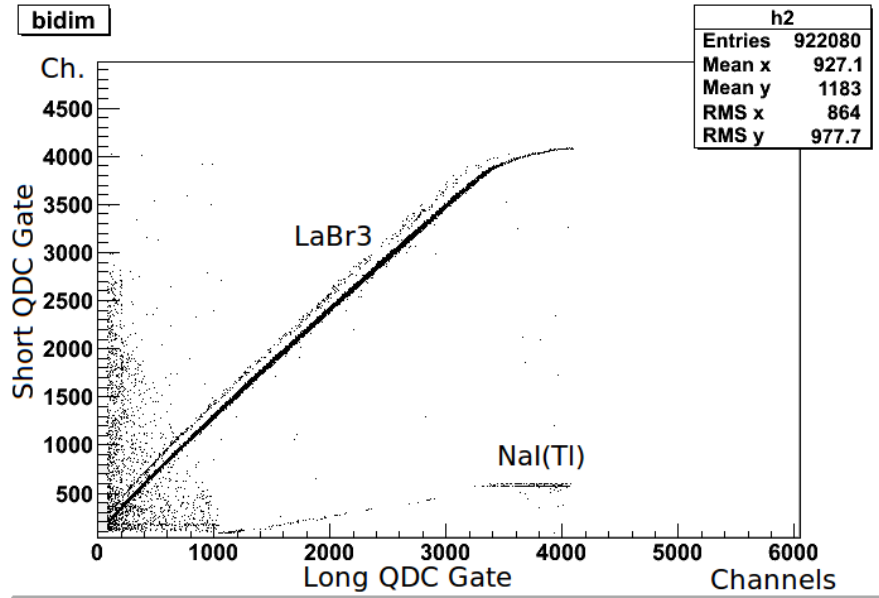


Figure 6.2: Discrimination of the fast and slow pulses within the "PW2" phoswich.

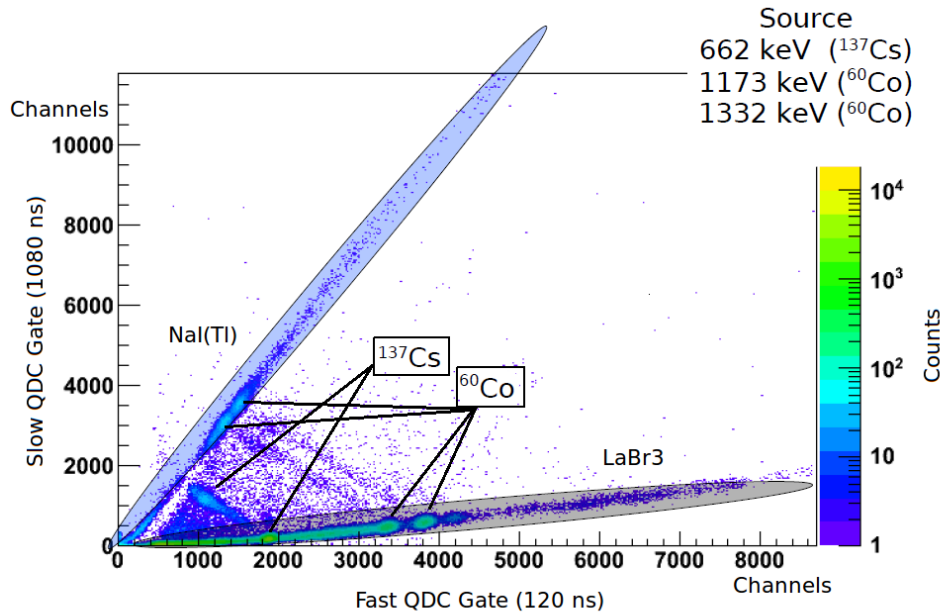


Figure 6.3: "PW2" phoswich calibration, with long and short timing gates on the Y and X axes respectively[49].

6.2 $^{27}\text{Al}(\text{p},\gamma)^{28}\text{Si}$ High Energy Beam Test

During the calibration tests with both phoswich detectors, the PMT was changed from the Photonis XP2020 model, to the PMTs used in Chateau de Cristal. The saturation with the latter PMTs was observed to be lower than what was previously seen, and was used throughout the experiment, with the final set-up presented in table 6.1.

Crystals	PMT	Bias (V)	Electronics
2" x 2" x 4" LaBr ₃ (Ce)	EMI	1400	QDC short and
PW1	XP2282	1600	long gates
PW2	XP2282	1600	2GHz Digitizer

Table 6.1: Various amplifier gains applied during the gain matching calibrations.

A LaBr₃(Ce) set-up was used along side both phoswich detectors in the experimental set-up, with a 1 GHz digitiser, and QDC in analog mode. It was found to perform very well, with good linearity (figure 6.4) for both gates of 80 and 150 ns. The FWHM resolutions of the 2^+ to ground and 10.54 transitions shown in figure 6.6, were found to be 2.47 % and 1.43 % respectively for the longer 150 ns gate[49]. The linearity however, did change as a function of the timing gates for the faster LaBr₃(Ce) pulses as shown in figure 6.4. In this figure, as series of gates were applied to the LaBr₃(Ce) signal on the QDC to observe the trends in linearity. The consequences of applying the correct gate on the signal is presented in the analysis of the experimental data.

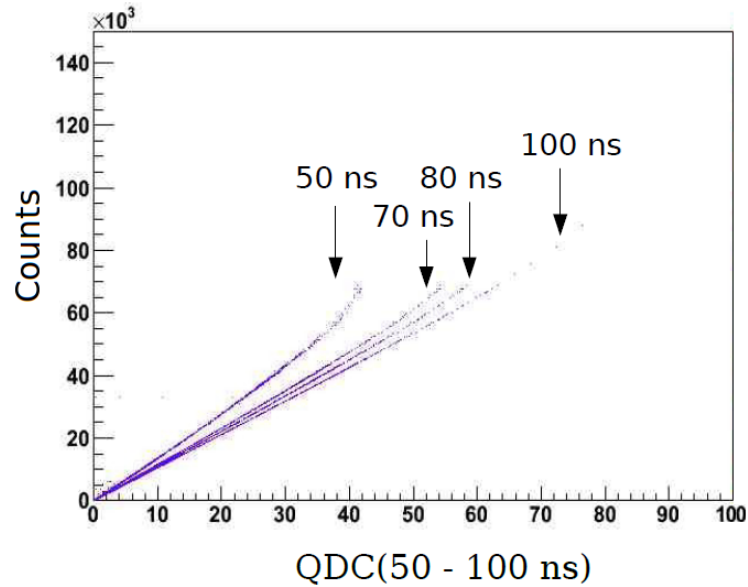


Figure 6.4: Linearity of the $\text{LaBr}_3(\text{Ce})$ scintillator changing as a function of the gating times[49].

Having specified the gates and timing parameters used during data acquisition, the analysis of the acquired pulses can now begin. The pulses were analysed using the software CFD method. In order to do this, the pulse height needs to be correctly calculated by differentiating the output signal, and evaluating the resulting bipolar distribution where the slope is zero over a constant period of time. This was done to ensure that the minimum was accurately measured, and would not be affected by walk or jitter effects that might become apparent during the experiment. Defining thresholds on either side of the window sets a pulse minimum, and allows for integration of this pulse so that the fast and slow signals from the phoswich detectors can be clearly identified, where the integrated pulse signal follows the formula: $da(i) = a(i+1) - a(i)$. An example of one of the many outputs created after performing software CFD on the acquired pulses is shown in figure 6.5.

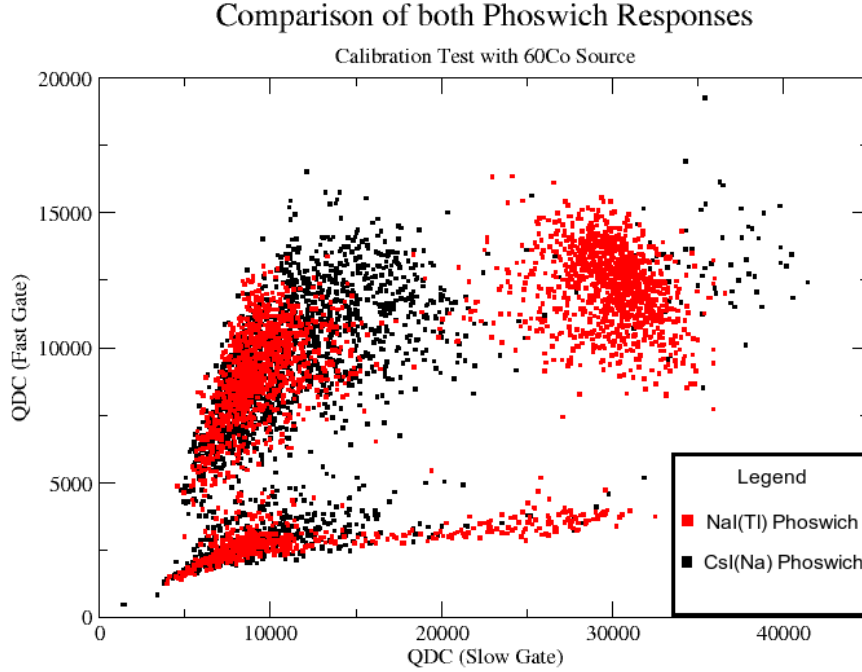


Figure 6.5: Outputs of both the NaI(Tl) and CsI(Na) phoswiches after software CFD.

The energy loss of the 767 keV proton beam through the $0.37\ \mu\text{m}$ aluminium target, was calculated using SRIM and Lise⁺⁺, two software packages widely used in γ -ray spectroscopy. It was found that the energy loss through the target was 20.35 keV, with an energy straggling σ , of 2.74 keV. The resonance strengths, $\omega\gamma$, around the 767 keV resonance are; 742, 760.4 and 773.6. These resonances are known to have high strengths from previous experiments[50][51], and therefore we can expect to see population of these states since $\Delta E \ll \Gamma$, especially the 773.6 keV resonance as its strength is higher than what we would expect for the 767 keV resonance.

Since it is approximately known what resonances are expected to be populated, calibrations can begin on the acquired spectra. Analysis of both the phoswich and $\text{LaBr}_3(\text{Ce})$ spectra were performed. Spectra recorded with the small 1" x 1" x 2" $\text{LaBr}_3(\text{Ce})$ scintillator were found to become very saturated. The saturation peak at ~ 5 MeV, was well below the expected resonance peaks at ~ 7 and ~ 10 MeV. As decreasing the applied bias of this smaller $\text{LaBr}_3(\text{Ce})$ detector

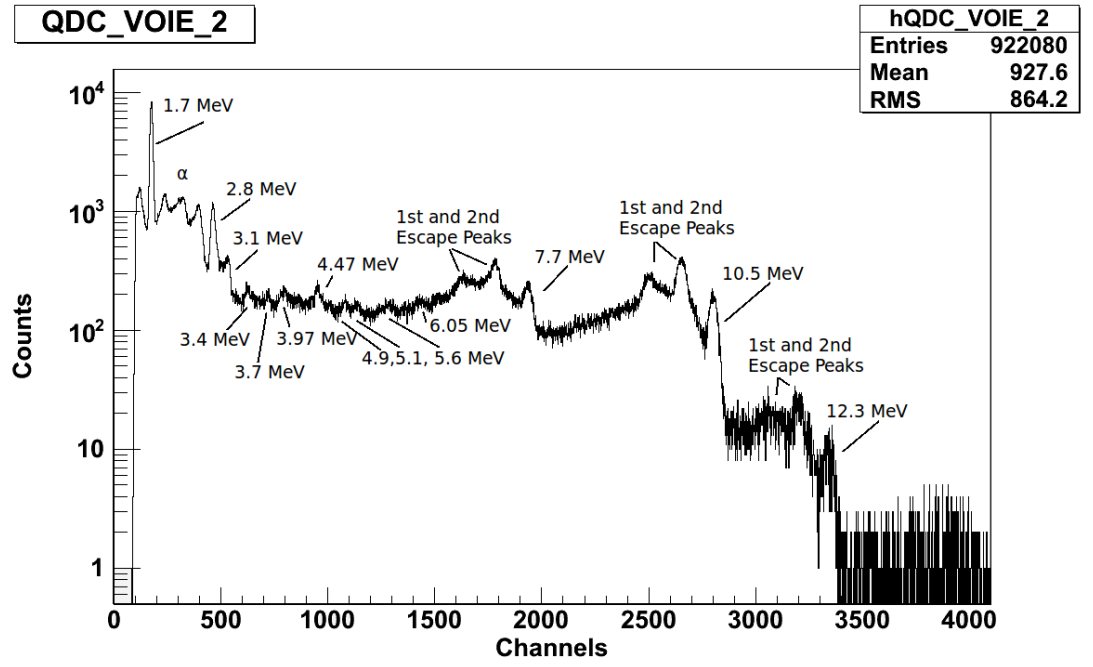


Figure 6.6: The populated levels with the large $\text{LaBr}_3(\text{Ce})$ scintillator.

would result in a reduction of the energy range detected, the larger 2" x 2" x 4" $\text{LaBr}_3(\text{Ce})$ scintillator was used. However, it was anticipated that due to the increase in size, the timing signal would be worse.

Two spectra from the 27th and 44th runs during the experiment show the difference in resolutions between the larger $\text{LaBr}_3(\text{Ce})$ scintillator and the phoswich detector containing the $\text{LaBr}_3(\text{Ce})$ and $\text{CsI}(\text{Na})$ scintillators. Both detectors are observed to be linear. Although at higher energies, the linearity within the phoswich detector begins to breakdown, as shown in figure 6.8. These are presented along with the acquired spectra for both the $\text{LaBr}_3(\text{Ce})$ scintillator and phoswich detector in figures 6.6 and 6.7 respectively.

Having examined the response of the detectors and their PMTs, the calibration of the recorded spectra can begin. The calibrations mainly focused on the more resolved runs with the larger $\text{LaBr}_3(\text{Ce})$ scintillator, showing the population of the 760, 767 and 774 keV resonances. It was expected that the energy resolution of the phoswich detector would be worse due to scintillation occurring in the $\text{CsI}(\text{Na})$ crystal, as well as in the $\text{LaBr}_3(\text{Ce})$ component. In the analysis,

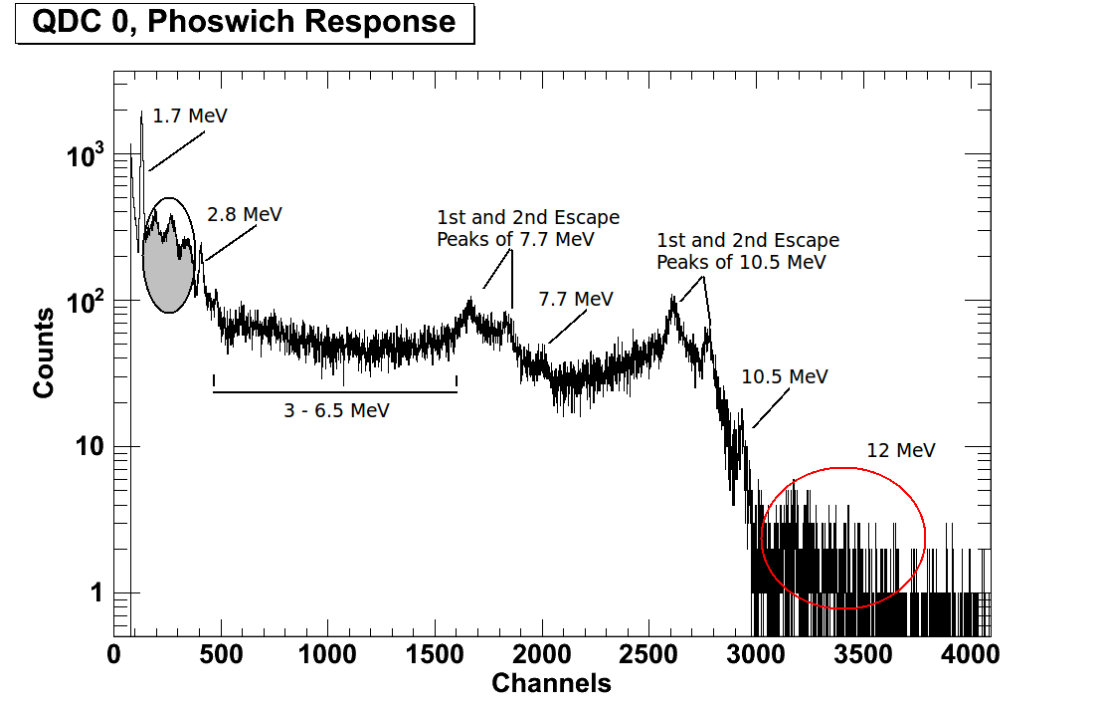


Figure 6.7: The populated levels with the phoswich detector (PW1).

it becomes obvious that at higher energies, there is a degradation in the energy resolution, particularly at around 5-6 MeV. Compton scattering is also observed to be a contributing factor to the reduction in peak heights, particularly within the 7-10 MeV region, and an absence of the 12.32 MeV transition as shown in figure 6.7.

It was expected that the resonance energies of 760, 767 and 774 keV will be heavily populated, with energy levels from the 774 keV region being noticeably strong. There was also some levels present from population of the 742 keV resonance, resulting in a fairly strong peak at ~ 3.4 MeV due to the intense decay from the resonance to a level at 8.92 MeV. Most of the transitions from the 742 keV resonance are in the higher 7-11 MeV region, with little in the middle 4-7 MeV region. This means that most of the subsequent γ rays from these energy level transitions are in coincidence with the other resonance regions, which have a far higher count rate. The higher energy region is dominated by the the 1^{st} and 2^{nd} escape peaks for the ~ 12 , 10.5, and 7.7 MeV γ -ray transitions. In the 4 - 7

6.2 $^{27}\text{Al}(p,\gamma)^{28}\text{Si}$ High Energy Beam Test

#	E_i	E_f	E_γ	Comments
1	-	-	1460.0	^{40}K
2	1778.9	0	1778.9	2^+ to 0^+ E2 transition (742,760,767,774 keV)
3	-	-	1870.0	^{227}Ac α contamination in $\text{LaBr}_3(\text{Ce})$
4	-	-	2320.0	" " " " " " " "
5	-	-	2620.0	" " " " " " " "
6	4617.8	1778.9	2838.9	4^+ to 2^+ E2 transition (742,767,774 keV)
7	r	9478.5	3063.6	$E_R = 760, 767$ keV
8	r	8920.0	3401.2	$E_R = 742$ keV
9	r	8590.0	3735.0	$E_R = 760$ and 767 keV
10	r	8420.0	3915.0	$E_R = 767$ and 742 keV
11	6276.0	1778.9	4496.8	3^+ to 2^+ M1 + E2 transition
11	r	7800.0	4525.0	$E_R = 760$ and 767 keV
12	6691.0	1778.9	4911.9	0^+ to 2^+ E2 transition ¹
13	6878.0	1778.9	5099.3	3^- to 2^+
14	r	6880.0	5447.4	$E_R = 760, 767$ and 774 keV
15	r	6282.0	6039.0	$E_R = 760$ and 767 keV
16	8590.0	1778.9	6878.6	$E_R = 760$ & 767 keV, Escape Peak
17	-	-	7216.3	Escape Peak
18	9316.1	1778.9	7537.2	$E_R = 767, 760$ and 742 keV
19	r	4617.8	7707.2	R to 4^+ , $E_R = 767$ keV
20	-	-	1778.9	Escape Peak
21	-	-	1778.9	Escape Peak
22	r	1778.9	10539	R to 2^{+2}
23	-	-	1778.9	Escape Peak
24	-	-	1778.9	Escape Peak
25	r	0	12331	R to 0^+ in 774 keV resonance

Table 6.2: Resonances identified from the $^{27}\text{Al}(p,\gamma)^{28}\text{Si}$ channel, centred at $E_p = 767\text{keV}$.

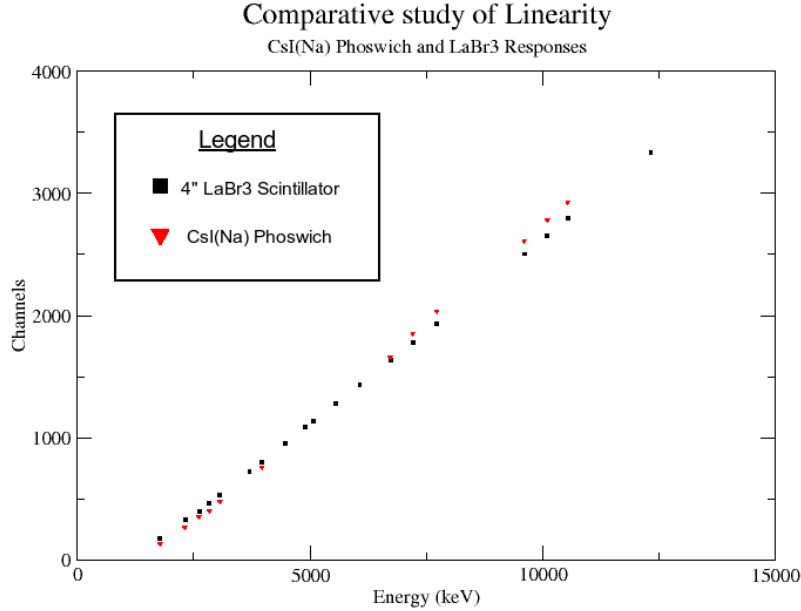


Figure 6.8: Linearity of the PW1 detector and $\text{LaBr}_3(\text{Ce})$ scintillator.

MeV region, the strongest resonance energies (760, 767, and 774 keV), populate this region with numerous transitions, largely given in table 6.2. For completeness these are the ~ 4.40 , 5.60, and 6.15 MeV γ -ray energies corresponding to transitions from the resonance at 774 keV (12.33 MeV) to levels at 7.93, 1.78 MeV. A number of the energy level transitions in the 774 keV are too weak, and are not observed due to more intense coincident energy transitions. Most of these occur in the 6-9 MeV range, although there are instances at lower energies where the α contamination might mask some energy transitions from all the populated resonance energies. The main resonance transitions are found in figure 6.9.

Overall, the beam test was successful in showing that the response of $\text{LaBr}_3(\text{Ce})$ scintillators at higher energies was very linear, and that the energy resolution at such energies was extremely good (~ 1 -1.5 % at 12 MeV). However, the response of the $\text{LaBr}_3(\text{Ce})/\text{CsI}(\text{Na})$ phoswich detector was more disappointing. The phoswich from York ($\text{LaBr}_3(\text{Ce})/\text{CsI}(\text{Na})$) was very hard to use effectively, and a very low amount of statistics was recorded when subjected to calibration

6.2 $^{27}\text{Al}(p,\gamma)^{28}\text{Si}$ High Energy Beam Test

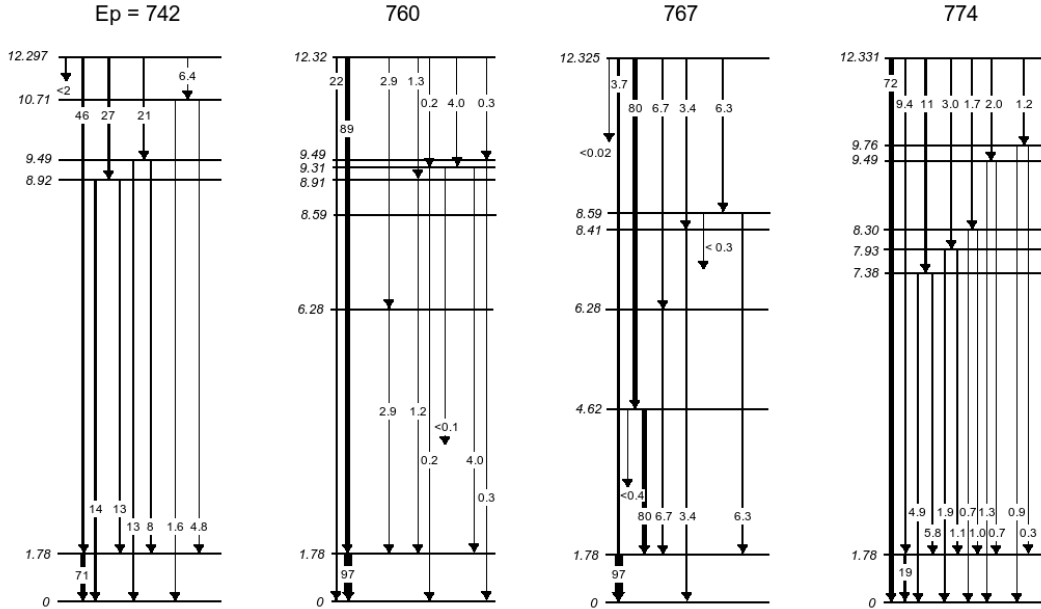


Figure 6.9: The decay schemes of the four populated resonances[50].

sources, and used in-beam. Care had to be exercised to ensure that the response from the $\text{LaBr}_3(\text{Ce})$ scintillator was optimised, and that saturation was avoided. In fulfilling this requirement, the gain had to be matched as accurately as possible in the PMT so that linearity, and energy resolution were maintained, and that there was no degradation of the signal due to saturation effects. Despite this optimisation of the response of the front end, the $\text{CsI}(\text{Na})$ behind was poorly represented. This might be due to a lower photon yield in $\text{CsI}(\text{Na})$, resulting in lower statistics due to the bias voltage being set too low. Unfortunately, increasing the gain and bias voltage produced highly non-linear spectra.

Chapter 7

Summary and Future Work

7.1 Summary

A substantial amount of progress in the development of the new photon array for the study of radiative and ion stable beams (PARIS), has been addressed in this work. The novel cubic design has been thoroughly tested under theoretical and experimental conditions. The calorimeter design allows for an inner layer of highly granular scintillators for fast timing, and high energy resolution measurements, consisting of $\text{LaBr}_3(\text{Ce})$ scintillators. The outer layer will incorporate another type of scintillator for the absorption of high energy γ -rays. Initially, three designs for the arrangement of each of these detectors were proposed involving various configurations of these two shells. These incorporated designs that included the "phoswich" method, as well as other set-ups with PMTs, and APDs. Initially, this thesis has described the details of numerous simulations performed in GEANT4, to obtain basic information regarding numerous configurations such a calorimeter can have.

Investigations of various potential geometries for the array wall were conducted; where the truncated pyramid design had the poorest absorption efficiency when compared to the rectangular, and conic designs. Other measurements of these geometries, including energy resolution, and fold, were also compared, where the conical design was found to be the best design. However, the creation of a conical $\text{LaBr}_3(\text{Ce})$ scintillator is costly, and thus the 2"x2"x4" array of rectangular

LaBr₃(Ce) crystals was the preferred geometry. Various amounts of segmentation of a "Prototype" wall were studied due to the need for the inner layer of the calorimeter to be highly granular for GDR physics cases, where it will act primarily as an energy spectrometer. Several parameters, such as changing the sizes of both the inner and outer crystals, adding gaps, and the inclusion of a doping concentration, were also investigated. A poorer than expected increase in absorption efficiency for γ rays higher than 5-10 MeV, for a thickness of 8" in the outer shell of crystals, was one of the outstanding observations from these simulations, where the addition of a doping concentration was rather insignificant. In general, the angle of incidence for simulated γ -rays was random, and further work was performed to observe the direct effect varying the angle had on the resulting energy resolution. In cases where the incident γ -ray passes through $\sqrt{2}$ material or more at $\theta > 45^\circ$ (compared to a γ ray travelling at $\theta = 0^\circ$), the energy resolution was observed to be worse by up to $\sim 45\%$.

This work was extended to larger arrays, where an increasing distance between the faces of the detectors and the source, became an increasingly important parameter. While a larger array meant better absorption, and lower fold (in the case of larger crystals), the increase in the source distance to tile the cubic array together limited any significant progress. Several other arrays were tested that followed the more conventional 4π geodesic geometry, including several CAD designs that were exported into GEANT4, by using FastRad to generate a GDML file. Comparisons of the absorption (photo-peak) efficiencies between the latest cubic design and AGATA array were also made, where the larger crystals in AGATA had a higher solid angle coverage of the source, and thus performed better than the cubic design.

All of these simulations concluded in the study of a nuclear structure case, performed in collaboration with the University of Oslo. A proposal to replace the CACTUS arrays 28 detectors of NaI(Tl) scintillators with LaBr₃(Ce) was investigated by determining the photo-peak absorption efficiencies for various sized cylindrical designs. Simulations revealed for γ rays between 0.5 and 20 MeV, that the 4"x4"x6" crystal was better due to its increase in absorption efficiency when compared with the smaller segment sizes (between 2 and 3% improvement when compared to a 3.5"x3.5"x6" crystal). Several comparisons of the energy

resolutions between the two arrays for numerous γ -rays were also presented, where the values for σ in the case of the $\text{LaBr}_3(\text{Ce})$ array, was ~ 4.8 times better than those found with the $\text{NaI}(\text{Tl})$ array. A $^{163}\text{Dy}(^3\text{He},^4\text{He})^{162}\text{Dy}$ reaction was subsequently simulated, where a comparison of the non-gated and gated spectra showed remarkable improvements, which could be furthered by improving the ToF measurements. Extraction of information regarding the energy level density from these γ - ^4He matrices can be improved substantially with $\text{LaBr}_3(\text{Ce})$ scintillators.

Tests were also performed with both a 1.5" $\text{LaBr}_3(\text{Ce})$ scintillator and phoswich detector, which consisted of two scintillators; 1"x1"x2" $\text{LaBr}_3(\text{Ce})$ and 1"x1"x6" $\text{CsI}(\text{Na})$; joined together with epoxy resin. The performance of the 1.5" $\text{LaBr}_3(\text{Ce})$ scintillator was very good, despite problems initially with saturation due to a high photon yield and poor gain-matching. This resulted in non-linear spectra, when mounted to a 2" Photonis PMT. Despite these problems, an energy resolution of 2.6 ± 0.2 % was observed when using a standard ^{137}Cs calibration source. The naturally occurring self-activity of the detector due to the radioisotope ^{139}La , and ^{227}Ac contamination was also studied, where a ratio of the light output from alphas in the scintillator when calibrated with gammas, was found to be $\alpha/\gamma = 0.65$, in good agreement with Hartwell et al.[35]. Placing the detector system in front of a AmBe neutron source resulted in a substantial amount of activation due to the large thermal neutron cross-sections of ^{139}La , ^{79}Br , and ^{81}Br present in the scintillator. A large number of pulse shapes were acquired for analysis, which were compared with γ -ray pulses recorded earlier with a ^{60}Co source. This ultimately revealed little or no discrimination between neutron and γ -ray particles.

Similar results were found for the phoswich detector, although a degradation of the signal was seen to contribute to a worse-than-expected timing and energy resolutions. Consequently, a FWHM of ~ 4 % was recorded with a ^{137}Cs source. The positioning of various sources with respect to the detector segments was also investigated. In some cases, higher energy γ -rays caused scintillation in both components of the detector resulting in the response of both the $\text{LaBr}_3(\text{Ce})$ and $\text{CsI}(\text{Na})$ scintillators, which were recorded in the same spectrum with different profiles. It was consequently found that applying the optimal bias and gain for the $\text{LaBr}_3(\text{Ce})$ scintillator, might not necessarily reflect in the performance of the $\text{CsI}(\text{Na})$ component, as in most cases too little gain was used, resulting in a very

low number of statistics. The FWHM timing resolution for the front-end of the phoswich, (where scintillation predominately occurs in the $\text{LaBr}_3(\text{Ce})$ segment), was found to be in the region of 650 ps when used in a start-stop set-up with a BaF_2 detector. Similarly, a timing resolution of 23.6 ns, was found where scintillation occurred predominately within the $\text{CsI}(\text{Na})$ scintillator. Improvement of this value was limited by the fast timing component of the BaF_2 scintillator, resulting in a poorly time matched experiment. Pile-up measurements with the phoswich were also presented, where a rough estimate of the threshold at which the rate of counts become saturated was found to be ~ 780 kHz for front-end scintillation of the detector.

In addition to the phoswich tests, another possibility was to use $\text{LaBr}_3(\text{Ce})$ or another scintillator with a novel SiPM detector. These detectors developed by SensL still have low dead space, and a large light collection area which is generated with a bias of ~ 28 V by an in-built power-board. Preliminary tests done with LEDs of various wavelengths show a degradation in the signal height (as $\lambda_{max} = \sim 520$ nm), resulting in total signal times of between 250-300 ns, and rise times of ~ 40 -60 ns for green/yellow LEDs when integrating the signal of all 16 channels. Temperature tests performed at IPHC in Strasbourg by mounting a 1"x1"x1" $\text{CsI}(\text{Tl})$ scintillator to the detector were also performed, where the noise threshold of 50-100 mV resulted in a poor S/N ratio. Consequently, poor spectra were recorded with standard ^{137}Cs and ^{60}Co sources. Temperature tests were performed with a green LED incident on the detector, which was mounted to a copper heat-sink that was filled with alcohol. This controlled the temperature of the detector, which ranged between 2° and 30° , in a thermally isolated box. Observations revealed a very stable, linear trend of decreasing resolution with decreasing temperature, where a resolution of ~ 10 % at 30° decreased to ~ 7.5 % at 2° .

Despite the shortfalls of this experiment, new arrays with FPC cables were purchased, and the power-boards constructed at the University of York. A small 1"x1"x1" $\text{CsI}(\text{Tl})$ scintillator was mounted to the detector and found to have a resolution of ~ 19 % FWHM for the 662 keV photo-peak from ^{137}Cs . However, the response from a ^{152}Eu calibration source was too poor to resolve any γ -ray lines, and no betas were detected with a ^{207}Bi source due to the high noise threshold.

Timing tests with a larger 1"x1"x6" CsI(Tl) scintillator (earlier found to have a FWHM $\sim 35\%$ at 662 keV) were performed with a 1"x1"x1" BaF₂ detector acting as the stop and start channels respectively. Despite some walk from the SensL array, a timing resolution of ~ 90 -100 ns FWHM was obtained using the ZCO triggering method, with a ²²Na source. This resolution was found to be significantly worse than what had previously been obtained with the phoswich.

Position sensitivity tests were also conducted by tiling four of these SiPM arrays along the length of the CsI(Tl) scintillator, and moving a ¹³⁷Cs source (attached to a lead collimator) along the side of the scintillator. Despite a noise threshold of ~ 50 mV, the signal heights were a respectable 0.2 to 1 V after gain-matching with a green LED. It was observed that position sensitivity was evident in these tests, where gammas were collimated from the source onto the desired detector, where the other detectors seemed to show a decrease in signal height accordingly for each position of the source. However, due to the high γ -ray energy, and small separation between each detector array, scattering within the crystal was not always localised in front of the desired detector. A mono-energetic source of lower energy, and better separation of these arrays along the edge of the scintillator should lead to a cleaner response in each case. Position sensitivity was also investigated with a small 1x1x30 mm LYSO(Ce) scintillator, by placing it horizontally and vertically along one of the arrays, so that it covered four detectors. The differences between the two set-ups are based on how the outputs are collectively summed when using a calibration source. Energy spectra were also taken, where due to the mismatch in the quantum efficiencies of both the array and scintillator, a 60% decrease in the overall light output was anticipated. Due to the small size of the scintillator, a lot of Compton scattering was observed when the array was tested with low energy sources. Despite the scintillator's high stopping power, incident γ -rays above ~ 500 keV were seen to pass through the material. Due to the high noise threshold and energy limitations of the sources used in calibration tests, spectra with poor S/N were obtained.

Numerous physics cases were outlined in the introduction to the thesis, where the incorporation of the PARIS set-up can further studies in areas such as GDR, heavy ion radiative capture, α -clustering, and hadron physics experiments. Thus,

it was imperative to study the response of both the phoswich and $\text{LaBr}_3(\text{Ce})$ detectors under experimental conditions. A well known resonant reaction; $^{27}\text{Al}(p,\gamma)^{28}\text{Si}$, was consequently studied using a proton beam energy of 767 keV impinging on a $100\mu\text{g}/\text{cm}^2$ aluminium target. Due to the large target thickness, four resonances were clearly seen at the beam energy with a large 2" x 2" x 4" $\text{LaBr}_3(\text{Ce})$ scintillator provided by one of the collaborative institutions. A smaller 1" x 1" x 2" $\text{LaBr}_3(\text{Ce})$ scintillator and $\text{LaBr}_3(\text{Ce})/\text{NaI}(\text{Tl})$ phoswich, with similar dimensions to the the phoswich detector used in previous tests in York, were also provided. Fast and slow gates used with several QDC modules revealed discrimination between the responses from both signals from each component of the $\text{LaBr}_3(\text{Ce})/\text{NaI}(\text{Tl})$ phoswich, which was not seen as clearly with the $\text{LaBr}_3(\text{Ce})/\text{CsI}(\text{Na})$ phoswich. This is likely to be due to poor gain matching when trying to optimise both signals to avoid saturation (primarily from the $\text{LaBr}_3(\text{Ce})$ scintillator). Despite this, both phoswiches were found to be quite linear below 10 MeV, although an increase in the gain and bias to improve statistics in the $\text{CsI}(\text{Na})$ component resulted in a degradation of this linearity. The 2" x 2" x 4" $\text{LaBr}_3(\text{Ce})$ scintillator used a 1 GHz digitiser and QDC in analogue mode, where it performed very well, with good linearity for gates of 150 ns and 80 ns. The linearity was seen to change as a function of the timing used to gate the pulses, where FWHM resolutions of the 2^+ to ground transition and 10.54 transition were found to be a respectable 2.47 and 1.43 % respectively with the longer 150 ns gate.

7.2 Future Work

The simulations seem to give an accurate description of the response from the scintillators, where further improvements to the existing PARIS simulation program can be made by adding the natural background due to self-activity, for example. A radiative capture experiment has already been simulated[52], for the spherical designs of the PARIS calorimeter, where an extension can be made by comparing the response for this set-up, with the results of a similar simulation done with the cubic geometry.

While no (n,γ) discrimination was found to be possible for the neutron tests, ToF separation between neutrons and gammas in large $\text{LaBr}_3(\text{Ce})$ scintillators has been performed by members of the collaboration. Since discrimination is very beneficial for the Jacobi shape transition case outlined in this thesis, a better study of the neutron activation needs to be addressed, as neutrons (especially at higher energies) become increasingly important for GDR scenarios. Since activation has been seen to occur at relatively low energies due to the large thermal neutron cross-sections, a better understanding of the threshold of this activation, and response of high energy neutrons, needs to be addressed with a neutron gun. These two studies could effectively be combined into one, and would be very beneficial information to know in completing the study of the response of these scintillators with neutrons.

There is also a lot of interest in trying to develop SiPMs that are sensitive to the blue end of the electromagnetic spectrum, where the maximum light emission from $\text{LaBr}_3(\text{Ce})$ occurs at $\lambda_{max} = 380$ nm. As of recently, only small pixel detectors or PIN diodes have been developed within this wavelength range, with current large APDs (such as the ones discussed in this chapter from SensL), predominately achieving maximum light collection in the green part of the EM spectrum at $\lambda_{max} \sim 520$ nm. The use of these detectors in unison with the two layers of scintillators proposed for PARIS, would further the reduction in dead space, and increase the overall efficiency of the calorimeter, where preliminary results are starting to investigate this possible option[53]. The alternative is to investigate the use of wave shifting fibres, where light collection can be achieved due to total internal reflection within the fibre. To maximise the light propagation along the fibre, a large shift between the optical absorption and emission bands are needed so that self-absorption is reduced as much as possible. The most common type of wave shifter allows absorption in the blue portion of the spectrum, and the re-emission to be in the green or yellow part of the electromagnetic spectrum, without substantial loss to the overall light output.

One of the most important factors to consider with this technique is the quantum efficiency of the wavelength shifter, and the probability that the peak emission wavelength of the scintillator matches the fibre, so that a wave-shifted photon will be emitted per absorbed photon. High quantum efficiencies are needed to

preserve the information in the signal as well as statistical information carried by the number of original photons from the scintillator. Another important factor one should note is the decay time of the wave-shifting molecules, especially when using them with $\text{LaBr}_3(\text{Ce})$ scintillators. The absorption and re-emission of the primary scintillation light can slow the light emission, especially if the lifetime of the wavelength shifting excited states are similar in length to that of the primary fluorescence, or longer. This can have severe implications on the timing resolution with $\text{LaBr}_3(\text{Ce})$, as the timing characteristics will be defined by the wave-shifter and not by the light from the scintillator.

This set-up could be used with the phoswich detector, although this needs to be investigated. It is likely that because of the weak $\text{CsI}(\text{Na})$ signals, any further loss of the information in the signal, and loss of light in this process would result in the response of this segment being completely lost.

There are many other extensions that can use the advantages found with the SiPM and phoswich detectors. The phoswich method works very well, and whether this research can be furthered by using SiPMs remains to be seen. The results with the novel SiPM arrays are a positive step, however a lot more work needs to be done in order to realise their true potential, where it is expected that a detector system with a large number of SiPM arrays, with an optimum quantum efficiency and timing response, will be a serious contender to the conventional detector arrays using PMTs. However, it all depends on the physics cases, and whether the detectors will ultimately be tailored for timing or energy measurements.

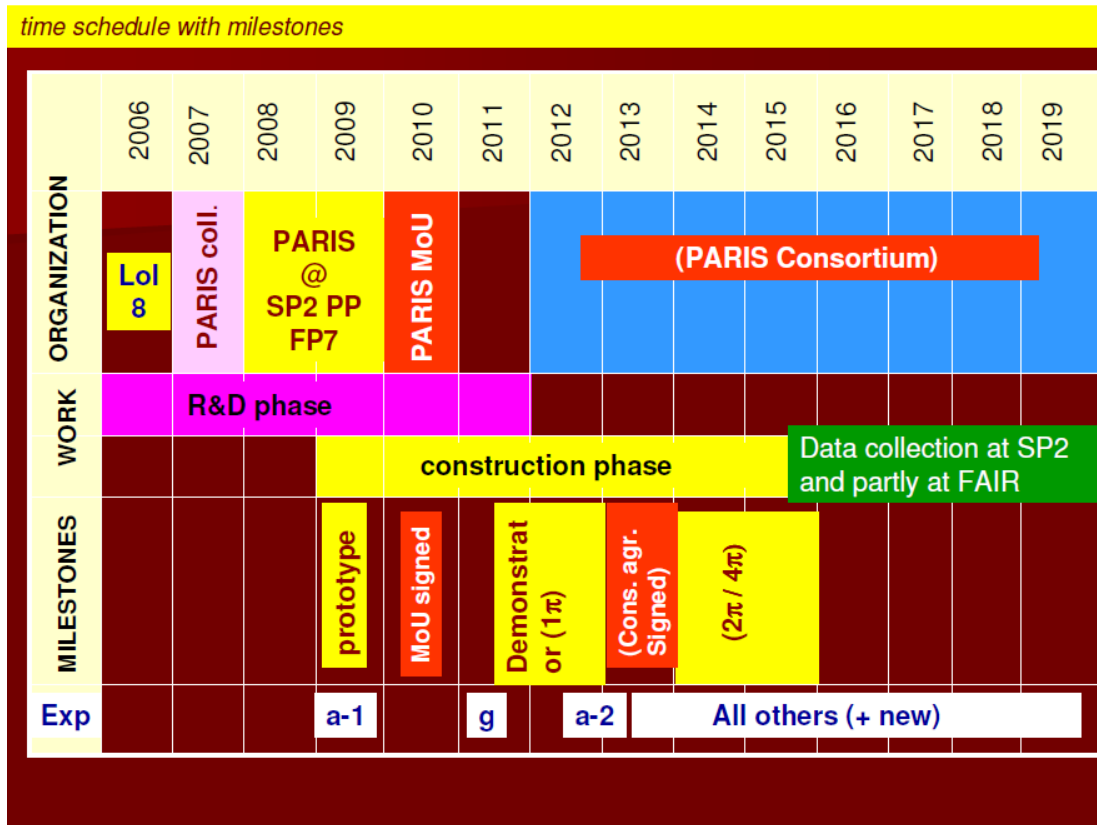


Figure 7.1: Timeline of the PARIS collaboration.

The PARIS collaboration still endeavours to maintain its progress in developing a highly efficient γ -ray calorimeter. The time-line of the progress expected from the collaboration is presented in figure 7.1. However, due to the deterioration of the present financial climate, the time-line is out of date, and behind schedule. However, many detectors and detector methods have been bought and tested, aiding to the progress of PARIS, where it is anticipated that a prototype array of $\text{LaBr}_3(\text{Ce})$ scintillators will be bought and tested under experimental conditions in the near future.

Appendices

Appendix A

Future Physics Cases

Physics Case	Recoil	v/c (cmms^{-1})	E_y range (MeV)	$\Delta E_y / E_y$ (%)	$\Delta \Sigma_y^{\text{sum}} / \Sigma_y^{\text{sum}}$ (%)	ΔM_y (units)	Ω coverage (sr) (finally)	ΔT of (ns)	Ancillaries (prototype scenario)	Miscellaneous
Jacobi transition	A~ 40-150	up to 10%	[0.1-30]	6	< 5	< ~ 5	$2\pi - 4\pi$	< 1	γ -calorimeter* AGATA ** HI spectro	High efficiency Beam rejection ?
Shape Phase Diagram & Hot GDR in n- rich nuclei	A~ 180	up to 11%	[0.1-30]	6	~ 3 < 5	< ~ 5	$2\pi - 4\pi$ >10% / 4π	< 1	γ -calorimeter HI spectro	High efficiency Beam rejection ?
Isospin mixing	A~ 60-100	up to 7%	[5-30]	6	-	-	up to 4π	< 1	γ -calorimeter HI spectro	High efficiency Beam rejection ?
Reaction dynamics	A~ 160-220	up to 7%	[0.1-25]	6-8	< 8	~ 4	up to 2π	< 1	γ -calorimeter n detector FF detector	Complex coupling
Collectivity vs. multifragmenta tion	A~ 120-200	up to 8%	[5-25]	5	-	-	up to 2π	< 1	γ -calorimeter LCP detector HI detector	Complex coupling

Figure A.1: Various parameters for numerous proposed physics cases intended for PARIS[54].

Physics Case	Recoil	v/c	E_γ range (MeV)	$\Delta E_\gamma / E_\gamma$ (%)	$\Delta \Sigma_\gamma^{sum} / \Sigma_\gamma^{sum}$ (%)	ΔM_γ (units)	Ω coverage (sr) (finally)	ΔT of (ns)	Ancillaries (prototype scenario)	Miscellaneous
Radiative Capture	A~ 20-30	up to 3%	[1-30]	< ~4	< 5	rough	$\sim 4\pi$	< 1	HI spectro	High efficiency High current ?
Multiple (normal) Coulex	A~ 40	up to 7%	[2-6]	~ 5	-	-	up to 2π	< 1	AGATA CD detectors	Complex coupling
Astrophysics	A~ 16-90	< 0.2%	[0.1-6]	-	< 5	rough	$\sim 4\pi$	< 1	γ -calorimeter	High efficiency Background
Shell structure at intermediate energies	A~ 16-40	up to 40%	[0.5-4]	~ 3	-	-	up to 4π	< 1	γ -calorimeter HI analyzer	High efficiency - very low I_{beam} - γ - γ coincidence
Relativistic Coulex	A~ 40	up to 50-60%	[1-4]	~ 4	-	ideally, $M_\gamma = 1$	forward with $\sim \pi / 3$ aperture	< 1	AGATA HI analyzer	Angular distribution Lorentz boost

Figure A.2: Various parameters for numerous proposed physics cases intended for PARIS[54].

Appendix B

Simulation Work

B.1 Using Add-back Techniques

The original trajectory of the incident γ -rays were replicated by adding their particle tracks; "addback". An addback algorithm was constructed to disentangle γ -ray tracks in numerous adjacent crystals, where an example of a simple addback algorithm was done with the central crystal. Investigation of the two escape peaks for a 15 MeV γ -ray (where the energy was deposited between 14.4 MeV and 15 MeV), was performed in ROOT. An increase in the number of counts is observed when add-back is included, allowing for better statistics.

LaBr ₃ (Integral Measurements)	
Without "addback"	With "addback"
9351	10042

Table B.1: Addback measurements for LaBr₃.

B.2 Examples of other PARIS Designs

CsI (Integral Measurements)	
Without "addback"	With "addback"
2479	2887

Table B.2: Addback measurements for CsI.

By adding these tracks, one can ultimately improve the energy resolution and resulting spectra. It should be said that although this improvement is small, its not negligible, as it improves the quality of energy spectra by $\sim 10\%$ in some cases. A newer algorithm is currently being sought and worked on within the collaboration to increase this measurement further, especially in the case of larger arrays.

B.2 Examples of other PARIS Designs

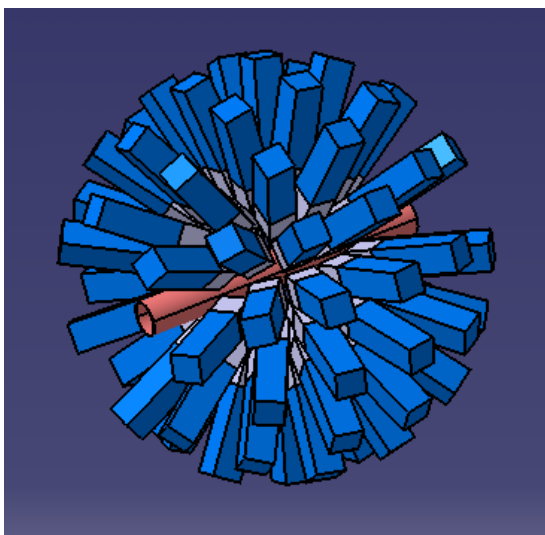


Figure B.1: A CAD drawing of a proposed 4π set-up for PARIS.

B.2 Examples of other PARIS Designs

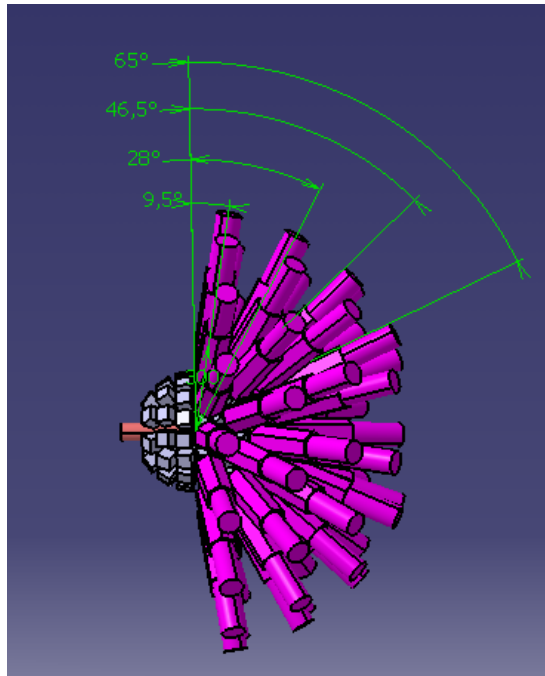


Figure B.2: One of the spherical designs for PARIS.

B.3 Additional AGATA Spectra

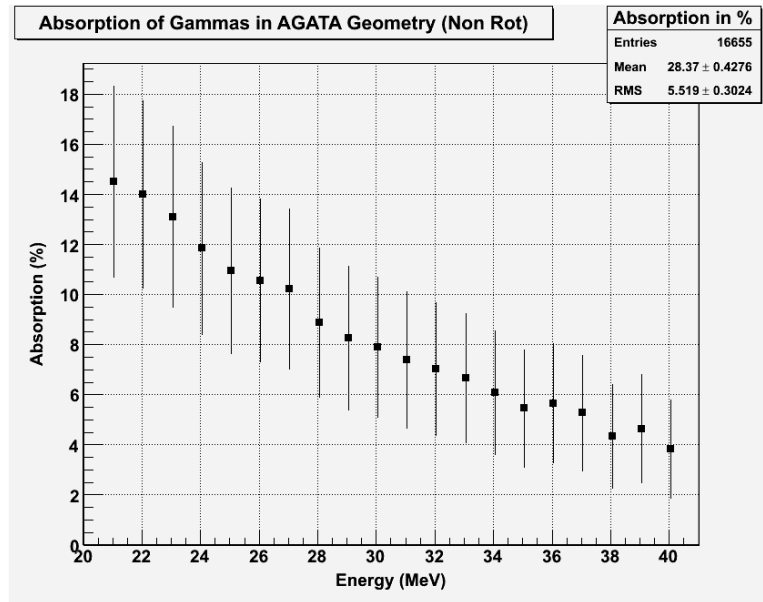


Figure B.3: Absorption efficiency of the LaBr₃(Ce) AGATA array between 20-40 MeV, (errors are statistical).

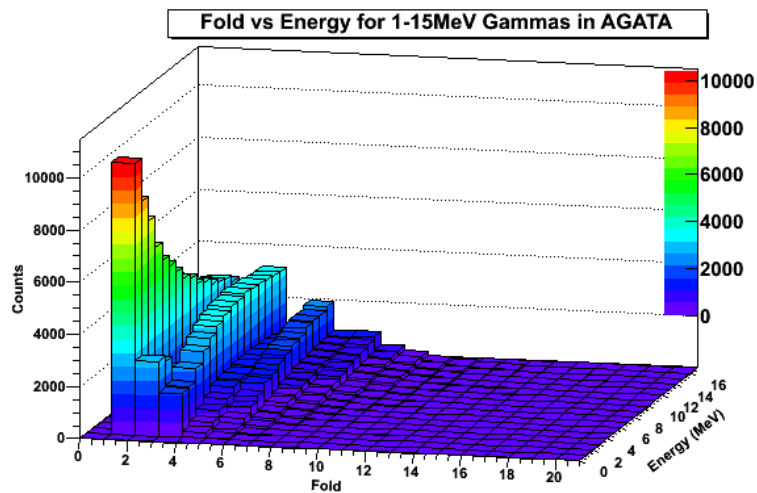


Figure B.4: Low energy Fold distributions of the LaBr₃(Ce) AGATA array

Appendix C

Simulation of Physics Case

C.1 Photo-peak Efficiency Response of CAC-TUS

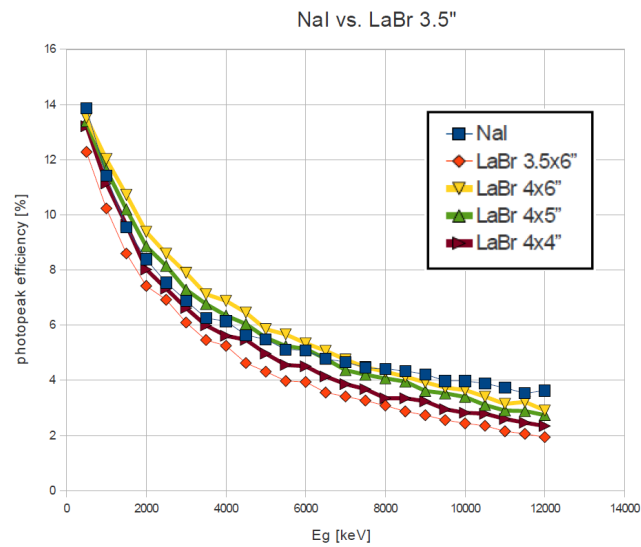


Figure C.1: Photo-peak efficiency for various E_γ [30]

C.2 Additional Gates of the Simulated ^{162}Dy case

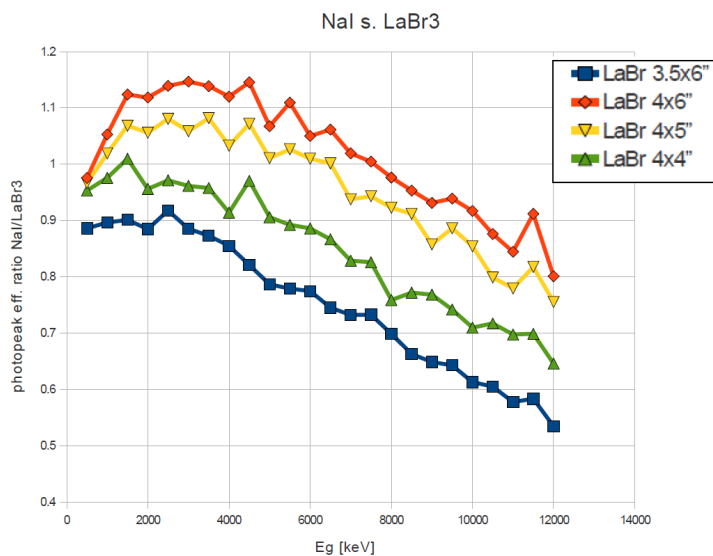


Figure C.2: NaI(Tl)/LaBr₃ ratio of photo-peak efficiency for E_γ [30].

C.2 Additional Gates of the Simulated ^{162}Dy case

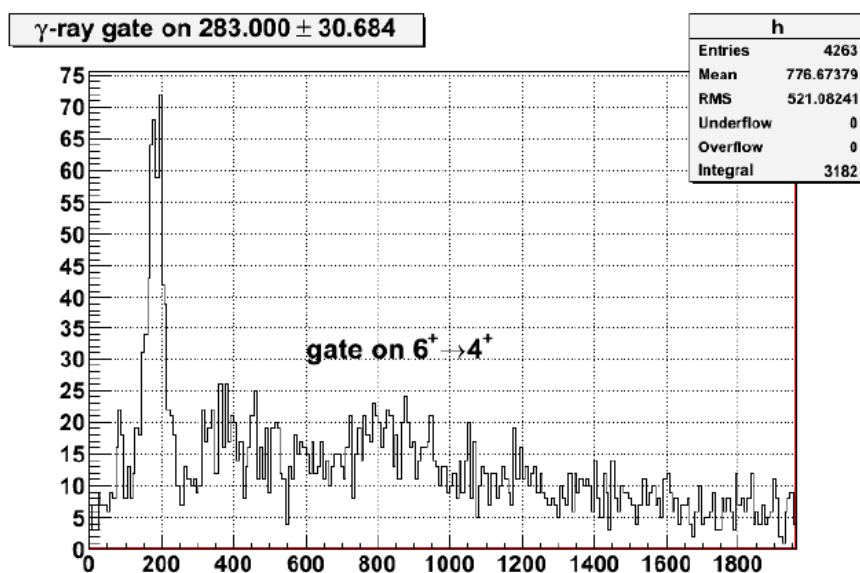


Figure C.3: NaI(Tl) spectrum gated on $6^+ \rightarrow 4^+$. [30]

C.2 Additional Gates of the Simulated ^{162}Dy case

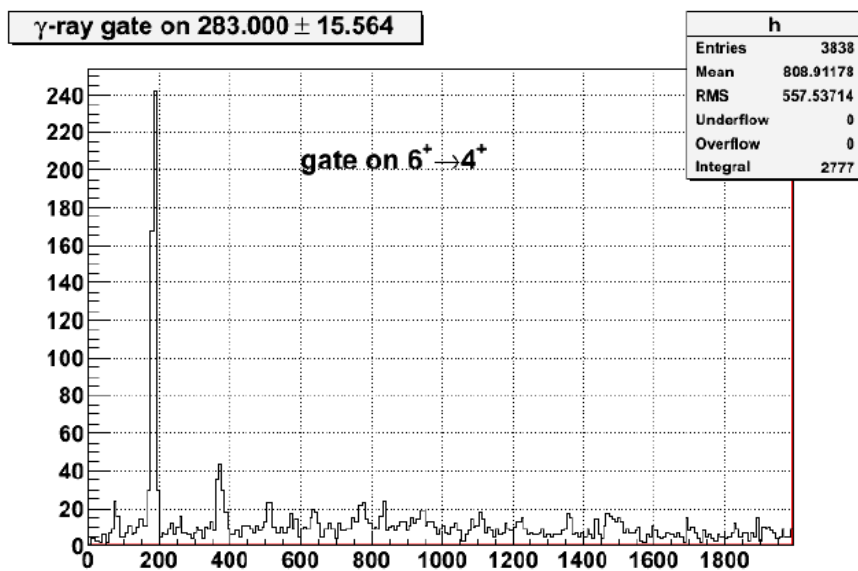


Figure C.4: LaBr₃ spectrum gated on $6^+ \rightarrow 4^+$. [30]

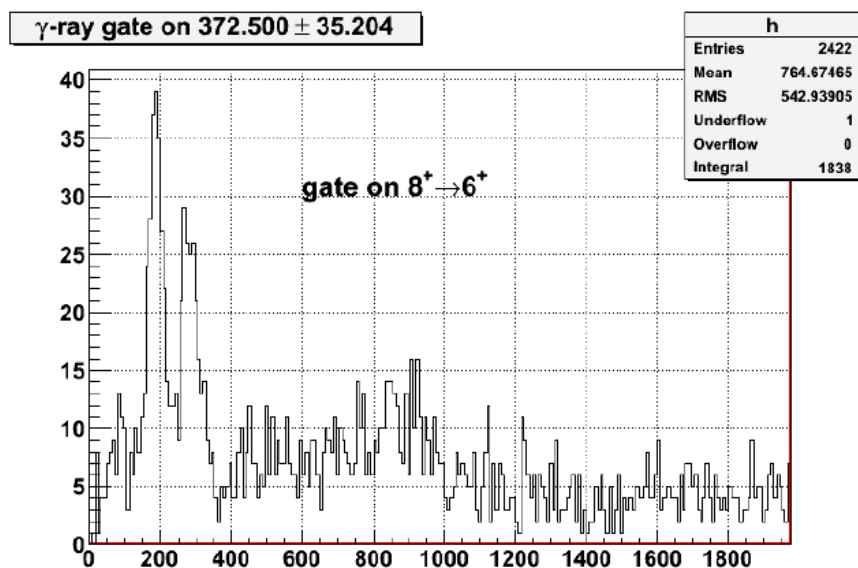


Figure C.5: NaI(Tl) spectrum gated on $8^+ \rightarrow 6^+$. [30]

C.2 Additional Gates of the Simulated ^{162}Dy case

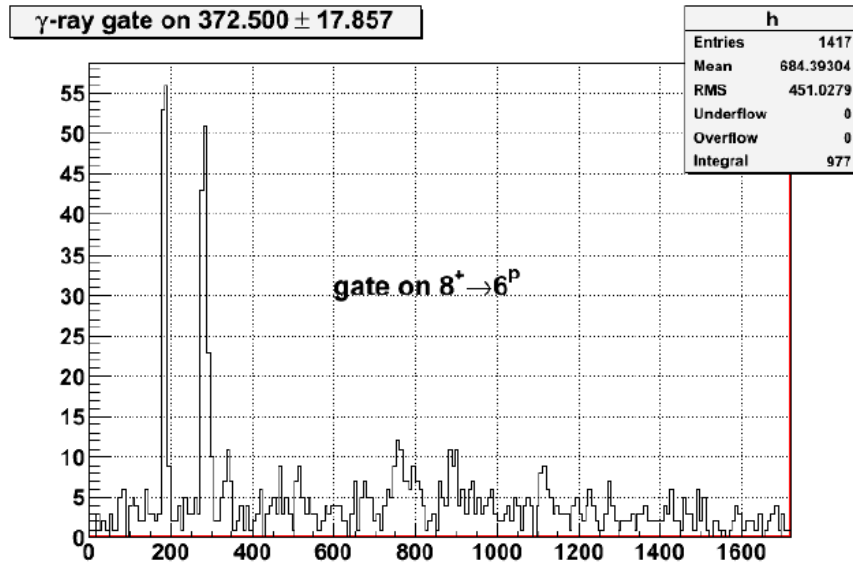


Figure C.6: LaBr₃ spectrum gated on $8^+ \rightarrow 6^+$. [30]

List of References

- [1] Adam Maj. Status of the PARIS Collaboration, May 2008. 2
- [2] A.Maj et al. The Paris Project. *ACTA Physica Polonica B*, 40(3):565–575, March 2009. 3, 7, 8
- [3] K.S.Shah, J.Glodo, M.Klugerman, W.W.Moses, S.E.Derenzo, and M.J.Weber. LaBr₃(Ce) Scintillators for Gamma Ray Spectroscopy. *Lawrence Berkeley National Laboratory, University of California*, LBNL-51793, 2002. 3, 24, 111, 121
- [4] Thierry Morin and Simon Holzman. S³: Super Separator Spectrometer, October 2010. 4
- [5] A.Maj et al. Search for Jacobi shape transitions in light nuclei. *European Phys. Journal A*, 20:165–166, March 2004. 6
- [6] A.Maj et al. Evidence for the Jacobi shape transition in hot ⁴⁶Ti. *Nuclear Physics A*, 731:319–326, 2004. 7
- [7] L. Paredes, R. Genis, M. Balczar, L. Tavera, and E. Camacho. Fast neutron leakage in 18 Mev medical electron accelerator. *Radiation Measurements*, 31:475–478, June 1999. 8
- [8] H. Oberhummer, H. Krauss, K. Gruen, T. Rauscher, H. Abele, P. Mohr, and G. Staudt. Alpha clustering and the stellar nucleosynthesis of carbon. *Z. Phys. A.*, 349:241–242, 1994. 10

LIST OF REFERENCES

- [9] D.G.Jenkins et al. Decay Strength distributions in $^{12}\text{C}(^{12}\text{C},\gamma)$ radiative capture. *Physical Review C*, 76:1–14, October 2007. 11
- [10] K.Langanke, C.Rolfs, and et al. Resonant and Intrastate Transitions to the 2^+ in ^8Be . *Z. Physics A*, 324:307–310, March 1986. 12
- [11] V.M.Datar, Suresh Kumar, and et al. Direct Observation of the 4^+ -to- 2^+ Gamma Transition in ^8Be . *Physics Review Letters*, 94:1–4, April 2005. 12, 13
- [12] C.M.Tarbet, D.P.Watts, and et al. Incoherent Neutral Pion Photoproduction on ^{12}C . *Physics Review Letters*, 100:1–5, April 2008. 14, 16
- [13] Wikipedia. Spin quantum number. 19
- [14] W.R.Leo. *Techniques for Nuclear and Particle Physics Experiments*. Springer-Verlag, New York LLC, Second Revised Edition edition, 1994. Chapter 7, pp158-159,[7.2]. 23, 31, 34, 35, 109
- [15] W.J.Kerman. Self Activity in Lanthanum Halides. *IEEE Trans. Nucl. Sci.*, 53:395–400, 2006. 23
- [16] M.Moszynski et al. New Photonis XP020D0 photomultiplier for fast timing in nuclear medicine. *NIM A*, 567:31–35, March 2006. 25
- [17] K. V. Shakhova, A. N. Panova, V. I. Goriletsky, Ya. A. Prikhod'ko, V. P. Gavrylyuk, S. P. Korsunova, and N. N. Kosinov. Luminescence and scintillation properties of Na-activated CsICsBr crystals. *Elsevier, NIM A* , 33:769–771, October 2001. 26
- [18] Bridgeport Instruments LLC. eMorpho MCA, September 2007. 26
- [19] Hilger Crystals Ltd. Properties of CsI(Tl), 1999. 27, 139
- [20] Tumpa Bhattacharjee, Swapan Kumar Basu, Chandi Charan Dey, and Mihir Baran Chatterjee. Comparative studies of YAG(Ce) and CsI(Tl) scintillators. *Elsevier, NIM A*, 484:364–368, May 2002. 27

LIST OF REFERENCES

- [21] Saint Gobain Cermaics and Plastics Ltd. NaI(Tl) and Polyscin NaI(Tl) Sodium Iodide Scintillation Material. *Saint Gobain Crystals and Scintillation Products*, 2005-8. ... 27
- [22] W.R.Leo. *Techniques for Nuclear and Particle Physics Experiments*. Springer-Verlag, New York LLC, Second Revised Edition edition, 1994. Chapter 8. 32, 33, 34
- [23] W.R.Leo. *Techniques for Nuclear and Particle Physics Experiments*. Springer-Verlag, New York LLC, Second Revised Edition edition, 1994. Chapter 14. 36, 38
- [24] CAEN S.p.A. Vme - V965: 16 Channel Dual Range Multievent QDC, 2000-2010. 38
- [25] S. Agostinelli and J. Allison et al. Geant4: A Simulation Toolkit. *Elsevier, NIM*, 506:250–303, July 2003. 44, 47
- [26] D.C.Radford. *Notes on the use of the program gf3*, HTML Version 1.1 edition, May 2002. 49
- [27] M.Ciemala. Remarks on granularity of PARIS. ... 52, 53
- [28] M. Ciemala, D. Balabanski, M. Csatlos, and J.M. Daugas et al. Measurements of high-energy γ -rays with LaBr₃(Ce) detectors. *NIM A*, 608:76–79, 2009. 54, 60, 105, 114, 115
- [29] M.Ciemala. Examples of a response of the labr₃ detector for 800 keV and 15 MeV in the case of cubic and perfect conical shapes, 2008. 77
- [30] Alexander Buerger. Efficiency Comparison NaI-LaBr. priv. comm. University of Oslo, September 2010. 93, 94, 96, 97, 98, 99, 191, 192, 193, 194
- [31] I. Huseby et al. K hindrance in primary γ -decay after thermal and average resonance neutron capture. *Physics Review C*, 55:1805–1809, April 1997. 94
- [32] M. Guttormsen et al. Nonstatistical Cooling of the Highly Excited ¹⁶¹Dy Nucleus. *Physics Review Letters*, 52:102–104, January 1984. 94

LIST OF REFERENCES

- [33] Oslo Cyclotron Laboratory. Nuclear Physics. 95
- [34] C.M.Rozsa, P.R.Menge, and M.R.Mayhugh. BrillLance Scintillators Performance Summary. *Saint-Gobain Crystals, Scintillation Products*, April 2008. www.detectors.saint-gobain.com. 101, 102, 105
- [35] J.K.Hartwell and R.J.Gehrke. LaBr₃(Ce) Scintillators for Gamma Ray Spectroscopy. *Appl. Radiat. Isot.*, 63:223, 2005. 102, 176
- [36] G.Pfennig, H.Klewe-Nebenius, et al. Karlsruhe Nuklidkarte, 1995. 108
- [37] C.Hoel et al. Pulse Shape Discrimination of La Halides. *Elsevier, NIM*, A540:205–208, April 2005. 111
- [38] Glen.F.Knoll. *Radiation Detection and Measurement*. John Wiley and Sons Inc., Hoboken, New Jersey, U.S.A, Third Edition edition, 2000. Chapter 10, pp344-345,[10.VII.A]. 111, 119
- [39] S.Brambilla, F.Camera, and M.Cuccarese et al. Digital Adaptive Timing and Energy Measurements of BaF₂ and LaBr₃ Scintillator Events. In *IEEE Nuclear Science Symposium Conference Record*, volume N15-113, 2007. 121
- [40] T. J. Paulus. Fast Timing Methods with Scintillation Detectors. *IEEE Transactions on Nuclear Science*, NS-32:1242–1249, June 1985. 123
- [41] W.R.Leo. *Techniques for Nuclear and Particle Physics Experiments*. Springer-Verlag, New York LLC, Second Revised Edition edition, 1994. Chapter 9, pp210,[9.7.3]. 125
- [42] Vladimir Solovyev. Performance of Sodium Iodide and BrillLanCe 350 and BrillLanCe 380 for High Count Rate Applications. http://www.detectors.saint-gobain.com/uploadedFiles/SGdetectors/Documents/Technical_Information_Notes/Performance-NaI-B350-B380-High-Count-Rate-Applications.pdf, November 2008. 127, 164

LIST OF REFERENCES

- [43] Glen.F.Knoll. *Radiation Detection and Measurement*. John Wiley and Sons Inc., Hoboken, New Jersey, U.S.A, Third Edition edition, 2000. Chapter 11, pp355,[11.2]. 133
- [44] Glen.F.Knoll. *Radiation Detection and Measurement*. John Wiley and Sons Inc., Hoboken, New Jersey, U.S.A, Third Edition edition, 2000. Chapter 11, pp356,[11.3]. 133
- [45] SensL. *SPMPlus Large Area Silicon Photomultiplier*, August 2008. 134, 135, 136, 137, 144
- [46] Saint Gobain Cermaics and Plastics Ltd. CsI(Tl) and CsI(Na) Scintillation Material. *Saint Gobain Crystals and Scintillation Products*, July 2008. ... 139
- [47] Saint Gobain Cermaics and Plastics Ltd. Prelude420 Scintillation Material. *Saint Gobain Crystals and Scintillation Products*, July 2008. http://www.detectors.saint-gobain.com/uploadedFiles/SGdetectors/Documents/Product_Data_Sheets/PreLude420-Data-Sheet.pdf. 154
- [48] Claus.E.Rolfs and William S. Rodney. *Cauldrons in the Cosmos: Nuclear Astrophysics (Theoretical Astrophysics)*. University Of Chicago Press, 1427 East 60th Street, Chicago, IL 60637 U.S.A., First Edition edition, 2005. ... 160, 161, 162
- [49] Olivier Dorvaux and Christian Finck et al. Test Strasbourg May 2010, 2010. 165, 166, 167
- [50] P.M.Endt and A. Heyligers. Energy levels in ^{28}Si from the $^{27}\text{Al}(p,\gamma)^{28}\text{Si}$ reaction. *Physica*, 26:230–254, April 1960. 168, 173
- [51] S. Harissopulos, C. Chronidou, and et al. The $^{27}\text{Al}(p,\gamma)^{28}\text{Si}$ reaction: direct capture cross-section and resonance strengths at $E_p = 0.2\text{-}1.12$ MeV. *The European Physical Journal A - Hadrons and Nuclei*, 9:479–489, December 2000. 168

LIST OF REFERENCES

- [52] Dorothee Lebhertz. *Decay modes of resonant radiative capture reactions in $^{12}\text{C} + ^{12}\text{C}$ and $^{12}\text{C} + ^{16}\text{O}$ collisions*. PhD thesis, Universit de Strasbourg, Strasbourg, France, 2010. 179
- [53] Jeremy Flamanc and Csaba Rozsa. Compact $\text{LaBr}_3(\text{Ce})$ Gamma Ray Detector with Si-APD Readout. In *AIP CAARI Conference Proceedings*, volume 1099, March 2009. 180
- [54] Christelle Schmitt. Towards the definitions of paris' key experiments, May 2008. 185, 186